Universidad
de La Laguna

Escuela de Doctorado
y Estudios de Posgrado

TÍTULO DE LA TESIS DOCTORAL

"Weighted Fourier Phase Slope as a Centroiding Method in a Shack-Hartmann Wavefront Sensor for Adaptative Optics in Astronomy"

AUTOR/A

HARESH	MANGHARAM	CHULANI

DIRECTOR/A

JOSE MANUEL	RODRIGUEZ	RAMOS

CODIRECTOR/A

DEPARTAMENTO O INSTITUTO UNIVERSITARIO

FECHA DE LECTURA

04/09/17

Weighted Fourier Phase Slope as a Centroiding Method in a Shack-Hartmann Wavefront Sensor for Adaptive Optics in Astronomy

Haresh Mangharam Chulani

Submitted in partial fulfilment of the requirements
for the degree of Doctor of Philosophy in
Physics and Engineering

Thesis director: Dr. José Manuel Rodríguez Ramos

June, 2017

To my parents,

Acknowledgements

Very many people have, knowingly or unknowingly, contributed to the accomplishment of the present work. Here is a list of just a few of them.

First of all, I would like to thank my thesis director, José Manuel Rodríguez Ramos, for his guidance, advice, and always open, positive and optimistic attitude, from the commencement till the completion of this work.

My special gratitude is for Ezequiel Ballesteros Ramírez, my colleague at the IAC (Instituto de Astrofísica de Canarias), for transmitting me encouragement and motivation to perform a research work like the present one, and for his thorough and disinterested revision of the full text.

This work was executed in parallel with my participation in the EDiFiSE (Equalized and Diffraction limited Field Spectrograph Experiment) project at the IAC, and received much input from it. I would like to thank the former principal investigator of the project, Jesús Jiménez Fuensalida, from whom I learnt about atmospheric turbulence characterization and emulation, Luis Fernando Rodríguez Ramos for his ever readiness to discuss any (mainly technical) topic, Ángel Alonso for the project management, Yolanda Martín for the FPGA and user interface programming, Félix Gracia for his support in dealing with the optical system, and Francesca Pinna and Enrique Joven for their help in the EMCCD (Electron Multiplying Charge Coupled Device) camera characterization method validation.

I would also like to thank Jose Antonio Acosta Pulido, EDiFiSE's present principal investigator, and Luzma Montoya, also from the IAC, for providing me with uselful and relevant bibliography.

Finally, I would like to express my gratitude to all my relatives and friends who have understandingly allowed me the time and space and heartfeltly wished for the successful completion of this work.

Sigh.- I caught this insight on the wing and quickly took the nearest shoddy words to fasten it lest it fly away from me. And now it has died of these barren words and hangs and flaps in them – and I hardly know any more, when I look at it, how I could have felt so happy when I caught this bird.

(Friedrich Nietzsche: “The Gay Science”, book IV, section 298)

Abstract

Among the latest developments in Adaptive Optics (AO) systems, Multi Object Adaptive Optics (MOAO) systems span a large sensing field of view in the order of arcminutes, and correct only the small portions of the sensed field of view where the scientific objects of interest are situated, in the order of arcseconds each. Thus, they operate in open loop correction mode, and their wavefront sensors need to deal with the large dynamic range of the uncorrected atmospheric turbulence. This means that they need to be sensitive in low light level scenarios as well as operate in larger fields of view as compared to the traditional closed loop correction mode operation. Besides, Shack-Hartmann wavefront sensors (SHWFS) continue to be the most widely employed and to have the most matured technology amongst wavefront sensors to be found in astronomy applications.

The objective of the present work is to explore the performance of an innovative centroiding algorithm at the subpupil image of a SHWFS, for point-like guiding sources. It has been named *Weighted Fourier Phase Slope*, because it estimates the image's displacement in the Fourier domain by directly computing the phase slope at several spatial frequencies, without the intermediate step of computing the phase; it then applies optimized weights to the phase slopes at each spatial frequency obtained by a Bayesian estimation method. The idea has been inspired by cepstrum deconvolution techniques, and this relationship is explained.

This algorithm's tilt estimation performance is characterized and contrasted with other known centroiding algorithms, such as Thresholded Centre of Gravity (TCoG) and Cross Correlation (CC), through numerical simulations in Matlab™, first at a subpupil level. Figures of merit such as computational cost, sensitivity in low light level conditions, linearity and preferred field of view of operation, and robustness against atmospheric turbulence high order aberrations of the spots, are all taken into account in open loop operation simulations. Some effort has also been made to extend this comparison to a closed loop operation situation. Results show a similar sensitivity to that of the CC algorithm, which is superior to the one of the TCoG algorithm when big fields of view are necessary, i.e., in the open loop correction case. On the other side, its advantage over the CC algorithm is an approximately one order of magnitude lower computational cost. Also, as there is no threshold application over the image, it is useful when the complete spot, including its low light level portion, is to be considered for the centroid computation.

Numerical simulations are then extended to the complete sensor's pupil with the aid of the Object Oriented Matlab™ for Adaptive Optics (OOMAO) toolbox, thus including the sensor's fitting error in the simulations. Results are shown as Strehl Ratio (SR) or Encircled Energy (EE) as a function of Natural Guide Star (NGS) magnitude, and are in good coincidence with the subpupil level simulations.

Finally, the laboratory optical setup of the EDiFiSE (Equalized and Diffraction limited Field Spectrograph Experiment) project has been employed to corroborate the results obtained by numerical simulations, and as a means to exemplify the algorithm's tuning in a real case, which is done by simulating the real system's geometry. In this regard, the EDiFiSE's EMCCD (Electron Multiplying Charge Coupled Device) detector at the SHWFS has been characterized and its gain and noise parameters have been measured and introduced in the simulated model.

Pointing the way to the future, the necessary steps to test the algorithm at a telescope's adaptive optics system are devised. Also, the means to extend the applicability of the algorithm to extended observed sources, such as with a Laser Guide Star (LGS) or in solar AO, is proposed.

Table of contents

Abstract ***9***

Table of contents ***11***

List of figures ***15***

List of tables ***21***

List of acronyms ***23***

Chapter 1. Atmospheric turbulence and adaptive optics ***25***

1.1. Imaging through turbulence **25**
- 1.1.1. The Kolmogorov turbulence model 25
- 1.1.2. The Fried Parameter r_0 27
- 1.1.3. Point Spread Function and Full Width Half Maximum 29
- 1.1.4. Strehl Ratio and Encircled Energy 29

1.2. Adaptive Optics systems **30**
- 1.2.1. Adaptive Optics compensation 30
- 1.2.2. Sources of errors in adaptive optics system 32
  - 1.2.2.1. Anisoplanatism 32
  - 1.2.2.2. Measurement error 33
  - 1.2.2.3. Deformable mirror fitting error 33
  - 1.2.2.4. Temporal error 34
  - 1.2.2.5. Other sources of error 34
- 1.2.3. Adaptive Optics system configurations 34
  - 1.2.3.1. Single Conjugated Adaptive Optics (SCAO) systems 34
  - 1.2.3.2. Ground Layer Adaptive Optics (GLAO) systems 35
  - 1.2.3.3. Multi-Conjugate Adaptive Optics (MCAO) systems 36
  - 1.2.3.4. Multi-Object Adaptive Optics (MOAO) systems 38

1.3. The Shack-Hartmann Wavefront Sensor (SHWFS) **39**
- 1.3.1. Principles of operation 39
- 1.3.2. Image processing and phase recovery at the SHWFS 41
  - 1.3.2.1. Zonal methods for phase recovery 42
  - 1.3.2.2. Modal methods for phase recovery. Zernike functions. 43

1.4. Centroiding methods in a SHWFS **45**
- 1.4.1. Centre of Gravity (CoG) based methods 46
  - 1.4.1.1. Thresholded centre of gravity (TCoG) 46
  - 1.4.1.2. Weighted centre of gravity (WCoG) 46
  - 1.4.1.3. Quad Cell (QC) 47
- 1.4.2. Cross-Correlation (CC) method 47
- 1.4.3. Matched Filter (MF) method 48

Chapter 2. Objective of the present work ***49***

2.1. Motivation of the work **49**

2.2. Objectives, methods and materials **51**

Chapter 3. The Weighted Fourier Phase Slope algorithm ***55***

3.1. Fourier Phase Slope **55**
  3.1.1. Further development of the Fourier phase slope formulation 58

3.2. Maximum-a-posteriori (MAP) weighting **59**

3.3. Comparison of computational cost of WFPS with other algorithms **61**
  3.3.1. Computational cost of the unidimensional and bi-dimensional FFT's 62
    3.3.1.1. Computational cost of the unidimensional FFT 62
    3.3.1.2. Computational cost of the 2D-FFT 63
  3.3.2. Computational cost of the WFPS algorithm 64
  3.3.3. Computational cost of the TCoG and WCoG algorithms 66
  3.3.4. Computational cost of the Cross Correlation algorithm 67
  3.3.5. Comparison between algorithms through examples and conclusions 68

Chapter 4. Numerical simulations at subpupil level ***71***

4.1. The simulation method **71**
  4.1.1. Simulation of Kolmogorov phase frames 71
    4.1.1.1. Verification of the phase simulation method 74
  4.1.2. Simulation of the pixelized images at the detector 75
  4.1.3. The Electron Multiplication CCD detector model 77
  4.1.4. Simulation workflow 79

4.2. Linearity and dynamic range **81**
  4.2.1. Optimum field of view 84

4.3. MAP weights **87**

4.4. Sensitivity in the presence of detector noises and spot deformation **95**

4.5. Effect of turbulence strength **99**

4.6. Closed-loop operation simulation **101**

4.7. Square subaperture **104**

4.8. Conclusions of this chapter **108**

Chapter 5. Numerical simulations at an entire pupil level ***111***

5.1. The Object Oriented Matlab Adaptive Optics toolbox **111**
  5.1.1. Features added to the OOMAO in the context of the present work 113
  5.1.2. The simulation workflow 115

5.2. Effect of estimating G-Tilt or Z-Tilt over the final PSF **118**

5.3. Strehl Ratio as a function of NGS magnitude **122**

5.4. Encircled Energy as a function of NGS magnitude **124**

5.5. Conclusions of the present chapter **125**

Chapter 6. Laboratory tests ***127***

6.1. The EDiFiSE project **127**

6.2. The laboratory test **128**
  6.2.1. The laboratory setup 128
  6.2.2. Description of the test 129

6.2.3. Test results 131

6.3. Conclusions of this chapter 136

Chapter 7. General conclusions and future work 137

7.1. General conclusions 137

7.2. Future work 138

Bibliography 141

Appendix A. Cepstrum analysis and homomorphic deconvolution 147

A.1. Definition of the complex cepstrum 148

A.2. Homomorphic deconvolution 148

A.3. De-echoing a unidimensional signal 151

A.4. De-echoing a bi-dimensional signal 153

A.5. De-noising Shack-Hartmann subaperture images 154

A.5.1. High order aberrations in the spot 155

A.5.2. Low light flux level 156

A.5.3. Limited field of view 157

Appendix B. Characterization of EDiFiSE's EMCCD camera 159

List of figures

Figure 1-1. Simplified schematic illustration of an adaptive optics system, by 2pem - Own work, CC BY-SA 3.0, https://commons.wikimedia.org/w/index.php?curid=15279624 ______________30

Figure 1-2. Closed-loop vs Open-loop configurations of an AO system, from Marlon V., 2014. ______31

Figure 1-3. Angular anisoplanatism in AO systems, from Quiros F., 2007. ______________________32

Figure 1-4. SCAO system squematic diagram, from Quirós F. (2007) ___________________________35

Figure 1-5. GLAO system squematic diagram, from Quirós F. (2007).___________________________36

Figure 1-6. MCAO system squematic diagrams, Star Oriented (left) and Layer Oriented (right), from Quirós F. (2007).____37

Figure 1-7. Schematic comparison of MCAO (a) systems with MOAO (b) systems, from Gavel, 2006. 38

Figure 1-8. Schematic diagram of the Shack-Hartmann wavefront sensor operation, Rodríguez-Ramos, 1998. ____40

Figure 1-9. Fried geometry with corresponding 'A' matrices in a SHWFS as depicted in Herrmann, 1980. ____42

Figure 2-1. One dimensional representation of the relationship between image displacement and linear phase slope shift in the Fourier domain, from Li, Huang and Gong, 2014.___________51

Figure 4-1. Comparison of theoretical Kolmogorov phase structure ([Eq. 4-1], solid line) with the phase structure obtained from a series of 50000 simulated phase frames, with D/r_0=1 and 32x32 pixels resolution per frame (diamond shapes).________________________________74

Figure 4-2. Sketch of a high resolution image as is obtained with a 1024 x 1024 2D-FFT, and of the final resolution image, obtained through decimation by block summation and selection of a central FoV. ____76

Figure 4-3. Schematic of the sources of noise in an Electron Multiplication Charge-Coupled Device._77

Figure 4-4. Core of the simulation workflow employed to compare the centroiding algorithms at a subpupil level ____79

Figure 4-5. (a) Estimated Z-Tilt as a function of applied Z-Tilt and FoV, for the WFPS algorithm with 4 x 4 spatial frequencies, circular subaperture with D/r_0=2.5, Nyquist sampling, high light flux level of 500000 photons, unity EMCCD gain, CIC=0.05 e^-/pixel/frame, RON=50 e^-r.m.s. (b) Same for the TCoG algorithm. ____82

Figure 4-6. (a) Estimated G-Tilt as a function of applied G-Tilt and FoV, for the WFPS algorithm with 4 x 4 spatial frequencies, circular subaperture with D/r_0=2.5, Nyquist sampling, high light flux level of 500000 photons, unity EMCCD gain, CIC=0.05 e^-/pixel/frame, RON=50 e^-r.m.s. (b) Same for the TCoG algorithm. ____83

Figure 4-7. (a) Estimated Z-Tilt as a function of applied Z-Tilt and centroiding algorithm, for a FoV of 8 x 8 pixels, circular subaperture with D/r_0=2.5, Nyquist sampling, high light flux level of 500000 photons, unity EMCCD gain, CIC=0.05 e^-/pixel/frame, RON=50 e^-r.m.s. (b) Same for G-Tilt estimation. ____84

Figure 4-8. Tilt estimation error in r.m.s. radians as a function of FoV and light flux level for the TCoG algorithm (red), the CC algorithm (green) and the WFPS algorithm with 4 x 4 spatial frequencies (blue), for Z-Tilt estimation (a) and G-Tilt estimation (b). D/r_0 is 2.5. CIC is 0.05 e^-/pix/frame and RON is 50 e^- rms. 85

Figure 4-9. Tilt estimation error in r.m.s. radians as a function of FoV and light flux level for the TCoG algorithm (red), the CC algorithm (green) and the WFPS algorithm with at most 4 x 4 spatial frequencies (blue), for Z-Tilt estimation (a) and G-Tilt estimation (b). D/r_0 is 1. CIC is 0.05 e^-/pix/frame and RON is 50 e^- rms. 86

Figure 4-10. Estimated tilt error in r.m.s. radians at the sensing wavelength as a function of incident light level at the subaperture in photons and several schemes of spatial frequencies selection for the WFPS algorithm (see text for further explanation). D/r_0 is 2.5. Nyquist sampling. FoV is 14 by 14 pixels. EMCCD gain for each light level is high without saturating a 14 bits detector. CIC is 0.05 e^-/pixel/frame. RON is 50 e^- rms. (a) is for Z-Tilt estimation and (b) for G-Tilt estimation. 88

Figure 4-11. Estimated tilt error in r.m.s. radians at the sensing wavelength as a function of incident light level at the subaperture in photons and several schemes of spatial frequencies selection for the WFPS algorithm. D/r_0 is 1. Nyquist sampling. FoV is 10 by 10 pixels. EMCCD gain for each light level is high without saturating a 14 bits detector. CIC is 0.05 e^-/pixel/frame. RON is 50 e^- rms. (a) is for Z-Tilt and (b) for G-Tilt estimation. 92

Figure 4-12. Tilt estimation error in r.m.s. radians at the sensing wavelength as a function of incident light level per subaperture in photons for the TCoG centroiding algorithm (red plots), CC centroiding algorithm (green plots) and WFPS centroiding algorithm with 6 spatial frequencies (blue plots). (a) is for Z-Tilt estimation with each subpanel for a different FoV: 10x10, 12x12, 14x14 and 16x16 pixels. (b) is for G-Tilt estimation, also with four subpanels for the same values of FoV as for the Z-Tilt estimation case. For the 10x10 pixels FoV case, a fourth algorithm corresponding to WFPS with 14X14 2D-FFT's and 6 spatial frequencies has been added, in cyan. D/r_0 is 2.5. Nyquist sampling. EMCCD gain for each light level is high without saturating a 14 bits detector. CIC is 0.05 e^-/pixel/frame. RON is 50 e^- rms. 96

Figure 4-13. Tilt estimation error in r.m.s. radians at the sensing wavelength as a function of incident light level per subaperture in photons for the TCoG centroiding algorithm (red plots), CC centroiding algorithm (green plots) and WFPS centroiding algorithm with 6 spatial frequencies (blue plots). (a) is for Z-Tilt estimation with each subpanel for a different FoV: 6x6, 8x8, 10x10 and 12x12 pixels. (b) is for G-Tilt estimation, also with four subpanels for the same values of FoV as for the Z-Tilt estimation case. D/r_0 is 1. Nyquist sampling. EMCCD gain for each light level is high without saturating a 14 bits detector. CIC is 0.05 e^-/pixel/frame. RON is 50 e^- rms. 98

Figure 4-14. Tilt estimation error in r.m.s. radians as a function of subpupil diameter to Fried parameter ratio (D/r_0) for incident light levels of 30, 50, 100, 200, 300 and 10000 photons and two centroiding algorithms: TCoG and WFPS with 6 spatial frequencies selected. FoV values are as per Table 4-8. (a) is for Z-Tilt estimation. (b) is for G-Tilt estimation. Nyquist sampling. QE is 97%. EMCCD gain for each light level is high without saturating a 14 bits detector. CIC is 0.05 e^-/pixel/frame. RON is 50 e^- rms. 100

Figure 4-15. Simulation of tilt estimation in a circular subaperture for closed loop operation and D/r_0=2.5. Estimation error in rms radians as a function of incident photons for Z-Tilt estimation and a 10x10 pixels FoV (a), Z-Tilt estimation and a 12x12 pixels FoV (b), G-Tilt *estimation and a 10x10 pixels FoV (c), and G-Tilt estimation and a 12x12 pixels FoV (d), for the TCoG algorithm (red traces), WCoG algorithm (orange traces), CC algorithm (green traces) and WFPS algorithm with 6 spatial frequencies (blue traces). Nyquist sampling. QE is 97%. EMCCD gain for each light level is high without saturating a 14 bits detector. CIC is 0.05 e^-/pixel/frame. RON is 50 e^- rms. 102*

Figure 4-16. Simulation of tilt estimation in a circular subaperture for closed loop operation and $D/r_0=1$. Estimation error in rms radians as a function of incident photons for Z-Tilt estimation and a 6x6 pixels FoV (a), Z-Tilt estimation and a 8x8 pixels FoV (b), G-Tilt estimation and a 6x6 pixels FoV (c), and G-Tilt estimation and a 8x8 pixels FoV (d), for the TCoG algorithm (red traces), WCoG algorithm (orange traces), CC algorithm (green traces) and WFPS algorithm with 6 spatial frequencies (blue traces). Nyquist sampling. QE is 97%. EMCCD gain for each light level is high without saturating a 14 bits detector. CIC is 0.05 e^-/pixel/frame. RON is 50 e^- rms. 103

Figure 4-17. The largest square shaped portion of the Kolmogorov circular phase is extracted to simulate a square subaperture. 104

Figure 4-18. Tilt estimation error in r.m.s. radians as a function of the number of incident photons in the subaperture, for a square shaped subaperture, with $D/r_0=2.5$ (D is the square side). (a) is for Z-Tilt estimation and (b) is for G-Tilt estimation. FoV's under study are 12x12, 14x14 and 16x16 pixels, and the simulated algorithms are TCoG, CC and WFPS with 6 spatial frequencies. Nyquist sampling of the spot. Detector's QE is 97%. EMCCD gain is high, without saturating a 14 bits detector. CIC is 0.05 e^-/pixel/frame. RON is 50 e^- r.m.s. 105

Figure 4-19. Tilt estimation error in r.m.s. radians as a function of the number of incident photons in the subaperture, for a square shaped subaperture, with $D/r_0=1$ (D is the square side). (a) is for Z-Tilt estimation and (b) is for G-Tilt estimation. FoV's under study are 8x8, 10x10 and 12x12 pixels, and the simulated algorithms are TCoG, CC and WFPS with 6 spatial frequencies. Nyquist sampling of the spot. Detector's QE is 97%. EMCCD gain is high, without saturating a 14 bits detector. CIC is 0.05 e^-/pixel/frame. RON is 50 e^- r.m.s. 106

Figure 5-1. OOMAO class diagram, from Conan and Correia, 2014. 112

Figure 5-2. Samples of SHWFS images created with the OOMAO for a 20 x 20 square subpupils configuration in a 4.2 m circular aperture with an 8.4% central obscuration. (a) Without any kind of noise, planar wavefront and magnitude 0 star. (b) For a magnitude 11 star, Fried parameter of 21 cm, EMCCD gain of 1000, CIC noise of 0.05 e^-/pixel/frame and RON of 50 rms e^-. (c) Same as in (b), for an 8.4 cm Fried parameter. 115

Figure 5-3. Core of the simulation workflow programmed in the OOMAO for the assessment of the effect of the centroiding algorithms at a pupil level. 116

Figure 5-4. 2D plots of the system PSF for a 4.2 m aperture with 8.4% central obscuration, 20x20 square subapertures, 500 Hz system working frequency and 200 frames integration spanned through 4 seconds. (a) is the PSF at diffraction limit spanning a 0.27" FoV. For the 21 cm r_0 case, a FoV of 1.35" is shown in panels (b) for no correction, and (c) and (d) for a correction of 130 Zernike modes after estimating G-Tilt or Z-Tilt at the subpupil level, respectively. Panels (e), (f) and (g) show 3.38" of FoV for an 8.4 cm r_0 case without turbulence compensation and compensating 130 Zernike modes out of G-Tilt and Z-Tilt estimation at subpupil level, respectively. The centroiding algorithm has been WFPS with 6 spatial frequencies involved.

NGS and science object magnitudes are both 5. QE at the SHWFS is 97%; EMCCD gain is 50; CIC noise is 0.05 e^-/pixel/frame and RON is 50 rms e^-. 118

Figure 5-5. Horizontal cuts of the corrected PSF's in Figure 5-4. (a) is for the 21 cm r_0 case. (b) is for the 8.4 cm r_0 case. Blue traces are for Z-Tilt estimation at subpupil level and violet traces are for G-Tilt estimation at subpupil level. Ordinate coordinate represents image counts normalized with respect to the peak at diffraction limit. 120

Figure 5-6. Encircled Energy graphs obtained from the PSF's in Figure 5-4. (a) is for the 21 cm r_0 case. (b) is for the 8.4 cm r_0 case. Black traces correspond to the diffraction limited case. Violet traces and blue traces are for G-Tilt and Z-Tilt estimation at the subpupil level, respectively. Red traces are for the uncorrected PSF's. 121

Figure 5-7. Strehl Ratio in percentage units obtained by Marechal's approximation as a function of star magnitude for two atmospheric conditions: (a) 21 cm r_0 and (b) 8.4 cm r_0; and three centroiding algorithms: TCoG (red traces), CC (green traces) and WFPS with 6 spatial frequencies (blue traces). System's aperture is 4.2 m wide, with a central obscuration of 8.4%. Optical throughput is the default unity. SHWFS has 20 x 20 square subapertures and a ~2.7" FoV in (a) or ~3.8" FoV in (b) with Nyquist sampling. Phase recovery is modal with optimal method and number of modes selected for each star magnitude. 122

Figure 5-8. Encircled Energy graphs as a function of star magnitude for two atmospheric conditions: (a) 21 cm r_0 and (b) 8.4 cm r_0; and three centroiding algorithms: TCoG (red traces), CC (green traces) and WFPS with 6 spatial frequencies (blue traces), all tuned to estimate G-Tilt. Diffraction limited and no correction cases are shown in black traces. System's aperture is 4.2 m wide, with a central obscuration of 8.4%. Optical throughput is the default unity. SHWFS has 20 x 20 square subapertures and a ~2.7" FoV in (a) or ~3.8" FoV in (b) with Nyquist sampling. Phase recovery is modal through pseudo-inverson with optimal method selected for each star magnitude and a fixed number of 130 Zernike modes. 124

Figure 6-1. Diagram of the portion of the optical laboratory setup of the EDiFiSE project which has been employed for the laboratory test in the present work. 128

Figure 6-2. View of the optical setup of the EDiFiSE project at the laboratory facilities of the IAC, courtesy by Dr. Félix Gracia Temich, from the EDiFiSE team. 129

Figure 6-3. (a) rms value of differences between estimated tilt and estimated true tilt at the SHWFS subpupils as a function of incident light level for the applied static turbulence with D/r_0~1. Values are obtained as averages among all centroid coordinates in the SHWFS image. Stars in red are for the TCoG algorithm, in green for the CC algorithm, and in blue and cyan for the WFPS algorithm involving the six lowermost spatial frequencies with 12 x 12 and 14 x 14 sized 2D-FFT's, respectively. (b) rms value of differences between estimated phases and estimated true phases at the DM actuator's coordinates as a function of incident light level for the same applied static turbulence. Phases are obtained by applying the control matrix to the vector of centroid coordinates. Shown values are averages among all the DM actuators. Colour code is as for panel (a) 133

Figure 6-4. (a) rms value of differences between estimated tilt and estimated true tilt at the SHWFS subpupils as a function of incident light level for the applied static turbulence with D/r_0~1.5. Values are obtained as averages among all centroid coordinates in the SHWFS image. Stars in red are for the TCoG algorithm, in green for the CC algorithm, and in blue and cyan for the WFPS algorithm involving the six lowermost spatial frequencies with 12 x 12 and 14 x 14 *sized 2D-FFT's, respectively. (b) rms value of differences between estimated phases and estimated true phases at the DM actuator's coordinates as a function of incident light level for the same applied static turbulence. Phases are obtained by applying the control matrix to the vector of centroid coordinates. Shown values are averages among all the DM actuators. Colour code is as for panel (a) ______ 134*

Figure 6-5. (a) rms value of differences between estimated tilt and estimated true tilt at the SHWFS subpupils as a function of incident light level for the applied static turbulence with $D/r_0 \sim 2$. Values are obtained as averages among all centroid coordinates in the SHWFS image. Stars in red are for the TCoG algorithm, in green for the CC algorithm, and in blue and cyan for the WFPS algorithm involving the six lowermost spatial frequencies with 12 x 12 and 14 x 14 sized 2D-FFT's, respectively. (b) rms value of differences between estimated phases and estimated true phases at the DM actuator's coordinates as a function of incident light level for the same applied static turbulence. Phases are obtained by applying the control matrix to the vector of centroid coordinates. Shown values are averages among all the DM actuators. Colour code is as for panel (a) ______ 135

Figure A-1. Canonic form for homomorphic systems with convolution as the input and the output operations. See text for an explanation. ______ 148

Figure A-2. Homomorphic deconvolution of a triangular sequence with an echo. (a) Input (solid line) and output (dashed line) sequences. (b) log-magnitude of the Fourier transform or, equivalently, real part of the complex cepstrum's Fourier transform of the input (solid line) and the output (dashed line). (c) Unwrapped phase of the Fourier transform or, equivalently, imaginary part of the complex cepstrum's Fourier transform of the input (solid line) and the output (dashed line). ______ 152

Figure A-3. 2D Gaussian shape with an echo before (a) and after (b) homomorphic deconvolution. 153

Figure A-4. (a) Simulated subaperture image for $D_{sub}/r_0=2.5$, FWHM(diff)=2 pixels, FoV=16x16 pixels, 5000 photons flux, CIC=0.05 e^-/pix/frame, $G_{emccd}=80$, RON=50 e^- rms. Green cross points to the perfect Z-tilt estimation; red cross is the image's CoG. Difference is mainly due to high order aberrations in the subpupil. (b) Same image after filtering in the cepstrum domain. Green cross points to the perfect Z-tilt estimation; blue cross is the image's CoG. ______ 155

Figure A-5. (a) Simulated subaperture image for $D_{sub}/r_0=2.5$, FWHM(diff)=2 pixels, FoV=16x16 pixels, 50 photons flux, CIC=0.05 e^-/pix/frame, $G_{emccd}=1000$, RON=50 e^- rms. Green cross points to the perfect Z-tilt estimation; red cross is the image's CoG. Difference is mainly due to spurious charge noise in a large FoV. (b) Same image after filtering in the cepstrum domain. Green cross points to the perfect Z-tilt estimation; blue cross is the image's CoG. ______ 156

Figure A-6. (a) Simulated subaperture image for $D_{sub}/r_0=2.5$, FWHM(diff)=2 pixels, FoV=12x12 pixels, 5000 photons flux, CIC=0.05 e^-/pix/frame, $G_{emccd}=80$, RON=50 e^- rms. Green cross points to the perfect Z-tilt estimation; red cross is the image's CoG. Difference is mainly due to truncation of the spot in a limited FoV. (b) Same image after filtering in the cepstrum domain, employing 16x16-point 2D-FFT's. Green cross points to the perfect Z-tilt estimation; blue cross is the image's CoG. ______ 157

Figure B-1. Histograms of dark images for a situation without EMCCD gain. Blue trace is for a real acquired signal from a single pixel of EDiFiSE's SHWFS detector. Green trace is for a simulated signal following the EMCCD model described in Hirsch et al, 2013. ______ 162

Figure B-2. Histograms of dark images for a situation with programmed EMCCD gain of 100. Blue trace is for a real acquired signal from a single pixel of EDiFiSE's SHWFS detector. Green trace is for a simulated signal following the EMCCD model described in Hirsch et al, 2013._____162

Figure B-3. Histograms of dark images for a situation with programmed EMCCD gain of 300. Blue trace is for a real acquired signal from a single pixel of EDiFiSE's SHWFS detector. Green trace is for a simulated signal following the EMCCD model described in Hirsch et al, 2013._____163

Figure B-4. Histograms of dark images for a situation with programmed EMCCD gain of 500. Blue trace is for a real acquired signal from a single pixel of EDiFiSE's SHWFS detector. Green trace is for a simulated signal following the EMCCD model described in Hirsch et al, 2013._____163

Figure B-5. Histograms of dark images for a situation with programmed EMCCD gain of 1000. Blue trace is for a real acquired signal from a single pixel of EDiFiSE's SHWFS detector. Green trace is for a simulated signal following the EMCCD model described in Hirsch et al, 2013._____164

List of tables

Table 3-1. Computational cost of the WFPS algorithm for an N by N image Ixy following the computation of the Fourier phase slopes according to equation [Eq. 3-17] and selecting Nf spatial frequencies. Total values are approximated assuming $N2 \gg 1$. 65

Table 3-2. Computational cost of the WFPS algorithm for an N by N image Ixy following the computation of the Fourier phase slopes according to equation [Eq. 3-14] by direct method computation of the 2D-FFT's focusing on Nf spatial frequencies exclusively. M has the same meaning as in [Eq. 3-28]. Total values are approximated assuming $N2 \gg 1$. 65

Table 3-3. Computational cost of the TCoG algorithm for an N by N image Ixy following the computation described in [Eq. 1-27]. Threshold T is an input to the algorithm. 66

Table 3-4. Computational cost of the WCoG algorithm for an N by N image Ixy following the computation described in [Eq. 1-26] and [Eq. 1-28]. Weights Wxy are predetermined and an input to the algorithm. 66

Table 3-5. Computational cost of the CC algorithm for an N by N image Ixy and an N_{ref} by N_{ref} image $Iref$. CC computation is done in the Fourier domain, with an N_{fft} by N_{fft} bi-dimensional FFT, being $N_{fft} \geq N + N_{ref} - 1$. TCoG is applied to the correlation figure, without previous interpolation. 67

Table 3-6. Example of computational cost comparison between WCoG, TCoG, WFPS and CC algorithms, for an ELT with 80 x 80 subpupils, 12 x 12 pixels per subpupil at the detector and 100 µsecs budgeted latency for centroids computation. 69

Table 3-7. Example of computational cost comparison between WCoG, TCoG, WFPS and CC algorithms, for an ELT with 80 x 80 subpupils, 16 x 16 pixels per subpupil at the detector and 100 µsecs budgeted latency for centroids computation. 69

Table 4-1. Covariance matrix for the first 14 zero mean Zernike functions (Z_2 to Z_{15}) of Kolmogorov turbulence phase. $(D/r_0)^{5/3}$ units. 73

Table 4-2. Optimal FoV in pixels x pixels as a function of light flux level for the TCoG, CC and WFPS (with 4x4 frequencies) algorithms, obtained from Figure 4-8. $D/r_0=2.5$. CIC=0.05 e^-/pix/frame. RON=50 e^- rms. 85

Table 4-3. Optimal FoV in pixels x pixels as a function of light flux level for the TCoG, CC and WFPS (with at most 4x4 frequencies) algorithms, obtained from Figure 4-9. $D/r_0=1$. CIC=0.05 e^-/pix/frame. RON=50 e^- rms. 86

Table 4-4. List of MAP weights for the calculation of the horizontal value of the centroid with the WFPS algorithm, as per [Eq. 3-23] (Wk, lx), when estimating Z-Tilt. D/r_0 is 2.5. Nyquist sampling. FoV is 14 by 14 pixels. EMCCD gain for each light level is high without saturating a 14 bits detector. CIC is 0.05 e^-/pixel/frame. RON is 50 e^- rms. Light level increases vertically in the table. Three different patterns of spatial frequencies selection are listed in a column each: 3 lowermost frequencies, 6 lowermost frequencies and 4x4 lowermost frequencies. 89

Table 4-5. List of MAP weights for the calculation of the horizontal value of the centroid with the WFPS algorithm, as per [Eq. 3-23] (Wk, lx), when estimating G-Tilt. D/r_0 is 2.5. Nyquist *sampling. FoV is 14 by 14 pixels. EMCCD gain for each light level is high without saturating a 14 bits detector. CIC is 0.05 e^-/pixel/frame. RON is 50 e^- rms. Light level increases vertically in the table. Three different patterns of spatial frequencies selection are listed in a column each: 3 lowermost frequencies, 6 lowermost frequencies and 4x4 lowermost frequencies. ______90*

Table 4-6. List of MAP weights for the calculation of the horizontal value of the centroid with the WFPS algorithm, as per [Eq. 3-23] (Wk, lx), when estimating Z-Tilt. D/r_0 is 1. Nyquist sampling. FoV is 10 by 10 pixels. EMCCD gain for each light level is high without saturating a 14 bits detector. CIC is 0.05 e^-/pixel/frame. RON is 50 e^- rms. Light level increases vertically in the table. Three different patterns of spatial frequencies selection are listed in a column each: 3 lowermost frequencies, 6 lowermost frequencies and 4x4 lowermost frequencies. ______93

Table 4-7. List of MAP weights for the calculation of the horizontal value of the centroid with the WFPS algorithm, as per [Eq. 3-23] (Wk, lx), when estimating G-Tilt. D/r_0 is 1. Nyquist sampling. FoV is 10 by 10 pixels. EMCCD gain for each light level is high without saturating a 14 bits detector. CIC is 0.05 e^-/pixel/frame. RON is 50 e^- rms. Light level increases vertically in the table. Three different patterns of spatial frequencies selection are listed in a column each: 3 lowermost frequencies, 6 lowermost frequencies and 4x4 lowermost frequencies. ______94

Table 4-8. Employed FoV in pixels by pixels for the assessment of the effect of turbulence strength, the results of which are illustrated in Figure 4-14. ________________________________101

Table B-1. Measured EMCCD gains vs. programmed gains, and sensitivity values obtained thereof. ____160

Table B-2. Estimated offset and subsequent CIC and RON values obtained by dark images histogram fitting for the listed programmed EMCCD gains.__________________________________164

List of acronyms

2D_DFT or 2D-DFT	Bi-dimensional Discrete Fourier Transform
2D_FFT or 2D-FFT	Bi-dimensional Fast Fourier Transform
A/D	Analog to Digital
ADU	Analog to Digital Unit
AO	Adaptive Optics
AO4ELT5	5th Adaptive Optics for Extremely Large Telescopes Conference
BS	Beam Splitter
CAOS	Code for Adaptive Optics Systems
CC	Cross-Correlation
CCD	Charge Coupled Device
CIC	Clock Induced Charge
CoG	Centre of Gravity
DM	Deformable Mirror
EDiFiSE	Equalized and Diffraction limited Field Spectrograph
EE	Encircled Energy
EIFU	Equalized Integral Field Unit
ELT	Extremely Large Telescope
EM	Electron Multiplication
EMCCD	Electron Multiplying Charge Coupled Device
ENF	Excess Noise Factor
FLOPS	Floating Point Operations Per Second
FFT	Fast Fourier Transform
F/O	Fibre Optic
FoV	Field of View
FoR	Field of Regard
FPGA	Field Programmable Gate Array
FPS	Fourier Phase Shift
FW	Filterwheel
FWHM	Full Width Half Maximum
Gflops	GigaFlop (10^9 FLOPS)
GLAO	Ground Layer Adaptive Optics
GPU	Graphical Processor Unit
GHRIL	Ground-based High Resolution Imaging Laboratory
GS	Guide Star
IAC	Instituto de Astrofísica de Canarias
IACAT	IAC’s Atmosphere and Telescope
IDL	Interactive Data Language
IEEE	Institute of Electrical and Electronics Engineers
IR	Infrared
LGS	Laser Guide Star
LMMSE	Linear Minimum Mean Square Error
LO-MCAO	Layer Oriented Multi-Conjugate Adaptive Optics

MAP	Maximum a Posteriori
MCAO	Multi Conjugate Adaptive Optics
MEMS	Microelectromechanical Systems
MF	Matched Filter
ML	Maximum Likelihood
MMSE	Minimum Mean Square Error
MOAO	Multi Object Adaptive Optics
MVM	Matrix Vector Multiplication
NGS	Natural Guide Star
OOMAO	Object Oriented Matlab for Adaptive Optics
OTF	Optical Transfer Function
PCI	Peripheral Component Interconnect bus
PDF	Probability Density Function
PI	Physik Instrumente
PSF	Point Spread Function
QC	Quad Cell
QE	Quantum Efficiency
RON	ReadOut Noise
SCAO	Single Conjugated Adaptive Optics
s-FDO	single frame Fourier Domain Offset
SHWFS	Shack-Hartmann Wavefront Sensor
SNR	Signal to Noise Ratio
SO-MCAO	Star Oriented Multi-Conjugate Adaptive Optics
SR	Strehl Ratio
TCoG	Thresholded Centre of Gravity
TT	Tip Tilt
WCoG	Weighted Centre of Gravity
WFC	Wavefront Controller
WFPS	Weighted Fourier Phase Slope
WFS	Wavefront Sensor
WHT	William Herschel Telescope
WIO	Workshop on Information Optics
XAO	eXtreme Adaptive Optics

Chapter 1. Atmospheric turbulence and adaptive optics

The problem of imaging through turbulence is introduced in this chapter, together with the metrics that will be used throughout this work to quantify the astronomical image quality. Adaptive optics (AO) systems are presented as real time solutions to the turbulence aberration. Different types of such systems are presented, from the simplest Single Conjugated Adaptive Optics (SCAO) systems to the recently developed Multi Object Adaptive Optics (MOAO) systems. The limitations and sources of errors they are encountered with are described. The consequently appeared sky coverage issue is mentioned. A particular emphasis is made in wavefront sensing elements (Wavefront Sensors -WFS-), especially the so-called Shack Hartmann wavefront sensor (SHWFS), which is the recipient of the algorithm introduced in this work. Finally, different other types of centroiding methods used in Shack Hartmann wavefront sensors are described, pointing out their advantages and disadvantages.

1.1. Imaging through turbulence

Atmospheric turbulence aberrates astronomical images when observing through ground based telescopes. Fluctuations in refractive index of the air mass across the two dimensions of the pupil aperture imply a non-uniform wavefront phase of the incoming light and therefore a serious limitation in angle resolution of the telescope. Extensive literature is available that helps in understanding the effect of atmospheric turbulence in astronomical observations (Roddier, 1981; Goodman, 1985; Tyson, 1991; Hardy, 1998). Here, only the definition and physical meaning of the Fried parameter, as a metric of turbulence strength, are given in the framework of the Kolmogorov turbulence model. Likewise, metrics of image quality and resolution such as the Full Width Half Maximum (FWHM), strehl ratio and encircled energy defined over the long-term Point Spread Function (PSF) of the optical system are introduced.

1.1.1. The Kolmogorov turbulence model

The properties of fluid flows are determined primarily by the well-known dimensionless Reynolds number $Re = V L / \nu$, where V is the fluid velocity, L a characteristic length scale, and ν the kinematic viscosity of the fluid. It is the ratio of inertial forces to viscous forces within the fluid, and gives the conditions under which a laminar flow becomes turbulent. When *Re* becomes larger than a critical value that depends on the geometry of the flow, the fluid will move turbulently. For air, $\nu \approx 15 \cdot 10^{-6}$ m^2 s^{-1}, so that for typical wind speeds of a few m s^{-1} and length scales of meters to kilometres, the Reynolds number will be $Re \gtrapprox 10^6$, meaning that air will move turbulently.

Turbulent flows are characterized by random vortices also known as *turbulent eddies*. The turbulent energy is generated by eddies on a large scale L_0, the *outer scale*. Non-linear behaviour of the flow implies that low spatial frequencies or large scale eddies give place to smaller scale or higher spatial frequency structures. Energy injected to large structures is transmitted to successively smaller structures in the so-called *energy cascade*, until viscosity becomes important, triggering kinetic energy dissipation as heat and stopping the cascade. This occurs at the *inner scale*, l_0. In equilibrium, the rate of energy transfer per unit mass (ϵ) must be equal to the rate of energy dissipation per unit mass at the smallest scales. The range of length scales $l_0 \leq l \leq L_0$ at which energy cascading takes place is known as the *inertial range*. For atmospheric turbulence, the inner scale l_0 is of the order of some millimetres, and the outer scale L_0 is of the order of tens of meters.

The original contribution of Kolmogorov (1961) is a model describing the turbulence spectrum, i.e., the turbulence strength as a function of the eddy length scale or spatial frequency, within the inertial range. This model is generally known as *Kolmogorov turbulence*.

The spatial structure of a random process can be described by *structure functions*. The structure function $D_x(R_1, R_2)$ of a random variable x measured at positions R_1 and R_2 is defined by

$$D_x(R_1, R_2) = \langle |x(R_1) - x(R_2)|^2 \rangle \qquad \text{[Eq. 1-1]}$$

that is, the structure function is the measurement of the expectation value of the quadratic difference of the values of x measured at two positions R_1 and R_2. Under the assumption that the turbulence is homogeneous and isotropic, the structure function of the turbulent velocity fluctuations field, $D_v(R_1, R_2)$, can only depend on $|R_1 - R_2|$, and can be written as $D_v(|R_1 - R_2|)$.

Kolmogorov's main hypothesis was that, within the inertial range, the structure function $D_v(|R_1 - R_2|)$ should only depend on the rate of energy transfer per unit mass ϵ, since energy dissipation due to viscosity only happens below the inner scale. Following a dimensional analysis aiming at cancelling out the viscosity contribution within the inertial range, he found that $D_v(|R_1 - R_2|)$ follows a 2/3 power law:

$$D_v(|R_1 - R_2|) = C_v^2 |R_1 - R_2|^{2/3} \qquad \text{[Eq. 1-2]}$$

where C_v^2 is the *velocity structure constant,* and only depends on ϵ.

However, velocity fluctuations by themselves do not affect light propagation. Temperature fluctuations induced by turbulent mixing of cold and hot air masses at different heights in the atmosphere, and the consequent changes in air density and refractive index, relate lightwave propagation with the velocity fluctuation field. Tatarski (1961) established this relationship and reached the conclusion that, for small temperature fluctuations, the refractive index structure function $D_n(R_1, R_2)$ measured at two positions R_1 and R_2 depends on the absolute distance $|R_1 - R_2|$ and follows a 2/3 power law:

$$D_n(|R_1 - R_2|) = C_n^2 |R_1 - R_2|^{2/3} \qquad \text{[Eq. 1-3]}$$

where C_n^2 is the *refractive index structure constant*, and is a measurement of the strength of the optical turbulence. It is usually expressed as a function of altitude h. The $C_n^2(h)$ profile above an astronomical observatory determines the observational optical quality of the site, and so great effort is done to characterize it. Experimental measures show that C_n^2 is concentrated in thin layers of one hundred to two hundred meters thick, where its value increases substantially. Furthermore, they show that most of the turbulence strength is concentrated in the first few kilometres of the atmosphere.

1.1.2. The Fried Parameter r_0

A plane wave coming from an astronomical object and entering the Earth through the atmosphere will see its phase distorted when reaching a ground based telescope. The resultant complex field at the telescope pupil $\psi(r) = A(r)\exp[j\phi(r)]$ will exhibit random fluctuations in the phase $\phi(r)$ and the amplitude $A(r)$ after propagation through the atmosphere. However, in most cases of interest, the near-field approximation can be assumed, which is valid as long as $h \ll D^2/\lambda$, where D is the telescope diameter, λ is the wavelength and h is the mean height of the turbulent layers over the telescope. Following this assumption, amplitude fluctuations may be neglected and only phase fluctuations should be considered (Tyson, 1991). This is equivalent to adopting a geometrical optics approach. Therefore, phase fluctuations in the telescope pupil $\phi(r)$ are directly linked to the vertical distribution of refractive index fluctuations $n(r, h)$ by:

$$\phi(r) = k \int_0^{\infty} n(r, h)\, dh \qquad \text{[Eq. 1-4]}$$

where $k = 2\pi/\lambda$ is the wavenumber at the observing wavelength λ. Based on this equation and the statistical descriptions of the refractive index fluctuations, Fried (1965) concluded that the phase $\phi(r)$ exhibits Gaussian statistics and its structure function can be expressed as:

$$D_\phi(|R_1 - R_2|) = \langle |\phi(R_1) - \phi(R_2)|^2 \rangle = 6.88 \left(\frac{r}{r_0}\right)^{5/3} \qquad \text{[Eq. 1-5]}$$

with $r = |R_1 - R_2|$ and r_0 being the *Fried parameter* defined as:

$$r_0 = \left[0.423\, k^2 \sec(\gamma) \int_0^{\infty} C_n^2(h)\, dh\right]^{-3/5} \qquad \text{[Eq. 1-6]}$$

where γ is the zenith angle of observation. r_0 involves the integral of the $C_n^2(h)$ profile, so it is a measure of the whole turbulence strength as seen from the telescope pupil.

Whilst turbulence in the inertial subrange cannot be characterized by any typical length scale, the first main contribution of Fried parameter is to allow for a definition of a characteristic length scale of the turbulent atmosphere in a statistical sense. Furthermore, the model for the atmospheric effect as a transfer function in the framework of linear systems theory gets really simplified.

The optical transfer function (OTF) of an optical system specifies how spatial frequencies are filtered by it and then handled to the next item in the optical chain (see Goodman, 2005, for example). For long exposures, the OTF of the atmosphere-telescope system is the product of the telescope transfer function and the atmospheric transfer function, the latter being equal to the wavefront coherence function, defined as

$$B_{\psi}(|R_1 - R_2|) = \langle \psi(R_1) \psi^*(R_2) \rangle \qquad \text{[Eq. 1-7]}$$

and which can be expressed as a function of the phase structure function $D_{\phi}(|R_1 - R_2|)$ in equation [Eq. 1-5], adopting the simple exponential expression:

$$B_{\psi}(r) = exp\left[-3.44 \left(\frac{r}{r_0}\right)^{5/3}\right] \qquad \text{[Eq. 1-8]}$$

again with $r = |R_1 - R_2|$ and r_0 the Fried parameter. An analysis of the expression in [Eq. 1-8] reveals the physical meaning of r_0. For large r_0's (larger than the physical dimensions of the other components in the optical chain, mainly the telescope's aperture), $B_{\psi}(r)$ will tend to unity and the OTF of the system will be dominated by the telescope aperture: the image will be diffraction-limited. Whereas for small r_0's, $B_{\psi}(r)$ will dominate the system's OTF, filtering out the high spatial content of the image and, therefore, limiting the system's angle resolution: we say the image will be *seeing-limited*, or limited by the atmospheric turbulence strength. Actually, the 0.423 constant in expression [Eq. 1-6] was chosen so that the resolution of seeing-limited images obtained through an atmosphere with turbulence characterized by a Fried parameter r_0 is the same as the resolution of diffraction-limited images taken with a telescope of diameter r_0. It can also be shown that the mean-square phase variation over an aperture of diameter r_0 is about 1 rad^2. So an extremely simplified version of the atmospheric turbulence would be that of constant phase r_0 sized patches, and random phases between the individual patches.

It is important to note from [Eq. 1-6] the $r_0 \propto \lambda^{6/5}$ dependency of the Fried parameter with wavelength. This means that, for a particular atmospheric turbulence strength, it is easier to get diffraction-limited images at longer wavelengths than at shorter ones. Typical values of r_0

are ~10-15 cm in the visible (500 nm) and ~54-90 cm in the infrared (2.2 μm), respectively.

1.1.3. Point Spread Function and Full Width Half Maximum

The response of an optical system to a point source is called its Point Spread Function (PSF). It is the system's impulse response, and so the OTF is its Fourier transform (see Goodman, 2005, for example). The shape of the PSF varies according to the system's pupil shape. The common pattern in all these shapes is a main lobe with a certain width, indicating that the original point source's energy is "spread" over a larger surface, surrounded by secondary lobes of decreasing amplitude as they get further away from the main lobe.

The width of the main lobe indicates the resolution capacity of the optical system. A common metric utilized in this sense is the Full Width Half Maximum, defined as the angular distance between the points of the main lobe where the intensity has decreased to half of the maximum, over a one-dimensional coordinate. It is expressed normally in arcseconds.

For diffraction-limited images in a circular aperture the PSF takes the form of an Airy disk, with $FWHM_{dif} = 1.03\lambda/D$, D being the pupil's diameter. Whereas for long exposures of seeing-limited images, the expression becomes $FWHM_{seeing} = 0.9759\lambda/r_0$.

1.1.4. Strehl Ratio and Encircled Energy

Two other metrics that quantify the optical image quality in the presence of turbulence are the Strehl Ratio (SR) and the Encircled Energy (EE).

The Strehl ratio is defined as the on-axis intensity in the image of a point source divided by the peak intensity in a hypothetical diffraction-limited image taken through the same aperture. For a circular aperture with an aberration function $\varphi(\rho,\theta)$, which describes the wavefront distortion in linear distance units as a function of the cylindrical coordinates (ρ,θ), the Strehl ratio is given by

$$SR = \frac{1}{\pi^2}\left|\int_0^1 \int_0^{2\pi} \rho d\rho d\theta e^{ik\varphi(\rho,\theta)}\right|^2 \qquad \text{[Eq. 1-9]}$$

From this equation, it is clear that 0 ≤ *SR* ≤ 1, that *SR* = 1 for constant φ, that $SR \ll 1$ for strongly varying φ, and that for any given (varying) φ, the Strehl ratio tends to be larger for longer wavelengths (smaller *k*). In the case of atmospheric turbulence, only the statistical properties of φ are known. If the r.m.s. phase error $\sigma_\Phi \equiv k\ \sigma_\varphi$ is smaller than about 2 rad, *SR* can be approximated by the so-called *extended Marechal approximation:*

$$SR = e^{-\sigma_\Phi^2} \qquad \text{[Eq. 1-10]}$$

Encircled energy is the integral of the point spread function over a disk of a given diameter, as a function of that diameter. In contrast to the SR, which only takes into account the on-axis light intensity, EE is an indication of how well light is being gathered in from the halo toward the centroid of the image. As a figure of merit, it is useful for determining object contrast with respect to sky background or with respect to the halo of a nearby bright star. It is normally expressed as encircled energy fraction, that is, the ratio from 0 to 1 of the encircled energy to the total PSF energy.

1.2. Adaptive Optics systems

As it has been pointed out in the discussion of the Fried parameter's physical meaning, in point 1.1.2, though telescopes with ever larger aperture sizes are being developed, the limitation imposed by the atmosphere implies no angular resolution improvement in the optical system, unless atmospheric turbulence is somehow compensated for. Adaptive optics systems come into play to partially achieve this compensation in real time. This technique is, as expected, not devoid of limitations, such as the need of an enough bright light source in the sky to be able to correctly sense the light wavefront, with the consequence of a limited portion of the sky where they can operate reliably. In order to overcome these limitations, increasingly complex AO systems are being developed, with more sensing and corrective elements, aiming at an improvement in spanned field of view (FoV) and at extending the turbulence correction to ever fainter scientific objects of interest.

1.2.1. Adaptive Optics compensation

Figure 1-1 shows a simplified schematic illustration of an AO system working in closed-loop compensation, by wikimedia.org. Light is shown with dotted lines, control connections with dashed lines. The wavefront enters the AO system at the top. The light first hits a tip–tilt (TT) mirror and is then directed to a deformable mirror (DM). The wavefront is corrected and part of the light is tapped off by a beamsplitter (BS). The residual errors (due to system latency, nonlinearities, etc.) are measured by a wavefront sensor (Shack-Hartmann in this case) and the control hardware then sends updated signals to the DM and the TT mirror. The two filterwheels (FW1 and FW2) are used during calibration only.

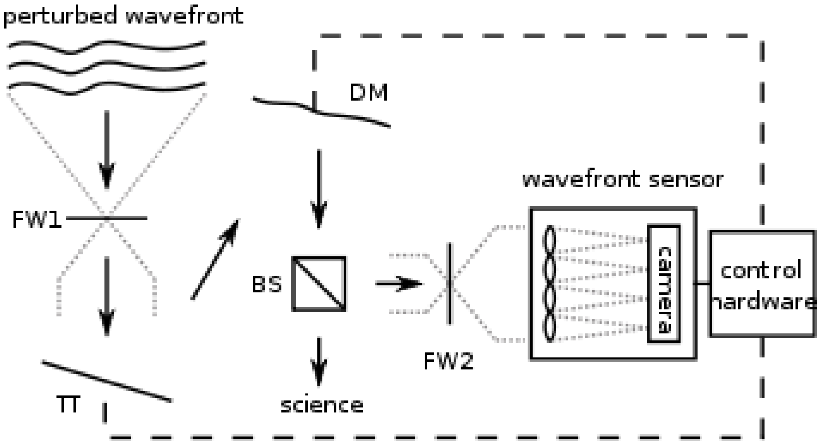

Figure 1-1. Simplified schematic illustration of an adaptive optics system, by 2pem - Own work, CC BY-SA 3.0, https://commons.wikimedia.org/w/index.php?curid=15279624

Proper servo design guarantees closed loop stability and a good attenuation of the wavefront perturbations, at the majority of the temporal frequencies where they are present, at the point in the optical path where the wavefront sensor is situated and, therefore, at the science detector.

So, the key elements of an AO system have already been introduced:

- The phase corrector is the deformable mirror. The most utilized one consists of a thin mirrored membrane with an array of length varying actuators that locally push or pull the membrane giving it the desired shape. Another type of DM is the bimorph, where the length varying material is in the membrane itself, and applied voltage generates a curvature in the membrane; this is why they are also called “curvature mirrors”, and are mainly used with curvature sensors in AO.
- The phase sensing element is the wavefront sensor. Section 1.3 gives a brief description of the most utilized one: the Shack Hartmann wavefront sensor. Others to be found in astronomical systems are the curvature (Roddier, Roddier and Roddier, 1988) and the pyramid (Ragazzoni, 1996) WFS’s.
- The control hardware, in charge of reconstructing the phase from the sensing values and calculating the commands to send to the corrective elements. It has to be fast enough to introduce as a small time lag to the loop as the perturbation attenuation bandwidth requires.

It is important to note here that closed loop operation of AO systems, though the norm, is not the only choice. Open loop operation is also possible. Closed loop has the advantage of a less dynamic range requirement in the sensor and of a good performance even in the presence of unmodeled nonlinearities or other error sources, mainly in the corrective elements. Open loop is the choice when correction is made over a small region of the whole sensed field of view.

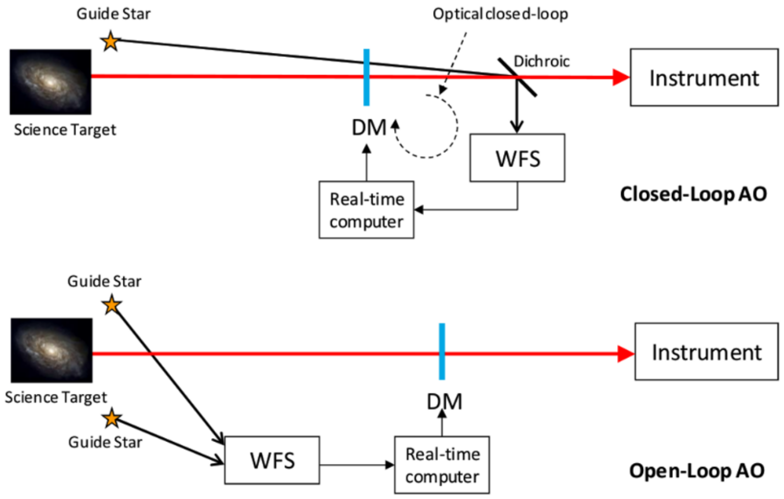

Figure 1-2. Closed-loop vs Open-loop configurations of an AO system, from Marlon V., 2014.

Figure 1-2 compares schematically both operating modes. In the closed loop case, the first element in the optical path is the corrective DM, so the WFS sees a corrected turbulence with small dynamic range. The science target has to be close enough to the guide star (GS) so that the sensed turbulence from the guide star's direction is a good approximation of the turbulence affecting the science object. Whereas in the open loop case, the first element in the optical path is the WFS sensing element, so it sees an uncorrected turbulence with large dynamic range. The corrected wavefront is not, in principle, monitored, so there is a stringent requirement for a precise modelling of the corrective DM element. The sensed field of view can be large by taking advantage of a cluster of GS's, and the target science object can be anywhere in the whole sensed field of view.

1.2.2. Sources of errors in adaptive optics system

Several factors prevent ideal turbulence correction in real AO systems (Hardy, 1998):

1.2.2.1. Anisoplanatism

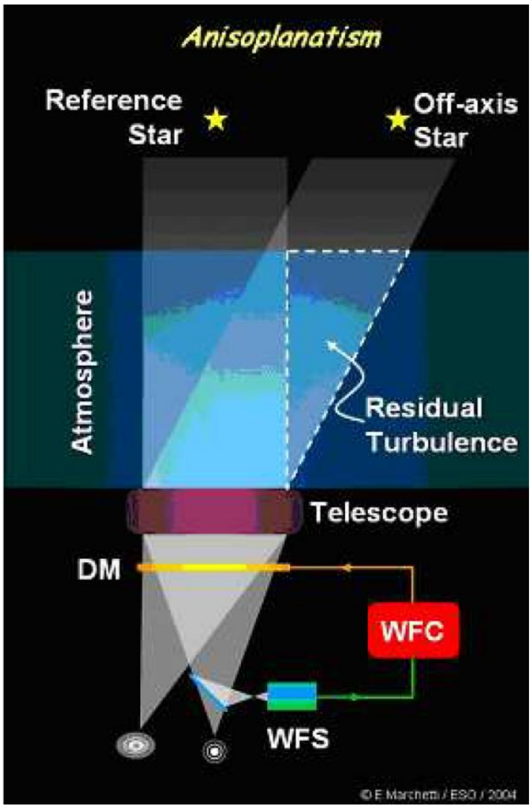

Figure 1-3. Angular anisoplanatism in AO systems, from Quiros F., 2007.

Anisoplanatism is one of the most important effects to limit AO system performance. As illustrated in Figure 1-3, in most astronomical applications the astronomical object of interest is extremely faint or emits most of its radiation in a spectral range unavailable for wavefront sensing, and so a close by reference or guide star GS is used for this purpose. The wavefront coming from the GS will be different from the one coming from the science object, and this phenomenon is known as *anisoplanatism*. For AO systems with a single WFS and single DM (SCAO systems, see point 1.2.3.1), the atmospheric turbulence compensation is only efficient within a FoV that varies from a few arcsec in the visible to a few tens of arcsec in the near infrared, called the *isoplanatic patch*.

In order to be able to measure the wavefront perturbations introduced by atmospheric turbulence with the required accuracy, the signal-to-noise ratio (SNR) on the WFS measurements should be kept as high as possible. This implies that bright stars should be used for wavefront sensing. The magnitude of the faintest GS that could be used for a given SCAO system is known as the *limiting magnitude*, and is determined by the level of performance sought and system parameters such as optics throughput, detector noise, etc.

The probability of finding a natural guide star (NGS) brighter than a given limiting magnitude and within a given FoV is known as de *sky coverage*. The sky coverage offered by SCAO systems is quite limited because a suitable GS must be found within the isoplanatic patch around the object of interest.

In order to overcome this limitation, the concept of *laser guide star* (LGS) has been proposed, which consists of creating an artificial star by projecting a laser beam on the sky. Two LGS technologies have been demonstrated: Rayleigh and sodium LGS's. LGS's boost the sky coverage because a LGS can be conveniently positioned within the isoplanatic patch of the object of interest. Several limitations are associated with LGS's, nevertheless, one of them being the so-called *focal anisoplanatism*. The issue here is that the LGS spot is produced at a finite altitude ($\sim 15 \text{ km for Rayleigh and } \sim 90 \text{ km for sodium LGS's}$) from where the LGS wavefront propagates down to the telescope pupil in a conical fashion. As a result, the atmospheric turbulence volume probed by the LGS wavefront is not exactly the same as the one traversed by the wavefront coming from the object of interest.

1.2.2.2. Measurement error

With the term *measurement error*, the difference between the actual wavefront reaching a WFS and its output estimated wavefront is referred to.

Here, the example of a Shack Hartmann wavefront sensor (SHWFS) will be taken (described in point 1.3). For this particular case, the two main sources of measurement error are:

- Finite spatial sampling of the front. This means limited spatial degrees of freedom for measurement and, hence, correction. Furthermore, high spatial frequencies become noise in the measured low spatial frequencies through aliasing.
- Measurement noise, which in turn comes from:
  - Photon noise, which is associated with light's photonic nature
  - Detector's noises, such as spurious thermal and CIC (Clock Induced Charge) noise, amplification noise, read out noise, etc.
  - Nonlinearities due to pixelation, limited FoV, etc.
  - Centroid anisoplanatism, due to high order asymmetric modes in the subpupil that deform the spot (Yura and Tavis, 1985).

1.2.2.3. Deformable mirror fitting error

In the same fashion as with the WFS, the fact that the DM is shaped with a finite number of actuators (or electrodes, in the case of bimorph DM's) placed at a certain distance from each other, which cannot be made arbitrarily small due to mechanical constraints, limits the number of spatial modes which can be corrected. This is called *fitting error* in the deformable mirror.

1.2.2.4. Temporal error

This fundamental error is caused by the inability of the AO system to respond instantly to the changes in the wavefront. Collecting enough photons for adequate SNR in the WFS measurements requires time, as well as reading the image from the detector. Processing the WFS data to obtain the correction command also requires time. Time delay occurs in the process of transferring the information among the pieces of AO system hardware (WFS to computer and then to DM). Finally, the DM is a mechanic system with a certain response time which is comparable to the rest of time delay sources. All this time delay means that the control system will always be responding to slightly out-of-date information about the atmospheric turbulence, and hence, will not be able to perform a perfect correction.

1.2.2.5. Other sources of error

There are also a number of error sources due to imperfections in the technology involved in making AO system elements. The most important of these are:

- Nonlinearities in the DM and WFS output, and the limited dynamic range of both the DM and WFS, which may cause errors due to saturation.
- Manufacturing defects such as irregularities in DM actuator or WFS subaperture positions, aberrations and geometrical misalignments of optical elements, which may deteriorate the system performance and even cause closed loop instability.
- Different optical paths to the WFS and to the science detector result in the so-called *non-common path* errors, which can also be significant.
- Scattered light in the system which causes background illumination of the sensor.

Additional error terms that arise when tomographically or 3-D sensing the wavefront (see point 1.2.3) have been called by Rigaut, Ellerbroek and Flicker (2000) as *generalized fitting*, *generalized anisoplanatism* and *generalized aliasing* errors.

When designing an AO system, the wise approach is to reach a balance among all the mentioned error terms in this point 1.2.2, rather than to eliminate anyone of the terms, since most of them are correlated to each other.

1.2.3. Adaptive Optics system configurations

1.2.3.1. Single Conjugated Adaptive Optics (SCAO) systems

The first and simplest AO systems developed, the Single Conjugated Adaptive Optics (SCAO) systems, consist of a single DM and a single WFS, normally both of them conjugated to the telescope’s pupil (see Figure 1-4). Most 4-m, 8-m and 10-m class telescopes have been equipped with such systems.

Closed loop operation of these systems is the norm, and so they have the advantage of not requiring a rigorous model of the corrective elements and achieving very good performance in on-axis correction. Indeed, when the term *eXtreme Adaptive Optics (XAO)* is used, referring to an AO system that achieves an extremely good performance, such as SR's higher than 90%, by default an SCAO configuration is assumed.

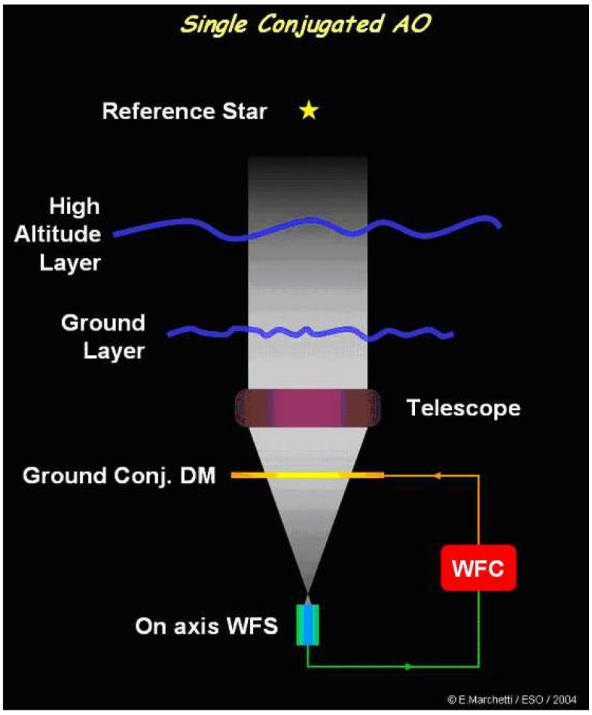

Figure 1-4. SCAO system squematic diagram, from Quirós F. (2007)

The main disadvantage of SCAO systems is anisoplanatism, as mentioned in point 1.2.2.1. This can lead to a sky coverage as low as ~3% due to the low probability of finding enough bright stars in the isoplanatic patch of fainter objects of interest (Assémat, Gendron and Hammer, 2007).

1.2.3.2. Ground Layer Adaptive Optics (GLAO) systems

As opposed to SCAO systems, which intend to achieve very good correction in a small FoV, Ground Layer Adaptive Optics (GLAO) systems intend to achieve a moderate correction but in a large FoV. The concept was envisaged by Rigaut (2002), and is illustrated in Figure 1-5. Taking advantage of the fact that most of the turbulence is concentrated in the first few kilometres above the telescope, as mentioned in point 1.1.1, using a single DM conjugated to a low altitude and compensating for only the ground turbulent layer is a means for achieving a moderate but uniform correction in a wide FoV.

In order to measure the wavefront perturbation introduced by the ground turbulent layer, it is required to have several WFS's coupled to different GS's distributed in the FoV. All WFS's will measure the contribution of the ground turbulent layer (see again Figure 1-5), but also each WFS (coupled to a GS in direction θ) will measure the contributions of the higher turbulent layers in the corresponding direction θ. In principle, the contributions of the higher altitude layers can be averaged out by simply averaging the wavefronts measured by all WFSs, as long as the number of WFSs is large.

Control configuration of the correction loop in GLAO systems is closed loop by norm.

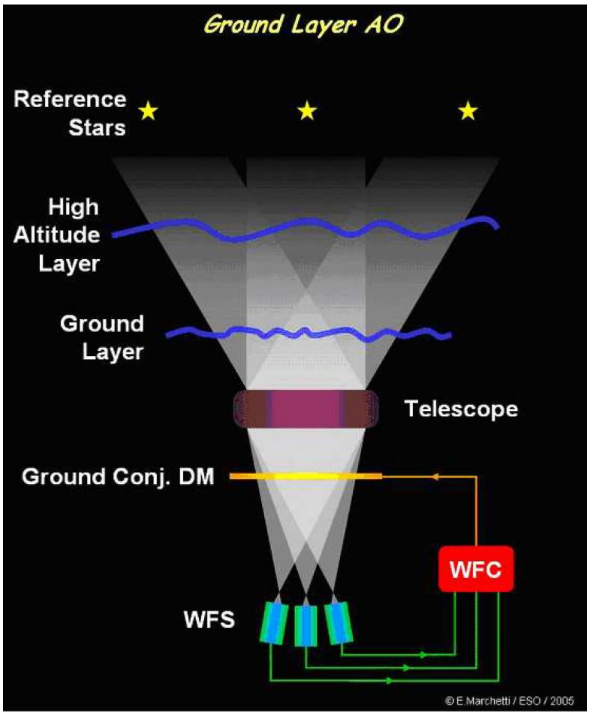

Figure 1-5. GLAO system squematic diagram, from Quirós F. (2007).

1.2.3.3. Multi-Conjugate Adaptive Optics (MCAO) systems

Multi-Conjugate Adaptive Optics (MCAO) systems can be seen as an extension of GLAO systems which intend to achieve the good correction performance of SCAO systems but in large FoV's of correction similar to those of GLAO systems.

Anisoplanatism that limits the corrected FoV in SCAO systems is due to the altitude distribution of turbulence, which makes it vary with the observation angle. The idea behind MCAO systems is to use several DM's conjugated to a different atmospheric height each, where the majority of the turbulence is concentrated, thereby considerably improving corrected FoV with respect to SCAO systems, and correction performance with respect to GLAO systems (Figure 1-6).

The necessity arises then to make a tomographic or 3D estimation of the turbulence in the intended correction FoV. Two approaches are taken for this purpose, giving place to two types of MCAO: Start Oriented (SO-MCAO) and Layer Oriented (LO-MCAO) as shown in Figure 1-6. In the former, each WFS is coupled to a GS and senses the whole turbulence in the direction of that GS; a Wavefront Controller or Computer (WFC) gathers the measurements from all WFS's and computes the tomographic estimation of the turbulence and, hence, the commands to each DM (Figure 1-6, left). In the latter, each WFS is conjugated to the height of a turbulence layer and receives the light from all the GS's; the DM's are conjugated to the same heights as the WFS's, and it is possible in principle to establish a loop control between each pair of WFS/DM conjugated at the same height (Figure 1-6, right).

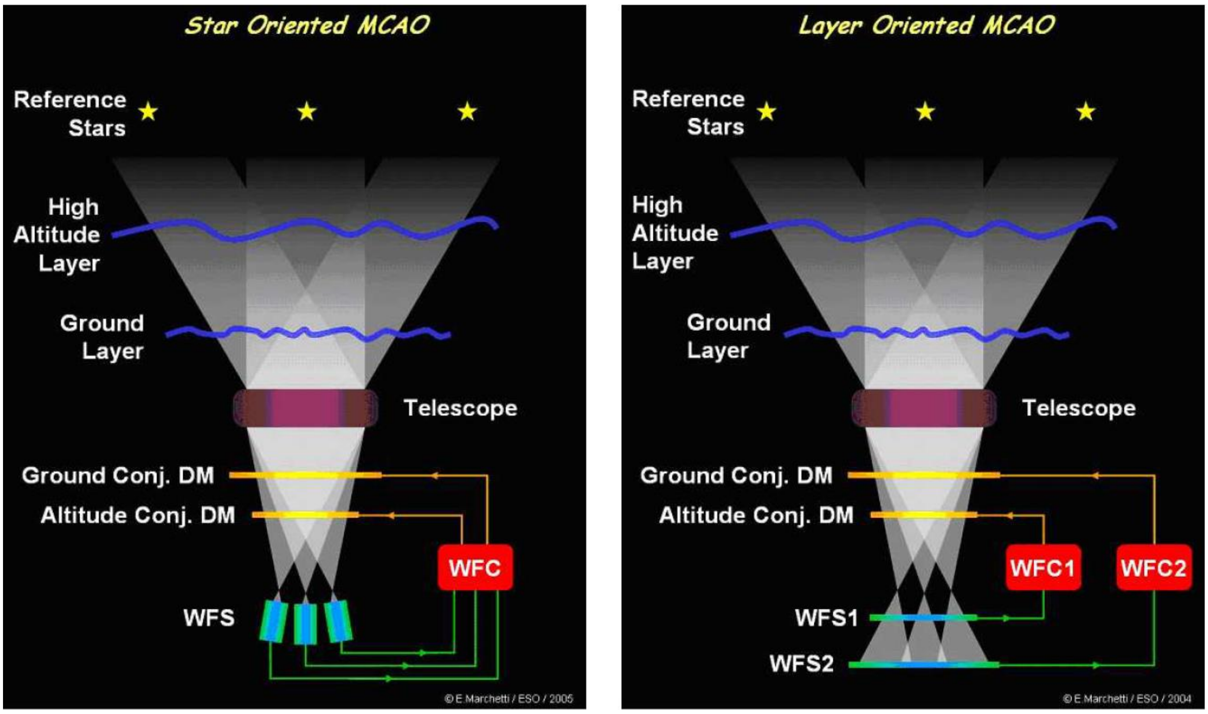

Figure 1-6. MCAO system squematic diagrams, Star Oriented (left) and Layer Oriented (right), from Quirós F. (2007).

AO control of DM's in MCAO is closed loop, allowing feedback of mirror shape to the control system, and this constitutes a point in favour for MCAO systems. However, there are several disadvantages in MCAO systems directly related to the wide field of operation, to the closed loop control strategy and to the MCAO concept itself (Gavel, 2006):

- MCAO requires a wide field optical relay with accessible positions for DM's at desired atmospheric conjugates, and this implies the use of powered optics. Due to being a wide field system, the powered optics in the relay must be larger than the deformable mirror which is conjugated to the pupil (ground layer), to avoid vignetting the off-axis beams. DM's not at the pupil must also be larger to cover the field, and must have the additional actuators associated with this larger "meta-pupil" so that beam footprints anywhere in the field will see AO correction.
- Physical optics inherent to the wide field of view places a lower limit on the size of the pupil in the optical relay and, in particular, on the size of the DM. For a 10-m class telescope, the limit will be on the order of 100 mm DM size. Therefore, mirrors in a wide-field MCAO relay will most likely be traditional large piezo DMs, which are costly and present greater nonlinearities than newer technologies such as MEMS (microelectromechanical systems) mirrors.
- There is a generalized anisoplanatism error due to finite number of DM's trying to correct a continuous atmospheric volume. Thus, there is a trade-off between the correction performance in a field of view versus the extent of that field of view.

– Science objects of interest are seen through the relay optics and the set of corrective DM's in series, so light throughput is reduced, background emission is increased and field distortion may be introduced.

1.2.3.4. Multi-Object Adaptive Optics (MOAO) systems

Here is where Multi-Object Adaptive Optics (MOAO) systems come into play, offering an elegant and clean solution to simultaneously observing tens of turbulence compensated faint objects of interest across a wide field of view. The concept of MOAO consists of, instead of correcting the whole wide FoV, the AO correction is performed only on the regions where the science objects of interest are, thanks to a DM conjugated to pupil for each object. The wavefront sensing is done in a similar fashion as in MCAO. Several bright NGS's possibly combined with LGS's are sensed across the FoV of interest and a tomographic reconstruction allows for an estimation of the on-axis wavefront in the pupil of each science object (Gavel, 2006; Assémat, Gendron and Hammer, 2007; Marlon, 2014). Figure 1-7 is a schematic illustration comparing the MCAO and MOAO concepts (Gavel, 2006).

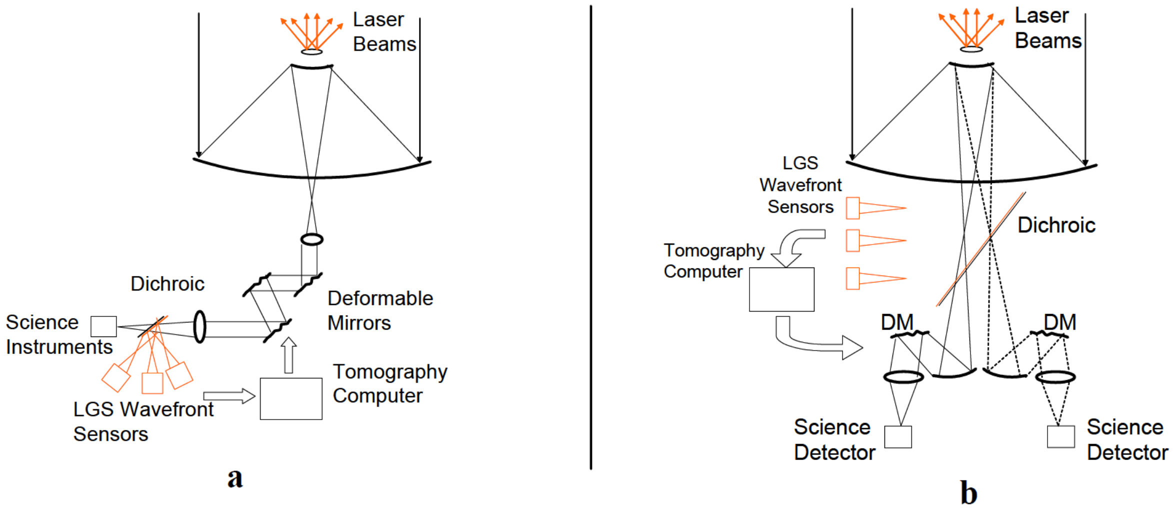

Figure 1-7. Schematic comparison of MCAO (a) systems with MOAO (b) systems, from Gavel, 2006.

As it can be seen, the most noticeable aspect of MOAO systems is the reduction of the number of optical surfaces to its strict minimum. Another important aspect is that WFS's and DM's become separate, physically and functionally independent items, which should optically occupy a small space in the focal plane of the telescope to avoid light obstruction and which can be moved around the focal plane as a positioner does with the IFU's (Integral Field Units) of a multi-object spectrograph (Assémat, Gendron and Hammer, 2007).

On the other hand, the challenge that these systems impose is the open loop control of the DM's. In that sense, effort has to be done in efficiently modelling the response of the DM, taking into account such effects as nonlinearities, hysteresis and drifting (see Guzmán et al, 2010, as an example of such works). Open loop operation also imposes tough requirements to WFS's, which should balance the need of a high dynamic range in order to provide reliable absolute open-loop measurements, with a high sensitivity versus flux level (Assémat, Gendron and Hammer, 2007).

Advantages of MOAO over MCAO systems are (Gavel, 2006):

- Lower isoplanatic error at the science field points. The whole turbulence as seen at the pupil is compensated for, and not only the turbulence at discrete heights.
- MOAO units are deployable on a wider field of regard (FoR[1]) than MCAO. Whereas MCAO systems can offer a 2 x 2 arcmin^2 FoV of correction, MOAO systems are envisaged for FoV's in the order of 10 x 10 arcmin^2 (Assémat, Gendron and Hammer, 2007).
- Sky coverage is enhanced by correcting tip/tilt stars with their own MOAO units, allowing dimmer tip/tilt stars than with MCAO (when LGS's are used).
- Reduced number of optical surfaces for AO correction minimizes emissivity and optimizes throughput. No field distortion is introduced by DM's in series.

There are already MOAO systems which have been tested on-sky. EAGLE is a multi-object IFU near-IR spectrograph conceived for the E-ELT, that will be able to analyse 20 spatially resolved galaxies at a time in a very large field of view (10') relying on a MOAO system. The instrument has a pathfinder, CANARY, which has already been tested in the William Herschel Telescope (WHT). On sky results may be found in Rousset et al (2011).

RAVEN is a MOAO system with 3 NGS's, a central LGS and two science pick-offs that feed the IRCS (Infrared Camera and Spectrograph) instrument of the 8-meter class Subaru telescope. Each corrected science FoV is 4" whereas the whole FoR from where the two science objects are selected and simultaneously analysed is of 2'. On-sky results can be seen at Larière et al, 2014, where the authors propose as future work the development of *advanced centroiding algorithms* suited for open loop AO. They mention the development in their group of a modified correlation algorithm which they have tested at the laboratory (Andersen et al, 2014).

1.3. The Shack-Hartmann Wavefront Sensor (SHWFS)

Wavefront sensors are key elements in AO systems, as they are the probes that sense the turbulence wavefront. The object of study of this work is centred around the Shack-Hartmann wavefront sensor (SHWFS), which is the most widely utilized WFS, not only in astronomical applications but also in medical, ophthalmological, communications and other optical applications. Other sensors used mainly in astronomical applications are the curvature sensor and the pyramidal sensor. They will not be treated in this work.

1.3.1. Principles of operation

The design of this sensor was based on an aperture array that had been developed in 1900 by Johannes Franz Hartmann as a means of tracing individual rays of light through the optical system of a large telescope, thereby testing the quality of the image (Hartmann, 1900). In the

---

[1] In MOAO systems, the term *Field of Regard* (*FoR*) is employed referring to the whole field of view from which science objects can be selected and analysed simultaneously, whereas the term *Field of View* (*FoV*) refers to the corrected field of view for each science object.

late 1960's, Roland Shack and Ben Platt modified the Hartmann screen by replacing the apertures in an opaque screen by an array of lenslets (Shack, 1971; Platt and Shack, 2001).

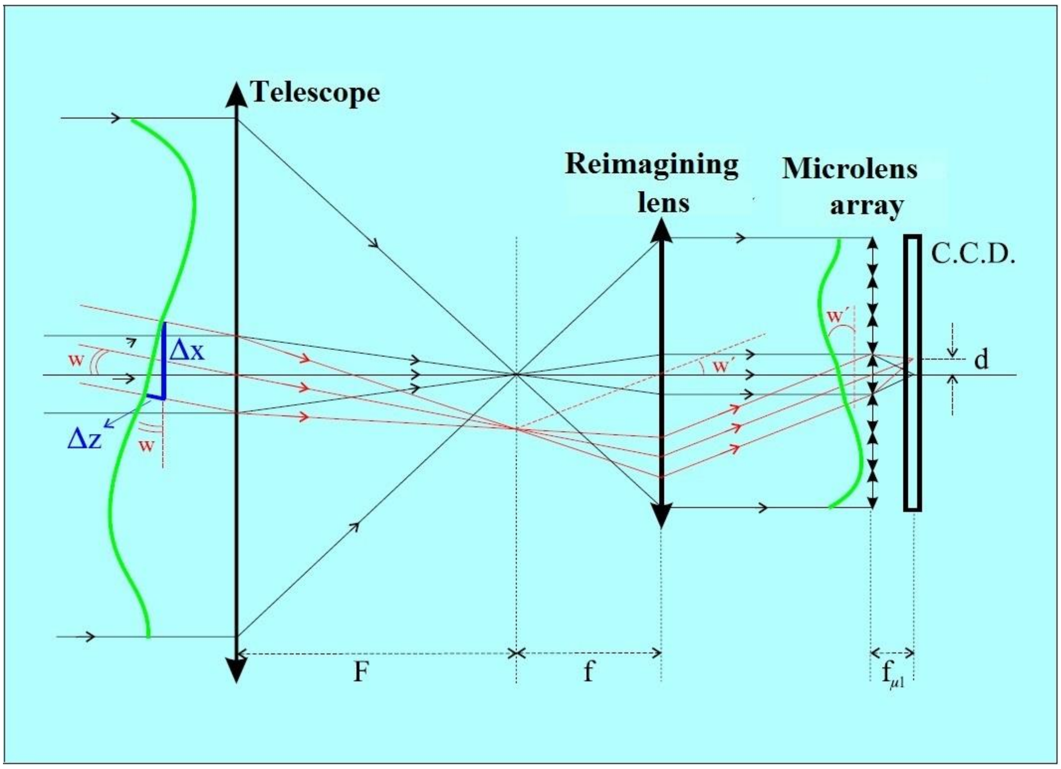

Figure 1-8. Schematic diagram of the Shack-Hartmann wavefront sensor operation, Rodríguez-Ramos, 1998.

Figure 1-8 schematically illustrates the operation of a SHWFS in a one-dimensional fashion (Rodríguez-Ramos, 1998). The detector is essentially composed of two components: a microlens array and a detector, the latter a CCD array in this case. The focal length of the microlenses is the same for all of them, and the detector is placed at this very distance from the microlens array. The local tilt of the wavefront across each microlens can then be calculated from the position of the focal spot on the sensor. Any phase aberration can be approximated by a set of discrete tilts. By measuring all of these tilts, the whole wavefront can be estimated.

Of course, the microlens array works in a telescope's pupil conjugated plane, where dimensions are scaled down and more manageable. This scaling towards the Hartmann-Shack sensor's input is dependent upon the ratio of the telescopes focal length (F) and the "reimagining" lens focal length (f), following the notation in Figure 1-8, and it affects both linear and angular magnitudes.

The same figure shows the optical path that a perturbed wavefront would follow, from the telescope pupil till the sensor's detector. Red lines show the portion of light that strike a single microlens, and which arrives to the telescope pupil tilted by an angle ω. This angle scales to an angle ω' at the output of the reimagining lens or the input of the microlens. The following relationship holds between both angles:

$$\frac{\tan\omega}{\tan\omega'} = \frac{f}{F} \qquad \text{[Eq. 1-11]}$$

Note that angle ω is produced by a linear wavefront displacement Δz along the wavefront optical axis *z* and across the subaperture width Δx, so for small angles, $\tan\omega = \Delta z/\Delta x$. Also, the spot displacement in the detector *d* is a consequence of wavefront angle of arrival ω' at the microlens, and so $\tan\omega' = d/f_{\mu l}$, where $f_{\mu l}$ is the microlens focal length. Therefore, there is relationship between the wavefront displacement at the system's pupil Δz and the spot displacement at the detector *d* which can be expressed as:

$$\frac{\Delta z}{\Delta x} = \frac{f}{F}\frac{d}{f_{\mu l}} \qquad \text{[Eq. 1-12]}$$

Δz is a wavefront displacement measured in linear units. Here the variable ϕ is introduced as the wavefront measured in radians, so that $\Delta\phi = (2\pi/\lambda)\Delta z$. Also, displacement *d* is measured in linear units and can be expressed as the product of the displacement in pixels *d'* and the pixel size d_{pix}, finally leading to an expression that relates wavefront peak to valley displacement Δϕ across the subaperture, in radians, to pixel displacement d' of the spot:

$$\frac{\Delta\phi}{\Delta x} = \left[\frac{2\pi}{\lambda}\frac{f}{F}\frac{d_{pix}}{f_{\mu l}}\right] d' \qquad \text{[Eq. 1-13]}$$

where all the terms into brackets are constants related to the system and sensor geometries.

1.3.2. Image processing and phase recovery at the SHWFS

It is clear from expression [Eq. 1-13] that the SHWFS senses phase gradient at every subaperture and, consequently, in the whole aperture of the system. This statement relies on the adequate measurement of the displacement of the spots at the detector. The normal procedure to determine the spots' displacements is to assign a certain portion of pixels of the detector to each spot (and that portion will determine the FoV of the sensor) and compute through some centroiding method the position of the spot in its assigned portion. This position will be compared to a reference position measured, for example, by illuminating the sensor with a plane wavefront. Point 1.4 is a review of the most employed centroiding methods in a SHWFS.

Wavefront phase reconstruction at the whole system's aperture is obtained from the measurements of the $2N^2$ average phase slopes at the array of N^2 subapertures. That is, in each subaperture a pair of gradients are measured, one in each orthogonal axis. This implies approximating the phase wavefront at the subaperture level to a plane, which is tilted according to the estimated gradients. A phase recovery method is applied then to all the measurements globally to obtain the whole aperture's phase.

These methods are classified in two big groups:

- Zonal methods, in which the phase at any point in the aperture is a function of the phase and phase slope estimations at neighbour points.

- Modal methods, in which the phase is expressed as a linear combination of a set of functions, which are orthogonal in the aperture. Zernike functions are the most employed for circular apertures (see point 1.3.2.2).

Chapter 5 of the present work consists of a set of simulation tests performed over the whole aperture of the SHWFS. For this purpose, the Object Oriented Matlab Adaptive Optics toolbox (OOMAO, Conan and Correia, 2014) has been utilized. Here, some of the phase recovery methods implemented in the toolbox and used in the tests are seen in detail.

1.3.2.1. Zonal methods for phase recovery

The starting point is a geometry consisting of phase gradients measured at certain points, and phase points where the phase is to be estimated. Figure 1-9 (Herrmann, 1980) shows a geometry that relates measured gradients and estimated phase points locations. Basically, gradient is considered to be measured at the subaperture centres, and phase is estimated at the corners of the subapertures. This geometry is called Fried geometry (Fried, 1977) and is the one employed in the OOMAO toolbox.

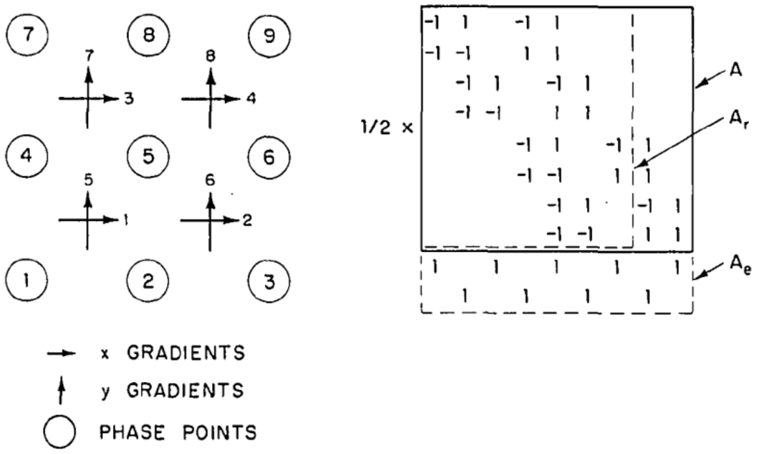

Figure 1-9. Fried geometry with corresponding 'A' matrices in a SHWFS as depicted in Herrmann, 1980.

Figure 1-9 shows a simple case of 2 x 2 subapertures, and so 8 measured gradients and 9 points where to estimate phase. It also shows the A matrix that relates gradients to phases for this particular case, according to the following expression (Herrman, 1980):

$$\Delta\phi = A\ \phi \qquad \text{[Eq. 1-14]}$$

where $\Delta\phi$ is a column vector of measured average phase gradients in both axes of each subaperture and ϕ is a column vector of phases in the corners of the subapertures. Matrix A has a deficiency in rank of 2 for Fried geometry. It is possible to define a reduced A matrix, called A_r in Figure 1-9, by equalling phase at points 8 and 9 to zero. Alternatively, two equations can be added to the system by imposing constraints to the sum of paired numbered phases and the sum of odd numbered phases, resulting in the extended matrix A_e. Both A_r and A_e are full rank and they lead to no indetermination when obtaining phases from gradients.

Least-squares minimum norm solution is the first zonal phase recovery method to be proposed (Fried, 1977; Hudgin, 1977; Herrmann, 1980). OOMAO calls it *Direct Fitting.* It is based on the generalized Moore-Penrose matrix inversion, and can be expressed as:

$$\widehat{\phi}_{LSMN} = A^{+}\,\Delta\phi \qquad \text{[Eq. 1-15]}$$

with A^{+} being the generalized inverse or pseudo-inverse of matrix A, and $\widehat{\phi}_{LSMN}$ the estimated phases from the measured gradients $\Delta\phi$.

Linear Minimum Mean Square Error (LMMSE)

Minimum Mean Square Error (MMSE) estimator is a Bayesian estimation method which minimizes the mean square error of the fitted values of the variable to be estimated, and it is given by the posterior mean of the parameter to be estimated. In the case being dealt with here, it would be expressed as:

$$\widehat{\phi}_{MMSE} = \langle \phi / \Delta\phi \rangle \qquad \text{[Eq. 1-16]}$$

MMSE becomes the linear MMSE or LMMSE when a linear dependency of the parameter to be estimated upon the measured variable is assumed. In our case, and taking into account that phase and phase gradients are zero mean variables, the LMMSE estimator of the phase would be:

$$\widehat{\phi}_{LMMSE} = C_{\phi\Delta\phi} C_{\Delta\phi}^{-1}\,\Delta\phi \qquad \text{[Eq. 1-17]}$$

where $C_{\phi\Delta\phi}$ is the cross-covariance matrix between ϕ and $\Delta\phi$, and $C_{\Delta\phi}$ is the auto-covariance matrix of $\Delta\phi$.

This is a second choice of zonal phase recovery method implemented in the OOMAO toolbox.

1.3.2.2. Modal methods for phase recovery. Zernike functions.

It is sometimes useful to represent a phase by the coefficients of an expansion in a set of basic functions. Zernike polynomials are very conveniently used because of their simplicity and physical meaning. This could be expressed as:

$$\phi(x, y) = \sum c_j\, Z_j(x, y) \qquad \text{[Eq. 1-18]}$$

x and *y* being the coordinates where phase ϕ and set of Zernike functions Z_j are defined, and c_j are the coefficients of the expansion.

The definition of Zernike functions for polar coordinates can be found in Noll, 1976. For *n* the radial order and *m* the azimuthal order, both nonnegative integers fulfilling *n*≥*m* and *n-m* even, a pair of even and odd Zernike functions are defined for *m*≠0 or a single function for *m*=0:

$$\left.\begin{aligned} Z_n^m(\rho,\theta) &= \sqrt{2(n+1)}R_n^m(\rho)\cos(m\theta) \\ Z_n^{-m}(\rho,\theta) &= \sqrt{2(n+1)}R_n^m(\rho)\sin(m\theta) \end{aligned}\right\} m \neq 0$$

$$Z_n^m(\rho,\theta) = \sqrt{(n+1)}R_n^0(\rho), \qquad m = 0 \qquad \text{[Eq. 1-19]}$$

with ρ the normalized radial distance $0 \leq \rho \leq 1$, and θ the azimuthal angle. The radial polynomials $R_n^m(\rho)$ are defined as:

$$R_n^m(\rho) = \sum_{s=0}^{(n-m)/2} \frac{(-1)^s(n-s)!}{s!\left[\frac{n+m}{2}-s\right]!\left[\frac{n-m}{2}-s\right]!}\rho^{n-2s} \qquad \text{[Eq. 1-20]}$$

Noll (1976) mapped the *m* and *n* indexes into a single index *j*, with the following rule: even Zernike functions -with azimuthal part $\cos(m\theta)$- receive even indexes *j*; odd Zernike functions -with azimuthal part $\sin(m\theta)$- receive odd indexes *j*; lower *n* values receive lower *j*; and within a given *n*, lower values of *m* receive lower *j*.

So, any wavefront phase $\phi(r,\theta)$ defined in a circular aperture with radius *R* as a function of radial coordinate r, $0 \leq r \leq R$, and azimuthal coordinate θ, can be expressed as:

$$\phi(r,\theta) = \phi(R\rho,\theta) = \sum_j c_j Z_j(\rho,\theta) \qquad \text{[Eq. 1-21]}$$

Zernike functions correspond to classic optical aberrations such as tilt, defocus, astigmatism, coma, spherical aberration, distortion, field curvature, etc. The coefficients c_j give and idea of the dominant aberrations in the propagation medium. Zernike modal phase recovery means estimating such Zernike coefficients. A vectorised expression from [Eq. 1-21] would be:

$$\phi = Zc \qquad \text{[Eq. 1-22]}$$

with ϕ a column vector of phases at the discrete point of estimation, *c* a column vector of coefficients and *Z* a matrix with as many columns as Zernike functions are used in the expansion and as many rows as evaluation coordinates of the same. Substituting ϕ in equation [Eq. 1-14] by its value in [Eq. 1-22], a relationship between measured phase gradients and Zernike coefficients is obtained:

$$\Delta\phi = (AZ)\ c \qquad \text{[Eq. 1-23]}$$

Product of matrixes AZ is equivalent to computing the phase difference of each Zernike function across the subapertures of the sensor. The OOMAO toolbox computes this matrix in a recursive manner (Stephenson P., 2014, for example). So, a first option of modal phase recovery offered by OOMAO is inverting the above expression [Eq. 1-23] in a minimum least squares sense to obtain a direct relationship between Zernike coefficients c and measured gradients $\Delta\phi$:

$$\hat{c}_g = (AZ)^+ \, \Delta\phi \qquad \text{[Eq. 1-24]}$$

A second option would be a two steps option. First, a zonal phase recovery method is applied to estimate the phases ϕ, for example by LSMN estimation; second, coefficients c are estimated by solving the set of equations in expression [Eq. 1-22] in a least squares sense:

$$\hat{c} = Z^+ A^+ \Delta\phi \qquad \text{[Eq. 1-25]}$$

Expressions [Eq. 1-24] and [Eq. 1-25] do not give the same results. In the first option, a least squares fit gives the minimum variance of the gradients, and hence the subscript g, whereas the second option gives a minimum variance of the phase (Herrmann, 1980).

1.4. Centroiding methods in a SHWFS

When a light wavefront strikes a SHWFS, a spots matrix is registered at the detector as a consequence of light going through the microlens array. Each spot is displaced, with respect to the plane wavefront case, a distance proportional to the average wavefront gradient as expressed in equation [Eq. 1-13]. Methods have been devised that deal globally with the matrix spots and obtain the phase gradient by spatial demodulation of the whole image in the detector (Carmon and Ribak, 2003; Talmi and Ribak, 2004; Sarver et al, 2006; Lukin et al, 2010). Nevertheless, the most common approach is the independent treatment of each subaperture, consisting of estimating the displacement of the corresponding spot at the detector, followed by a phase recovery method that deals globally with the gradients matrix, such as those described in point 1.3.2. The methods employed to estimate the displacement of each spot in its assigned portion of detector are generally called *centroiding methods*, both when absolute displacement is estimated and when the displacement is relative to a reference spot.

It is convenient to clarify that two possible definitions for a circular subaperture phase tilt can be found (see Tyler, 1994, for example). One is the *G-tilt*, which is the average phase gradient over the aperture. The other one is the *Z-tilt*, or Zernike tilt, and is the tilt of the best planar approximation of the phase in a least squares error sense. For symmetric spots, both tilts coincide. However, when asymmetric phase modes dominate, both tilts differ. Centre of gravity based centroiding methods actually estimate G-tilt, whereas when minimizing phase estimation error or maximizing Strehl ratio is desired, a Z-tilt estimation in the subperture would be preferred.

Three are the most known and favourite centroiding method families which are foreseen to be employed in ELT's (Thomas et al, 2006; Gradatour et al, 2010; Lardière et al, 2010): centre of gravity (CoG), cross-correlation (CC) and matched filter (MF).

1.4.1. Centre of Gravity (CoG) based methods

The centre of gravity algorithm applies to each spot image *I*, defined across the *x*-horizontal coordinate and *y*-vertical coordinate, the following function:

$$cog(I) = \left(\sum_{x,y} xI(x,y) \Big/ \sum_{x,y} I(x,y) \,, \sum_{x,y} yI(x,y) \Big/ \sum_{x,y} I(x,y) \right) \qquad \text{[Eq. 1-26]}$$

In the absence of noise, it is a direct estimator of the average phase gradient at the aperture or G-tilt. It is a linear estimator for small spot's displacements, such as in closed loop system's operation. However, it is very much affected by spot's truncation and by detector's noise when a large FoV, implying more detector's pixels into play, and high dynamic range are required, such as in open loop operation. The following are variations to the simple CoG that intend to improve its robustness against these effects.

1.4.1.1. Thresholded centre of gravity (TCoG)

It applies a threshold *T* to the image *I*, and only those pixels with a brighter intensity than *T* are taken into account for CoG computation, according to the following expression:

$$tcog(I) = \begin{pmatrix} \sum_{x,y\ /\ I \geq T} x[I(x,y) - T] \Big/ \sum_{x,y\ /\ I \geq T} [I(x,y) - T] \,, \\ \sum_{x,y\ /\ I \geq T} y[I(x,y) - T] \Big/ \sum_{x,y\ /\ I \geq T} [I(x,y) - T] \end{pmatrix} \qquad \text{[Eq. 1-27]}$$

Threshold *T* is normally a fraction of the spot's maximum intensity, with a lower bound which depends on the detector's noise. It is preferably determined by optimization, since thresholding is itself a source of nonlinear noise (Arines and Ares, 2002).

1.4.1.2. Weighted centre of gravity (WCoG)

It applies a weight *W* to the image *I* before centroiding, and so its formulation is:

$$wcog(I, W) = cog(I \times W) \qquad \text{[Eq. 1-28]}$$

Weight *W* is normally a Gaussian centred at the image's centre, intending to give more weight to brighter pixels and to attenuate noisy pixels, for an assumed centred spot. So WCoG method is adequate for small displacements in the spot, as in closed loop operation in XAO systems (Nicolle, 2004; Fusco, 2004). It becomes nonlinear for big displacements as the spot's shape gets distorted, and needs careful calibration and linearization to compensate spot's distortion and gain dynamic range (Lardière et al, 2010). Optimization of the width of the

Gaussian weight W is convenient in this sense, to get a good compromise between noise rejection and linearity.

Some variations of this algorithm have been proposed that intend to gain in dynamic range: IWC or Intensity Weighted Centroiding, in which weights are the pixel intensities themselves, and IWCoG, for Iteratively Weighted Centre of Gravity, where weights are iteratively displaced to the measured spot position (Vyas, Roopashree and Prasad, 2009a).

1.4.1.3. Quad Cell (QC)

Quad Cell is the particular case of a CoG with only 2 x 2 pixels or cells. Numbering those pixels from 1 to 4, starting upward to the left and in anti-clockwise direction, its formula would be:

$$qc(I) = \left(\frac{1}{G_x}\frac{I_1 + I_2 - I_3 - I_4}{I_1 + I_2 + I_3 + I_4} \quad , \quad \frac{1}{G_y}\frac{I_1 - I_2 + I_3 - I_4}{I_1 + I_2 + I_3 + I_4} \right) \qquad \text{[Eq. 1-29]}$$

This method is very sensitive to spot's shape variations. $G_x$and $G_y$intend to compensate for gain variations in *x* and *y* axis due to different spot's elongation. It is a preferred method for very low light flux level, but it is only suitable for closed loop operation and needs calibration and compensation for its nonlinearities.

1.4.2. Cross-Correlation (CC) method

Cross-correlation method applied for extended objects can be applied also to point-like sources (Poyneer et al, 2004). The cross-correlation between the snapshot or *live* image *I* and a reference image I_0 is computed, and a *correlation figure* is obtained. Centroid of the correlation figure is an estimation of displacement between live and reference images. For subpixel accuracy, this centroid can be computed with a CoG, habitually thresholded, or with curve fitting methods. Correlation can be computed in the image domain, but for computational cost reasons, it is preferably performed in the Fourier domain (Sidick et al, 2008).

It has been reported (Poyneer et al, 2004; Thomas et al, 2006; Gradatour et al, 2010; Lardière et al, 2010) that CC is more robust than CoG based methods against detector noise; it is more linear allowing for a higher dynamic range, and it is less impacted by variations in the spot shape. The cons are a much higher computational cost and the need for a proper reference selection. Nonetheless, at high light flux level both CC and CoG methods perform similarly and are limited by photonic noise.

Recently, CC performance in the RAVEN MOAO system for the Subaru telescope for natural and laser guide stars has been reported (Andersen et al, 2014). An increase in 0.5 to 1 in limiting magnitude is predicted at a cost of a decrease of frequency system from 250 to 150 Hz, so it CC is particularly suited to very low light flux levels. They report CC is more robust than other methods against spot undersampling and large FoV's.

1.4.3. Matched Filter (MF) method[2]

Matched Filter method is based on a first order approximation of the Taylor expansion of the spot's image intensity *I* as a function of spot displacement with respect to a reference spot's image I_0 (Lardière et al, 2010):

$$I = I_0 + (d_x - d_{0x})\frac{\partial I}{\partial d_x} + (d_y - d_{0y})\frac{\partial I}{\partial d_y} \quad \text{[Eq. 1-30]}$$

with (d_x, d_y) the coordinates of the live spot and (d_{0x}, d_{0y}) the coordinates of the reference spot. This Taylor expansion is only valid if the current image *I* is a shifted copy of the reference image I_0 and if the shift is of a very small amount (a fraction of a pixel). [Eq. 1-30] can be expressed for each subaperture in a matrix notation as:

$$I - I_0 = G_{mf}(d - d_0) \quad \text{[Eq. 1-31]}$$

with G_{mf} the *matched filter gain* matrix composed of the pixel intensity derivatives for both x- and y-directions. [Eq. 1-31] can be solved for each lenslet slope *d* as:

$$\hat{d}_{mf} = R\,(I - I_0) + d_0 \quad \text{[Eq. 1-32]}$$

with *R* the pseudo-inverse of the matrix G_{mf}.

MF method is suited for low flux level. It requires proper reference selection and refreshment; and a correct calibration against the updated reference.

---

[2] Some authors use the terms *Matched Filter* and *Cross-Correlation* interchangeably (Leroux and Dainty, 2010, for example). It is not the case in the present work.

Chapter 2. Objective of the present work

2.1. Motivation of the work

The centroiding method in a Shack Hartmann wavefront sensor plays a crucial role in determining the robustness of the sensor against the measurement noise described in point 1.2.2.2. With the recent interest in MOAO systems, in which turbulence is sensed and compensated for in open loop, the requirement of balancing sensitivity respect to light flux level with a high dynamic range has become a very desirable trait in wavefront sensors. Moreover, a very low light level situation calls for a configuration with high subaperture size to Fried parameter ratio and, hence, a centroiding method which is robust against high order aberrations in the spot is required. All this should be combined with a fast algorithm with low computational cost in order to keep the temporal error described in point 1.2.2.4 as low as possible.

The success of the CoG based methods is understandable from the point of view of simplicity and low hardware resources requirement. However, they are prone to noise when many pixels per subaperture come into play, such as when a large dynamic range or field of view is required. WCoG and QC are adaptations of pure CoG that make the sensor more sensitive, but at the cost of lowering the dynamic range, making them suitable only for closed loop system operation. TCoG is perhaps the CoG derived method which best balances sensitivity and dynamic range requirement; yet, threshold cannot be kept high in low light level conditions, and non-Gaussian type of noise such as CIC noise in Electron Multiplying CCD's (EMCCD's) cannot be fully managed with a simple threshold.

Hardware speed and processing capabilities are in continuous growth. Modern GPU's (Graphical Processor Units), which were in principle thought for commercial applications with a high computational demand due to video processing, such as 3D games, are taken advantage of in scientific applications where the high computational load is parallelizable. Another hardware processing component which is parallel in nature is the FPGA (Field Programmable Gate Array). It is programmable hardware, and was in principle thought of as a digital electronics prototyping component. More recently, it has been used for scientific parallel demanding computation, such as computing the 2D-FFT (bi-dimensional Fast Fourier

Transform) or in a full-FPGA AO system (Rodríguez-Ramos J.M et al, 2008; Chulani H.M. et al, 2016). Processing components such as GPU's and FPGA's allow for centroiding methods with a certain computational complexity to be implemented in a SHWFS and still its computational latency be negligible in comparison to the latency due to other required operations such as light integration, image read and DM shape change.

Some authors have proposed shifting from the image domain to transformed domains where denoising filters are easier to apply. In this sense, the Zernike expansion of the image has been proposed (Vyas, Roopashree and Prasad, 2009b), followed even by feature extraction and Gaussian pattern matching techniques (Vyas, Roopashree and Prasad, 2010). A somewhat similar method is the Gram-Charlier expansion of the Gaussian fit of the image and subsequent filtering proposed by Ruggiu, Solomon and Loos (1998).

The Fourier transform of a discrete image I_{xy} is its expansion into a base of discrete exponentials, according to the expression (Oppenheim and Schafer, 1989)

$$\mathbb{I}(\omega_x, \omega_y) = \mathcal{F}\{I_{xy}\}\big|_{\omega_x,\omega_y} = \sum_x \sum_y I_{xy} e^{-j\omega_x x} e^{-j\omega_y y} \qquad \text{[Eq. 2-1]}$$

with $\mathcal{F}\{\cdot\}$ the Fourier transform operation, $\omega_x = 2\pi f_x$, $\omega_y = 2\pi f_y$, f_x and f_y the spatial frequencies in the x- and y-axis, respectively, and $-\pi \leq \omega_x \leq \pi$, $-\pi \leq \omega_y \leq \pi$, or, alternatively, ω_x and ω_y ranging any interval of length 2π, since the Fourier transform is periodic in both axes with period 2π.

Fast algorithms have been developed that compute a discrete version of the Fourier transform of a discrete signal (Fast Fourier Transform, abbreviated FFT). Besides, many operations in the image domain have their counterparts in the Fourier domain. Cross-correlation in the image domain, for example, becomes a multiplication (and conjugation of one of the terms) in the Fourier domain. Furthermore, displacement in the image domain is equivalent to a planar phase addition in the Fourier domain ([Eq. 2-2]). This has led to the CC centroiding method being completely calculated in the Fourier domain, as described in Sidick et al, 2008. After multiplication of the image's Fourier transform by the reference's Fourier conjugate, a least squares fit is applied to the phase of the product to compute its slope, and so, the displacement of the correlation figure.

The relationship between image displacement and Fourier phase slope can be easily derived from [Eq. 2-1] and expressed as

$$\mathcal{F}\{I_{xy}(x - x_0, y - y_0)\}\big|_{\omega_x,\omega_y} = \mathbb{I}(\omega_x, \omega_y) e^{-j\omega_x x_0} e^{-j\omega_y y_0} \qquad \text{[Eq. 2-2]}$$

This is represented in a one-dimensional simplification in Figure 2-1 (Li, Huang and Gong, 2014). Based in this very principle, professor J. P. Fillard and his group at the Université de Montpellier proposed a method they called Fourier Phase Shift (FPS) as an alternative to the CoG centroiding method (Fillard, 1992; Fillard et al, 1993), back in the 90's. It consisted of applying a least squares planar fit to the phase of the image's Fourier transform to obtain its slope, thus estimating what he called *a best symmetric centre* of the spot, since a plane

Fourier phase corresponds to a symmetric spot in the image domain. He reported an improved immunity of the FPS method against bias background components and additive noise in the image, with respect to the pure CoG method. More recently, Li, Huang and Gong (2014) have proposed the s-FDO method (single frame Fourier Domain Offset estimation algorithm), essentially the same as professor Fillard's, and have reported greater immunity to low spatial frequency intensity variations over the whole SHWFS's aperture than with CoG, such as when sensing a laser beam.

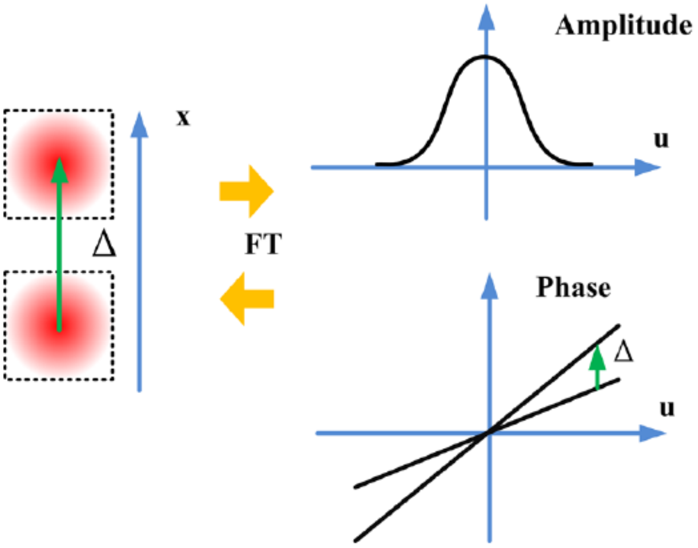

Figure 2-1. One dimensional representation of the relationship between image displacement and linear phase slope shift in the Fourier domain, from Li, Huang and Gong, 2014.

A planar fitting to the phase in the Fourier domain can be viewed from the *cepstrum* analysis and filtering perspective as a powerful denoising tool that eliminates, not only additive noise and pixels illuminated by spurious noisy charge, but also asymmetries in the spot due to truncation or atmospheric higher order aberrations. This will be treated in detail in Appendix A.

As final examples of antecedents that intend to improve the traditional centroiding methods, Bayesian methods will hereby be mentioned. Sallberg, Welsh and Roggemann (1997) and van Dam and Lane (2000) are two examples of Bayesian techniques applied in the image domain that intend to maximize the estimated centroids probability (MAP or Maximum a Posteriori technique) or minimize their estimation error (MMSE or Minimum Mean Square Error technique), given a certain measured light distribution in the detector, by introducing *a priori* knowledge of the turbulence that originates the spots displacements. Both references report a considerable improvement of Bayesian techniques over the traditional centroiding methods, especially for well-defined spots with subaperture size equal to the Fried parameter.

2.2. Objectives, methods and materials

The objective of the present work is to explore the performance of a centroiding method formulated as an optimized Bayesian estimator in the Fourier domain, in a Shack Hartmann wavefront sensor. The scope of the present work is limited to night time astronomical adaptive optics applications, where a natural guide star is the sensing light source. This novel algorithm's mathematical expression will be derived, and its advantages and disadvantages with respect to most utilized centroiding methods such as TCoG, WCoG and CC will be determined, according to the following figures of merit:

- Real time implementation feasibility. In that sense, the number of operations to be performed in a system cycle per SHWFS subaperture and whole aperture will be worked out and contrasted with the computational power of modern processors and co-processors.
- Balance between sensitivity and dynamic range. In that sense, the behaviour of the centroiding method will be evaluated as a function of light flux level, detector noises and required field of view for open and closed loop operation.
- The effect of spot truncation due to a limited number of pixels (and hence, limited field of view) in the sensor will be determined and compared with the behaviour of the other centroiding methods.
- Robustness against high order aberrations in the spot, more noticeable as the size of the subaperture with respect to the Fried parameter increases, will be evaluated and compared.

The proposed algorithm's characteristics in terms of sensitivity, dynamic range and robustness against spot's deformation will be determined firstly at a subaperture level through numerical simulation. MATLAB™[3] software package will be used for this purpose.

Numerical simulations will then be extended to the whole SHWFS aperture with the aid of a free open MATLAB toolbox called *Object Oriented Matlab for Adaptive Optics toolbox* (OOMAO, Conan and Correia, 2014). The whole sensor's behaviour with this new proposed centroid method can be thus evaluated, and Strehl Ratio as well as Encircled Energy figures due to measurement and fitting errors can be estimated.

Finally, the work done by the author for the EDiFiSE (Equalized and Diffraction limited Field Spectrograph Experiment) project at the IAC (Instituto de Astrofísica de Canarias) has created the opportunity of utilizing its adaptive optics setup at the optical laboratory facility of the institute. This setup consists of a full-FPGA closed loop controlled SCAO system with a SHWFS that comprises a microlens array and an EMCCD Andor Ixon+ detector of 128 by 128 pixels (Chulani et al, 2016). It receives a perturbed light wavefront from the IACAT (IAC's Atmosphere and Telescope) ground support equipment (Moreno-Raso et al, 2010). Inside the IACAT, Kolmogorov turbulence is emulated by phase plates with the appropriate refractive index drawing, with five phase plates in total that emulate a different Fried parameter each, and the possibility of combining up to three phase plates simultaneously in the optical bench. The aperture and focal length characteristics of three different telescopes can also be emulated; the 4,2 m William Herschel Telescope's configuration will be selected. Light source is intensity regulated.

---

[3] MATLAB is a registered trademark of The Mathworks, Inc.

The SHWFS will be utilized in this setup to acquire image sequences distorted by static turbulent patterns, with different light fluxes and turbulence strengths, and without applying any correction, so that dynamic range requirement at the wavefront sensor is high. Image sequences will be processed offline with different centroiding algorithms and the wavefront recovery error determined for each sequence and each algorithm. Applied static wavefront perturbation is actually unknown, but can be estimated as an average of wavefront phases recovered by the centroiding methods under study in a very bright light level situation. The objective is to compare each algorithm's characteristics of sensitivity, dynamic range and robustness against spots deformation due to limited FoV and/or turbulence.

A previous step is the complete sensitivity, gain and noise characterization of the EMCCD detector, in order to correctly estimate the flux level and SNR's from the recorded images.

Chapter 3. The Weighted Fourier Phase Slope algorithm

This chapter presents the mathematical definition of the centroiding method under study in this work. It has been given the name *Weighted Fourier Phase Slope* (abbreviated *WFPS*), because it first calculates the slopes, or derivatives with respect to both spatial frequency axes, of the image's Fourier phase, and then averages these slopes with optimized weights in order to obtain the centroid's horizontal and vertical coordinates in the image domain. The computational cost of such an algorithm is also presented, and contrasted with other known algorithms.

This innovative centroiding method has been presented in the IEEE 12th Workshop on Information Optics (Chulani and Rodríguez-Ramos, 2013) and has been accepted for presentation at the 5th Adaptive Optics for Extremely Large Telescopes Conference (Chulani and Rodríguez-Ramos, 2017).

3.1. Fourier Phase Slope

For a given SHWFS subaperture image I_{xy}, its Fourier transform is

$$\mathbb{I}(\omega_x, \omega_y) = \mathcal{F}\{I_{xy}\}\big|_{\omega_x,\omega_y} = \sum_x \sum_y I_{xy} e^{-j\omega_x x} e^{-j\omega_y y} \qquad \text{[Eq. 3-1]}$$

following the notation in [Eq. 2-1], and can be expressed as

$$\mathbb{I}(\omega_x, \omega_y) = \left|\mathbb{I}(\omega_x, \omega_y)\right| e^{j\,arg\left(\mathbb{I}(\omega_x,\omega_y)\right)} \qquad \text{[Eq. 3-2]}$$

with $\left|\mathbb{I}(\omega_x, \omega_y)\right|$ and $arg\left(\mathbb{I}(\omega_x, \omega_y)\right)$ being the magnitude and angle or phase, respectively, of the complex number $\mathbb{I}(\omega_x, \omega_y)$. The Fourier phase slopes with respect to both horizontal and vertical axes are the phase derivatives with respect to the spatial frequency in those axes:

$$\frac{\partial}{\partial \omega_x} arg\left(\mathbb{I}(\omega_x, \omega_y)\right) \quad ,, \quad \frac{\partial}{\partial \omega_y} arg\left(\mathbb{I}(\omega_x, \omega_y)\right) \qquad \text{[Eq. 3-3]}$$

$arg(\cdot)$ in [Eq. 3-3] is the "unwrapped" phase defined such that it satisfies the requirement of continuity:

$$arg\left(\mathbb{I}(\omega_x,\omega_y)\right) = ARG\left(\mathbb{I}(\omega_x,\omega_y)\right) + 2\pi r(\omega_x,\omega_y) \qquad \text{[Eq. 3-4]}$$

where $ARG\left(\mathbb{I}(\omega_x,\omega_y)\right)$ is the principal value of the phase, and is not necessarily a continuous surface, but is limited to an interval of length 2π as would typically be obtained from an arctangent subroutine:

$$-\pi < ARG\left(\mathbb{I}(\omega_x,\omega_y)\right) \le \pi \qquad \text{[Eq. 3-5]}$$

and $r(\omega_x,\omega_y)$ takes on the appropriate integer values to make $arg\left(\mathbb{I}(\omega_x,\omega_y)\right)$ a continuous surface. Unwrapping the phase is a necessary operation so that the derivatives in [Eq. 3-3] are defined and non-singular in the range $-\pi \le \omega_x \le \pi, -\pi \le \omega_y \le \pi$ of spatial frequencies in the Fourier domain.

There is a way of obtaining the slopes in [Eq. 3-3] without the need of explicitly calculating the phase and unwrapping it, through the Fourier's logarithmic derivative (Oppenheim and Schafer, 1989). Now, let us focus our derivation of the slopes in [Eq. 3-3] on the horizontal axis first. For the derivative of the Fourier's logarithm, the following relationship holds:

$$\frac{\partial}{\partial\omega_x}\left(log\left[\mathbb{I}(\omega_x,\omega_y)\right]\right) = \frac{\frac{\partial}{\partial\omega_x}\left(\mathbb{I}(\omega_x,\omega_y)\right)}{\mathbb{I}(\omega_x,\omega_y)} \qquad \text{[Eq. 3-6]}$$

From [Eq. 3-1], the derivative of the image's Fourier transform can be obtained:

$$\begin{aligned}\frac{\partial}{\partial\omega_x}\left(\mathbb{I}(\omega_x,\omega_y)\right) &= \sum_x\sum_y(-jxI_{xy})e^{-j\omega_x x}e^{-j\omega_y y}\\ &= \mathcal{F}\{-jxI_{xy}\}\big|_{\omega_x,\omega_y}\end{aligned} \qquad \text{[Eq. 3-7]}$$

Substituting in [Eq. 3-6]:

$$\frac{\partial}{\partial\omega_x}\left(log\left[\mathbb{I}(\omega_x,\omega_y)\right]\right) = \frac{\mathcal{F}\{-jxI_{xy}\}\big|_{\omega_x,\omega_y}}{\mathcal{F}\{I_{xy}\}\big|_{\omega_x,\omega_y}} \qquad \text{[Eq. 3-8]}$$

On the other hand, from [Eq. 3-2] we get:

$$\begin{aligned}\frac{\partial}{\partial\omega_x}\left(arg\left(\mathbb{I}(\omega_x,\omega_y)\right)\right) &= \frac{\partial}{\partial\omega_x}\left(Im\{log\left[\mathbb{I}(\omega_x,\omega_y)\right]\}\right)\\ &= Im\left\{\frac{\partial}{\partial\omega_x}\left(log\left[\mathbb{I}(\omega_x,\omega_y)\right]\right)\right\}\end{aligned} \qquad \text{[Eq. 3-9]}$$

with $Im\{\cdot\}$ being the operation of taking the imaginary part. Finally, by combining [Eq. 3-8] and [Eq. 3-9] we get:

$$\frac{\partial}{\partial \omega_x}\left(arg\left(\mathcal{F}\{I_{xy}\}\big|_{\omega_x,\omega_y}\right)\right) = -Re\left\{\frac{\mathcal{F}\{xI_{xy}\}\big|_{\omega_x,\omega_y}}{\mathcal{F}\{I_{xy}\}\big|_{\omega_x,\omega_y}}\right\} \qquad \text{[Eq. 3-10]}$$

with $Re\{\cdot\}$ being the operation of taking the real part. [Eq. 3-10] expresses the horizontal Fourier phase slope of image I_{xy} in the Fourier domain as a function of a quotient of Fourier transforms involving the image itself and the horizontal coordinate x. It is a direct means of obtaining the phase slope bypassing the need of explicitly calculating and unwrapping the phase.

For the vertical Fourier phase slope, in a similar fashion, the following expression is obtained:

$$\frac{\partial}{\partial \omega_y}\left(arg\left(\mathcal{F}\{I_{xy}\}\big|_{\omega_x,\omega_y}\right)\right) = -Re\left\{\frac{\mathcal{F}\{yI_{xy}\}\big|_{\omega_x,\omega_y}}{\mathcal{F}\{I_{xy}\}\big|_{\omega_x,\omega_y}}\right\} \qquad \text{[Eq. 3-11]}$$

Units of the slopes in [Eq. 3-10] and [Eq. 3-11] are the same as for the image's horizontal and vertical coordinates, x and y, respectively.

It is interesting to note that the Fourier phase slope at the zero spatial frequency is the image's CoG. This can be seen by evaluating [Eq. 3-10] and [Eq. 3-11] at $\omega_x = \omega_y = 0$:

$$\begin{aligned}
\frac{\partial}{\partial \omega_x}\left(arg\left(\mathbb{I}(\omega_x,\omega_y)\right)\right)\Big|_{\omega_x=\omega_y=0} &= -Re\left\{\frac{\sum_x\sum_y xI_{xy}}{\sum_x\sum_y I_{xy}}\right\} = -\frac{\sum_x\sum_y xI_{xy}}{\sum_x\sum_y I_{xy}} \\
\frac{\partial}{\partial \omega_y}\left(arg\left(\mathbb{I}(\omega_x,\omega_y)\right)\right)\Big|_{\omega_x=\omega_y=0} &= -Re\left\{\frac{\sum_x\sum_y yI_{xy}}{\sum_x\sum_y I_{xy}}\right\} = -\frac{\sum_x\sum_y yI_{xy}}{\sum_x\sum_y I_{xy}}
\end{aligned} \qquad \text{[Eq. 3-12]}$$

Here, the negative sign indicates that a negative slope in the Fourier's phase is a positive displacement in the image domain, as seen in [Eq. 2-2].

In practice, a discrete version of the bi-dimensional Fourier transform is utilized, the so-called *Bi-dimensional Discrete Fourier Transform (2D_DFT)*, that evaluates the Fourier transform at discrete frequencies $\omega_x = 2\pi k/N$ and $\omega_y = 2\pi l/N$, with $N\times N$ the number of spatial frequencies evaluated, and k and l integers that take values between 0 and $N-1$. Furthermore, the algorithm that implements the 2D_DFT has been optimized to maximize computational speed, and has been named *Bi-dimensional Fast Fourier Transform (2D_FFT)*. In this work, the terms 2D_DFT and 2D_FFT are used as synonyms and interchangeably. Its mathematical definition is:

$$\mathbb{I}(k,l) = 2D\_FFT\{I_{xy}\}\big|_{k,l} = \sum_x\sum_y I_{xy}e^{-j2\pi xk/N}e^{-j2\pi yl/N} \qquad \text{[Eq. 3-13]}$$

The value of $N\times N$ will be at least the size of the original image I_{xy}, but it can be made larger if spot's truncation is suspected due to limited FoV (see example in point A.5.3), in order to increase dynamic range.

Emphasizing the use of the 2D_FFT in equations [Eq. 3-10] and [Eq. 3-11], we obtain the final expressions for the discrete Fourier phase slopes:

$$
\begin{aligned}
S^{x}_{k,l} &= -Re\left\{\frac{2D\_FFT\{xI_{xy}\}\big|_{k,l}}{2D\_FFT\{I_{xy}\}\big|_{k,l}}\right\}\\
S^{y}_{k,l} &= -Re\left\{\frac{2D\_FFT\{yI_{xy}\}\big|_{k,l}}{2D\_FFT\{I_{xy}\}\big|_{k,l}}\right\}
\end{aligned}
\qquad \text{[Eq. 3-14]}
$$

When interest is in image displacement rather than in Fourier's phase slope, then the sign in [Eq. 3-14] should be changed from negative to positive, as explained before. Following the notation of [Eq. 1-13]:

$$
\begin{aligned}
d'^{x}_{k,l} &= Re\left\{\frac{2D\_FFT\{xI_{xy}\}\big|_{k,l}}{2D\_FFT\{I_{xy}\}\big|_{k,l}}\right\}\\
d'^{y}_{k,l} &= Re\left\{\frac{2D\_FFT\{yI_{xy}\}\big|_{k,l}}{2D\_FFT\{I_{xy}\}\big|_{k,l}}\right\}
\end{aligned}
\qquad \text{[Eq. 3-15]}
$$

with $d'^{x}_{k,l}$ and $d'^{y}_{k,l}$ being spot's displacement estimators, measured in pixels, calculated at each spatial frequency determined by the pair of values of k and l.

3.1.1. Further development of the Fourier phase slope formulation

The biggest portion in the computational cost of the WFPS algorithm consists of obtaining the slopes in equation [Eq. 3-14], so the natural question arises whether this formulation is simplifiable. As the real part of a quotient of complex numbers is taken for each pair of k and l values, the computational cost might be reduced if the imaginary part is not computed.

Let us express the 2D_FFT in [Eq. 3-13] as a function of its real and imaginary parts:

$$
\begin{aligned}
&2D\_FFT\{I_{xy}\}\big|_{k,l}\\
&= \sum_{x}\sum_{y} I_{xy}\cos\left[\frac{2\pi}{N}(xk+yl)\right]\\
&-j\sum_{x}\sum_{y} I_{xy}\sin\left[\frac{2\pi}{N}(xk+yl)\right]
\end{aligned}
\qquad \text{[Eq. 3-16]}
$$

Then [Eq. 3-14] can be expressed as:

$$
\begin{aligned}
S^{x}_{k,l} = -\frac{\alpha^{x}_{k,l}c_{k,l}+\beta^{x}_{k,l}d_{k,l}}{\left(\gamma_{k,l}\right)^{2}+\left(\delta_{k,l}\right)^{2}} \quad ,, \quad & S^{y}_{k,l} = -\frac{\alpha^{y}_{k,l}c_{k,l}+\beta^{y}_{k,l}d_{k,l}}{\left(\gamma_{k,l}\right)^{2}+\left(\delta_{k,l}\right)^{2}}\\
\alpha^{x}_{k,l} &= \sum\nolimits_{x}\sum\nolimits_{y} xI_{xy}\cos\left[\frac{2\pi}{N}(xk+yl)\right]\\
\alpha^{y}_{k,l} &= \sum\nolimits_{x}\sum\nolimits_{y} yI_{xy}\cos\left[\frac{2\pi}{N}(xk+yl)\right]\\
\beta^{x}_{k,l} &= \sum\nolimits_{x}\sum\nolimits_{y} xI_{xy}\sin\left[\frac{2\pi}{N}(xk+yl)\right]\\
\beta^{y}_{k,l} &= \sum\nolimits_{x}\sum\nolimits_{y} yI_{xy}\sin\left[\frac{2\pi}{N}(xk+yl)\right]\\
\gamma_{k,l} &= \sum\nolimits_{x}\sum\nolimits_{y} I_{xy}\cos\left[\frac{2\pi}{N}(xk+yl)\right]
\end{aligned}
\qquad \text{[Eq. 3-17]}
$$

$$\delta_{k,l} = \sum_x \sum_y I_{xy} \sin\left[\frac{2\pi}{N}(xk + yl)\right]$$

In section 3.3 the computational cost comparison between [Eq. 3-14] and [Eq. 3-17] will be shown.

3.2. Maximum-a-posteriori (MAP) weighting

Evaluation of equations [Eq. 3-14] or [Eq. 3-17] give a pair of matrices, one for horizontal and the other for vertical Fourier phase slopes of the image I_{xy}. After the change of sign in [Eq. 3-15], an averaging method is needed to reduce each matrix to a single coordinate, thus obtaining the horizontal and the vertical coordinates of the estimated centroid of the image.

For a perfectly symmetric and well sampled spot in a noiseless image and with infinite field of view, the corresponding phase in the Fourier domain would be planar, and so, any two entries, one from each of the pair of phase slope matrices defined in [Eq. 3-14] or [Eq. 3-17], would define a perfect estimator of the phase tilt in the subpupil. This holds true both for Z-tilt and G-tilt at the subpupil, which are equal for a symmetric spot, as explained in the introduction of section 1.4. However, for a real non-symmetric pixelized spot in a noisy image with limited FoV, the same pair of entries would be a noisy estimator of the phase tilt, and so the following expression holds:

$$d_v'^x = H \times d'^x + E^x$$

$$d_v'^y = H \times d'^y + E^y \qquad \text{[Eq. 3-18]}$$

where $d_v'^x$ and $d_v'^y$ are rearrangements of $d_{k,l}'^x$ and $d_{k,l}'^y$ in vector format, respectively; d'^x and d'^y are the spot's displacement in pixels related to $\Delta\phi^x$ and $\Delta\phi^y$, the true horizontal and vertical phase tilts at the subpupil (equation [Eq. 1-13] details this relationship); H is an observation vector with the same size as $d_v'^x$ or $d_v'^y$ with unity entries; and, finally, E^x and E^y are error vectors. Because of symmetry properties in the 2D_FFT, only the first quadrant of $d_{k,l}'^x$ and $d_{k,l}'^y$ are vectorized, and so $d_v'^x$, $d_v'^y$, H, E^x and E^y are, at most, of length $N^2/4$.

Measurement errors in vectors E^x and E^y are larger for higher spatial frequencies, where energy of the spot decays. Also, they are not independent from each other but there is a strong correlation between adjacent spatial frequencies, actually taking the form of ripples added to the planar phase. Asymmetries in the spot of a subpupil image due to high order aberrations or due to truncation when FoV is limited, and even noise due to spurious charge in the detector, can be regarded as similar to spatial reverberation of the spot. Thus, they will originate the errors in vectors E^x and E^y in the form of ripples added to the planar phase, and a strong correlation between adjacent spatial frequencies will be seen (see example in Appendix A, section A.3, showing that an echo in the time domain reflects as an additive ripple in the phase of the Fourier domain).

Appendix A introduces the cepstrum analysis techniques to separate a principal or main signal from its repetition in time or space, as in the case of isolating reverberation from a principal acoustical signal. Examples in section A.5 show that cepstrum techniques can successfully denoise the subpupil images of a SHWFS. The technique consists of low pass prefiltering the image in the cepstrum domain, which is equivalent to smoothing the Fourier spectrum shape, and then calculating the CoG over the filtered image. As we are only interested in finding the centroid of the image, it is not necessary as part of the centroiding method to obtain the resulting image of the cepstrum filtering operation. It just suffices to smooth the phase slope in the Fourier domain by averaging or weighting it around the origin of frequencies and then taking the phase slope at this same frequency origin.

Now, an appropriate estimation method to obtain the necessary phase slope weights is the Maximum-a-Posteriori Bayesian estimator[4]. For the pair of centroid coordinates d'^x and d'^y which are observed through vector H giving rise to observed displacements $d_v'^x$ and $d_v'^y$ with errors E^x and E^y ([Eq. 3-18]), and assuming Gaussian probability distributions for displacements and errors, MAP estimators of the centroid coordinates are given by (Srinath and Rajasekaran, 1979, for example):

$$\hat{d}_{WFPS}'^x = \left(H^T V_{E^x}^{-1} H + V_{d'^x}^{-1}\right)^{-1} \left(H^T V_{E^x}^{-1} d_v'^x + V_{d'^x}^{-1} \mu_{d'^x}\right)$$
$$\hat{d}_{WFPS}'^y = \left(H^T V_{E^y}^{-1} H + V_{d'^y}^{-1}\right)^{-1} \left(H^T V_{E^y}^{-1} d_v'^y + V_{d'^y}^{-1} \mu_{d'^y}\right) \qquad \text{[Eq. 3-19]}$$

V_{E^x} and V_{E^y} are the covariance matrices of errors E^x and E^y. Their role is to give more weight to the cleanest or less noisy displacement measurements in $d_v'^x$ and $d_v'^y$. A second, equally important role, is to take advantage of the covariances among the errors at different spatial frequencies in order to cancel out noise, in an optimized way. For example, if two displacements in $d_v'^x$ or $d_v'^y$ have negative error covariance between them, and the other displacements are uncorrelated or have very small covariance with the rest, the first two will sum in [Eq. 3-19] with high weights and with the same sign in order to cancel noise. Hence, by this manner, ripples in the Fourier phase slope that make up the errors in E^x and E^y are smoothed in an optimized way.

$\mu_{d'^x}$ and $\mu_{d'^y}$ are the *a priori* means of displacements d'^x and d'^y; $V_{d'^x}$ and $V_{d'^y}$ are their *a priori* variances. Their role is to give weight to the *a priori* knowledge of the magnitude to estimate, improving the estimation when the measurement error is above the *a priori* variance. In the present work, and with the aim of fairness when comparing with other centroiding methods, this *a priori* knowledge is not taken into account, and [Eq. 3-19] is simplified to:

$$\hat{d}_{WFPS}'^x = \left(H^T V_{E^x}^{-1} H\right)^{-1} \left(H^T V_{E^x}^{-1} d_v'^x\right)$$
$$\hat{d}_{WFPS}'^y = \left(H^T V_{E^y}^{-1} H\right)^{-1} \left(H^T V_{E^y}^{-1} d_v'^y\right) \qquad \text{[Eq. 3-20]}$$

---

[4] Linear Minimum Mean Square Error (LMMSE), another Bayesian estimator, would give the same result under the same assumptions of Gaussian distributions and linear relationship between observed and estimated magnitudes ([Eq. 3-18]).

which can be expressed as:

$$\hat{d}'^{x}_{WFPS} = W_v^{x} \times d'^{x}_{v}$$
$$\hat{d}'^{y}_{WFPS} = W_v^{y} \times d'^{y}_{v} \qquad \text{[Eq. 3-21]}$$

with W_v^{x} and W_v^{y} being row vectors consisting of the MAP weights for the horizontal and vertical displacement estimation, respectively, that we were looking for:

$$W_v^{x} = \left(H^T V_{E^x}^{-1} H\right)^{-1} H^T V_{E^x}^{-1}$$
$$W_v^{y} = \left(H^T V_{E^y}^{-1} H\right)^{-1} H^T V_{E^y}^{-1} \qquad \text{[Eq. 3-22]}$$

Finally, vectors can be rearranged into matrices in an inverse manner as was done in [Eq. 3-18], and [Eq. 3-21] can be expressed as:

$$\hat{d}'^{x}_{WFPS} = \sum\nolimits_{x} W^{x}_{k,l} \times d'^{x}_{k,l}$$
$$\hat{d}'^{y}_{WFPS} = \sum\nolimits_{y} W^{y}_{k,l} \times d'^{y}_{k,l} \qquad \text{[Eq. 3-23]}$$

with multiplication in [Eq. 3-23] being element-wise. [Eq. 3-23] expresses the Weighted Fourier Phase Slope estimation of the spot displacement in the horizontal and vertical axes, $\hat{d}'^{x}_{WFPS}$ and $\hat{d}'^{y}_{WFPS}$, respectively, as weighted combinations of the displacements $d'^{x}_{k,l}$ and $d'^{y}_{k,l}$ or, equivalently, of the phase slopes $S^{x}_{k,l}$ and $S^{y}_{k,l}$ ([Eq. 3-14]), calculated at the different spatial frequencies in the Fourier domain determined by indexes k and l, with applied MAP weights $W^{x}_{k.l}$ and $W^{y}_{k,l}$.

It is convenient to clarify here that error vectors E^x and E^y in [Eq. 3-18] and, therefore, their covariance matrices V_{E^x} and V_{E^y} in [Eq. 3-22], and the derived weights $W^{x}_{k.l}$ and $W^{y}_{k,l}$ in [Eq. 3-23], can only be obtained in simulations where the applied phase tilt in the subpupil is known.

3.3. Comparison of computational cost of WFPS with other algorithms

One of the figures of merit that allows a comparison of the WFPS algorithm with other known algorithms is its computational cost. This section aims at giving such a comparison. Here, the computational cost is measured in terms of the number of arithmetic multiplications and additions required for processing a SHWFS image. Other operations, such as indexing, are not being counted for, as they are normally performed without speed penalization in a microprocessor.

First, an estimation of the computational cost for the 2D_FFT algorithm will be given; second, the WFPS algorithm will be evaluated; and, finally, it will be compared with the TCoG, the WCoG and the CC algorithms.

3.3.1. Computational cost of the unidimensional and bi-dimensional FFT’s

The $N \times N$-point 2D_FFT algorithm as defined in [Eq. 3-13] is computed by applying a unidimensional N-point FFT to each row of image I_{xy}, and then applying the N-point unidimensional FFT to each column of the result; or vice versa: first columns, then rows. The unidimensional N-point FFT would be expressed as:

$$\mathbb{I}(k) = FFT\{I(x)\}|_k = \sum_x I(x) e^{-j2\pi xk/N} \qquad \text{[Eq. 3-24]}$$

with $I(x)$ any of the rows or columns of the image I_{xy}, and index k ranging from 0 to $N-1$.

3.3.1.1. Computational cost of the unidimensional FFT

The computational cost of the N-point unidimensional FFT is an amply dealt with topic by Oppenheim and Schafer, 1989. Here, we are interested in efficiently computing the FFT in two different cases: when all frequencies are required (all values of index k ranging from 0 to $N-1$ in [Eq. 3-24]); and when only a subset of frequencies are required. Also, we will distinguish between $I(x)$ being a real or complex number sequence in our derivations. All the presented results are taken or derived from the mentioned reference.

When a limited number M of frequencies are required out of the total of N, with M smaller than $log_2 N$, then the direct computation of the FFT in [Eq. 3-24], in which each frequency k is computed independently, is the most computationally efficient method. The number of operations in this case, when $I(x)$ is real, is MN real by complex multiplications and $M(N-1)$ complex additions or, equivalently, $2MN$ real multiplications and $2M(N-1)$ real additions. When $I(x)$ is complex, then the required number of operations is MN complex multiplications and $M(N-1)$ complex additions or, equivalently, $4MN$ real multiplications and $M(4N-2)$ real additions. The correspondence between complex and real operations is as follows: 2 real multiplications for a real by complex multiplication; 4 real multiplications and 2 real additions for a complex multiplication; and 2 real additions for a complex addition.

When all N frequencies of the FFT are required, the most efficient way is to decompose its computation into stages where the smallest possible FFT’s are calculated; the output of a stage is the input to the next stage, after some reordering of the sequence’s elements, so here there is almost no difference in computational cost whether the original sequence $I(x)$ is real or complex.

The applied algorithms for N being a power of 2 and the whole FFT computed, are called *decimation-in-time* and *decimation-in-frequency,* and both lead to the same computational cost. The required number of operations in this case is $(N/2)log_2 N$ complex multiplications and $Nlog_2 N$ complex additions or, equivalently, $2Nlog_2 N$ real multiplications and $3Nlog_2 N$ real additions.

For N other than a power of 2, but not a prime number, there is still great room for computational cost improvement with respect to the direct computation. Algorithms such as the *Cooley-Tukey FFT* and the *Prime Factors FFT* take advantage of N being a composite number of the form $N = N_1 N_2 \cdots N_v$ to break down the computation of the FFT into v stages of N_i-point FFT's. If we call $\mu(N_i)$ and $\sigma(N_i)$ to the number of complex multiplications and complex additions required for a N_i-point FFT, respectively, then for the *Cooley-Tukey* algorithm the following expressions hold:

$$\mu_{CT}(N) = N\left(\sum_{i=1}^{v} \frac{\mu(N_i)}{N_i} + (v-1)\right) \qquad \text{[Eq. 3-25]}$$

with $\mu_{CT}(N)$ the required number of complex multiplications for the *Cooley-Tukey* N-point FFT, and

$$\sigma(N) = N\left(\sum_{i=1}^{v} \frac{\sigma(N_i)}{N_i}\right) \qquad \text{[Eq. 3-26]}$$

For the *Primer Factors* algorithm, the number of additions is given by [Eq. 3-26] as well. The number of multiplications $\mu_{PF}(N)$ is slightly improved, at the expense of greater complexity of the indexing and programming of the algorithm, and is given by:

$$\mu_{PF}(N) = N\left(\sum_{i=1}^{v} \frac{\mu(N_i)}{N_i}\right) \qquad \text{[Eq. 3-27]}$$

3.3.1.2. Computational cost of the 2D-FFT

So far, the computational cost of the unidimensional N-point FFT has been presented. As for the N- by N-point 2D-FFT of a real image I_{xy}, let us also consider two different cases: when only a subset of N_f frequencies are required, and when the whole $N\times N$ 2D-FFT is computed.

$$\mathbb{I} = \begin{pmatrix} {\color{green}\mathbb{I}_{0,0}} & {\color{green}\mathbb{I}_{0,1}} & {\color{green}\cdots} & {\color{green}\mathbb{I}_{0,M-1}} & \cdots & \mathbb{I}_{0,N-2} & \mathbb{I}_{0,N-1} \\ {\color{green}\mathbb{I}_{1,0}} & {\color{green}\mathbb{I}_{1,1}} & & & & & \\ & {\color{green}\vdots} & & & & & \\ {\color{green}\mathbb{I}_{M-1,0}} & & & & & & \\ & \vdots & & & & & \\ \mathbb{I}_{N-2,0} & \mathbb{I}_{N-2,1} & & \cdots & & \mathbb{I}_{N-2,N-2} & \mathbb{I}_{N-2,N-1} \\ \mathbb{I}_{N-1,0} & \mathbb{I}_{N-1,1} & & \cdots & & \mathbb{I}_{N-1,N-2} & \mathbb{I}_{N-1,N-1} \end{pmatrix} \qquad \text{[Eq. 3-28]}$$

[Eq. 3-28] shows the matrix $\mathbb{I}(k,l)$ as the result of applying the $N\times N$ 2D-FFT to image I_{xy} according to [Eq. 3-13]. A green character font points out the subset of the result that is actually needed, summing up N_f frequencies. M is the number of rows or columns (whichever is less) spanned by the N_f frequencies. In the example in [Eq. 3-28], the 2D-FFT can be calculated in the following steps: first, N-point unidimensional FFT's are applied to each of the N rows of the real valued image I_{xy}, and only the required M frequencies are calculated (via direct method), giving as a result a matrix of N rows by M columns; second, N-point unidimensional FFT's are applied to each of the resulting complex valued M columns, and only the frequencies pointed out by green font are calculated (via direct method), which in total sum up N_f frequencies.

This process sums up a total of MN^2 complex by real multiplications and $MN(N-1)$ complex additions for the N horizontal N-point FFT's; and $N_f N$ complex multiplications and $N_f(N-1)$ complex additions for the M vertical N-point FFT's. Or, equivalently, $N(2MN+4N_f)$ real multiplications and $N\left(2MN+4N_f\right)-(2MN+2N_f)$ real additions.

When the complete $N \times N$ 2D-FFT is required, then the unidimensional FFT's are calculated wholly through the most appropriate and efficient method, which depends upon the value of N, as it has been discussed above in point 3.3.1.1. The number of required operations is then $2N$ times the required number of operations for the N-point unidimensional FFT.

3.3.2. Computational cost of the WFPS algorithm

It will be proven in the next chapter that only a small number of spatial frequencies are involved with significant weight in the computation of the WFPS centroiding method for habitual system's geometries and noises. These spatial frequencies are located at the lowermost corner in the first quadrant of the Fourier domain, just as the green coloured entries in the matrix of [Eq. 3-28]. In the derivation of the computational cost of the WFPS algorithm, it will be assumed that the 2D-FFT's involved are evaluated only at a small set of spatial frequencies located in such manner.

On the other hand, two possible ways to compute the phase slopes in WFPS have been presented in point 3.1, and here the computational cost for both of them will be derived. We will start with the formulation for the phase slope in point 3.1.1. Table 3-1 summarizes the computational cost of the WFPS algorithm for an *N* by *N* image I_{xy} for which N_f Fourier phase slopes are calculated following the expression [Eq. 3-17]. Only those operations directly involving the live image I_{xy} are taken into account. The rest of operations can be computed offline and their results stored, such as the product of coordinates and sines or cosines in [Eq. 3-17]. The total number of operations required is clearly dominated by the calculation of the phase slopes: for each spatial frequency, $\sim 6N^2$ real multiplications are required, and the same approximate number of real additions.

Table 3-2, on the other hand, summarizes the computational cost of the WFPS algorithm for an *N* by *N* image I_{xy} when the N_f Fourier phase slopes are calculated by direct evaluation of the 2D-FFT's in expression [Eq. 3-14]. The number of operations reflected for the 2D-FFT's has been derived in point 3.3.1.2, and *M* has the same meaning as in [Eq. 3-28]. Here, the total values are dominated by the computation of the 2D-FFT's, and depend upon the number N_f of spatial frequencies evaluated and their distribution in the frequency domain.

	#Real multiplications	**#Real additions**	**#Real divisions**	
$\boldsymbol{\alpha^x}$	N^2	N^2-1		
$\boldsymbol{\alpha^y}$	N^2	N^2-1		
$\boldsymbol{\beta^x}$	N^2	N^2-1		
$\boldsymbol{\beta^y}$	N^2	N^2-1		
$\boldsymbol{\gamma}$	N^2	N^2-1		
$\boldsymbol{\delta}$	N^2	N^2-1		
$\boldsymbol{d'^x = \frac{\alpha^x\gamma+\beta^x\delta}{\gamma^2+\delta^2}}$	4	2	1	
$\boldsymbol{d'^y = \frac{\alpha^y\gamma+\beta^y\delta}{\gamma^2+\delta^2}}$	2	1	1	
Total per frequency	$6N^2+6$	$6N^2-3$	2	
# frequencies				$\times N_f$
$\boldsymbol{\Sigma}\ (\boldsymbol{d'^x \times W^x})$	N_f	N_f-1		
$\boldsymbol{\Sigma}\ (\boldsymbol{d'^y \times W^y})$	N_f	N_f-1		
TOTAL (approx.)	$\sim 6N_fN^2$	$\sim 6N_fN^2$	$2N_f$	

Table 3-1. Computational cost of the WFPS algorithm for an N by N image I_{xy} following the computation of the Fourier phase slopes according to equation [Eq. 3-17] and selecting N_f spatial frequencies. Total values are approximated assuming $N^2 \gg 1$.

	#Real multiplications	**#Real additions**	**#Real divisions**	
$\boldsymbol{2D\_FFT\{xI_{xy}\}}$	$N(2MN+4N_f)$	$N(2MN+4N_f)-(2MN+2N_f)$		
$\boldsymbol{2D\_FFT\{yI_{xy}\}}$	$N(2MN+4N_f)$	$N(2MN+4N_f)-(2MN+2N_f)$		
$\boldsymbol{2D\_FFT\{I_{xy}\}}$	$N(2MN+4N_f)$	$N(2MN+4N_f)-(2MN+2N_f)$		
Total 2D-FFT's (direct method)	$3N(2MN+4N_f)$	$3[N(2MN+4N_f)-(2MN+2N_f)]$		
$\boldsymbol{d'^x = \frac{\alpha^x\gamma+\beta^x\delta}{\gamma^2+\delta^2}}$	4	2	1	
$\boldsymbol{d'^y = \frac{\alpha^y\gamma+\beta^y\delta}{\gamma^2+\delta^2}}$	2	1	1	
Total per frequency	6	3	2	
# frequencies				$\times N_f$
$\boldsymbol{\Sigma}\ (\boldsymbol{d'^x \times W^x})$	N_f	N_f-1		
$\boldsymbol{\Sigma}\ (\boldsymbol{d'^y \times W^y})$	N_f	N_f-1		
TOTAL (approx.)	$\sim 6MN^2+12N_fN$	$\sim 6MN(N-1)+12N_fN$	$2N_f$	

Table 3-2. Computational cost of the WFPS algorithm for an N by N image I_{xy} following the computation of the Fourier phase slopes according to equation [Eq. 3-14] by direct method computation of the 2D-FFT's focusing on N_f spatial frequencies exclusively. M has the same meaning as in [Eq. 3-28]. Total values are approximated assuming $N^2 \gg 1$.

Let us take as an example, for the purpose of comparing both methods of computing the phase slopes, a case where $N = 12$, $N_f = 6$ and $M = 3$. Following the computation in [Eq. 3-17] and according to Table 3-1, the required number of operations would be ~ 5184 real multiplications per image and the same approximate number of real sums. Whereas following the 2D-FFT's computation in [Eq. 3-14] and according to Table 3-2, the required number of operations would be ~ 3456 real multiplications and ~ 3240 real sums per image, slightly less than in the previous case, but in the same order of magnitude.

3.3.3. Computational cost of the TCoG and WCoG algorithms

Table 3-3 and Table 3-4 summarize the computational cost of the TCoG and the WCoG algorithms, respectively, for an *N* by *N* image I_{xy}, following the computation described in equations [Eq. 1-26] to [Eq. 1-28]. Threshold *T* is predetermined and an input to the TCoG algorithm. Similarly, weights *W* are predetermined, fixed, and an input to the WCoG algorithm. The total number of operations is an order of magnitude less than in the WFPS algorithm case, approximately.

	#Real multiplications	***#Real additions***	***#Real divisions***	***#Real comparisons***
$\boldsymbol{I_{xy} - T}$		N^2		N^2
$\boldsymbol{\Sigma x(I_{xy} - T)}$	N^2	$N^2 - 1$		
$\boldsymbol{\Sigma y(I_{xy} - T)}$	N^2	$N^2 - 1$		
$\boldsymbol{\Sigma(I_{xy} - T)}$		$N^2 - 1$		
$\boldsymbol{\Sigma x(I_{xy} - T) / \Sigma(I_{xy} - T)}$			1	
$\boldsymbol{\Sigma y(I_{xy} - T) / \Sigma(I_{xy} - T)}$			1	
TOTAL	$2N^2$	$4N^2 - 3$	2	N^2

Table 3-3. Computational cost of the TCoG algorithm for an N by N image I_{xy} following the computation described in [Eq. 1-27]. Threshold T is an input to the algorithm.

	#Real multiplications	***#Real additions***	***#Real divisions***
$\boldsymbol{W_{xy} I_{xy}}$	N^2		
$\boldsymbol{\Sigma x W_{xy} I_{xy}}$	N^2	$N^2 - 1$	
$\boldsymbol{\Sigma y W_{xy} I_{xy}}$	N^2	$N^2 - 1$	
$\boldsymbol{\Sigma W_{xy} I_{xy}}$		$N^2 - 1$	
$\boldsymbol{\Sigma x W_{xy} I_{xy} / \Sigma W_{xy} I_{xy}}$			1
$\boldsymbol{\Sigma y W_{xy} I_{xy} / \Sigma W_{xy} I_{xy}}$			1
TOTAL	$3N^2$	$3N^2 - 3$	2

Table 3-4. Computational cost of the WCoG algorithm for an N by N image I_{xy} following the computation described in [Eq. 1-26] and [Eq. 1-28]. Weights W_{xy} are predetermined and an input to the algorithm.

3.3.4. Computational cost of the Cross Correlation algorithm

For the evaluation of the computational cost of the CC algorithm, cross-correlation in the Fourier domain is assumed, and subsequent application of the TCoG algorithm to the correlation figure in order to obtain the final centroid coordinates. Thus, the CC algorithm, applied to an *N* by *N* pixels size live image I_{xy} and a N_{ref} by N_{ref} pixels size reference image I_{ref}, is composed of the following operations:

1. Zero padding the *N* by *N* pixels size live image I_{xy} to complete a N_{fft} by N_{fft} pixels size image, being $N_{fft} \geq N + N_{ref} - 1$. This is necessary to avoid aliasing in the image domain, since the signal in the Fourier domain is discretized.
2. Calculating the N_{fft} by N_{fft} 2D-FFT of the zero-padded live image.
3. Multiplying in the Fourier domain live and reference images: $\mathbb{I} \times \mathbb{I}_{ref}$. The reference image in the Fourier domain has been precalculated with the adequate resolution. Matrices are multiplied element-wise.
4. Assuming no interpolation or increase in the original image resolution is required, a N_{fft} by N_{fft} inverse 2D-FFT gives the correlation figure.
5. A TCoG algorithm is applied to the correlation figure and the final centroid obtained.

	#Real multiplications	***#Real additions***	***#Real divisions***	***#Real comparisons***
$\boldsymbol{2D\_FFT\{I_{xy}\}}$	$8N_{fft}\mu(N_{fft})$	$4N_{fft}\left(\mu(N_{fft})+\sigma(N_{fft})\right)$		
$\mathbb{I}\times\mathbb{I}_{\boldsymbol{ref}}$	$4N_{fft}^2$	$2N_{fft}^2$		
$\boldsymbol{i\_2D\_FFT\{\mathbb{I}\times\mathbb{I}_{ref}\}}$	$8N_{fft}\mu(N_{fft})$	$4N_{fft}\left(\mu(N_{fft})+\sigma(N_{fft})\right)$		
TCoG	$2N_{fft}^2$	$4N_{fft}^2-3$	2	N_{fft}^2
TOTAL (approx.)	$N_{fft}(16\mu(N_{fft})+6N_{fft})$	$\sim N_{fft}(8\mu(N_{fft})+8\sigma(N_{fft})+6N_{fft})$	2	N_{fft}^2

Table 3-5. Computational cost of the CC algorithm for an N by N image I_{xy} and an N_{ref} by N_{ref} image I_{ref}. CC computation is done in the Fourier domain, with an N_{fft} by N_{fft} bi-dimensional FFT, being $N_{fft} \geq N + N_{ref} - 1$. TCoG is applied to the correlation figure, without previous interpolation.

Table 3-5 summarizes the computational cost of the above described CC algorithm. Notation in equations [Eq. 3-25] to [Eq. 3-27] has been followed: $\mu(N_{fft})$ is the number of complex multiplications for an N_{fft}-point unidimensional FFT, and $\sigma(N_{fft})$ is the number of complex additions. Whole $N_{fft}\times N_{fft}$ bi-dimensional FFT's are calculated, and so, the number of operations for a 2D-FFT is $2N_{fft}$ times that required for a unidimensional FFT. Inverse 2D-FFT requires the same number of operations as the direct 2D-FFT.

The total number of multiplications and additions for the CC algorithm depends upon the chosen size of the 2D-FFT, which is in any case bigger than the live image's size. Also, the efficiency of the unidimensional FFT's calculation plays an important role through the values of $\mu(N_{fft})$ and $\sigma(N_{fft})$, and this depends upon the chosen value of N_{fft}. Comparison with WFPS algorithm will be made through examples in the following point.

3.3.5. Comparison between algorithms through examples and conclusions

As an example of SHWFS configuration, for the purpose of comparing the computational cost of the centroiding algorithms seen in the previous points, we will take the case of an ELT with 80 by 80 subpupils and 12 by 12 pixels of the detector assigned to each subpupil. We will assign for the computation of all the centroids of a SHWFS image an allowed latency of 100 µsecs, and then work out the computational power required for the computation of each centroiding method for the whole pupil or SHWFS image.

For the WFPS algorithm, we again assume that the number of spatial frequencies involved in the computation of Fourier phase slopes is $N_f = 6$, and the columns and rows spanned by them is $M = 3$. We also assume that the 2D-FFT's are of size 12 by 12, same as the subpupil image's size. Following [Eq. 3-17] for the computation of the phase slopes and according to Table 3-1, the required number of operations would be ~ 5184 real multiplications per image and the same approximate number of real sums, per subpupil and per frame. Regarding both multiplications and additions as floating point operations, this makes a computational requirement of ~ 665 Gflops. Whereas partially calculating the 2D-FFT's in [Eq. 3-14] and according to Table 3-2, the required number of operations would be ~ 3456 real multiplications and ~ 3240 real sums per image and per subpupil, which gives a computational requirement of ~ 430 Gflops.

For the TCoG algorithm, the number of required operations according to Table 3-3 is ~ 1008 floating point operations per image per subpupil, including real comparisons. Whereas for the WCoG algorithm, the number of required operations according to Table 3-4 is ~ 864 floating point operations per image per subpupil. This implies a total computational requirement of ~ 65 Gflops for the TCoG and ~ 55 Gflops for the WCoG.

As for the CC algorithm, there are several options to be considered. First, the size of the reference image is an option. We will consider a favourable case with N_{ref} = 4 pixels, and a less favourable case with N_{ref} = 6 pixels. Second, the size of the unidimensional FFT (N_{fft}) affects computational efficiency.

In the case of N_{ref} = 4 pixels, the most efficient value for N_{fft} is 16. The efficient schemes for a power of 2 size unidimensional FFT can be applied, resulting in µ(16)=32 complex multiplications and σ(16)=64 complex additions. Following the derivation summarized in Table 3-5, this makes a requirement of ~ 9728 real multiplications, ~ 13824 real additions and 256 real comparisons per subpupil per frame, for a total of ~ 1524 Gflops.

With N_{ref} = 6 pixels the situation is less favourable. By choosing N_{fft}=18, we have µ(18)= σ(16)=144 complex multiplications or additions, and a total requirement of ~ 5578 Gflops. Choosing N_{fft}=32 makes the unidimensional FFT's more efficient, with µ(32)=80 complex multiplications and σ(32)=160 complex additions, but the 2D-FFT size becomes much larger and the total computational requirement is ~ 7406 Gflops.

Table 3-6 summarizes the results just obtained in this example.

In the first example described above, 80 x 80 subpupils in an ELT implies a subpupil diameter or side size of around half a metre, for a pupil size of $\sim$40 metres. On the other hand, Fried parameters in the visible wavelength for a good observing site are in the order of 15-20 cm. Thus, subpupil size to Fried parameter ratios in this example are in the order of 3. In open loop observations, a bigger than 12 x 12 pixels FoV is required to cope with the spots' tilt movements. So here we illustrate a second example where, in an ELT with 80 x 80 subpupils, this time 16 x 16 pixels at the detector are assigned to each subpupil. Table 3-7 summarizes the results obtained in this second example.

COMPUTATIONAL COST COMPARISON

80 x 80 subpupils, 12 x 12 pixels per subpupil, 100 µsecs. latency

WCoG	***TCoG***
~55 Gflops	~65 Gflops
WFPS	***CC***
N_f= 6 frequencies, spanning M = 3 columns ***Phase slopes as f(α,β,γ,δ) [Eq. 3-17]*** ~665 Gflops ***Partial computation of 2D-FFT's (N_{fft}=12)*** ~430 Gflops	***N_{ref}= 4, N_{fft}= 16*** ~1524 Gflops ***N_{ref}= 6, N_{fft}= 18*** ~5578 Gflops ***N_{ref}= 6, N_{fft}= 32*** ~7406 Gflops

Table 3-6. Example of computational cost comparison between WCoG, TCoG, WFPS and CC algorithms, for an ELT with 80 x 80 subpupils, 12 x 12 pixels per subpupil at the detector and 100 µsecs budgeted latency for centroids computation.

COMPUTATIONAL COST COMPARISON

80 x 80 subpupils, 16 x 16 pixels per subpupil, 100 µsecs. latency

WCoG	***TCoG***
~98 Gflops	~115 Gflops
WFPS	***CC***
N_f= 6 frequencies, spanning M = 3 columns ***Phase slopes as f(α,β,γ,δ) [Eq. 3-17]*** ~1180 Gflops ***Partial computation of 2D-FFT's (N_{fft}=16)*** ~719 Gflops	***N_{ref}= 4, N_{fft}= 20*** ~7706 Gflops ***N_{ref}= 6, N_{fft}= 24*** ~11096 Gflops ***N_{ref}= 6, N_{fft}= 32*** ~7406 Gflops

Table 3-7. Example of computational cost comparison between WCoG, TCoG, WFPS and CC algorithms, for an ELT with 80 x 80 subpupils, 16 x 16 pixels per subpupil at the detector and 100 µsecs budgeted latency for centroids computation.

We are considering in Table 3-7 the generic formulation of the *Prime Factors FFT* algorithm ([Eq. 3-26] and [Eq. 3-27]), and so $\mu(20) = \sigma(20)=180$ and $\mu(24) = \sigma(24)=216$. In this second example, the most efficient value for the CC algorithm is $N_{fft} = 32$.

Both examples are showing us an increase in computational cost of one order of magnitude when shifting from CoG derived algorithms to WFPS algorithm, and again an increase of another order of magnitude when comparing WFPS with the CC algorithm, except when the case is very favourable to the CC algorithm, such as when the sum of N and N_{ref} is a power of 2. Even in this latter case, the CC algorithm requires more than 3 times the computational power required for the WFPS algorithm.

Finally, let us compare the required computational power obtained in these examples for the evaluated centroiding algorithms with commercial elements of computation. Let us take, as an example, systems based on the Tesla G80 GPU from Nvidia[5]. The CoG based centroiding algorithms can fit into a C870 PCI Express computing module, comprising one G80 based GPU, and hence 128 streaming processor cores at 1.35 GHz, for a total processing power of 345.6 GFlops, computed in a conservative manner. The WFPS algorithm would require one S870 computing server which comes in a 1U form factor for a standard 19-inch rack and comprises four G80 based GPU's, making up a total processing power of 1382.4 Gflops. Cross correlation, for the 16 x 16 FoV case, would require at least half a dozen of S870 servers.

---

[5] The processing power specifications of these elements have been taken from the English version of Wikipedia, at the "Nvidia Tesla" entry, as of May, 2017.

Chapter 4. Numerical simulations at subpupil level

In this chapter, the behaviour of the Weighted Fourier Phase Slope algorithm and its comparison with other known centroiding methods will be evaluated and understood through numerical simulations at a subpupil level. In this kind of simulation, a single Shack-Hartmann subaperture is illuminated with a wavefront fulfilling Kolmogorov phase statistiscs; an image is thus formed at the detector situated at the microlense's focal plane, and the appropriate detector's gain and noise model is applied to obtain a close to real subpupil image. The incident phase tilt is then estimated by applying different centroiding methods to this image, and the result is compared to the known applied tilt, thus obtaining an estimation error for each centroiding method that allows for their behaviour comparison. Light level flux, detector noises, FoV, atmospheric turbulence strength and any other parameter defining the system can be easily changed in simulation, and hence sensitivity and linearity of the centroiding methods with different FoV's, and their robustness against such effects as higher orders of turbulence phase, can be easily evaluated. Moreover, optimization of every centroiding method's parameters, such as MAP weights for the WFPS as expressed in [Eq. 3-22], is achieved through this type of simulation.

4.1. The simulation method

4.1.1. Simulation of Kolmogorov phase frames

The approach to simulate independent Kolmogorov phase frames has been taken from Roddier, 1990. Roddier's approach consists in expanding the phase into a functions base for which the coefficients covariance matrix is known and diagonal, that is, the contribution of each function to the total phase energy is known and uncorrelated to the other functions' contributions. Such a base is called a Karhunen-Loève base of functions.

A Kolmogorov phase ϕ is characterized by its spatial structure function as expressed in [Eq. 1-5]:

$$D_{\phi}(r) = 6.88\left(\frac{r}{r_0}\right)^{5/3} \qquad \text{[Eq. 4-1]}$$

with r being the distance between the two evaluated points in space and r_0 being the *Fried parameter* which characterizes the turbulence strength. Such a structure function gives place to a Wiener spatial power spectrum expressed as:

$$W_{\phi}(f) = \frac{0.023}{{r_0}^{5/3} f^{11/3}} \qquad \text{[Eq. 4-2]}$$

where f is the wave spatial frequency. For a Kolmogorov phase expressed into a Zernike functions expansion, such as in [Eq. 1-21]:

$$\phi(r,\theta) = \phi(R\rho,\theta) = \sum_j c_j Z_j(\rho,\theta) \qquad \text{[Eq. 4-3]}$$

with r and θ the polar radial and azimuthal coordinates, respectively, and ρ the radial coordinate normalized by the aperture radius R, knowledge of the Wiener power spectrum function in [Eq. 4-2] allows to obtain the covariance matrix of the Zernike coefficients c_j (Noll, 1976; Roddier, 1990). The result thus obtained is expressed as:

$$\langle c_j^* c_{j'} \rangle = \frac{K_{zz'}\delta_z \Gamma\left[\left(n + n' - \frac{5}{3}\right)/2\right] (D/r_0)^{5/3}}{\Gamma\left[\left(n - n' + \frac{17}{3}\right)/2\right] \Gamma\left[\left(n' - n + \frac{17}{3}\right)/2\right] \Gamma\left[\left(n + n' + \frac{23}{3}\right)/2\right]} \qquad \text{[Eq. 4-4]}$$

δ_z is a logical Kronecker symbol the value of which is:

$$\delta_z = (m = m') \wedge \left(\overline{parity(j,j')} \vee (m = 0)\right) \qquad \text{[Eq. 4-5]}$$

and n, m, n' and m' are the radial and azimuthal orders of Z_j and $Z_{j'}$. In other words, covariance can only be non-zero for Zernike functions with the same azimuthal order. Furthermore, for Zernike functions with non-zero azimuthal order, the parity of their indexes must be the same, i.e., the covariance between an even and an odd function is zero.

As for the $K_{zz'}$ factor, its value is:

$$K_{zz'} = 2.2698\,(-1)^{(n+n'-2m)/2}\sqrt{(n+1)(n'+1)} \qquad \text{[Eq. 4-6]}$$

Finally, D/r_0 is the ratio of the pupil's diameter to the Fried parameter.

This covariance of Zernike's coefficients for Kolmogorov turbulence as expressed in [Eq. 4-4] was found already implemented in an IDL subroutine for the CAOS simulation tool[6], adapted

---

[6] CAOS stands for Code for Adaptive Optics Systems, and is a programming environment for AO modelling and post-AO imaging, based on IDL language. IDL stands for Interactive Data Language, and is a programming language used for data analysis.

to work in the MATLAB™ environment and used to generate the phase frames for all the simulations described in this chapter.

0.4557	0	0	0	0	0	-0.0144	0	0	0	0	0	0	0
0	0.4557	0	0	0	-0.0144	0	0	0	0	0	0	0	0
0	0	0.0236	0	0	0	0	0	0	-0.0039	0	0	0	0
0	0	0	0.0236	0	0	0	0	0	0	0	-0.0039	0	0
0	0	0	0	0.0236	0	0	0	0	0	-0.0039	0	0	0
0	-0.0144	0	0	0	0.0063	0	0	0	0	0	0	0	0
-0.0144	0	0	0	0	0	0.0063	0	0	0	0	0	0	0
0	0	0	0	0	0	0	0.0063	0	0	0	0	0	0
0	0	0	0	0	0	0	0	0.0063	0	0	0	0	0
0	0	-0.0039	0	0	0	0	0	0	0.0025	0	00	0	0
0	0	0	0	-0.0039	0	0	0	0	0	0.0025	00	0	0
0	0	0	-0.0039	0	0	0	0	0	0	0	0.0025	0	0
0	0	0	0	0	0	0	0	0	0	0	0	0.0025	0
0	0	0	0	0	0	0	0	0	0	0	0	0	0.0025

Table 4-1. Covariance matrix for the first 14 zero mean Zernike functions (Z_2 to Z_{15}) of Kolmogorov turbulence phase. $(D/r_0)^{5/3}$ units.

Table 4-1 shows the covariance matrix V_Z for the first 15 Zernike functions except Z_1 or piston, for a Kolmogorov turbulence phase, in $(D/r_0)^{5/3}$ units. Off diagonal non-zero elements correspond to the cross covariance of terms with same azimuthal order and same parity, according to [Eq. 4-5]. Thus, Kolmogorov phase cannot be simulated by generating random independent Zernike coefficients, because these non-zero cross covariances should be taken into account.

The Zernike expansion of the phase as in [Eq. 4-3] can be vectorised and expressed as in [Eq. 1-22]:

$$\phi = Zc \qquad \text{[Eq. 4-7]}$$

with ϕ a column vector of phases at the coordinates of interest, Z a matrix with as many columns as Zernike functions and as many rows as coordinates in which the functions are evaluated, and c a column vector of Zernike coefficients. The covariance matrix V_Z can then be expressed as:

$$V_Z = \langle cc^T \rangle \qquad \text{[Eq. 4-8]}$$

c is regarded as real-valued, and c^T is the transpose of c. Angular brackets denote temporal averaging. Being V_Z a Hermitian matrix, a unitary matrix U and a diagonal matrix V_{KL} can be found such that:

$$V_{KL} = U\, V_Z U^T \qquad \text{[Eq. 4-9]}$$

by a singular value decomposition (SVD) of V_Z, for example. If we employ the unitary matrix U for a function set transformation, the new coefficient vector would be:

$$d = U\,\mathrm{c} \qquad \text{[Eq. 4-10]}$$

for which the covariance matrix is:

$$\langle dd^T \rangle = \langle Ucc^T U^T \rangle = U\langle cc^T \rangle U^T = \ U\,V_Z U^T \ = V_{KL} \qquad \text{[Eq. 4-11]}$$

which is diagonal, and the phase in [Eq. 4-7] can be expressed as

$$\phi = (Z\,U^T)\,d = K\_L\,d \qquad \text{[Eq. 4-12]}$$

This means that, by developing the Kolmogorov phase ϕ into a linear combination of a set of functions defined by $K\_L = Z\,U^T$, the resultant coefficients d have a diagonal covariance matrix V_{KL} and, hence, are statistically independent. Such a function base is called a Karhunen-Loève base. The method for simulating Kolmogorov phase frames has therefore consisted of generating random d coefficients with Gaussian distribution, zero mean and variance determined by V_{KL}, and applying them to a phase expansion into a Karhunen-Loève base of functions according to [Eq. 4-12].

4.1.1.1. Verification of the phase simulation method

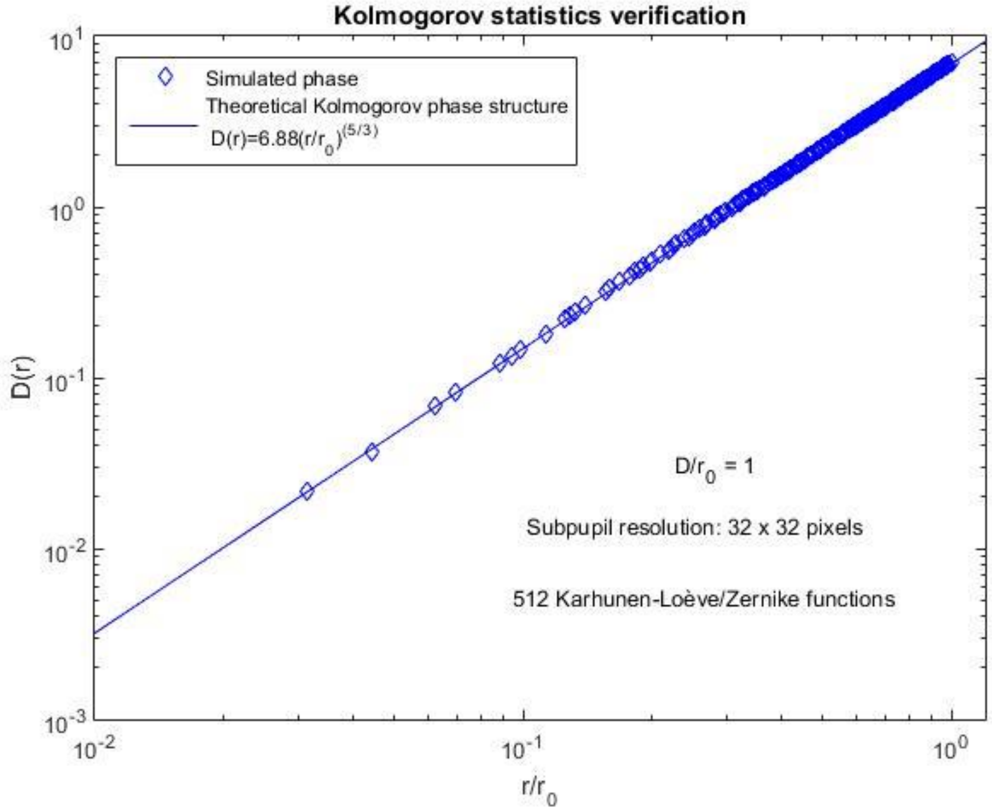

Figure 4-1. Comparison of theoretical Kolmogorov phase structure ([Eq. 4-1], solid line) with the phase structure obtained from a series of 50000 simulated phase frames, with D/r₀=1 and 32x32 pixels resolution per frame (diamond shapes).

Verification of a simulated series of phase frames can be done by calculating the phase structure as a function of the distance between the two coordinates involved in the subpupil and by comparing the result with the theoretical Kolmogorov phase structure as expressed in [Eq. 1-5] or [Eq. 4-1]. Figure 4-1 shows such a comparison for the case of a series of 50000 simulated phase frames, for a circular subpupil with $D/r_0=1$, 32 x 32 pixels of resolution per frame and 512 Zernike (or Karhunen-Loève) functions involved. A very good coincidence with the theoretical Kolmogorov law can be verified. The same verification has been done for the other D/r_0 ratios employed throughout this chapter.

4.1.2. Simulation of the pixelized images at the detector

The complex amplitude of the field in the focal plane of a lens is the Fraunhofer diffraction pattern of the field incident on the lens (Goodman, 2005), when the physical extent of the input is much smaller than the lens aperture. On the other hand, the intensity distribution at the detector is the square of the complex field modulus. Thus, the image at the detector as a consequence of the incident field on the Shack-Hartmann microlens has been calculated as the square of the magnitude of a bi-dimensional Fourier transform of the incident field:

$$I(x,y) = \left| \iint_{-\infty}^{\infty} A(x',y') e^{j\phi(x',y')} e^{-j\frac{2\pi}{\lambda f_{\mu l}}(xx'+yy')} dx'dy' \right|^2 \qquad \text{[Eq. 4-13]}$$

x, y, x', and y', are distance coordinates at the focal plane or detector and the subpupil plane, respectively. The incident complex field $A(x',y')e^{j\phi(x',y')}$ has a constant magnitude A for coordinates x' and y' spanned by the subaperture, and zero magnitude out of the subaperture. A is given a value such that the desired photon flux is obtained. $\phi(x',y')$ is the phase of the incident field and is obtained through simulation as explained in point 4.1.1. The Fourier transform is evaluated at frequencies $f_x = x/\lambda f_{\mu l}$ and $f_y = y/\lambda f_{\mu l}$, with λ being the sensing wavelength and $f_{\mu l}$ the microlens focal length.

In practice, both the field at the pupil and the image intensity at the focal plane are obtained in discretized coordinates, and the Fourier transform in [Eq. 4-13] is implemented through a discrete 2D-DFT. Let us assume discretization is of the same size in both orthogonal coordinates, and let us focus on a single coordinate to see the implications of such discretization.

A subpupil of size D (being D the circular subaperture's diameter or the square subaperture's side[7]) is divided into N_p pixels or sections and the phases are obtained at their borders. Resolution at the subpupil is therefore D/N_p, which implies a periodicity in the image domain with period:

$$\frac{\Delta x_{max}}{\lambda f_{\mu l}} = \frac{N_p}{D} \qquad \text{[Eq. 4-14]}$$

---

[7] In the case of a square subaperture, the Kolomogorov phase as an expansion of the Karhunen-Loève set of functions is obtained first in a circular subaperture, and then the phase subset corresponding to the biggest possible inscribed square is selected (see section 4.7).

being Δx_{max} the maximum range in the horizontal coordinate x which can be calculated with this resolution at the pupil. Same analysis applies for the vertical coordinate y. Taking into account that $\Delta x/f_{\mu l}$ is the angular distance spanned by the linear distance Δx, and that λ/D is approximately the *FWHM* at diffraction limit, [Eq. 4-14] can be expressed as:

$$FoV_{max} = N_p \, FWHM_{diff} \qquad \text{[Eq. 4-15]}$$

which means that the maximum angular *FoV* obtainable by simulation is N_p times the *FWHM* at diffraction limit.

On the other hand, the image domain is also discretized and obtained with a 2D-FFT of size N_{fft} by N_{fft}. Hence, $\Delta x_{max} = N_{fft}\Delta x_{pix}$, with Δx_{pix} the linear image's pixel size, and [Eq. 4-14] can be expressed as:

$$\frac{\lambda/D}{\Delta x_{pix}/f_{\mu l}} = \frac{FWHM_{diff}}{\Delta x_{pix}/f_{\mu l}} = \frac{N_{fft}}{N_p} \qquad \text{[Eq. 4-16]}$$

which states that the ratio N_{fft}/N_p is the diffraction *FWHM* size in pixels.

N_p has been selected to be $N_p = 32$ throughout the simulations presented in this chapter, and it has been verified that *aliasing* effects in the image domain with this pupil resolution is negligible. On the other hand, N_{fft} is given a value of $N_{fft} = 64$, which implies a diffraction *FWHM* size of two pixels, the same spot's resolution as in the OOMAO, and which is known to be in the optimum range (Thomas et al, 2006). Note that λ and $f_{\mu l}$ are not explicitly selected in the simulation, but are implicitly chosen through the selection of the ratio N_{fft}/N_p and, therefore, of the spot's size.

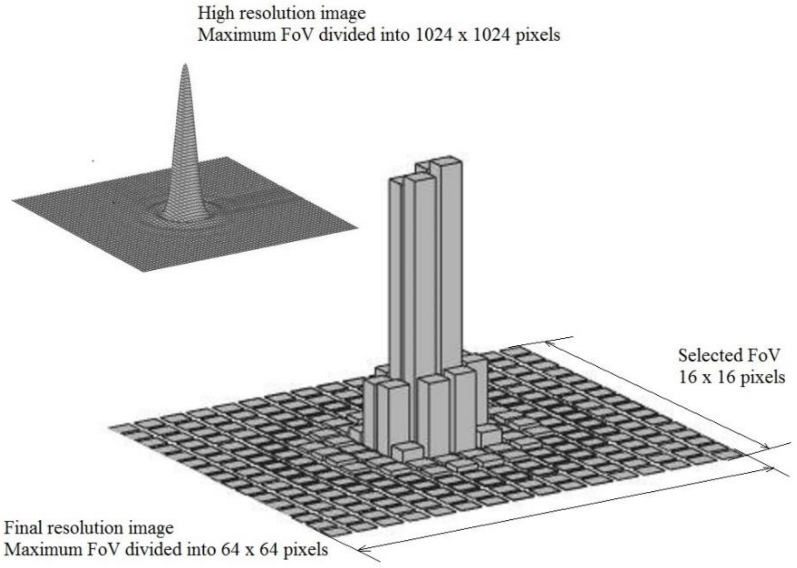

Figure 4-2. Sketch of a high resolution image as is obtained with a 1024 x 1024 2D-FFT, and of the final resolution image, obtained through decimation by block summation and selection of a central FoV.

Actually, the employed 2D-FFT is 1024 x 1024 sized, so that the image is first obtained with a close to continuous resolution. It is then decimated by simple block summation to the final resolution of 64 x 64, thus simulating the effect of pixelation at the detector. Finally, the desired *FoV* is selected out of the calculated *FoV_{max}* by selecting the appropriate central range in the image. This has been sketched in Figure 4-2.

4.1.3. The Electron Multiplication CCD detector model

Electron Multiplication (EM) Charge-Coupled Devices (EMCCDs) are used to take images under low-light conditions and for photon-counting experiments. They are applied in a wide range of scientific fields, such as single molecule microscopy, astronomy, spectroscopy and biomedical imaging. Imaging under low-light conditions presents the problem that the signal can be low compared to the readout noise. EMCCDs overcome this problem by amplifying the signal in an electron-multiplication register, previous to the readout electronics. This reduces the effective readout noise to less than one electron, at the price, however, of introducing an amplification noise. Noise and gain model for an EMCCD detector has been taken from Hirsch et. al., 2013.

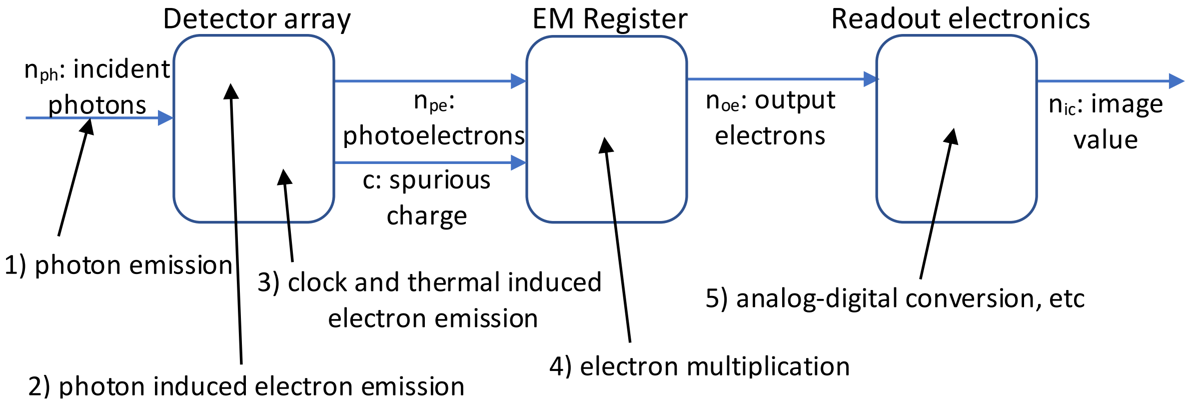

Figure 4-3. Schematic of the sources of noise in an Electron Multiplication Charge-Coupled Device.

Figure 4-3 is a schematic representation of the main blocks in an EMCCD for a gain and noise statistical model derivation.

First, the emission of light from a light source is a statistical process itself with Poisson distribution. So, for a mean incident light intensity I, the probability density function $p(n_{ph};I)$ of the incident number of photons n_{ph} is a Poisson distribution $P(n_{ph};I)$.

$$p(n_{ph};I) = P(n_{ph};I) \qquad \text{[Eq. 4-17]}$$

When a photon hits the exposed part of the detector array, there is a chance that it creates a photoelectron. This stochastic process is the second source of noise. The number of electrons expected per photon is the quantum efficiency of the detector, q (or *QE*), and depends on the detector material and the wavelength of the light. The probability of getting n_{pe}

photoelectrons from a light source is again a Poisson distribution where the mean is the product of intensity and quantum efficiency:

$$p(n_{pe}; I, q) = P(n_{pe}; Iq) \qquad \text{[Eq. 4-18]}$$

The third source of noise stems from spurious charge, which consists of two components. The read-out process shifts the electrons through the system of bins by means of changing electrode voltages. During the shift process, there is a chance that unwanted electrons are created, which is known as clock induced charge (CIC). The CIC occurs in the detector array and its readout register as well as in the EM register. Only the CIC in the detector array is considered in the present work since this yields sufficiently accurate results. The detector array is also affected by thermally induced dark current, which is usually reduced by the cooling of the detector. While the dark current is time-dependent, the CIC only depends on the number of readout transfers. However, for a particular exposure duration and EMCCD configuration, from the point of view of a noise model, the spurious charges coming from the CIC and dark current can be considered to be one source of noise, governed by a Poisson distribution with emission rate $c = tc_{dark} + c_{CIC}$, where t is the exposure time.

The sum of two independent Poisson distributions is another Poisson distribution with mean the sum of the means, so the probability of n_{ie} electrons entering the EM register can be expressed as:

$$p(n_{ie}; I, q, c) = P(n_{ie}; Iq + c) \qquad \text{[Eq. 4-19]}$$

Expression [Eq. 4-19] is the Poisson contribution to the end-to-end probability distribution of the proposed EMCCD model.

In the EM register, the electrons are shifted using a higher clock voltage than in the detector array and readout register to create more electrons through impact ionisation, which is also a stochastic process and the fourth source of noise. The chosen approach in Hirsch et al, 2013, to model the probability to get n_{oe} output electrons from a EM register with gain g and n_{ie} input electrons, is the gamma distribution:

$$p(n_{oe}; n_{ie}, g) = \gamma(n_{oe}; n_{ie}, g) = {n_{oe}}^{n_{ie}-1} \frac{e^{-n_{oe}/g}}{\Gamma(n_{ie}) g^{n_{ie}}} \qquad \text{[Eq. 4-20]}$$

with n_{ie} the shape parameter and g the scale parameter in the gamma distribution. An exception is made to [Eq. 4-20] when n_{ie} is zero, that is, no electrons enter the EM register, for which case the output n_{oe} is equalled to zero also. This means that the assumption is made that no electrons are created in the EM register for a null input, and that spurious charges are not created inside the EM register, which is only an approximation. [Eq. 4-20] is the gamma contribution to the overall statistical model for the EMCCD.

Finally, the electronics that amplifies the signal and converts it into discrete image values creates read-out noise (RON), which is modelled by a normal distribution with standard deviation r. There is also a proportionality factor f that characterizes the A/D conversion, sometimes called *sensitivity* of the detector, and measured in electrons per ADU (Analog to Digital Unit or count). In other words, the following expression holds: $f = \langle n_{oe} \rangle / \langle n_{ic} \rangle$, with n_{ic} the number of image discrete counts. Thus, the normal contribution to the EMCCD model can be expressed as:

$$p(fn_{ic}; n_{oe}, r) = N(fn_{ic}; n_{oe}, r) \quad \text{[Eq. 4-21]}$$

with $N(fn_{ic}; n_{oe}, r)$ the normal distribution of the process fn_{ic}, with n_{oe} mean value and standard deviation r. Ultimate quantization of n_{ic} into an integer value adds to the final total noise amount.

4.1.4. Simulation workflow

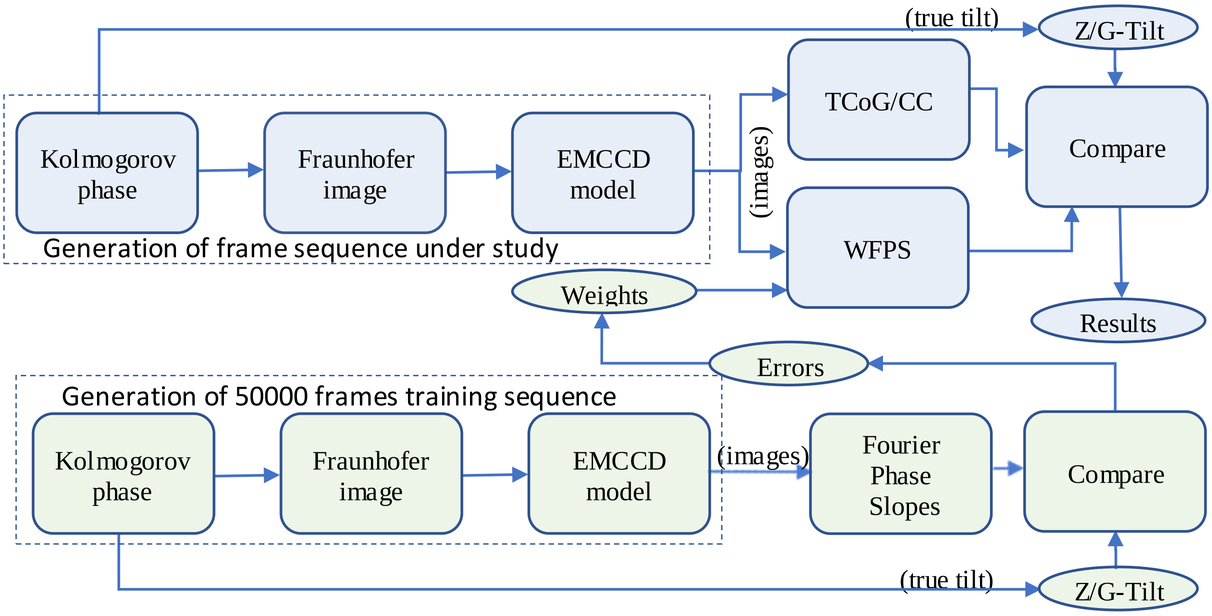

Figure 4-4. Core of the simulation workflow employed to compare the centroiding algorithms at a subpupil level

Figure 4-4 shows as a block diagram the operations that are performed at the core of every simulation aiming to compare the different centroiding algorithms' performance at a subpupil level.

A sequence under study is created by first simulating the Kolomogorov phase frames (point 4.1.1). Here, the ratio of the subaperture size to Fried parameter, D/r_0 is selected. Resolution at the pupil has been fixed to $D/32$ sized pixels, and the number of Zernike (or Karhunen-Loève) modes employed is 512. Then the images at the detector plane are obtained (point 4.1.2), and at this step the FoV size in pixels is selected. The diffraction FWHM size has been fixed to two pixels. The following step is applying the EMCCD gain and noise model to the image, as described in point 4.1.3. Light flux level in photons is also selected here. The result of the previous simulation steps is a close to real sequence of images under study. The different centroiding algorithms under study are applied to this image sequence to estimate the phase tilt at the subpupil, and then compare the estimation with the true applied tilt. This true tilt can be the Zernike tilt (Z-Tilt), which was obtained at the first step of the simulation, or the G-Tilt, which is obtained by applying a true CoG to a version of the image sequence with maximum FoV and exempt of noise.

A parallel training sequence, with 50000 frames and with exactly the same system parameters as the sequence under study, is simulated in order to obtain the necessary weights for the WFPS algorithm. The Fourier phase slopes of the sequence at a set of spatial frequencies are obtained by applying [Eq. 3-15] to each image, and the resulting spot's displacement measurements are compared to the true applied phase tilt to obtain the measurement errors. MAP weights are a function of the measurement error covariance matrix, as expressed in [Eq. 3-22]. The number and order of the spatial frequencies involved in the WFPS algorithm, and consequently the number of weights, are selectable in the simulation.

As for the control algorithms, TCoG's threshold is a unique value for the whole sequence under study, and is calculated by minimizing the tilt estimation error of the whole sequence under study itself. For the CC algorithm, the reference image is a bi-dimensional Gaussian shape for which the FWHM and the spanned FoV are selectable parameters. The correlation figure is obtained with no interpolation, i.e., with the same resolution as the live and reference images. The centroid is calculated over the correlation figure with a TCoG algorithm, for which the threshold is again a unique value for the whole sequence and is calculated by minimization of the final tilt estimation error for the whole sequence under study.

The centroiding algorithms give the result of spot's displacement in pixel units. In order to compare their outputs with the system's input phase tilt and to give the final estimation errors in wave radians at the sensing wavelength, a conversion from displacement in pixels to wave radians becomes mandatory. Expression [Eq. 1-13] was obtained through geometrical considerations and relates displacement in pixels d' with the peak to valley phase tilt $\Delta\phi$ across the subaperture width at the telescope's pupil plane Δx:

$$\frac{\Delta\phi}{\Delta x} = \left[\frac{2\pi}{\lambda}\frac{f}{F}\frac{d_{pix}}{f_{\mu l}}\right] d' \qquad \text{[Eq. 4-22]}$$

with F/f the magnification factor of the phase tilt from the telescope's aperture to the SHWFS's input, and $d_{pix}/f_{\mu l}$ the angular pixel size. Taking into account that the size of the SHWFS's subaperture D is $D = \Delta x f/F$, and substituting [Eq. 4-16] into [Eq. 4-22], we get:

$$\Delta\phi = \left[2\pi\frac{N_p}{N_{fft}}\right] d' \qquad \text{[Eq. 4-23]}$$

with N_p and N_{fft} the simulation parameters corresponding to the number of pixels in one dimension in the subpupil's domain and the number of pixels in one dimension for the maximum FoV in the image domain, respectively. Finally, with the aim of giving the estimation error results in r.m.s. radians, peak to valley tilt is divided by a factor of four when the subaperture is circular, resulting in:

$$\Delta\phi_{rms} = \left[\frac{\pi}{2}\frac{N_p}{N_{fft}}\right]d' \qquad \text{[Eq. 4-24]}$$

with N_p the number of phase pixels spanned by the aperture's diameter. For a square subaperture, the factor[8] relating peak to valley and r.m.s. phase is $2\sqrt{3}$, and so:

$$\Delta\phi_{rms}^{SQR} = \left[\frac{\pi}{\sqrt{3}}\frac{N_p}{N_{fft}}\right]d' \qquad \text{[Eq. 4-25]}$$

with N_p the number of phase pixels spanned by the aperture's side.

As an example, the true horizontal Z-tilt, given in r.m.s. wave radians at the sensing wavelength, for a circular subaperture, is the coefficient of the second Zernike function in the phase Zernike expansion, c_2 in [Eq. 4-3]. For a given estimated horizontal spot's displacement $\hat{d}'^x$, given in pixels, and obtained by any of the centroiding methods, the estimated horizontal Z-tilt in r.m.s. radians would be $\hat{c}_2 = \hat{d}'^x(\pi/2)\left(N_p/N_{fft}\right)$.

4.2. Linearity and dynamic range

One of the main concerns regarding centroiding algorithms is their linearity when operation in large dynamic ranges is required. Some illustrations are shown in this section that compare the WFPS with other algorithms in this respect. Open loop observation is assumed with a large subaperture size to Fried parameter ratio ($D/r_0=2.5$) so that the spot's tilt excursion, and hence the required dynamic range, are large.

Figure 4-5 shows the estimated Z-Tilt, in r.m.s. radians at the sensing wavelength, as a function of applied Z-Tilt and the FoV extent in pixels by pixels for the WFPS algorithm (a) and the TCoG algorithm (b), for a circular subaperture with $D/r_0=2.5$, Nyquist sampling (FWHM at diffraction of 2 pixels), high light flux level of 500000 photons, QE value of 97%, unity EMCCD gain, CIC noise of 0.05 e^-/pixel/frame, RON noise of 50 e^- r.m.s. and sensitivity of 10 e^-/ADU.[9]

Non-smooth aspect of the graphs is due to the spot's deformation in response to high order aberrations in the atmospheric turbulence, and not because of detector noises, which are negligible with respect to the light flux level. Response is plotted up to an absolute value of 5 r.m.s. radians of applied tilt across the subaperture, which correspond to 6.37 pixels of spot's displacement, according to equation [Eq. 4-24]. Recovered Z-Tilt shows a very good linearity for FoV's of 16 x 16 and 14 x 14 pixels, for both algorithms. It only starts worsening when the FoV is reduced to 12 x 12 pixels, at both extremes of the graph, for applied tilts greater (in absolute value) than 4 r.m.s. radians (5.1 pixels of displacement). When FoV is further reduced to 8 x 8 pixels, linearity is only maintained up to 2 r.m.s. radians of applied tilt. TCoG algorithm can even completely lose the tilt estimation for applied tilts close to 5 r.m.s. radians, when

---

[8] This factor has been derived by the author

[9] Unless otherwise stated, simulations in this section are for a Nyquist sampled spot (FWHM at diffraction of 2 pixels) and typical values of detector parameters: RON of 50 e^- r.m.s., CIC of 0.05 e^-/pixel/frame, QE of 97% (which is the Andor Ixon 860 EMCCD response at wavelengths between 500 and 600 nm), and sensitivity of 10 e^-/ADU.

the spot almost gets out of the observed FoV and only its tail remains inside. WFPS, however, has the capacity to keep up with the estimation, as long as the tail's intensity is over the background noise (see point A.5.2 for an example that explains this behaviour).

The reason for such a good linearity behaviour of both algorithms when the FoV is adequate is that, for a high light flux level, the TCoG makes use of the threshold to eliminate the tails of the spot and concentrate in the central more symmetric part of the spot, thereby correctly estimating the Z-Tilt even when the spot may be slightly truncated. WFPS, on the other hand, overcomes spot's truncation by giving very small weight to the zero spatial frequency and larger weights to other frequencies that are less affected by spot's truncation.

(a) WFPS (4x4 freqs.) centroiding method. Z-Tilt estimation. $D/r_0=2.5$

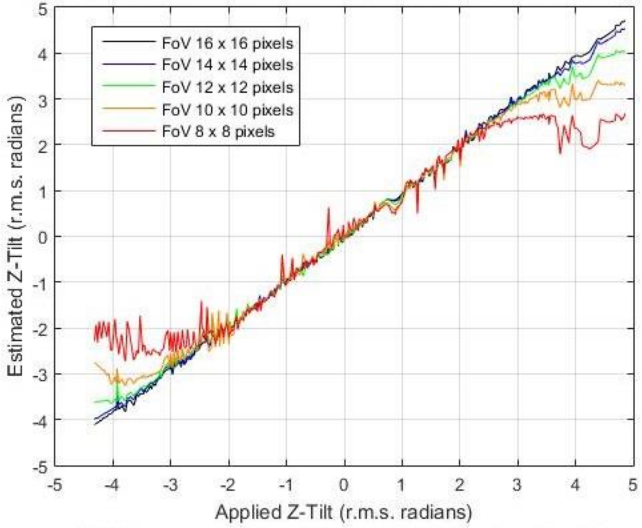

(b) TCoG centroiding method. Z-Tilt estimation. $D/r_0=2.5$

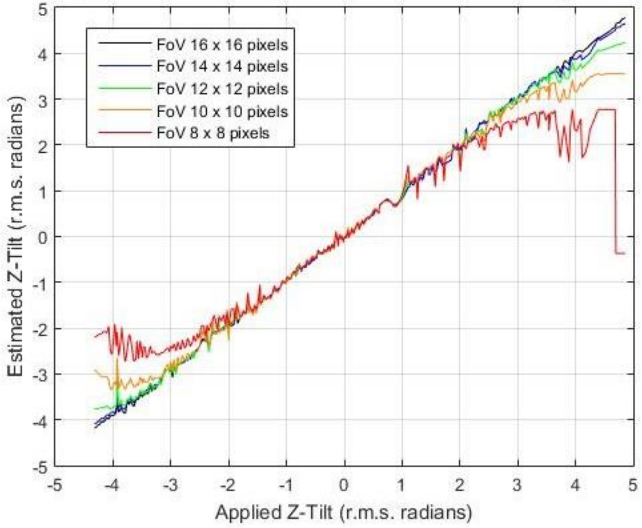

Figure 4-5. (a) Estimated Z-Tilt as a function of applied Z-Tilt and FoV, for the WFPS algorithm with 4 x 4 spatial frequencies, circular subaperture with $D/r_0=2.5$, Nyquist sampling, high light flux level of 500000 photons, unity EMCCD gain, CIC=0.05 e^-/pixel/frame, RON=50 e^-r.m.s. (b) Same for the TCoG algorithm.

Figure 4-6 shows the result of a repetition of the previous experiment, maintaining all the system's parameters, with the only difference that G-Tilt is estimated. Both algorithms see their linearity worsened, even for the largest 16 x 16 pixels FoV. This is because G-Tilt is correctly estimated by a pure CoG. So TCoG's optimal threshold is zero or close by, and WFPS tends to give a high weight to zero spatial frequency. In both cases, truncation of the spot affects the estimated G-Tilt. In any case, overall behaviour of both algorithms with respect to linearity when estimating G-Tilt is again very similar.

(a) WFPS (4x4 freqs.) centroiding method. G-Tilt estimation. D/r$_0$=2.5

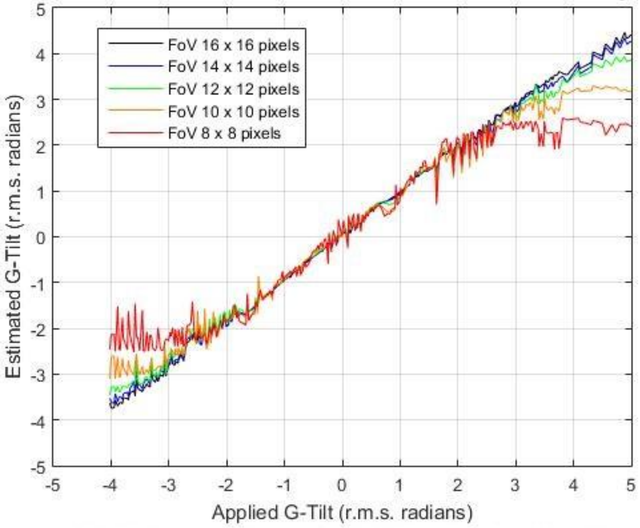

(b) TCoG centroiding method. G-Tilt estimation. D/r$_0$=2.5

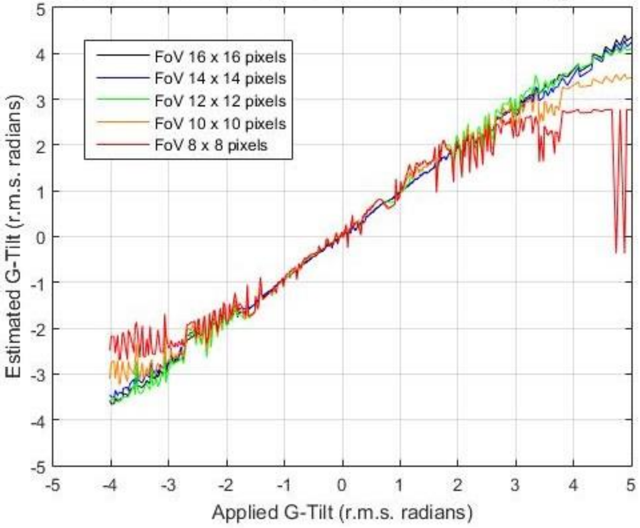

Figure 4-6. (a) Estimated G-Tilt as a function of applied G-Tilt and FoV, for the WFPS algorithm with 4 x 4 spatial frequencies, circular subaperture with D/r$_0$=2.5, Nyquist sampling, high light flux level of 500000 photons, unity EMCCD gain, CIC=0.05 e$^-$/pixel/frame, RON=50 e$^-$r.m.s. (b) Same for the TCoG algorithm.

Figure 4-7 concentrates on the particular case of a FoV of 8 x 8 pixels, for a system with the same parameters as the previous simulations, and for estimation of Z-Tilt (a) and G-Tilt (b) with TCoG, CC, WFPS and a version of WFPS that employs 16 x 16 2D-FFT's. CC algorithm employs a 2D Gaussian reference with FWHM of 2 pixels, FoV of 8 pixels, and no interpolation. Centroid is computed by a TCoG over the correlation figure.[10] A very similar behaviour can be seen between the CC and TCoG algorithms. The WFPS with augmented 2D-FFT size has the

---

[10] Unless otherwise stated, the CC algorithm will employ a 2D Gaussian as a reference, with FWHM=2 pixels, FoV=8pixels, and no interpolation. Centroid is computed by a TCoG over the correlation figure.

capacity to slightly improve linearity with respect to TCoG. For example, a 6% improvement is seen when estimating Z-Tilt with 3 rms radians applied.

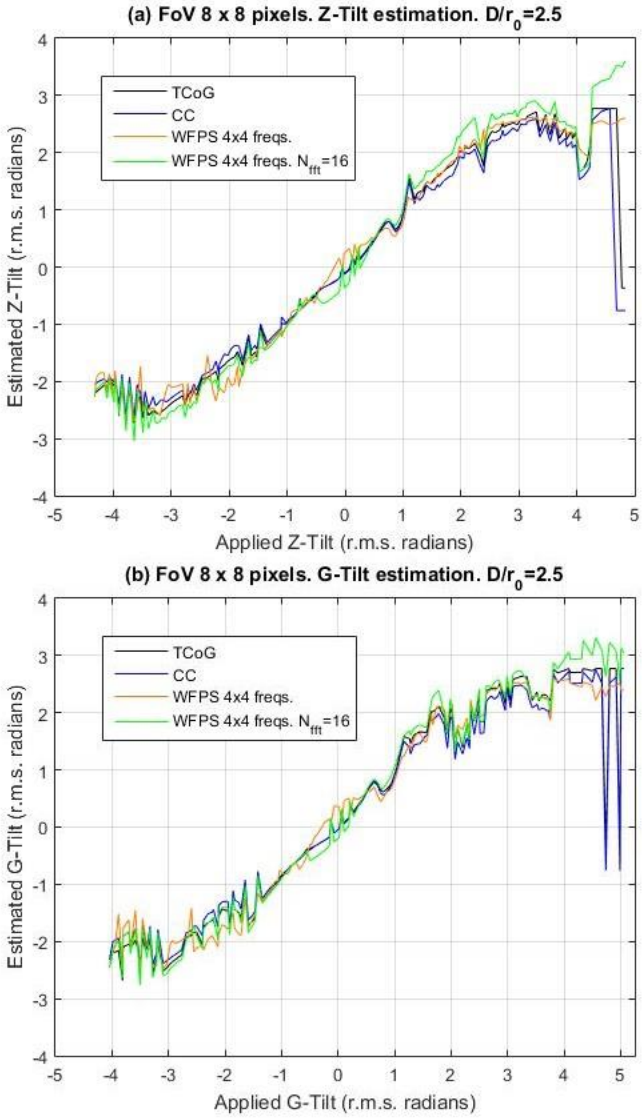

Figure 4-7. (a) Estimated Z-Tilt as a function of applied Z-Tilt and centroiding algorithm, for a FoV of 8 x 8 pixels, circular subaperture with $D/r_0=2.5$, Nyquist sampling, high light flux level of 500000 photons, unity EMCCD gain, CIC=0.05 e^-/pixel/frame, RON=50 e^-r.m.s. (b) Same for G-Tilt estimation.

4.2.1. Optimum field of view

A question that naturally arises is what field of view or dynamic range would be the optimum in every situation, and this depends on the turbulence strength, the light flux level and the robustness of the centroiding algorithm against detector noise. Turbulence strength calls for large FoV's so that linearity is maintained, as it has just been explained. On the other hand, as the signal to noise ratio gets lower, lower FoV's will be preferred in order to reduce noisy pixels. This will be truer for those centroiding algorithms which are more affected by the detector's noises.

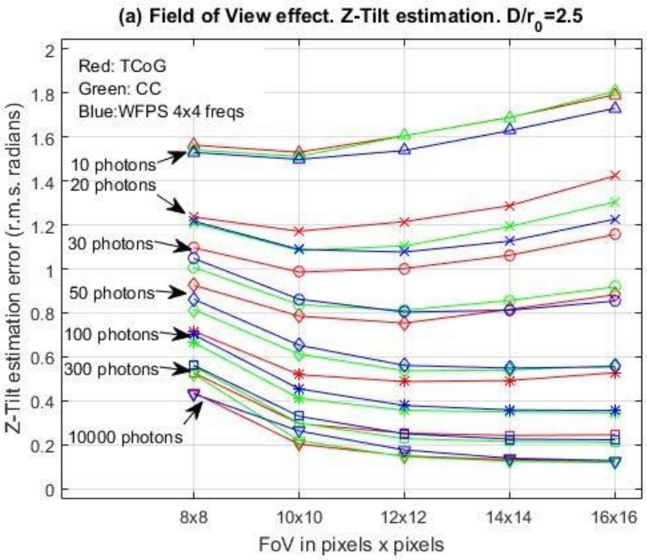

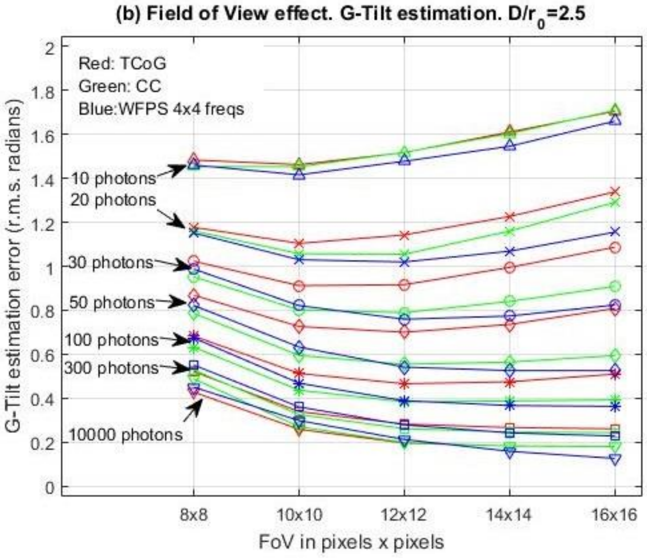

Figure 4-8. Tilt estimation error in r.m.s. radians as a function of FoV and light flux level for the TCoG algorithm (red), the CC algorithm (green) and the WFPS algorithm with 4 x 4 spatial frequencies (blue), for Z-Tilt estimation (a) and G-Tilt estimation (b). D/r$_0$ is 2.5. CIC is 0.05 e$^-$/pix/frame and RON is 50 e$^-$ rms.

Optimal FoV for Z-Tilt/G-Tilt estimation (pixels x pixels). D/r$_0$=2.5

#photons (per subpupil)	**TCoG**	**CC**	**WFPS (4x4 freqs)**
10	10x10/10x10	10x10/10x10	10x10/10x10
20	10x10/10x10	10x10/12x12	12x12/12x12
30	10x10/10x10	12x12/12x12	12x12/12x12
50	12x12/12x12	12x12/12x12	14x14/16x16
100	12x12/12x12	16x16/12x12	16x16/16x16
300	14x14/16x16	16x16/16x16	16x16/16x16
10000	16x16/16x16	16x16/16x16	16x16/16x16

Table 4-2. Optimal FoV in pixels x pixels as a function of light flux level for the TCoG, CC and WFPS (with 4x4 frequencies) algorithms, obtained from Figure 4-8. D/r$_0$=2.5. CIC=0.05 e$^-$/pix/frame. RON=50 e$^-$ rms.

(a) Field of View effect. Z-Tilt estimation. $D/r_0=1$

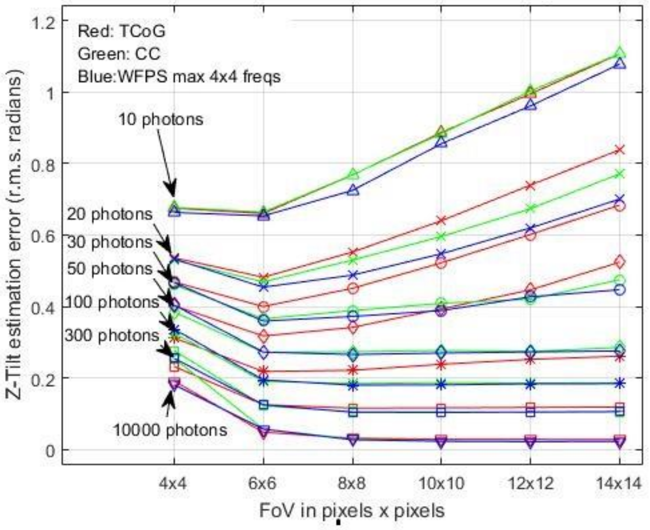

(b) Field of View effect. G-Tilt estimation. $D/r_0=1$

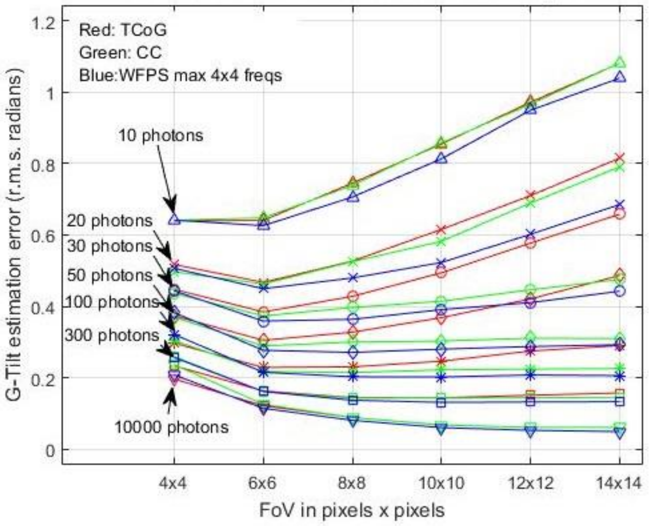

Figure 4-9. Tilt estimation error in r.m.s. radians as a function of FoV and light flux level for the TCoG algorithm (red), the CC algorithm (green) and the WFPS algorithm with at most 4 x 4 spatial frequencies (blue), for Z-Tilt estimation (a) and G-Tilt estimation (b). D/r_0 is 1. CIC is 0.05 e^-/pix/frame and RON is 50 e^- rms.

Optimal FoV for Z-Tilt/G-Tilt estimation (pixels x pixels). D/r_0=1

#photons (per subpupil)	***TCoG***	***CC***	***WFPS (4x4 freqs at most)***
10	6x6/4x4	6x6/4x4	6x6/6x6
20	6x6/6x6	6x6/6x6	6x6/6x6
30	6x6/6x6	6x6/6x6	6x6/6x6
50	6x6/6x6	6x6/6x6	8x8/8x8
100	6x6/6x6	8x8/8x8	8x8/10x10
300	8x8/10x10	12x12/8x8	10x10/10x10
10000	14x14/14x14	14x14/12x12	12x12/14x14

Table 4-3. Optimal FoV in pixels x pixels as a function of light flux level for the TCoG, CC and WFPS (with at most 4x4 frequencies) algorithms, obtained from Figure 4-9. D/r_0=1. CIC=0.05 e^-/pix/frame. RON=50 e^- rms.

Figure 4-8 shows the dependence of the tilt estimation error in r.m.s. radians at the sensing wavelength with the FoV in pixels by pixels and light flux level in photons, for the TCoG algorithm (red lines), the CC algorithm (green lines) and the WFPS algorithm with 4x4 spatial frequencies (blue lines), when estimating Z-Tilt (a) and estimating G-Tilt (b). D/r_0 is 2.5. CIC is 0.05 e^-/pix/frame and RON is 50 e^- rms. Selected EM gain for each light level is high without saturating a 14 bits detector. Table 4-2 collects the optimal FoV values for the different light flux levels and the three algorithms under study. A general conclusion that can be extracted from this simulation is that the WFPS algorithm is the least affected by detector noise among the three evaluated algorithms, calling for bigger FoV's for each light level under study, and giving as a result a better tilt estimation at the optimal FoV. CC algorithm would be in the second place in this respect, with a very similar behaviour. However, TCoG is very much affected by detector noise, and requires small optimal FoV's. Moreover, red traces in Figure 4-8 tend to rapidly increase with FoV value for light levels below 100 photons, indicating that TCoG algorithm is very sensitive to the optimal selection of FoV. WFPS and CC are much more tolerant in this sense, allowing for a broader range of FoV selection with little or no penalization in tilt estimation error for light levels above 30 photons. For low light level such as 30 to 50 photons, TCoG must work with FoV's in the order of 10x10 to 12x12 pixels, whereas CC and WFPS can work with FoV's of 12x12 to even 16x16 pixels.

Figure 4-9 and Table 4-3 illustrate the result for an identical simulation for D/r_0=1. The WFPS employs 2 x 2 spatial frequencies for the 4 x 4 pixels FoV, 3 x 3 spatial frequencies for the 6 x 6 pixels FoV, and 4 x 4 spatial frequencies for the rest of FoV values. Very similar conclusions to the previous simulations can be extracted. TCoG requires as low a FoV as 6x6 pixels for light levels of 100 photons and below, whereas CC and WFPS work better with higher FoV's of 8x8 or 10x10 pixels for 50 photons of incident light or above.

4.3. MAP weights

Once the working FoV is decided, we are in a position to determine the number of spatial frequencies to involve in the WFPS algorithm and the value of their corresponding MAP weights. The number of spatial frequencies has a direct impact on the computational cost of the algorithm, as seen in point 3.3.2 (see Tables 3-1 and 3-2), and a certain impact on the tilt estimation error, as will be seen in the present point.

Note here that the numerical simulation of the system at a subpupil level is a must in order to obtain the necessary MAP weights for the WFPS algorithm. These weights are a function of the tilt estimation error covariance matrices V_{E^x} and V_{E^y} as expressed in [Eq. 3-22], with tilt estimation error vectors E^x and E^y defined in [Eq. 3-18]. These error covariance matrices can only be determined when a sufficiently large set of input phases to the system and their corresponding recovered phase tilts at the involved spatial frequencies are known, and this is only feasible through numerical simulation. This is the reason why, for every simulation performed in this chapter and for every sequence of turbulent phases under study, a parallel much larger sequence of 50000 frames with the same system parameters is always utilized to obtain the error covariance matrices and thereby the MAP weights for the WFPS algorithm, as shown in the simulation workflow in Figure 4-4.

Figure 4-10 illustrates the effect of the selected number of spatial frequencies that participate in the WFPS algorithm over the tilt estimation error, expressed in r.m.s. radians at the sensing wavelength, and as a function also of the incident light level in the subaperture, expressed in photons. The D/r$_0$ ratio is 2.5. The size of the 2D-FFT's employed in the WFPS algorithm is 14x14 in this case, the same as the FoV size, which is 14x14 pixels. Therefore, the maximum number of spatial frequencies involved is 7x7, corresponding to the first quadrant of the Fourier space. In order to lower the computational cost, the lowermost, more reliable spatial frequencies are selected, in the following patterns: 4x4, 3x3, lowermost 6, 2x2, lowermost 3. The lowermost 6 are the ones for which the sum of their horizontal and vertical indexes values *k* and *l* is at most 2. For the lowermost 3, this sum is at most 1.

Part (a) of the figure shows the result for Z-Tilt estimation, and part (b) shows the same result

(a) #spatial freqs effect on WFPS. D/r$_0$=2.5. FoV 14x14 pix. ZTilt estimation

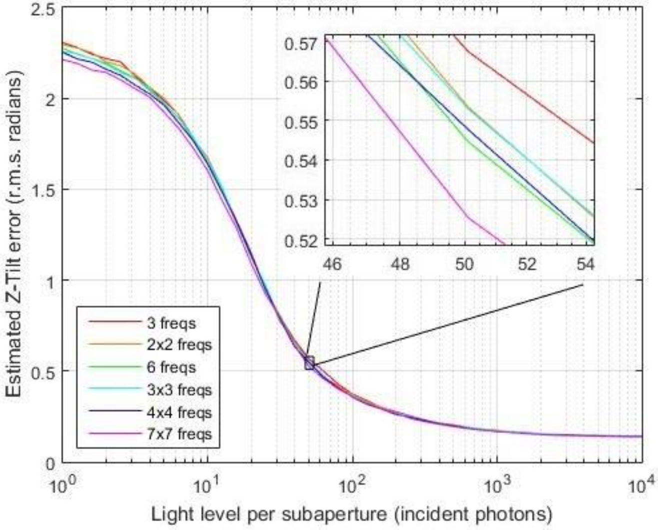

(b) #spatial freqs effect on WFPS. D/r$_0$=2.5. FoV 14x14 pix. GTilt estimation

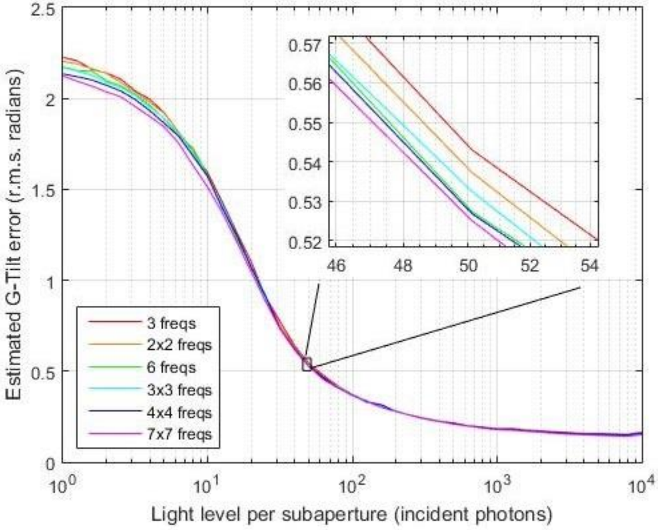

Figure 4-10. Estimated tilt error in r.m.s. radians at the sensing wavelength as a function of incident light level at the subaperture in photons and several schemes of spatial frequencies selection for the WFPS algorithm (see text for further explanation). D/r$_0$ is 2.5. Nyquist sampling. FoV is 14 by 14 pixels. EMCCD gain for each light level is high without saturating a 14 bits detector. CIC is 0.05 e$^-$/pixel/frame. RON is 50 e$^-$ rms. (a) is for Z-Tilt estimation and (b) for G-Tilt estimation.

	MAP weights for WFPS horizontal centroid ($W^{x}_{k,l}$). Z-Tilt estimation. D/r_0=2.5. FoV=14x14 pixels.		
Photons	***3 frequencies***	***6 frequencies***	***4 x 4 frequencies***
10	0.9265 0.0350 0.0386	0.9330 0.0314 -0.0227 0.0409 0.0189 -0.0014	1.0019 0.0336 -0.0214 -0.0101 0.0440 0.0210 -0.0001 -0.0082 0.0033 -0.0027 -0.0045 -0.0103 -0.0098 -0.0099 -0.0124 -0.0144
20	0.7850 0.0956 0.1194	0.7166 0.0860 0.0048 0.1238 0.0535 0.0152	0.7224 0.0870 0.0030 -0.0025 0.1163 0.0526 0.0116 -0.0011 0.0133 0.0084 0.0047 -0.0039 -0.0009 -0.0009 -0.0029 -0.0071
30	0.6573 0.1532 0.1895	0.5636 0.1390 0.0232 0.1854 0.0680 0.0207	0.5385 0.1339 0.0192 0.0029 0.1828 0.0674 0.0167 0.0029 0.0184 0.0092 0.0063 -0.0004 0.0024 0.0033 -0.0001 -0.0035
50	0.5455 0.2250 0.2296	0.4560 0.1996 0.0294 0.2337 0.0646 0.0168	0.4326 0.1891 0.0286 0.0046 0.2191 0.0629 0.0161 0.0060 0.0159 0.0102 0.0073 0.0016 0.0042 0.0030 0.0011 -0.0023
100	0.4442 0.3029 0.2530	0.4050 0.2669 0.0306 0.2399 0.0426 0.0150	0.3801 0.2564 0.0255 0.0077 0.2280 0.0371 0.0139 0.0071 0.0118 0.0085 0.0077 0.0037 0.0064 0.0048 0.0017 -0.0005
200	0.3772 0.3394 0.2834	0.3600 0.3088 0.0247 0.2702 0.0238 0.0125	0.3378 0.2848 0.0196 0.0109 0.2559 0.0186 0.0112 0.0088 0.0109 0.0120 0.0090 0.0045 0.0054 0.0056 0.0040 0.0010
500	0.2885 0.3592 0.3523	0.2910 0.3414 0.0178 0.3359 0.0063 0.0077	0.2772 0.3123 0.0098 0.0128 0.3210 0.0046 0.0090 0.0098 0.0018 0.0081 0.0090 0.0063 0.0067 0.0058 0.0051 0.0007
1000	0.2468 0.3702 0.3830	0.2497 0.3594 0.0134 0.3719 0.0005 0.0050	0.2475 0.3295 0.0058 0.0127 0.3485 -0.0083 0.0104 0.0095 0.0009 0.0114 0.0103 0.0061 0.0036 0.0050 0.0049 0.0022
10000	0.2055 0.3601 0.4343	0.2000 0.3517 0.0120 0.4428 -0.0047 -0.0018	0.1987 0.3211 0.0050 0.0113 0.4190 -0.0062 0.0081 0.0120 -0.0071 0.0074 0.0096 0.0078 0.0020 0.0056 0.0046 0.0010

Table 4-4. List of MAP weights for the calculation of the horizontal value of the centroid with the WFPS algorithm, as per [Eq. 3-23] ($W^{x}_{k,l}$), when estimating Z-Tilt. D/r_0 is 2.5. Nyquist sampling. FoV is 14 by 14 pixels. EMCCD gain for each light level is high without saturating a 14 bits detector. CIC is 0.05 e^-/pixel/frame. RON is 50 e^- rms. Light level increases vertically in the table. Three different patterns of spatial frequencies selection are listed in a column each: 3 lowermost frequencies, 6 lowermost frequencies and 4x4 lowermost frequencies.

	MAP weights for WFPS horizontal centroid ($W^x_{k,l}$). G-Tilt estimation. D/r_0=2.5. FoV=14x14 pixels.								
Photons	**3 frequencies**		**6 frequencies**			**4 x 4 frequencies**			
10	0.9345	0.0305	0.9509	0.0288	-0.0232	1.0194	0.0311	-0.0190	-0.0106
	0.0350		0.0357	0.0122		0.0387	0.0190	-0.0018	-0.0120
			-0.0045			0.0007	-0.0023	-0.0055	-0.0116
						-0.0106	-0.0094	-0.0140	-0.0120
20	0.8007	0.0857	0.7443	0.0788	0.0025	0.7650	0.0755	-0.0006	-0.0028
	0.1135		0.1143	0.0456		0.1078	0.0456	0.0095	-0.0012
			0.0146			0.0133	0.0062	0.0027	-0.0049
						-0.0015	-0.0018	-0.0041	-0.0087
30	0.6885	0.1348	0.6190	0.1220	0.0167	0.6082	0.1246	0.0163	0.0007
	0.1767		0.1692	0.0563		0.1620	0.0560	0.0119	0.0014
			0.0168			0.0152	0.0075	0.0039	-0.0020
						0.0006	0.0003	-0.0023	-0.0045
50	0.6036	0.1928	0.5476	0.1718	0.0229	0.5328	0.1614	0.0188	0.0023
	0.2036		0.1998	0.0441		0.2001	0.0493	0.0101	0.0014
			0.0137			0.0119	0.0060	0.0050	0.0002
						0.0012	0.0004	0.0004	-0.0014
100	0.5607	0.2202	0.5392	0.2025	0.0134	0.5337	0.2012	0.0124	0.0030
	0.2192		0.2177	0.0215		0.2066	0.0177	0.0041	0.0031
			0.0057			0.0050	0.0038	0.0039	0.0026
						0.0015	0.0009	0.0007	-0.0004
200	0.5734	0.2025	0.5660	0.2023	0.0022	0.5670	0.1996	0.0016	0.0038
	0.2241		0.2343	-0.0004		0.2268	-0.0017	-0.0012	0.0029
			-0.0043			-0.0040	-0.0003	0.0018	0.0028
						-0.0007	0.0004	0.0001	0.0010
500	0.6243	0.1703	0.6181	0.1908	-0.0086	0.6159	0.1906	-0.0087	0.0016
	0.2054		0.2331	-0.0218		0.2327	-0.0146	-0.0042	0.0016
			-0.0116			-0.0112	-0.0029	-0.0007	0.0026
						-0.0024	-0.0027	0.0003	0.0021
1000	0.6825	0.1467	0.6644	0.1755	-0.0126	0.6678	0.1790	-0.0099	0.0009
	0.1708		0.2127	-0.0250		0.2082	-0.0174	-0.0073	0.0001
			-0.0150			-0.0132	-0.0041	-0.0013	0.0003
						-0.0040	-0.0018	-0.0003	0.0030
10000	0.6385	0.1436	0.6053	0.1805	-0.0174	0.6024	0.1881	-0.0133	-0.0016
	0.2180		0.2972	-0.0358		0.3081	-0.0252	-0.0073	-0.0044
			-0.0298			-0.0253	-0.0077	-0.0039	0.0003
						-0.0066	-0.0031	-0.0021	0.0016

Table 4-5. List of MAP weights for the calculation of the horizontal value of the centroid with the WFPS algorithm, as per [Eq. 3-23] ($W^x_{k,l}$), when estimating G-Tilt. D/r_0 is 2.5. Nyquist sampling. FoV is 14 by 14 pixels. EMCCD gain for each light level is high without saturating a 14 bits detector. CIC is 0.05 e^-/pixel/frame. RON is 50 e^- rms. Light level increases vertically in the table. Three different patterns of spatial frequencies selection are listed in a column each: 3 lowermost frequencies, 6 lowermost frequencies and 4x4 lowermost frequencies.

for G-Tilt estimation. In both cases, an order of magnitude of magnification of the plot is necessary to appreciate the change in behaviour of the WFPS algorithm when estimating the tilt. The magnification is done around 50 photons of incident light, and only a less than 10% variation in tilt estimation error can be appreciated between the best and the worst case for the Z-Tilt estimation, and less than 5% variation for the G-Tilt estimation. A good compromise between computational cost and estimation performance that will be used throughout the work is to utilize the lowermost 6 spatial frequencies.

Tables 4-4 and 4-5 list the MAP weights $W_{k,l}^{x}$ for the calculation of the horizontal value of the centroids, corresponding to the previous simulation, for the Z-Tilt and G-Tilt estimation, respectively, and for a selected number of representative light levels and three spatial frequencies patterns: lowermost 3, lowermost 6 and lowermost 4x4. Vertical weights are the transpose of horizontal weights, that is, $W_{k,l}^{y} = W_{l,k}^{x}$.

The listed weights values are just as they were obtained from the simulation applied to a 50000 frames sequence realization. They should not be taken as exact values, in the sense that they are repeatedly obtained only within a certain error margin, when different realizations of the 50000 frames training sequence are utilized. This error margin is of a few percent points, less than 5%, for the largest weight values, and increases for lower values, being 10 to 20% a common error margin for weight values around 0.01. Not only the error margin depends upon the weight value, but also on the signal level at the particular spatial frequency, being sometimes quite big when the spatial frequency is probably near a null of signal. In general, it has been seen that a 50000 frames long training sequence is a good compromise between simulation time and resources consumption and weights calculation precision.

At very low light level, below 50 photons, weights for Z-Tilt and G-Tilt estimation tend to be quite similar, indicating that when detector noises dominate, the error distribution throughout the spatial frequencies is similar for both cases, regardless of the exact spot shape and whether Z-Tilt or G-Tilt is being estimated. For light levels of 100 photons and above, when estimating Z-Tilt, there is a clear tendency of the three lowermost frequencies to accumulate the major portion of the total weight, with more or less equally distributed values, and with a decreasing value for the zero spatial frequency weight as light increases. Whereas when estimating G-Tilt, the weight at zero spatial frequency is always the dominant, and tends to increase with increasing light level above 100 photons. This was an expected behaviour for moderate to high light levels, when high order atmospheric turbulence effects dominate measurement noise. The algorithm tends to distribute the weights among more spatial frequencies when estimating Z-Tilt in order to smooth the Fourier phase and symmetrize the spot, whereas it concentrates the weight at the zero spatial frequency when estimating G-Tilt, for it looks for a near pure CoG calculation.

By careful study of the weights, we also find a justification to employ only the lowermost six, as the weights beyond these tend to be of the order of 0.01 or below, thus indicating that their contribution to the final centroid estimation is low. This is both valid for G-Tilt and for Z-Tilt estimation, though more evident for the former due to the weight concentration at zero spatial frequency.

Finally, it is fair to mention that some effort has been made to assess the algorithm's performance degradation with the use of non-optimal weights. It has been seen that weights variation of 10 to even 15% in their values leads to almost no variation in estimation performance. This kind of tests should be further and more extensively performed.

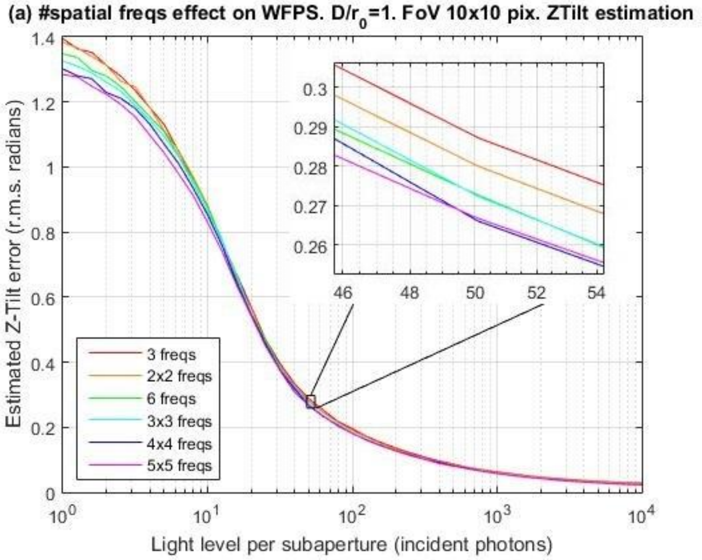

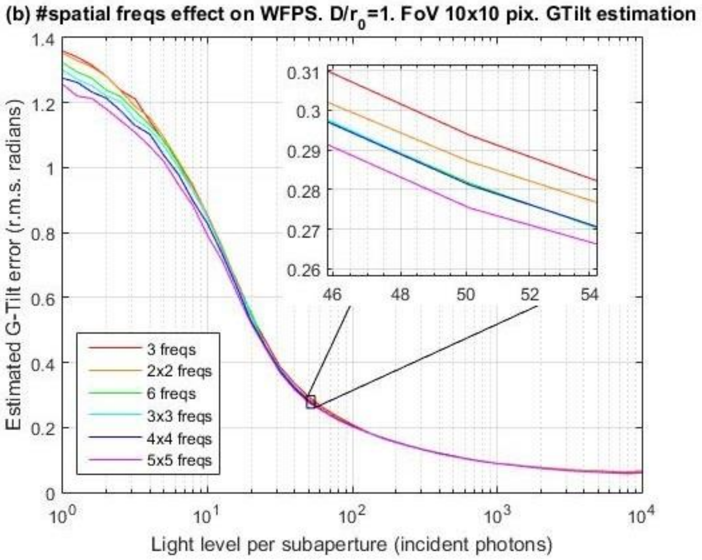

Figure 4-11. Estimated tilt error in r.m.s. radians at the sensing wavelength as a function of incident light level at the subaperture in photons and several schemes of spatial frequencies selection for the WFPS algorithm. D/r_0 is 1. Nyquist sampling. FoV is 10 by 10 pixels. EMCCD gain for each light level is high without saturating a 14 bits detector. CIC is 0.05 e^-/pixel/frame. RON is 50 e^- rms. (a) is for Z-Tilt and (b) for G-Tilt estimation.

Figure 4-11 and Tables 4-6 and 4-7 show the results of a repetition of the previous simulation for a case with $D/r_0=1$ and a FoV of 10x10 pixels. In this case, the maximum number of spatial frequencies involved is 5x5. Again, the employment of only the six lowermost frequencies is a good choice, and this can be seen both from the estimation performance in the figure and from the weights values in the tables. Also, the same considerations regarding repeatability, error margins and performance dependence on optimal weights made for the previous case, are valid here.

	MAP weights for WFPS horizontal centroid ($W^{x}_{k,l}$). Z-Tilt estimation. D/r_0=1. FoV=10x10 pixels.		
Photons	**3 frequencies**	**6 frequencies**	**4 x 4 frequencies**
10	0.9358 0.0255	0.9475 0.0256 -0.0248	1.0595 0.0260 -0.0226 -0.0131
	0.0387	0.0379 0.0203	0.0509 0.0227 -0.0052 -0.0142
		-0.0066	0.0006 -0.0026 -0.0120 -0.0176
			-0.0168 -0.0150 -0.0202 -0.0204
20	0.7615 0.1035	0.6822 0.0910 0.0141	0.7204 0.0862 0.0123 -0.0070
	0.1350	0.1360 0.0586	0.1462 0.0657 0.0105 -0.0101
		0.0180	0.0212 0.0046 -0.0024 -0.0113
			-0.0066 -0.0086 -0.0099 -0.0113
30	0.6393 0.1961	0.4987 0.1634 0.0431	0.5271 0.1637 0.0410 -0.0053
	0.1646	0.1870 0.0858	0.1770 0.0848 0.0109 -0.0050
		0.0220	0.0265 0.0056 -0.0004 -0.0058
			-0.0030 -0.0042 -0.0054 -0.0075
50	0.5397 0.2676	0.4301 0.2187 0.0564	0.4330 0.2008 0.0550 -0.0051
	0.1927	0.1827 0.0831	0.1893 0.0934 0.0158 -0.0031
		0.0290	0.0274 0.0103 -0.0007 -0.0045
			-0.0002 -0.0031 -0.0037 -0.0046
100	0.4640 0.3228	0.3742 0.2568 0.0780	0.3830 0.2552 0.0781 -0.0036
	0.2132	0.1747 0.0854	0.1731 0.0721 0.0123 -0.0034
		0.0309	0.0313 0.0113 0.0012 -0.0026
			-0.0010 -0.0017 -0.0021 -0.0031
200	0.4183 0.3588	0.3559 0.2837 0.0813	0.3623 0.2793 0.0745 -0.0042
	0.2229	0.1744 0.0689	0.1632 0.0541 0.0126 -0.0023
		0.0357	0.0443 0.0226 0.0032 -0.0028
			-0.0007 -0.0024 -0.0020 -0.0018
500	0.3490 0.3792	0.3390 0.3062 0.0785	0.3378 0.2982 0.0704 -0.0046
	0.2718	0.1750 0.0551	0.1727 0.0330 0.0127 -0.0031
		0.0463	0.0586 0.0293 0.0079 -0.0030
			-0.0039 -0.0047 -0.0005 -0.0008
1000	0.3171 0.3943	0.3239 0.3245 0.0759	0.3332 0.3079 0.0630 -0.0005
	0.2886	0.1860 0.0408	0.1675 0.0142 0.0136 -0.0006
		0.0489	0.0608 0.0397 0.0159 -0.0044
			-0.0018 -0.0047 -0.0032 -0.0008
10000	0.2822 0.3943	0.2977 0.3436 0.0773	0.2886 0.3005 0.0723 0.0192
	0.3236	0.2126 0.0221	0.1674 0.0156 0.0187 0.0083
		0.0466	0.0330 0.0541 0.0216 -0.0016
			0.0053 -0.0010 0.0002 -0.0024

Table 4-6. List of MAP weights for the calculation of the horizontal value of the centroid with the WFPS algorithm, as per [Eq. 3-23] ($W^{x}_{k,l}$), when estimating Z-Tilt. D/r_0 is 1. Nyquist sampling. FoV is 10 by 10 pixels. EMCCD gain for each light level is high without saturating a 14 bits detector. CIC is 0.05 e^-/pixel/frame. RON is 50 e^- rms. Light level increases vertically in the table. Three different patterns of spatial frequencies selection are listed in a column each: 3 lowermost frequencies, 6 lowermost frequencies and 4x4 lowermost frequencies.

	MAP weights for WFPS horizontal centroid ($W^{x}_{k,l}$). G-Tilt estimation. D/r_0=1. FoV=10x10 pixels.		
Photons	**3 frequencies**	**6 frequencies**	**4 x 4 frequencies**
10	0.9360 0.0225	0.9622 0.0191 -0.0280	1.0680 0.0257 -0.0188 -0.0132
	0.0414	0.0373 0.0167	0.0447 0.0219 -0.0041 -0.0165
		-0.0072	0.0032 -0.0056 -0.0140 -0.0194
			-0.0173 -0.0172 -0.0181 -0.0193
20	0.7790 0.0902	0.7035 0.0833 0.0112	0.7748 0.0804 0.0121 -0.0055
	0.1307	0.1311 0.0552	0.1114 0.0596 0.0076 -0.0087
		0.0157	0.0168 0.0043 -0.0029 -0.0089
			-0.0073 -0.0098 -0.0099 -0.0141
30	0.6539 0.1621	0.5638 0.1355 0.0363	0.5835 0.1361 0.0360 -0.0052
	0.1840	0.1689 0.0733	0.1685 0.0749 0.0109 -0.0051
		0.0222	0.0238 0.0049 -0.0007 -0.0065
			-0.0033 -0.0048 -0.0062 -0.0068
50	0.6008 0.2158	0.5105 0.1733 0.0518	0.5154 0.1646 0.0477 -0.0042
	0.1834	0.1719 0.0708	0.1742 0.0772 0.0137 -0.0031
		0.0217	0.0214 0.0085 0.0009 -0.0041
			-0.0016 -0.0023 -0.0035 -0.0048
100	0.6029 0.2181	0.5382 0.1720 0.0548	0.5411 0.1673 0.0508 -0.0025
	0.1791	0.1620 0.0559	0.1634 0.0473 0.0076 -0.0012
		0.0171	0.0215 0.0103 0.0017 -0.0020
			0.0003 -0.0008 -0.0020 -0.0030
200	0.6413 0.1796	0.6158 0.1503 0.0345	0.6226 0.1439 0.0323 0.0017
	0.1791	0.1701 0.0264	0.1566 0.0230 0.0034 0.0004
		0.0029	0.0058 0.0059 0.0062 -0.0012
			0.0018 -0.0002 -0.0005 -0.0018
500	0.7535 0.1100	0.7502 0.1130 -0.0100	0.7425 0.1020 -0.0061 0.0103
	0.1366	0.1595 0.0012	0.1472 0.0064 -0.0043 0.0060
		-0.0140	-0.0208 -0.0008 0.0081 -0.0004
			0.0064 0.0041 0.0003 -0.0010
1000	0.8408 0.0657	0.8338 0.0892 -0.0469	0.8270 0.0832 -0.0373 0.0158
	0.0935	0.1513 -0.0026	0.1295 0.0061 -0.0094 0.0083
		-0.0248	-0.0409 0.0004 0.0026 0.0008
			0.0099 0.0022 0.0021 -0.0005
10000	0.9025 0.0326	0.8772 0.0998 -0.1376	0.8856 0.1402 -0.1103 0.0032
	0.0648	0.2363 -0.0068	0.1887 0.0201 -0.0153 0.0069
		-0.0689	-0.0899 0.0057 -0.0430 0.0219
			-0.0105 -0.0128 0.0075 0.0018

Table 4-7. List of MAP weights for the calculation of the horizontal value of the centroid with the WFPS algorithm, as per [Eq. 3-23] ($W^{x}_{k,l}$), when estimating G-Tilt. D/r_0 is 1. Nyquist sampling. FoV is 10 by 10 pixels. EMCCD gain for each light level is high without saturating a 14 bits detector. CIC is 0.05 e^-/pixel/frame. RON is 50 e^- rms. Light level increases vertically in the table. Three different patterns of spatial frequencies selection are listed in a column each: 3 lowermost frequencies, 6 lowermost frequencies and 4x4 lowermost frequencies.

4.4. Sensitivity in the presence of detector noises and spot deformation

In practice, a SHWFS works with a FoV optimized for a particular observation scenario, or just determined by the available number of pixels per subaperture at the detector. It is interesting to assess the behaviour of a centroiding algorithm as a function of incident light for a number of possible FoV values.

Figure 4-12 consists of plots of tilt estimation error in r.m.s. radians at the sensing wavelength as a function of incident light level per subaperture in photons, with logarithmic scales at both abscissae and ordinates, for three centroiding algorithms: TCoG plotted in red, CC plotted in green and WFPS with six spatial frequencies plotted in blue. The upper part, labelled as (a), is for Z-Tilt estimation, and in turn comprises four subpanels, each for a different FoV value: 10x10, 12x12, 14x14 and 16x16 pixels. The lower part, labelled as (b), is for G-Tilt estimation, and also consists of four subpanels for the same FoV values as for Z-Tilt estimation. For the 10x10 pixels FoV case, a fourth algorithm corresponding to WFPS with 14X14 2D-FFT's and 6 spatial frequencies has been added, in cyan. The rest of parameters that define the system are a D/r_0 ratio of 2.5, Nyquist sampling at the diffraction limit, a detector's QE of 97%, CIC noise of 0.05 e^-/pixel/frame, a high EMCCD gain but below saturation of a 14 bits detector, and a RON noise of 50 e^- rms.

The strongest trait of the WFPS algorithm is its good sensitivity for light levels from 20 to 200 photons per subaperture, in the same order as the CC algorithm's sensitivity, when compared to the TCoG algorithm's sensitivity, and this difference in the algorithms behaviour at low to moderate light levels becomes more evident as the FoV value increases. For example, in the case of Z-Tilt estimation with a FoV of 16x16 pixels, the WFPS and CC algorithms give an estimation error of 0.55 rms radians at 50 incident photons, whereas TCoG gives an error of 0.9 rms radians for the same light level, or a similar error of 0.53 rms radians at double the light level, or 100 incident photons. In other words, WFPS and CC when compared with TCoG at 50 photons of incident light have a ∼40% less estimation error or the same error at half the light level. In the case of G-Tilt estimation for the same FoV of 16x16 pixels, the results of the same comparison around 50 photons of incident light are quite similar, with an improvement of ∼33% in estimation error or same performance at half the light level. When the FoV value is decreased, this improvement in estimation error also decreases. For example, at a FoV value of 10x10 pixels, the improvement is of a ∼20% for Z-Tilt estimation and of a ∼12% for G-Tilt estimation, at the same light level of 50 photons, for the WFPS algorithm with 10x10 2D-FFT's over the TCoG. We had already seen in point 4.2.1 that TCoG works better in smaller FoV's and WFPS calls for larger FoV's.

For low to moderate light levels such as in the examples just mentioned, detector noises are the main cause of tilt estimation error. Thresholding is an insufficient tool to fight against this type of noise in these light level scenarios. A cross-correlation previous to thresholding and centroid computation shows itself to be a good option to eliminate noise. WFPS, on its side, is also good at supressing noise at these light levels by smoothing the Fourier phase, as is illustrated in the example in point A.5.2, appendix A.

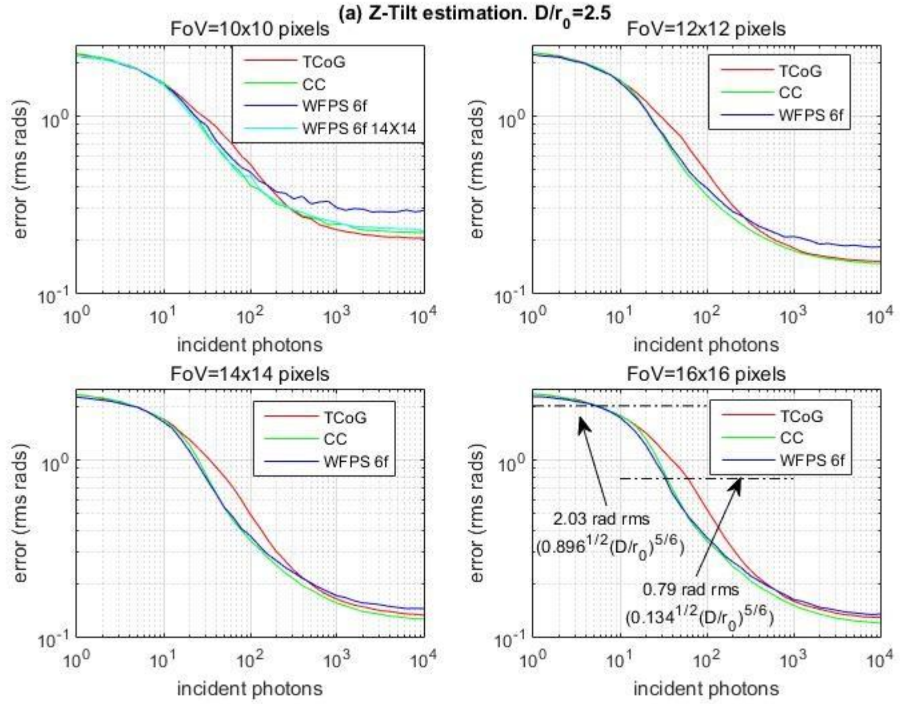

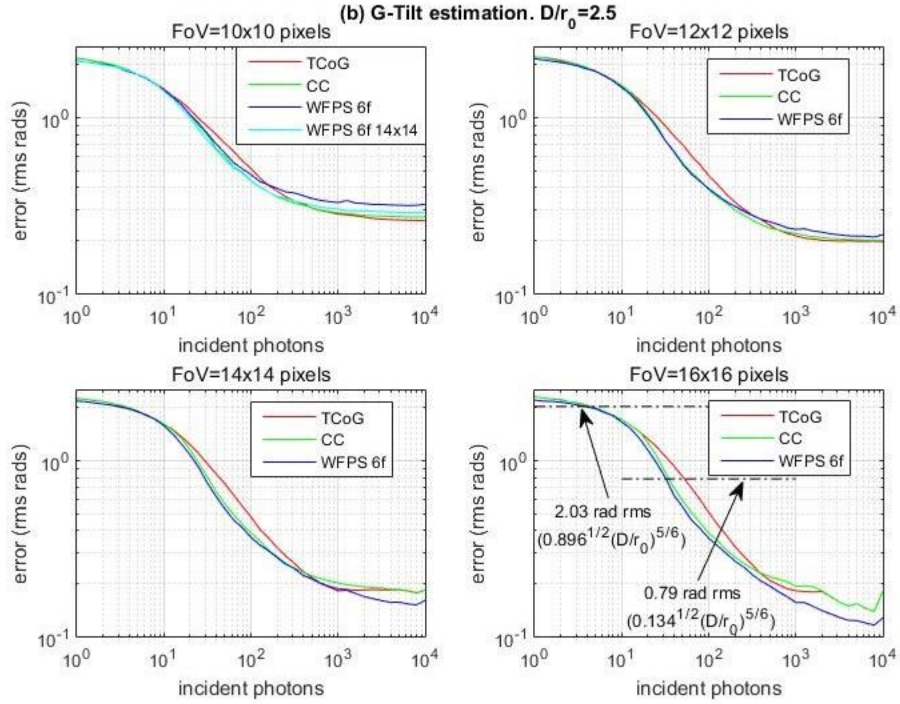

Figure 4-12. Tilt estimation error in r.m.s. radians at the sensing wavelength as a function of incident light level per subaperture in photons for the TCoG centroiding algorithm (red plots), CC centroiding algorithm (green plots) and WFPS centroiding algorithm with 6 spatial frequencies (blue plots). (a) is for Z-Tilt estimation with each subpanel for a different FoV: 10x10, 12x12, 14x14 and 16x16 pixels. (b) is for G-Tilt estimation, also with four subpanels for the same values of FoV as for the Z-Tilt estimation case. For the 10x10 pixels FoV case, a fourth algorithm corresponding to WFPS with 14X14 2D-FFT's and 6 spatial frequencies has been added, in cyan. D/r_0 is 2.5. Nyquist sampling. EMCCD gain for each light level is high without saturating a 14 bits detector. CIC is 0.05 e^-/pixel/frame. RON is 50 e^- rms.

For high light levels of 1000 to 10000 photons per subaperture, detector noises become less important, and measurement noise is dominated by spot's deformation due to high order turbulent phase modes, truncation due to limited FoV, and light shot (intrinsic Poisson) noise. Note in Figure 4-12 that, for these light levels, the tilt estimation errors are at most in the order of ~0.3 r.m.s. radians, or one twentieth of wavelength size, for the worst cases, and hence it can be stated that all the algorithms work fine in these scenarios. However, certain minor differences can be seen, and it is interesting to reflect on them because it throws light on the particularities of each algorithm.

For the Z-Tilt estimation in Figure 4-12(a), for the 10x10 pixels case, it can be seen that, for high light levels, the WFPS algorithm (blue trace) has a tilt estimation error of the order of ~0.3 r.m.s. radians, whereas CC (green trace) and TCoG (red trace) have errors in the order of ~0.2 r.m.s. radians, slightly higher for the CC algorithm. In this scenario, the dominating error cause is truncation of the spot due to limited FoV. It was seen in point 4.2 that for a D/r_0 ratio of 2.5, a minimum of 12x12 pixels FoV was necessary to adequately cope for the whole dynamic range of the signal. The reason for the CC and TCoG algorithms' better behaviour in this scenario is a powerful tool they have to estimate Z-Tilt over a truncated spot: thresholding. The Z-Tilt information is in the more symmetric part of the spot around its maximum, and thresholding is an adequate means to eliminate the low light level asymmetric part of the spot, including the effect of truncation due to limited FoV. WFPS, on its side, can deal with spot's truncation by employing a larger 2D-FFT size than the FoV. A fourth trace in cyan colour has been added to the figure for the 10x10 FoV case, corresponding to a WFPS algorithm employing 14x14 2D-FFT's, and selecting the six lowermost spatial frequencies. Note that this last trace gets confounded with the green trace of the CC algorithm. This improvement is explained because of the symmetrizing capacity of the WFPS algorithm over a spot right in the border of the FoV when a larger 2D-FFT is employed, as illustrated in the example in point A.5.3, appendix A.

Continuing with the Z-Tilt estimation case, as the FoV gets larger, and for high light levels, the behaviour of all algorithms is very similar. In this scenario, atmospheric turbulence high order modes dominate the noise. Thresholding is a good means of selecting the symmetric part of the spot, as was explained, and so this similarity in their behaviour is not surprising.

For G-Tilt estimation (Figure 4-12-b), high light levels and a FoV of 10x10 pixels, all the algorithms have a tilt estimation error around ~0.3 r.m.s. radians. The reason is that, in this case, for G-Tilt estimation, thresholding is not a good tool to employ against spot's truncation, because the G-Tilt information is precisely in the asymmetric part of the spot. The only means to improve this is increasing the FoV and letting this information in, as can be seen in the following subpanels for FoV's of 12x12, 14x14 and 16x16 pixels. Something that catches the attention is that the WFPS outperforms the other two when FoV increases (see the 16x16 FoV subpanel at light levels from 1000 to 10000 photons). The reason for this is a better capacity of the WFPS algorithm to reach a compromise between filtering out the detector noise which is still present and respecting the spot's asymmetries, whereas CC and TCoG cannot reach such a compromise by simple thresholding.

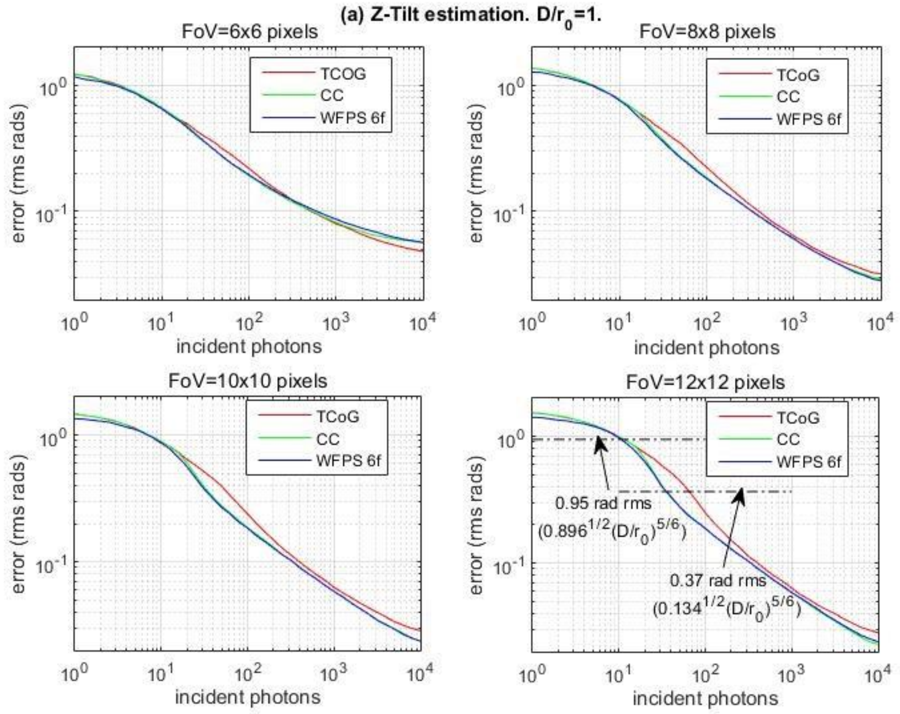

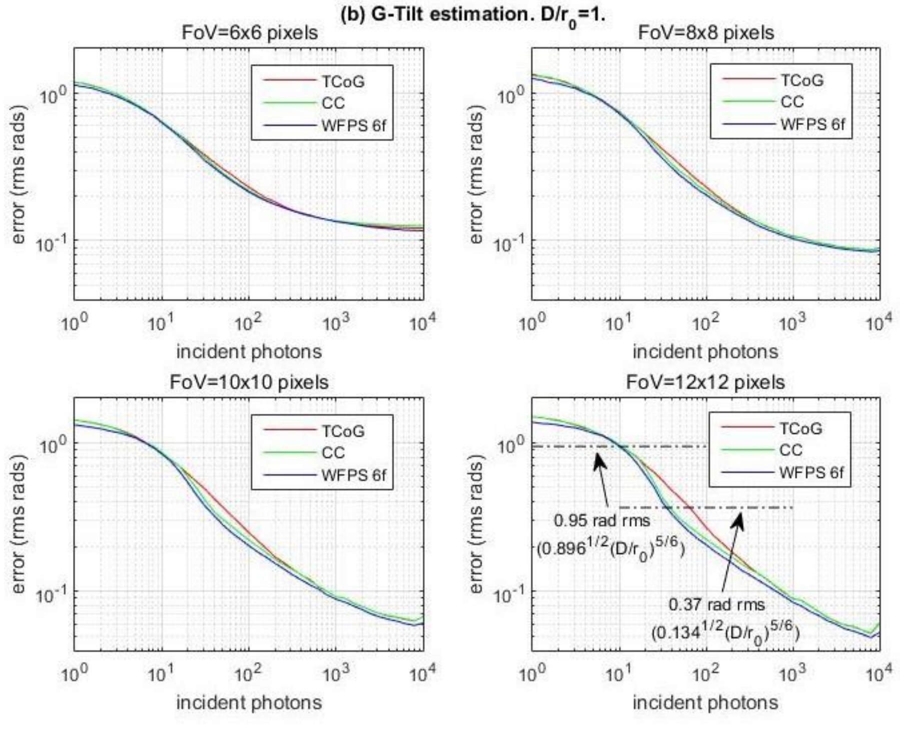

Figure 4-13. Tilt estimation error in r.m.s. radians at the sensing wavelength as a function of incident light level per subaperture in photons for the TCoG centroiding algorithm (red plots), CC centroiding algorithm (green plots) and WFPS centroiding algorithm with 6 spatial frequencies (blue plots). (a) is for Z-Tilt estimation with each subpanel for a different FoV: 6x6, 8x8, 10x10 and 12x12 pixels. (b) is for G-Tilt estimation, also with four subpanels for the same values of FoV as for the Z-Tilt estimation case. D/r_0 is 1. Nyquist sampling. EMCCD gain for each light level is high without saturating a 14 bits detector. CIC is 0.05 e^-/pixel/frame. RON is 50 e^- rms.

Straight lines corresponding to 2.03 and 0.79 rms radians have been added to the graph. 2.03 rms radians correspond to the energy in the tip and tilt modes in a turbulence following Kolmogorov statistics, when D/r_0 ratio is 2.5, according to the Noll coefficients derived in Noll, 1976. In the same reference, the remaining turbulent energy when tip and tilt are corrected can be found in the third Noll coefficient, and gives a value of 0.79 rms radians for the same D/r_0 ratio, being this a kind of fitting error at the subpupil level.

Figure 4-13 shows the results for a repetition of the previous simulation with the same system parameters values except that the D/r_0 ratio value is unity, and FoV's values are 6x6, 8x8, 10x10 and 12x12 pixels. It is interesting to see that, because the spot is less aberrated by atmospheric turbulence than in the previous $D/r_0=2.5$ case, all the considerations regarding spot's deformation and truncation, though still present, are much ameliorated. For the smallest FoV values the behaviour of the algorithms is quite indistinguishable, especially for G-Tilt estimation. When the FoV value increases, an improved behaviour can be seen in the CC and WFPS algorithms with respect to the TCoG algorithm for light levels between 20 and 200 photons, due to their robustness against detector noises, as was seen in for the $D/r_0=2.5$ case.

4.5. Effect of turbulence strength

Increase in turbulence strength has a twofold effect on tilt estimation in a subpupil of a SHWFS. First, when sensing the wavefront in an open loop configuration, the tilt dynamic range will increase, and a larger FoV will be required. A larger FoV implies more detector pixels and, hence, more measurement noise. Second, high order aberrations will be more pronounced, the spot will be further away from its diffraction shape and its energy disseminated among more pixels, all this making tilt estimation noisier.

The purpose of the present point is to show the results of a simulation that assesses the effect of turbulence strength in subpupil tilt estimation, for two centroinding algorithms: TCoG and WFPS with 6 spatial frequencies; CC algorithm, as was seen in point 4.4, has a behaviour almost identical to WFPS, in almost all system configurations simulated. As the turbulence strength increases, the FoV will be also increased in the simulation, as per shown in Table 4-8. Two light level regimes are considered for the purpose of FoV selection. When incident light level is 200 photons or below, the selected FoV is slightly smaller for the TCoG algorithm than for the WFPS algorithm. When light level is 300 photons or above, the FoV is larger than for the dimmer light level, and the same for both algorithms. The intention is to be as close as possible to the optimum field of view determined in point 4.2.1. For the D/r_0 ratios not studied in the mentioned point, FoV values have been approximately inferred from the corresponding to the studied D/r_0 ratios.

As regards the other system configuration parameters, they do not vary with respect to the previous simulations. Open loop observation is assumed, in a circular subpupil. D/r_0 ratio varies from 0.5, corresponding to a very well sampled pupil, or a very good turbulence scenario, to 3. Above a ratio of 3, the overall correction that the system can achieve from the recovered phase modes becomes too low. Sampling of the spot follows the Nyquist criteria, that is, FWHM of the spot at diffraction limit is 2 pixels. Simulated QE of the detector is 97%, and the EMCCD gain is as high as possible without saturating a 14 bits detector. CIC noise is 0.05 e$^-$/pixel/frame, and RON is 50 r.m.s. e$^-$.

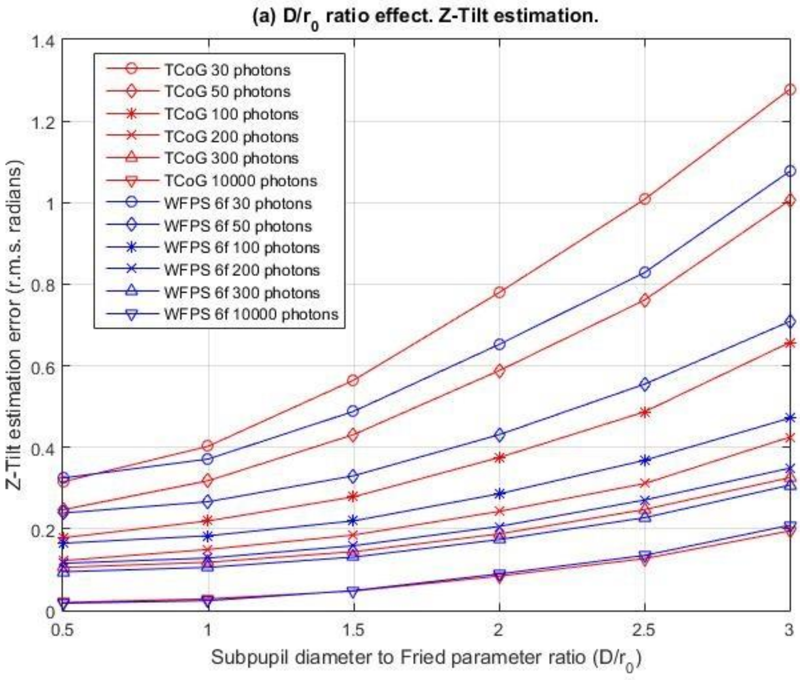
(a) D/r$_0$ ratio effect. Z-Tilt estimation.

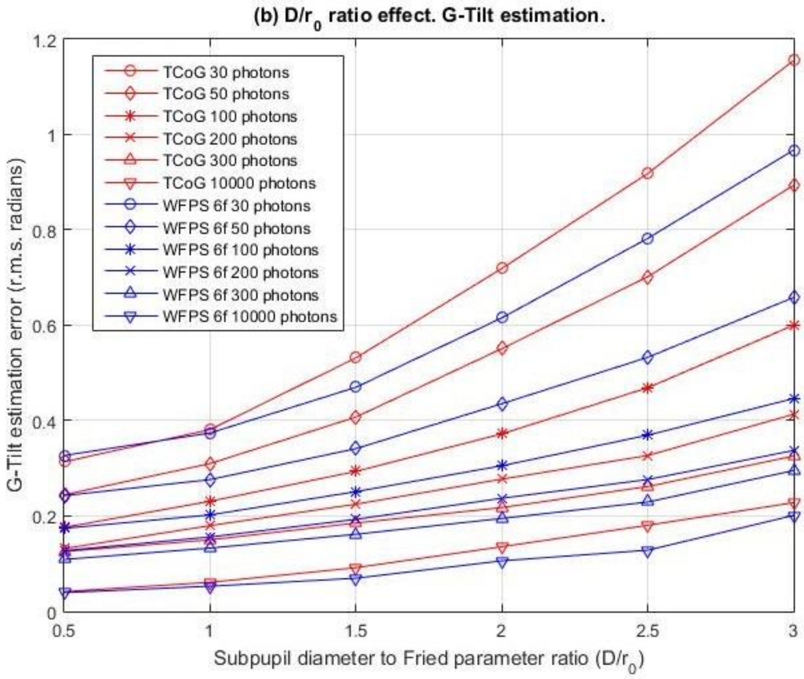
(b) D/r$_0$ ratio effect. G-Tilt estimation.

Figure 4-14. Tilt estimation error in r.m.s. radians as a function of subpupil diameter to Fried parameter ratio (D/r$_0$) for incident light levels of 30, 50, 100, 200, 300 and 10000 photons and two centroiding algorithms: TCoG and WFPS with 6 spatial frequencies selected. FoV values are as per Table 4-8. (a) is for Z-Tilt estimation. (b) is for G-Tilt estimation. Nyquist sampling. QE is 97%. EMCCD gain for each light level is high without saturating a 14 bits detector. CIC is 0.05 e$^-$/pixel/frame. RON is 50 e$^-$ rms.

Employed FoV (pixels x pixels) for turbulence strength effect assessment							
		D/r₀					
#photons per subaperture		***0.5***	***1***	***1.5***	***2***	***2.5***	***3***
200 and below	***TCoG***	6x6	6x6	8x8	10x10	12x12	14x14
	WFPS 6f	8x8	8x8	10x10	12x12	14x14	16x16
300 and above	***TCoG*** ***WFPS 6f***	12x12	12x12	14x14	14x14	16x16	16x16

Table 4-8. Employed FoV in pixels by pixels for the assessment of the effect of turbulence strength, the results of which are illustrated in Figure 4-14.

Figure 4-14 shows the result of the simulation. Tilt estimation error is plotted versus the D/r_0 ratio for the two mentioned algorithms and light levels of 30, 50, 100, 200, 300 and 10000 photons per subaperture. Red traces are for the TCoG algorithm and blue traces are for the WFPS algorithm. (a) subpanel is for Z-Tilt estimation and (b) is for G-Tilt. All the graphs, especially the ones for 30, 50 and 100 photons, clearly indicate that WFPS algorithm permits to operate at worse turbulence strength scenarios for a particular performance assessed by tilt estimation error. For example, at a 100 photons light regime, performance with the WFPS algorithm at a particular D/r_0 ratio is similar to the performance with the TCoG algorithm at a 0.5 smaller D/ r_0 ratio. If, for example, the system requires a maximum tilt estimation error at subpupil level of 0.4 r.m.s. radians, which is approximately ~λ/15 (at the sensing wavelength), and the subaperture diameter is 40 cm, for the TCoG algorithm the Fried paramenter r_0 should not go much below 20 cm, whereas for the WFPS algorithm it can go as low as 16 cm, for a light regime of 100 photons.

4.6. Closed-loop operation simulation

So far, all simulations in this chapter have assumed that the system works in open loop correction and, so, the atmosphere is sensed in its full dynamic range, without any correction. In the present point, closed loop system correction is assumed. As explained in point 1.2.1 and illustrated in Figure 1-2, in closed loop operation, the corrective deformable mirror comes in the optical path before the wavefront sensor, and so, the latter senses a corrected wavefront. For a SHWFS, this means that the spot corresponding to each subaperture will stay near the set-point reference when the correction is good. Therefore, at a subpupil level, closed loop operation can be simulated by attenuating the tip and tilt modes by a correction factor. In the present point, an attenuation factor of 10 has been employed for all scenarios. This implies that the assumption is made that the servo correction is independent of such variables as measurement noise, image size or computational cost. Moreover, system instabilities are not being taken into account, even when the wavefront measurement is dominated by noise. These assumptions are justified because the present simulations do not intend to assess the closed loop behaviour of the system, but just to compare the performance of several centroiding algorithms when the system geometry has been adequated to closed loop operation.

The main modification in the simulation workflow with respect to the open loop scenario is the attenuation of the tip and tilt modes when generating the phase frames. As seen in point 4.1.1, a unitary matrix U relates Zernike coefficients with Karhunen-Loève coefficients, as in [Eq. 4-10], or equivalently the Zernike base with the Karhunen-Loève base, as in [Eq. 4-12]. Inspection of such matrix reveals that the Zernike tip and tilt modes are identical to the first two Karhunen-Loéve modes with an error in amplitude of 0.05%. Hence, tip and tilt attenuation has been achieved by simply dividing the two first Karhunen-Loéve coefficients by the desired attenuation factor. The result is a spot that hardly moves away from the centre of the FoV, but still gets aberrated by the high order atmospheric modes.

As regards the FoV selection, no optimum FoV study has been done, as in the case of open loop simulation. However, the spot changes in time have been visually inspected and a FoV has been selected that copes with the spot's deformations most of the time.

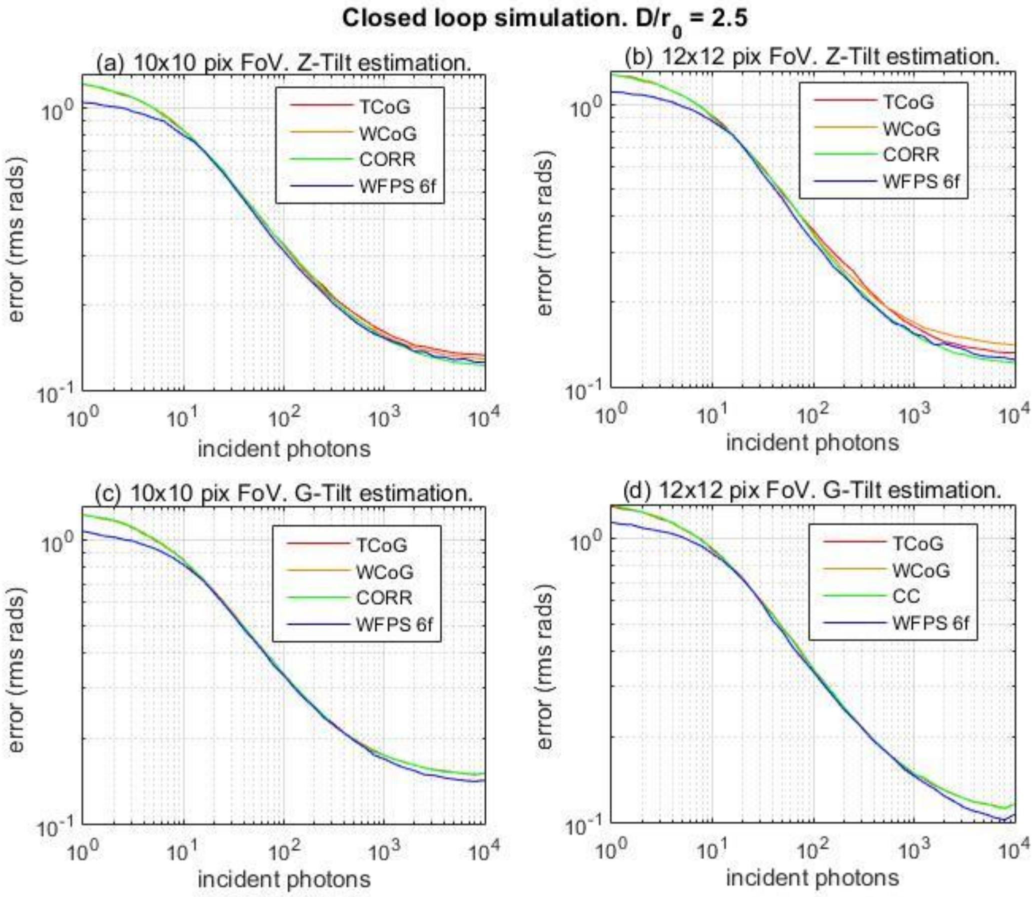

Figure 4-15. Simulation of tilt estimation in a circular subaperture for closed loop operation and D/r_0=2.5. Estimation error in rms radians as a function of incident photons for Z-Tilt estimation and a 10x10 pixels FoV (a), Z-Tilt estimation and a 12x12 pixels FoV (b), G-Tilt estimation and a 10x10 pixels FoV (c), and G-Tilt estimation and a 12x12 pixels FoV (d), for the TCoG algorithm (red traces), WCoG algorithm (orange traces), CC algorithm (green traces) and WFPS algorithm with 6 spatial frequencies (blue traces). Nyquist sampling. QE is 97%. EMCCD gain for each light level is high without saturating a 14 bits detector. CIC is 0.05 e^-/pixel/frame. RON is 50 e^- rms.

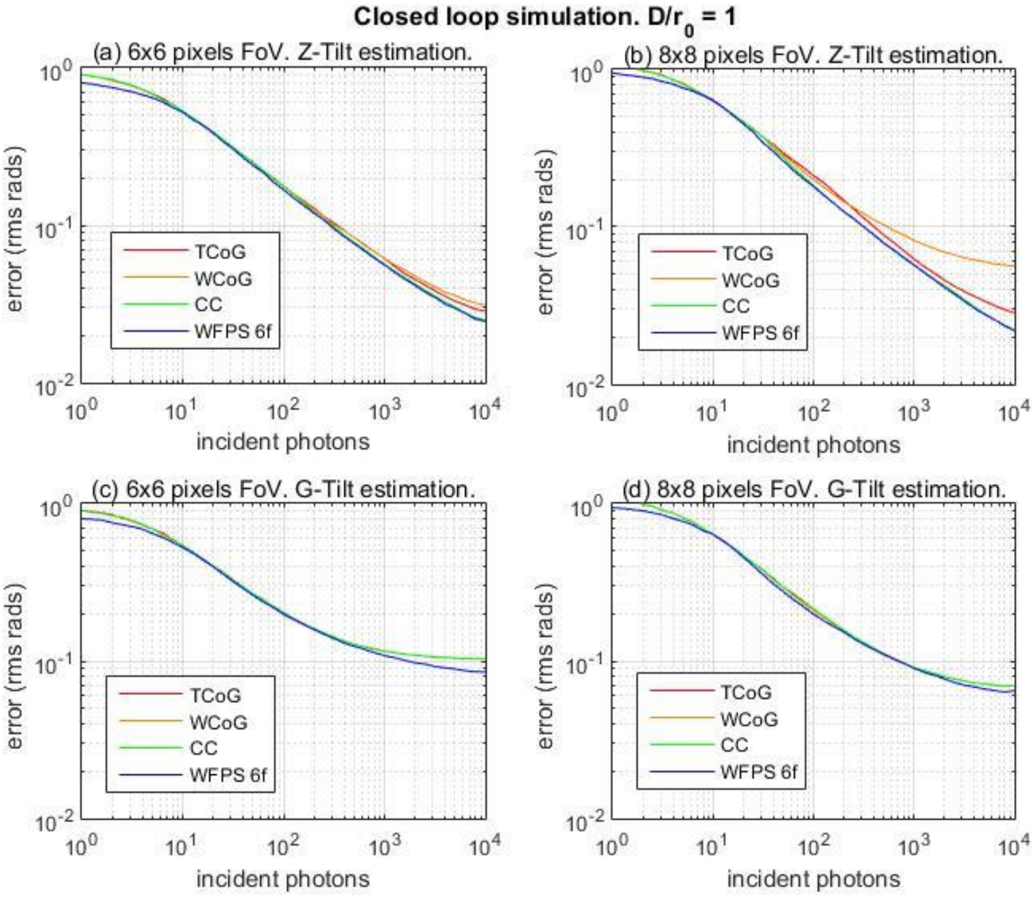

Figure 4-16. Simulation of tilt estimation in a circular subaperture for closed loop operation and D/r₀=1. Estimation error in rms radians as a function of incident photons for Z-Tilt estimation and a 6x6 pixels FoV (a), Z-Tilt estimation and a 8x8 pixels FoV (b), G-Tilt estimation and a 6x6 pixels FoV (c), and G-Tilt estimation and a 8x8 pixels FoV (d), for the TCoG algorithm (red traces), WCoG algorithm (orange traces), CC algorithm (green traces) and WFPS algorithm with 6 spatial frequencies (blue traces). Nyquist sampling. QE is 97%. EMCCD gain for each light level is high without saturating a 14 bits detector. CIC is 0.05 e^-/pixel/frame. RON is 50 e^- rms.

Figure 4-15 show the result of tilt estimation error in r.m.s. radians for the sensing wavelength as a function of incident photons per subaperture, for a closed loop scenario with $D/r_0=2.5$. Selected FoV's are 10x10 and 12x12 pixels, and for each FoV both Z-Tilt and G-Tilt have been estimated, making up a total of four subpanels labelled from (a) to (d). In each case, four algorithms have been simulated: TCoG (red traces), WCoG (orange traces), CC (green traces) and WFPS with 6 spatial frequencies (blue traces). WCoG algorithm, which was explained in point 1.4.1.2, has been added as an algorithm which is appropriate for closed loop operation when weights are kept fixed in the FoV. Width of the Gaussian weights are optimized by minimizing the tilt estimation error of the sequence of images under study. Figure 4-16 shows the same kind of results for a scenario with $D/r_0=1$ and selected FoV's of 6x6 and 8x8 pixels.

As a general conclusion extracted from these results, there is hardly any difference in performance between the simulated algorithms for the most common light level regimes, from 10 to 1000 photons. The reduced number of pixels involved implies a reduced amount of detector noise, and the simple TCoG is sufficient to get a near optimum performance. As the spot does not move much from the centre of the FoV, the effect of an evenly distributed noise across the FoV is small, and the WFPS algorithm tends to give high weight values to the zero spatial frequency, thus getting near a CoG algorithm.

On the other hand, the selected FoV's are small enough and sufficient, and this can be seen in the estimation error for high light level conditions: for Z-Tilt estimation there is not much change with increased FoV, whereas for G-Tilt estimation there is a slight, small improvement when FoV increases, as more of the spot's "skirt" is captured.

4.7. Square subaperture

Manufacturers offer both circular and square shaped microlenses arrays. So far, the simulations in this chapter have assumed a circular shaped subaperture. In this point, results are shown of an assessment of the applicability of the WFPS algorithm to the case of a square shaped microlens.

Zernike functions are in principle defined for a circular aperture. The simulation method of Kolmogorov phase frames as explained in point 4.1.1 has the Zernike coefficients' covariance matrix for Kolmogorov turbulence as a starting point, and this assumes a circular aperture in the system. In order to simulate Kolmogorov turbulence as seen from a square subaperture, first a turbulent phase in a circular subaperture has been simulated, and then a square shaped piece of that phase has been selected, as shown in Figure 4-17.

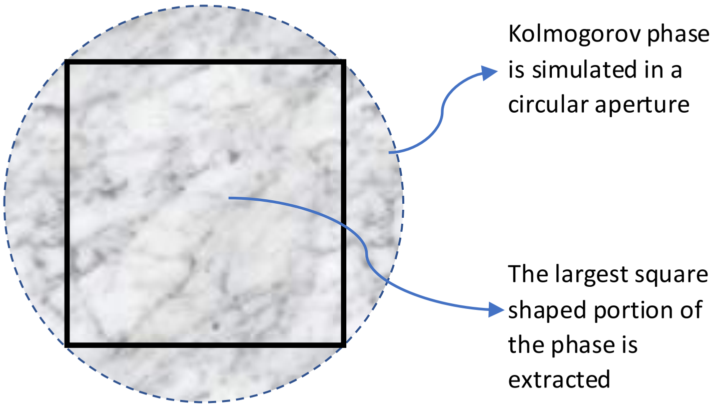

Figure 4-17. The largest square shaped portion of the Kolmogorov circular phase is extracted to simulate a square subaperture.

From the square shaped phase thus obtained, an image in the focal plane of the microlens is derived as explained in point 4.1.2. All the exposed formulation in the mentioned point is valid for a square subaperture, taking into account that *D* is the side of the square and that N_p is the number of pixels of phase corresponding to the length of *D.*

Another necessary issue to consider when the aperture is square in shape is the definition of Zernike tilt, which is in principle dependent upon the Zernike tip and tilt modes defined in a circular aperture. The equivalent modes for a square subaperture are a horizontally inclined plane and a vertically inclined plane over the square, which we may call Z_2^{SQR} and Z_3^{SQR}, respectively. If ϕ^{SQR} is the square shaped phase extracted from the circular shaped phase ϕ,

(a) Square subpupil. D/r_0=2.5. Z-Tilt estimation.

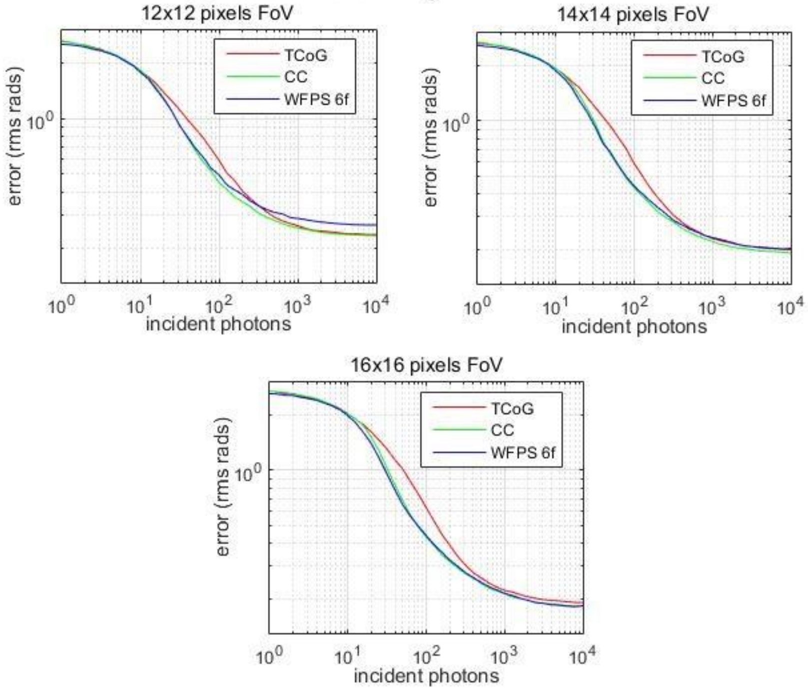

(b) Square subpupil. D/r_0=2.5. G-Tilt estimation.

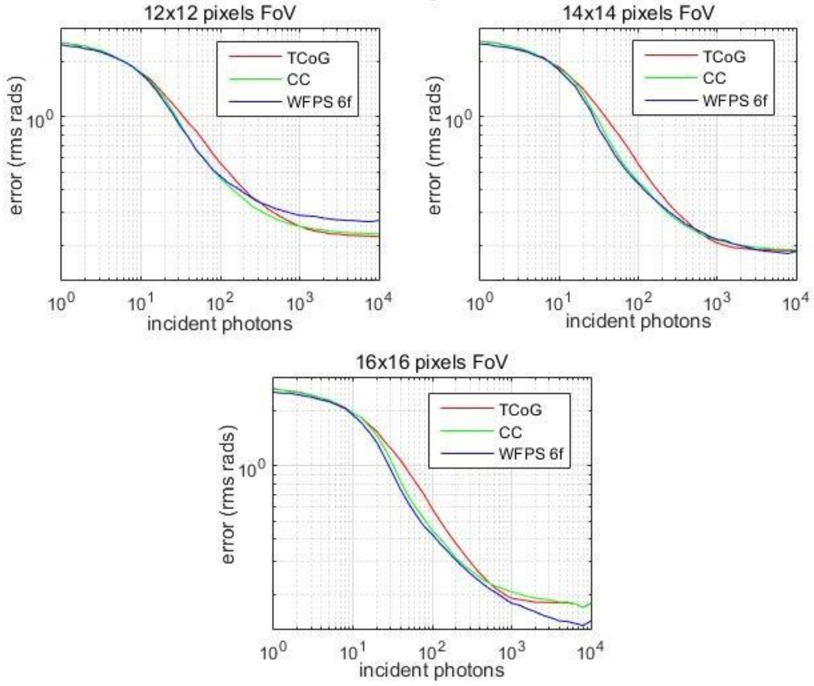

Figure 4-18. Tilt estimation error in r.m.s. radians as a function of the number of incident photons in the subaperture, for a square shaped subaperture, with D/r_0=2.5 (D is the square side). (a) is for Z-Tilt estimation and (b) is for G-Tilt estimation. FoV's under study are 12x12, 14x14 and 16x16 pixels, and the simulated algorithms are TCoG, CC and WFPS with 6 spatial frequencies. Nyquist sampling of the spot. Detector's QE is 97%. EMCCD gain is high, without saturating a 14 bits detector. CIC is 0.05 e^-/pixel/frame. RON is 50 e^- r.m.s.

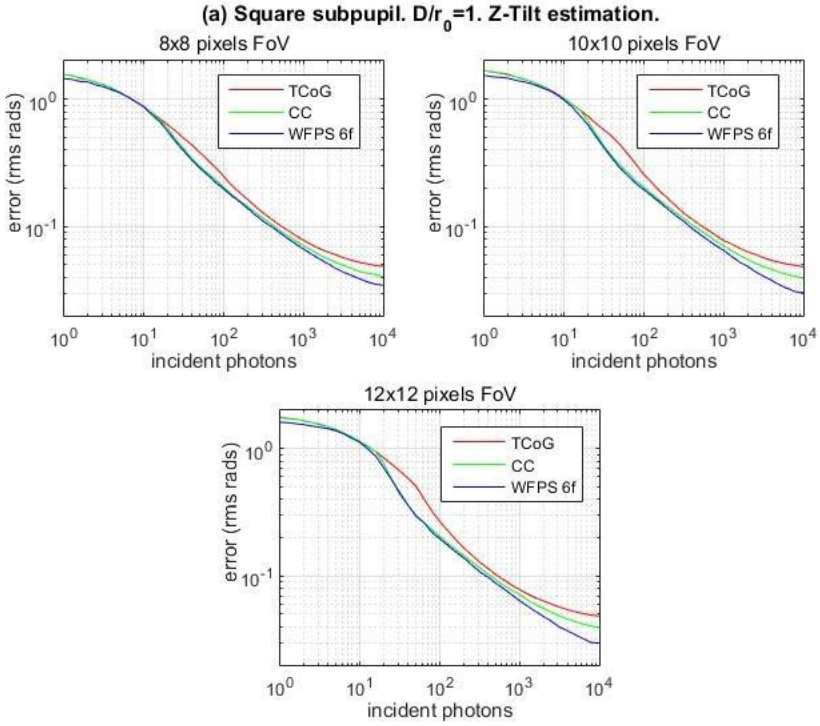

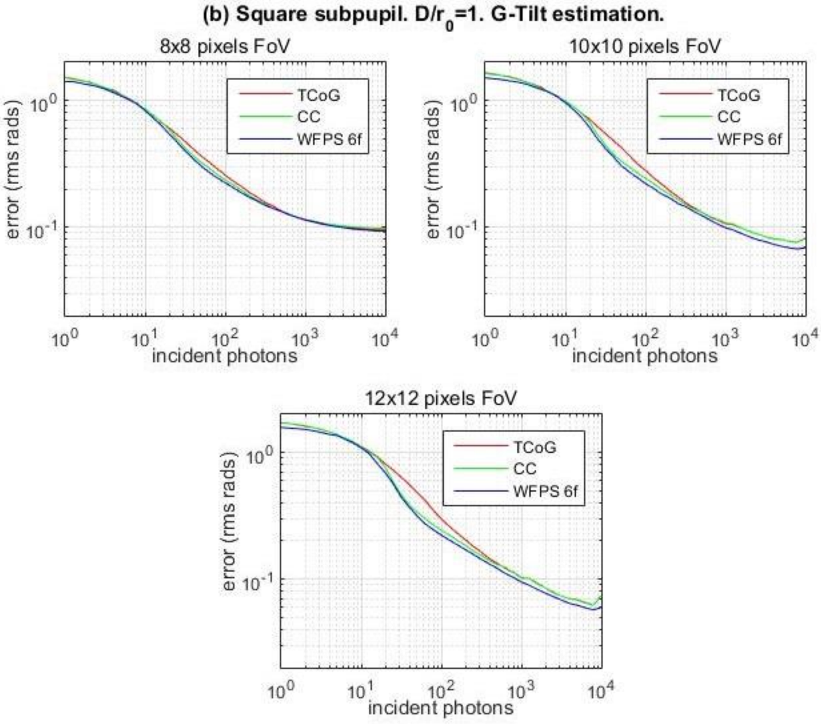

Figure 4-19. Tilt estimation error in r.m.s. radians as a function of the number of incident photons in the subaperture, for a square shaped subaperture, with D/r$_0$=1 (D is the square side). (a) is for Z-Tilt estimation and (b) is for G-Tilt estimation. FoV's under study are 8x8, 10x10 and 12x12 pixels, and the simulated algorithms are TCoG, CC and WFPS with 6 spatial frequencies. Nyquist sampling of the spot. Detector's QE is 97%. EMCCD gain is high, without saturating a 14 bits detector. CIC is 0.05 e$^-$/pixel/frame. RON is 50 e$^-$ r.m.s.

then the coefficients which quantify the amount of tip and tilt in the square aperture can be calculated by orthogonal projection of ϕ^{SQR} over Z_2^{SQR} and Z_3^{SQR}, as in [Eq. 4-26]:

$$c_2^{SQR} = \frac{\iint \phi^{SQR} \cdot Z_2^{SQR} dxdy}{\iint Z_2^{SQR} \cdot Z_2^{SQR} dxdy}$$

$$c_3^{SQR} = \frac{\iint \phi^{SQR} \cdot Z_3^{SQR} dxdy}{\iint Z_3^{SQR} \cdot Z_3^{SQR} dxdy} \quad \text{[Eq. 4-26]}$$

c_2^{SQR} and c_3^{SQR} would be the coefficients of an expansion of ϕ^{SQR}over a set of orthogonal functions in the square subaperture, with tip and tilt represented by Z_2^{SQR} and Z_3^{SQR}.

As for the r.m.s. tip and tilt values related to the c_2^{SQR} and c_3^{SQR} coefficients, these can be calculated as:

$$\Delta\phi_{rms}^{SQR}\big|_{horiz} = c_2^{SQR} \left[\frac{1}{S^{SQR}} \iint Z_2^{SQR} \cdot Z_2^{SQR} dxdy\right]^{1/2}$$

$$\Delta\phi_{rms}^{SQR}\big|_{vert} = c_3^{SQR} \left[\frac{1}{S^{SQR}} \iint Z_3^{SQR} \cdot Z_3^{SQR} dxdy\right]^{1/2} \quad \text{[Eq. 4-27]}$$

with S^{SQR} being the area of the square subaperture. These are the true tilt r.m.s. values to be compared with the r.m.s. recovered tilt values from the image's displacement and obtained from [Eq. 4-25].

When comparing the images at focal plane corresponding to a square subpupil and a circular subpupil with the diameter length equal to the square subpupil's side, the most evident difference is that a cross shaped spot comes out of the square subpupil, whereas the spot for the circular subaperture is circularly symmetric. Second, more light passes through the square subaperture, approximately a 25% more. And third, more turbulence is seen through the square subaperture, leading to a more aberrated spot.

Figure 4-18 shows the results of the tilt recovery error in r.m.s. radians as a function of incident photons per subaperture for image sequences obtained from a square shaped subpupil. The ratio of subaperture side to Fried parameter is $D/r_0=2.5$. Open loop sensing is assumed. Spot's sampling follows Nyquist criterion and, so, FWHM at diffraction limit is 2 pixels wide. FoV's under study are 12x12, 14x14, and 16x16 pixels. The applied centroiding algorithms are TCoG (red traces), CC (green traces) and WFPS with six spatial frequencies (blue traces). Panel (a) is for Z-Tilt estimation and panel (b) is for G-Tilt estimation. The detector's gain and noise parameters are as for the rest of simulations in this chapter.

A very similar behaviour of all the algorithms to the circular subpupil case (section 4.4) can be seen. For low to moderate light levels, detector noise dominates and the spot's shape is unimportant. Errors are somewhat higher than for the circular subpupil case for the three algorithms at a particular light level, most probably because of the increase in higher order turbulent aberrations, but this gets compensated for the most common light levels by the fact that more light gets through the square subpupil. Tilt estimation improvement of CC and

WFPS algorithms over the TCoG algorithm for light levels from 20 to 200 incident photons is very similar to the circular subpupil case. For example, for the 16x16 pixels FoV case and for 50 incident photons, CC and WFPS commit an error of ∼0.65 rms radians when estimating Z-Tilt, which is in the order of one tenth of the sensing wavelength, whereas TCoG's error is in the order of ∼1 rms radian for the same light level, or the same error at double the light level, or 100 incident photons. Error estimation improvement at 50 photons is, therefore, of ∼35%. Very similar figures can be seen for the G-Tilt estimation.

MAP weights for the WFPS algorithm are also very similar to the circular subpupil case for low to moderate light levels, thus indicating that detector noise dominates. For high light levels above 500 photons, weights are more concentrated at zero spatial frequency than for the circular subpupil case, probably because of the increased spot's aberration. At these light levels, the three algorithms have a similar tilt estimation error. For the case of 16x16 pixels FoV and G-Tilt estimation, WFPS outperforms the other two, because it can better take into account the assymetries of the spot in the presence of noise, same as happened in the circular subpupil case.

Figure 4-19 shows the results of an identical simulation when reducing the D/r_0 ratio to unity and the FoV's to 8x8, 10x10 and 12x12 pixels. As it was seen for the circular subpupil case, the three algorithm's performances tend to get closer to each other, especially for the lowest FoV case of 8x8 pixels. For the larger FoV's and light levels of 20 to 200 incident photons, an improvement of tilt estimation for CC and WFPS algorithms as compared to the TCoG algorithm can be seen, which can reach a ∼40% for 12x12 pixels FoV and Z-Tilt estimation at 50 incident photons. At high light levels, performance of the three algorithms is again very similar to each other and to the circular subpupil case.

4.8. Conclusions of this chapter

The Weighted Fourier Phase Slope algorithm has been characterized and compared to other commonly used algorithms such as TCoG and CC for open loop wavefront sensing and also to WCoG for closed loop wavefront sensing.

It has been seen that the selection of the lowermost six spatial frequencies in the WFPS algorithm is a good compromise between tilt estimation performance and computational cost, thus leading to a hardware speed requirement of one order of magnitude less than for the CC algorithm implemented in the Fourier domain (this last issue was seen in section 3.3, point 3.3.5). Further increasing the number of spatial frequencies leads to only a slight improvement in tilt estimation performance.

The required linearity when observing in open loop configuration is equally good for WFPS, CC and TCoG algorithms when the selected FoV spans the tilt's full dynamic range. When the FoV is shortened, TCoG and CC increase their threshold values in order to overcome the spot's truncation effect over the tilt estimation. WFPS algorithm does not have this advantage, unless a thresholded variation of it is implemented. However, it can overcome the spot's truncation and reach a similar tilt estimation performance than the other two algorithms by employing larger 2D-FFT's than the size of the FoV.

As regards sensitivity in low to moderate light level conditions, CC and WFPS algorithms, while being very similar to each other, outperform the TCoG algorithm for light levels between 20 and 200 photons for typical values of detector's gain and CIC and RON noises. Simple thresholding finds itself to be limited in the simultaneous presence of turbulence high order aberrations and non-Gaussian type of detector's noise, such as amplified CIC noise, for the mentioned light levels. By prefiltering with a correlation such as in the CC algorithm or by smoothing the phase in the Fourier domain such as in the WFPS algorithm, more robust centroiding algorithms are achieved in the presence of the mentioned measurement noises. As the selected or required FoV is increased, this tilt estimation performance difference between the CC and WFPS algorithms on one side and the TCoG algorithm on the other side become increasingly evident, as more FoV means more detector pixels and, hence, noise. In this respect, both CC and WFPS algorithms, at the mentioned light levels, prefer to work with larger FoV's than the TCoG algorithm, and are able to cope with worse turbulence scenarios, maintaining tilt estimation performance.

For high light levels, the three algorithms perform equally as tilt estimation error is concerned. An exception is the case of large FoV's and G-Tilt estimation, where the assymetries of the spot, contained in its low light level portion, are required to be taken into account, in the presence of noise. Here, the WFPS outperforms the CC and TCoG algorithms, because its mechanism to supress noise does not use thresholding the image at any moment.

In closed loop wavefront sensing, the required FoV is rather small as the spot is kept fixed at the reference set-point. The amount of noise in this scenario is therefore small, and the four studied algorithms (WCoG was added) perform in a very similar manner as regards tilt estimation.

Finally, an evaluation of the performance of TCoG, CC and WFPS algorithms for open loop sensing through a square shaped subaperture was made, showing a very similar behaviour as seen in the circular shaped subaperture.

Chapter 5. Numerical simulations at an entire pupil level

There are two main sources of measurement error in a Shack-Hartmann Wavefront Sensor, as it was explained in point 1.2.2.2. First, tilt estimation is affected by measurement noise in each subpupil, due to the detector's noises, pixelation, limited FoV and turbulence high order aberrations. This is the measurement error at the subpupil level and was the object of study in the previous chapter. Second, a limited number of subpupils implies a limited number of phase modes recovered, and a consequent fitting error in the estimated phase. This second source of error works at the entire pupil level, and becomes the dominant measurement error when tilt estimation at the subpupil level is good. The purpose of the present chapter is to assess the effect of varying the centroiding algorithm at the subpupil level on the global performance of the SHWFS at the entire pupil level, thus including the fitting error in the simulation.

The selected tool for this purpose is the Object Oriented Matlab toolbox for Adaptive Optics (OOMAO, Conan and Correia, 2014). Results are presented as Strehl Ratio (SR) or Encircled Energy (EE) of the system PSF as a function of star magnitude, for a particular system configuration and centroiding algorithm, after compensation with the estimated phase at the entire sensor pupil.

5.1. The Object Oriented Matlab Adaptive Optics toolbox

The OOMAO toolbox is a freely available[11] extension of the Matlab™ language, consisting of a library of Matlab classes oriented towards the numerical modelling of AO systems. Figure 5-1 shows the OOMAO class diagram with the objects disposed as in a closed-loop controlled system. It has been taken from Conan and Correia, 2014, and shows a complete set of classes corresponding to an advanced stage of development of the tool. The OA system is created by selecting and instantiating objects from the available classes, initializing and configuring them, and assembling them throughout an optical path. The main classes used during a simulation are:

---

[11] It is downloadable at https://github.com/rconan/OOMAO, as of May, 2017.

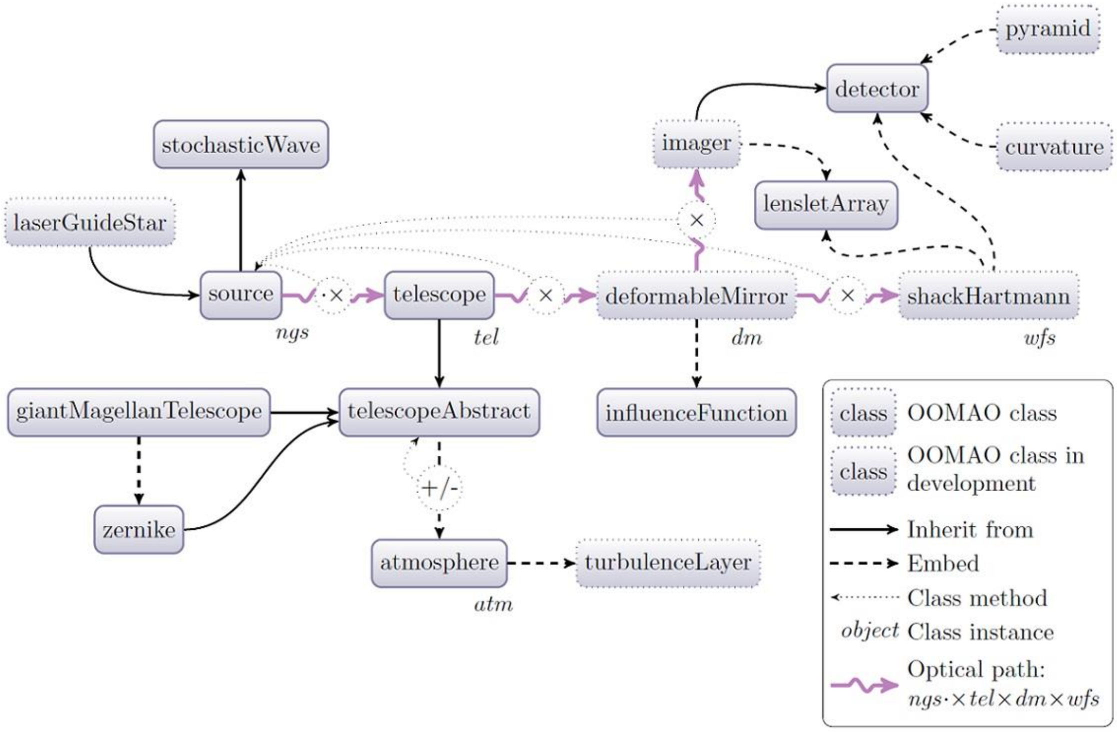

Figure 5-1. OOMAO class diagram, from Conan and Correia, 2014.

- *source*: It can be a single source or an asterism, and a NGS or a LGS. It inherits from the *stochasticWave* class the properties of *amplitude* and *phase* of an optical wave, which is propagated through the optical system with the use of the overloaded Matlab operators .× and ×.
- *telescope*: It contains properties such as the aperture size, central obscuration size, and spatial and temporal resolution of the system. It is a child of the *telescopeAbstract* class, which embeds an *atmosphere* class instance in order to create the complete optical system which precedes the AO sensing and corrective components.
- *atmosphere*: The atmospheric phase aberration as a function of time is created in this class. It embeds one or more *turbulenceLayer* instances, each with a user defined height and wind speed and direction.
- *deformableMirror*: The compensation of the atmospheric phase is implemented here. This object has not been used in the present work. A z*ernike* object has been used instead in order to subtract a user defined number of Zernike modes from the propagating wave.
- *shackHartmann*: This class implements the Shack-Hartmann wavefront sensor. Its properties are related to the phase recovery at each subpupil and at the whole pupil as well. For example, the selected centroiding algorithm and the values of its associated parameters such as the TCoG threshold are found in this class, as well as matrixes that relate phase gradients in the subpupils with phase values in the subpupils' corners for a Fried geometry sensor. Since a SHWFS is composed basically

of a lenslet array and a detector, two classes can be found embedded in the *shackHartmann* class:

  - *lensletArray*: Properties such as the number of lenslets, number of detector pixels per lenslet and percentage of light as a criterion to include the subpupils in the borders, define the objects in this class. Lenslets are square shaped. By default, the images at the detector are Nyquist sampled, i. e., the FWHM is 2 pixels wide. This can be changed to any desired width by the *nyquistSampling* property in this class.
  - *detector*: The main task of this class is to add photonic noise to the light, add a background light, apply a quantum efficiency and add the readout noise.
- *imager*: This class implements the generation of the final turbulence compensated PSF as seen by the science detector. It is actually a child of the *detector* class, and also embeds an instantation of the *lensletArray* class to generate a 1 x 1 lenslet array. It contains properties that allow to define the starting and ending times of light integration, as well as methods that calculate the Strehl Ratio and Encircled Energy[12] over the PSF.

This tool was selected for the whole SHWFS simulation without dedicating much effort to investigating, comparing and selecting among other tools, mainly because its free cost and the possibility of reusing Matlab code that was programmed for the simulations at the subpupil level. Very strong points that could be observed in its design characteristics are its modularity due to the object-oriented programming, a vectorised code in line with Matlab's good programming practice, and Matlab's parallel computing capabilities usage. The only weak point to mention is the lack of detailed code documentation, probably because it is a tool under development yet.

5.1.1. Features added to the OOMAO in the context of the present work

Some features were added to the *shackHartmann* and its embedded classes *lensletArray* and *detector*, necessary to achieve the desired simulation results. These have been the following:

- The possibility of defining a circular subpupil array has been added to the *lensletArray* class. The public properties *subpupilShape* and *circularSubpupilRadius* have been added, that allow to select between a square shaped and a circular shaped subpupil, and define a radius size in pixels for the circular shaped case. A private property called *circularSubpupilMask* is used as a mask in the Fraunhoffer image generation at the *propagateThrough* method. It is calculated in the *setCircularSubpupilMask* method, which is called when the number of pixels per lenslet is defined.

  No significant differences were found in the simulation results between circular and square shaped subpupils, and so the results for circular subpupils will not be shown.

- The gain and noise model of an EMCCD camera, as explained in point 4.1.3, has been added to the *detector* class through the properties *emccdGain* and *CICNoise*. The CIC

---

[12] The Encircled Energy calculation was not implemented at the time the author downloaded the toolbox.

noise is like a background light with Poisson distribution; it is not affected by the quantum efficiency, and it is amplified by the EMCCD gain. The EMCCD gain is implemented through a gamma distribution, as expressed in equation [Eq. 4-20]. Both items are applied to the image before adding readout noise. In the final offset subtraction, the mean value of background light, affected by the quantum efficiency and the EMCCD gain, is subtracted; and the mean CIC noise affected only by the EMCCD gain is subtracted as well.

- The correlation centroiding algorithm has been implemented in the *shackHartmann* class. The correlation reference is the diffraction limited image, and is set with the *setCorrelationReference* method, which should be called after propagating a planar wavefront to the SHWFS. The correlation is executed in the Fourier domain, in the *dataProcessing* method, where the rest of centroiding algorithms are to be found. A thresholding can be applied to the correlation figure, through the *correlationThreshold* public property, and finally a centre of gravity is applied to the thresholded correlation figure.
- The Weighted Fourier Phase Slope algorithm has been implemented in the *shackHartmann* class, at the *dataProcessing* method. Public properties *wfpsWeightsX* and *wfpsWeightsY* have been included to contain the Bayesian weights at the working spatial frequencies for the horizontal and vertical centroids calculation, respectively.
- An encircled energy computation function has been implemented, where the input parameters are the PSF, wavelength, pupil diameter, Nyquist sampling factor, total amount of light at the pupil and a vector of circle diameters in arcsecs, and the output is the EE as a function of the specified circle diameters.

Figure 5-2 shows three samples of the SHWFS detector's images created with the OOMAO for a 20 x 20 square subpupils configuration in a 4.2 m. circular aperture with a central obscuration of an 8.4% of the aperture's surface and Nyquist sampling. This will be the working configuration throughout the simulations presented in this chapter. The first panel, labelled (a), is for the case of a planar wavefront, a FoV of 10 x 10 pixels, which for a source wavelength of 550 nm. is a ~2.7" FoV, a very brilliant star of zero magnitude and no noise sources. In the second panel, labelled (b), the star magnitude is 11. For the default optical throughput of unity, this means ~31.5 incident photons per subpupil at a system frequency of 500 Hz. Atmospheric turbulence has been added, with a Fried parameter of 21 cm, which is equal to the subpupil side size. Poisson photon noise has been enabled; a quantum efficiency of 97% and an EMCCD gain of 1000 have been applied; and a CIC noise of 0.05 e^-/pixel/frame and a RON noise of 50 rms e^- have been added. RON noise is not actually visible in the figure. The spurious visible noise corresponds to the CIC noise which, when amplified by the EM register, reaches habitual pixel peak values in the order of ~3000 – 5000 digital counts for the default detector sensitivity of 1 e^-/ADU, thus becoming noticeable against the spots' peak values of ~5000 – 10000 digital counts. In the third panel, labelled (c), the FoV has been increased to 14 x 14 pixels, corresponding to a ~3.8" FoV, in order to cope with the increase in turbulence strength corresponding to a Fried parameter of 8.4 cm, 2.5 times smaller than the square subpupil's side size. The spots are visibly more diffused and the image gives a global appearance of being noisier for the same amount of incident light and added noise.

The main purpose of Figure 5-2 is to illustrate the importance of an appropriate detector gain and noise model. The EMCCD gain is a stochastic process that contributes, together with the atmospheric turbulence and Poisson noise, to deform the spots. Moreover, the effect of the spurious CIC noise cannot be modelled with an additive normal noise, such as is done for RON.

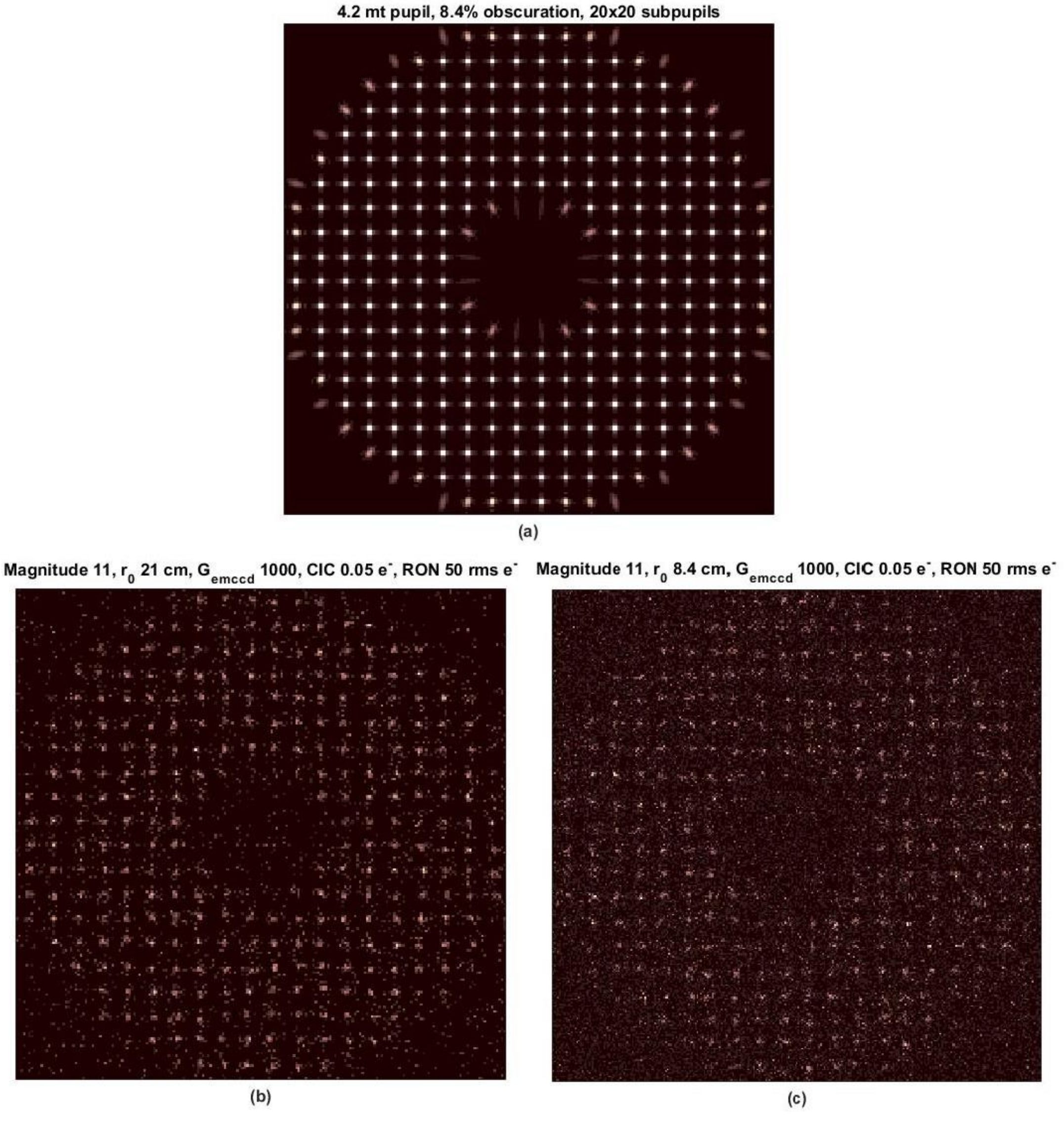

Figure 5-2. Samples of SHWFS images created with the OOMAO for a 20 x 20 square subpupils configuration in a 4.2 m circular aperture with an 8.4% central obscuration. (a) Without any kind of noise, planar wavefront and magnitude 0 star. (b) For a magnitude 11 star, Fried parameter of 21 cm, EMCCD gain of 1000, CIC noise of 0.05 e^-/pixel/frame and RON of 50 rms e^-. (c) Same as in (b), for an 8.4 cm Fried parameter.

5.1.2. The simulation workflow

With a very similar symbology as in Figure 5-1, Figure 5-3 illustrates the core of the simulation workflow employed for the evaluation of the effect of the different centroiding algorithms over the SHWFS performance at the whole pupil level using the OOMAO toolbox.

There are two optical paths that share a *telescope* instance with a 4.2 m. pupil diameter size and an 8.4% of central obscuration. The *telescope* instance embeds an *atmosphere* instance, which is initialized and configured following a model used in several examples included in the toolbox: a three-layer model with 0, 5 and 12 km. altitude and fractional r_0's of 0.5, 0.3 and 0.2, respectively; wind speeds are 10, 5 and 20 m/s, and wind directions are 0, π/2 and π. The system frequency has been set to 500 Hz.

Each optical path has its own source. The one labelled *ngs* represents the Natural Guide Start and its light ends up in the *shackHartmann* object. The second one, labelled *science*, represents the scientific object of interest and its light ends up in the *imager* object through a *zernike* object. Both light sources are set to the default wavelength of 550 nm, and therefore the sensing system performance evaluation is made at the WFS sensing wavelength.

The SHWFS observes the full dynamic range of the atmosphere, as in an open loop configuration. The *shackHartmann* object is configured to have a matrix of 20 x 20 square shaped lenslets, and only the subpupils with a minimum of 85% of light with respect to the most illuminated one are considered for the phase recovery computation. Sampling of the spots follows the Nyquist criterion. The number of detector pixels per lenslet has been set to 10 x 10 for the case of a 21 cm r_0, making up a ~2.7" FoV, and 14 x 14 for the case of an 8.4 cm r_0, making up a ~3.8" FoV. As regards the detector model, a QE of 97% has been applied; since star magnitudes under study are over 7.5, an EMCCD gain value of 1000 has been applied, unless otherwise stated; CIC noise has been set to 0.05 e^-/pixel/frame, and RON to 50 rms e^-. The sensitivity of the detector is the default 1 e^-/ADU. It is through the *shackHartmann* properties that the centroiding algorithm is selected: Thresholded Centre of Gravity, Correlation or Weighted Fourier Phase Slope.

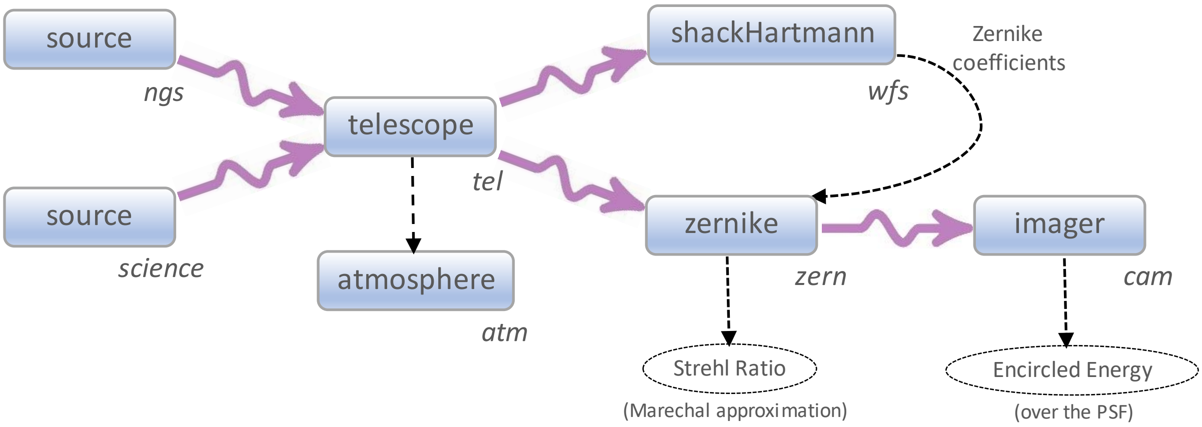

Figure 5-3. Core of the simulation workflow programmed in the OOMAO for the assessment of the effect of the centroiding algorithms at a pupil level.

At the other optical path, an *imager* object receives a compensated wavefront. The corrector element is a *zernike* object that receives the corrective Zernike coefficient values from the *shackHartmann* instance. This correction is applied with the same spatial resolution in the pupil as the one defined in the *telescope* and *shackHartmann* objects, i.e., the number of lenslets multiplied by the number of detector pixels per lenslet. After this correction, the final

Strehl Ratio can be easily calculated by the Marechal approximation, even before the computation of the PSF. An average residual phase is computed for this purpose, by integrating during a period of 4 seconds.

Finally, the *imager* object receives the wavefront with the residual phase, and integrates 200 frames with a temporal sampling period of 20 ms to compute the system PSF. Sampling is four times finer than the Nyquist criterion, i.e., the FWHM of the PSF at diffraction limit is 8 pixels wide. The selected FoV is 50 times the FWHM at diffraction, 1.35" or 400 pixels, for the 21 cm r_0 case, and 125 times the FWHM at diffraction, 3.38" or 1000 pixels, for the 8.4 cm r_0 case, in order to span a ~95% of the PSF energy. By knowing the total light energy at the whole pupil, the Encircled Energy as a function of circle diameter in arcseconds can be computed over the PSF.

A study was conducted to determine the most appropriate phase recovery method among the offered by the OOMAO toolbox. As explained in point 1.3.2, the OOMAO toolbox offers zonal and modal methods for phase recovery. Two zonal methods were studied and compared: the Least-Square Minimum Norm (LSMN) and the Linear Minimum Mean Square Error (LMMSE) methods (see point 1.3.2.1). The LMMSE method consistently gave better phase estimation results, with a ~40% error improvement when fitting error dominates, i.e., for high SNR, and so was selected as the zonal method of preference. Moreover, this zonal method apparently outperforms the modal methods for situations with enough light, say ~50 photons or more per subpupil. This assessment is not actually reliable from the point of view of the author, because phase estimation is optimized (and, consequently, phase errors are minimized) only at the subpupil corners for a zonal phase recovery and Fried geometry SHWFS, and therefore the performance assessment at such a discretized pupil cannot be extrapolated to the whole pupil. A better, more reliable assessment is done through a modal phase recovery method, which allows for an evaluation with an arbitrarily large resolution over the whole pupil.

The OOMAO offers several ways of phase recovery as a function of Zernike modes. The methods that rely on the pseudo-inversion of matrixes that relate phase or phase slopes with modes (see point 1.3.2.2) consistently gave better estimation results than the methods that rely on the orthogonal projection of the phase or phase slopes over the modes or modes slopes, because the discretized modes are not actually orthogonal over the discretized pupil. So, orthogonal projection methods were disregarded, and the two modal phase recovery methods which were studied are based on pseudo-inversion as explained in point 1.3.2.2. The first one, described by [Eq. 1-25], employs two pseudo-inversions: one to recover phases from phase slopes[13], and the other to recover modes from phases. The second one, described by [Eq. 1-24], directly recovers modes from phase slopes through a single pseudo-inversion. When there are more than ~50 incident photons per subaperture for the TCoG algoritm or more then ~30 photons per subaperture for the CC and WFPS algorithms, the first method ([Eq. 1-25]) performs better. When there is less light, then the second is the method of choice ([Eq. 1-24]). As regards the optimal number of Zernike modes to recover, it seems to depend

---

[13] For this first step, zonal LMMSE method was employed.

only on the lenslet pitch, and not on the size of the central obscuration. For a 20 x 20 lenslet array, the optimal number of modes is around 110 to 140, usually somewhat lower for the first method ([Eq. 1-25]) and higher for the second ([Eq. 1-24]), within the mentioned range. Only a slight decreasing tendency in the optimal number of modes was observed when light goes below 25 photons per subpupil.

5.2. Effect of estimating G-Tilt or Z-Tilt over the final PSF

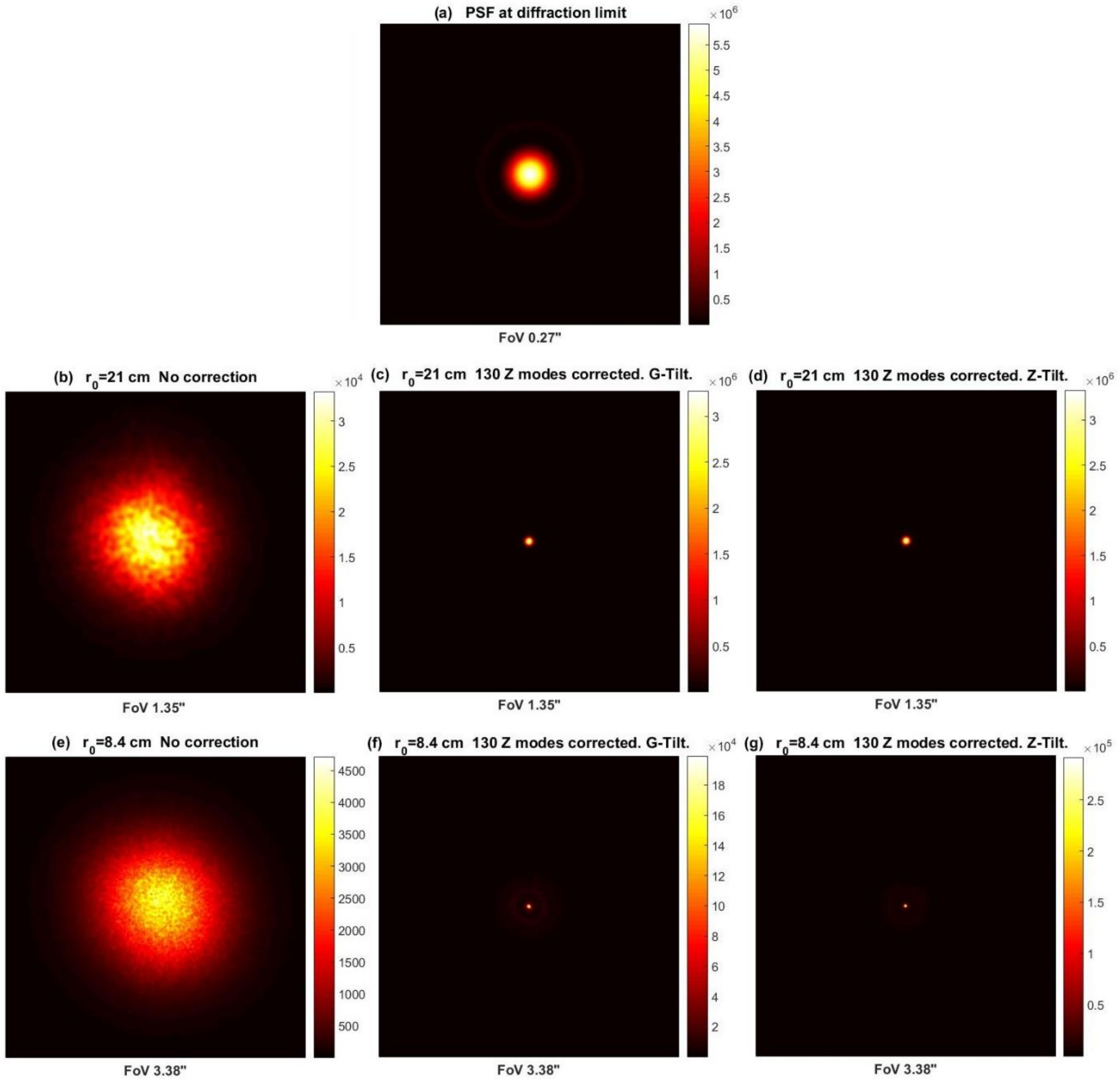

Figure 5-4. 2D plots of the system PSF for a 4.2 m aperture with 8.4% central obscuration, 20x20 square subapertures, 500 Hz system working frequency and 200 frames integration spanned through 4 seconds. (a) is the PSF at diffraction limit spanning a 0.27” FoV. For the 21 cm r_0 case, a FoV of 1.35” is shown in panels (b) for no correction, and (c) and (d) for a correction of 130 Zernike modes after estimating G-Tilt or Z-Tilt at the subpupil level, respectively. Panels (e), (f) and (g) show 3.38” of FoV for an 8.4 cm r_0 case without turbulence compensation and compensating 130 Zernike modes out of G-Tilt and Z-Tilt estimation at subpupil level, respectively. The centroiding algorithm has been WFPS with 6 spatial frequencies involved. NGS and science object magnitudes are both 5. QE at the SHWFS is 97%; EMCCD gain is 50; CIC noise is 0.05 e^-/pixel/frame and RON is 50 rms e^-.

Throughout chapter 4 it was seen that the WFPS algorithm can be tuned to estimate both Z-Tilt and G-Tilt at the subpupil. When estimating G-Tilt for bright guide stars (or abundant light at subpupil level) and when the FoV is large enough to cope with the spot's tilt movements and high order aberrations, WFPS outperforms the two centroiding algorithms used for a comparison purpose, the CC and the TCoG, thanks to its capacity to overcome noise without thresholding the image. As for Z-Tilt estimation for high light level, the three algorithms perform similarly; the WFPS may need to employ larger 2D-FFT's than the FoV if the latter is small. The present point shows results of a test aimed to assess the effect of estimating G-Tilt or Z-Tilt at the subpupil level over the final corrected PSF, using the OOMAO tool.

PSF's have been obtained for a system with a 4.2 m aperture and 8.4% central obscuration, 20 x 20 square subapertures, a NGS and a science object both with magnitude 5 and 500 Hz of working frequency. They are represented in 2D format in Figure 5-4. Light level from the NGS at the subpupil is ~8000 incident photons per system light integration period; hence, it is a very high light level situation. The phase recovery method is the two-step modal method: first a zonal LMMSE estimation of phases and then a modal estimation through a pseudo-inverted Zernike modes matrix. The centroiding algorithm is the WFPS involving 6 spatial frequencies and tuned to estimate either G-Tilt or Z-Tilt at the subpupil. The detector's parameters at the SHWFS have been set to a 97% QE, a 50 EMCCD gain, a 0.05 e^-/pixel/frame of CIC noise and a 50 rms e^- RON noise. PSF's are obtained by integrating 200 frames separated from each other by 20 msegs., spanning a total of 4 seconds of integration. Panel (a) shows a diffraction limited PSF within a ~0.27" FoV, ~10 times the diffraction limited FWHM at a 550 nm wavelength. For the 21 cm r_0 case, a 10 x 10 pixels FoV is selected at the SHWFS which, for a Nyquist sampling, is a ~2.7" FoV. At the *imager* object, a ~1.35" FoV is selected, ~50 times the FWHM at diffraction limit. Panels (b), (c) and (d) show the no correction case, and the 130 Zernike modes corrected cases out of G-Tilt and Z-Tilt estimation, respectively. For the 8.4 cm r_0 case, a 14x14 pixels FoV is selected at the SHWFS, corresponding to a ~3.8" FoV at Nyquist sampling. Panels (e), (f) and (g) show the obtained PSF's for no turbulence compensation, and 130 Zernike modes correction out of G-Tilt and Z-Tilt estimation, respectively, within a ~3.38" FoV, ~125 times the diffraction limited FWHM. Figure 5-4 is useful to verify that the correction is good, and the phase recovery method, number of modes, selected FoV's, integration times, etc., are correct. However, it does not allow to properly appreciate the differences in the corrected PSF's out of G-Tilt and Z-Tilt estimations, which are apparently equivalent in the figure.

Figure 5-5 shows horizontal cuts of the corrected PSF's for the 21 cm r_0 case (a) and 8.4 cm r_0 case (b) out of Z-Tilt estimations (blue traces) and G-Tilt estimations (violet traces); ordinate scale is logarithmic, representing image counts normalized with respect to the peak at diffraction limit, which, at the peak, is actually the achieved Strehl Ratio; abscissa spans the central 0.27" of the PSF, which is ~10 times the diffraction limited FWHM. The difference in Z-Tilt and G-Tilt over a circular aperture leads to a tilt difference variance of $0.241(d/r_0)^{5/3}$ rads^2 (taken from Thomas et al, 2006), meaning that it is greater for worse turbulence conditions, and this is applicable to square apertures also. This is why the difference between PSF's is more appreciable in panel (b) for the 8.4 cm r_0 case than in panel (a) for the 21 cm r_0 case.

The first and most obvious difference is that Z-Tilt estimation at subpupil level leads to a higher SR at the system corrected PSF. The achieved SR's are, for the 21cm r_0, 56.3% for Z-Tilt estimation and 55.4% for G-Tilt estimation. The difference is much bigger and evident in the figure for an 8.4 cm r_0: 4.93% for Z-Tilt as compared to a 3.39% for G-Tilt. The best fitting plane approximating a given wavefront in the least square error sense corresponds to the Z-Tilt. The minimization of the phase error at a subpupil level is extrapolated to the pupil level and, applying for example Marechal's approximation ([Eq. 1-10]), this implies a higher SR.

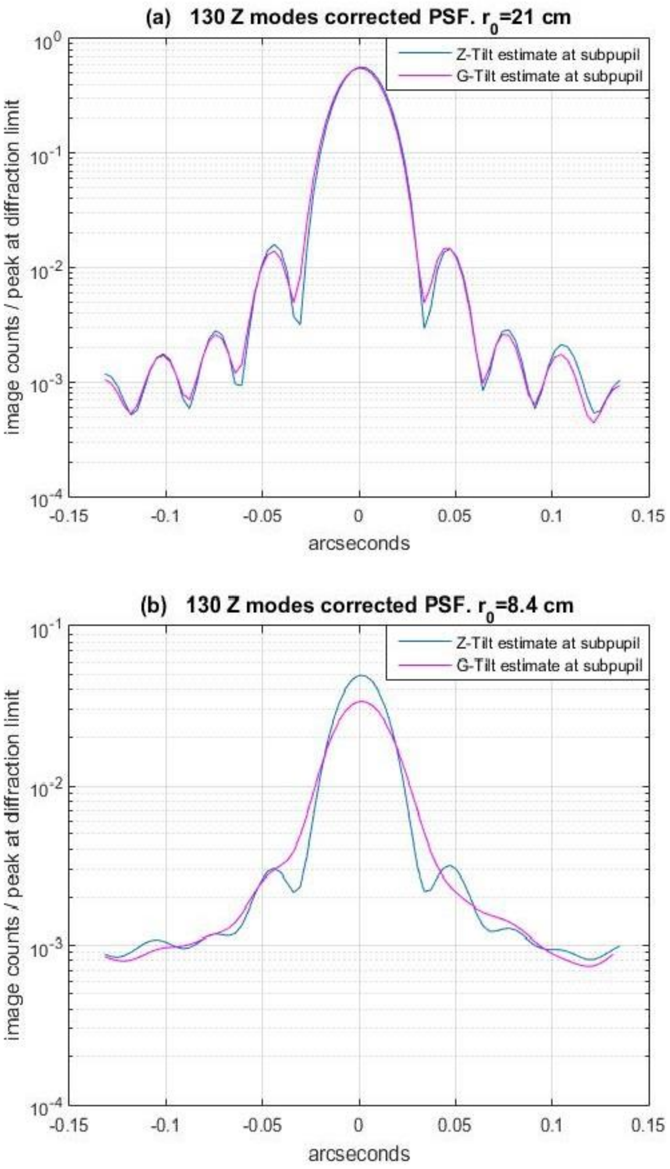

Figure 5-5. Horizontal cuts of the corrected PSF's in Figure 5-4. (a) is for the 21 cm r_0 case. (b) is for the 8.4 cm r_0 case. Blue traces are for Z-Tilt estimation at subpupil level and violet traces are for G-Tilt estimation at subpupil level. Ordinate coordinate represents image counts normalized with respect to the peak at diffraction limit.

The second difference that catches the attention is that Z-Tilt leads to more defined secondary lobes in the PSF, whereas G-Tilt leads to a smoother type of PSF shape (at least in the central represented zone), as seen more clearly in panel (b). This could imply a better Encircled Energy characteristic for PSF's obtained out of G-Tilt estimation at the subpupil level.

Figure 5-6 shows Encircled Energy graphs as a function of spanned FoV for the PSF’s represented in Figure 5-4. Diffraction limited (black traces), uncorrected (red traces) and corrected out of G-Tilt estimation (violet traces) and Z-Tilt estimation (blue traces) cases are represented, for the 21 cm r_0 case (panel “a”) and 8.4 cm r_0 case (panel “b”).

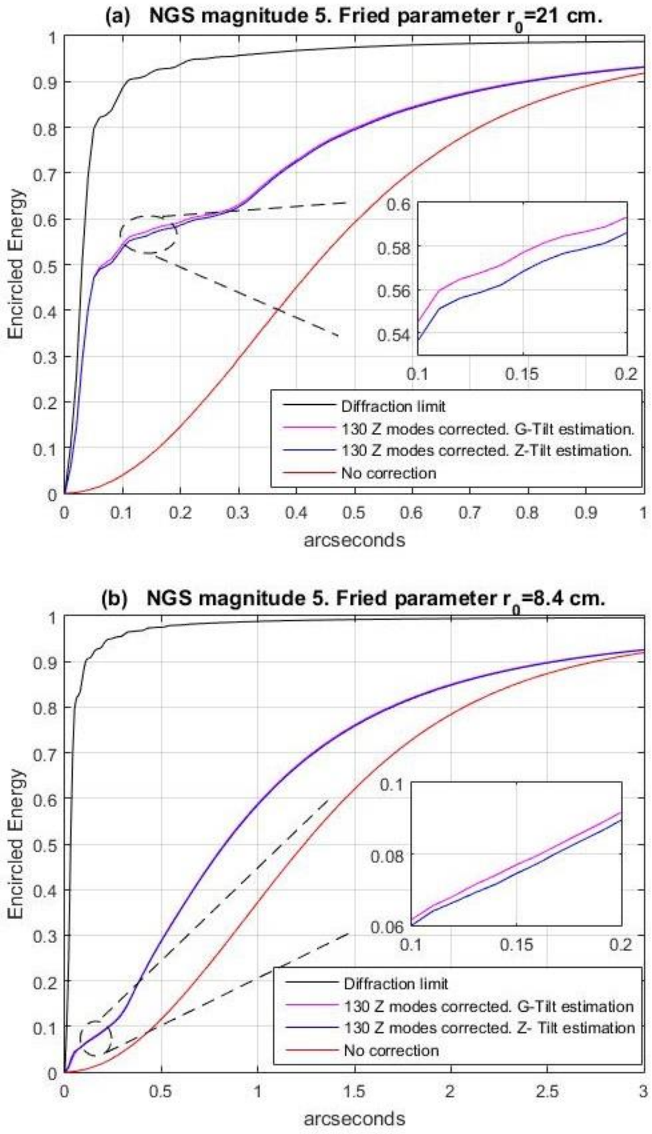

Figure 5-6. Encircled Energy graphs obtained from the PSF’s in Figure 5-4. (a) is for the 21 cm r_0 case. (b) is for the 8.4 cm r_0 case. Black traces correspond to the diffraction limited case. Violet traces and blue traces are for G-Tilt and Z-Tilt estimation at the subpupil level, respectively. Red traces are for the uncorrected PSF’s.

For both turbulence conditions, and for greater than 50 miliarcsecs FoV’s, EE is higher for the turbulence compensated PSF obtained out of G-Tilt estimation at the subpupil level than for the one obtained out of Z-Tilt estimations. The difference reaches a ∼1% for the 21 cm r_0 case, and ∼0.25% for the 8.4 cm r_0. It seems that centering the spots at each subpupil according to a mean phase gradient (G-Tilt) rather than minimizing the phase quadratic error (Z-Tilt) leads to more final PSF’s energy concentrated in less space, though the difference is very modest.

From these results, the decision is taken to estimate Z-Tilt at the subpupil level when looking for SR results at the whole pupil level, and to estimate G-Tilt at the subpupil level when looking for EE results at the whole pupil level.

5.3. Strehl Ratio as a function of NGS magnitude

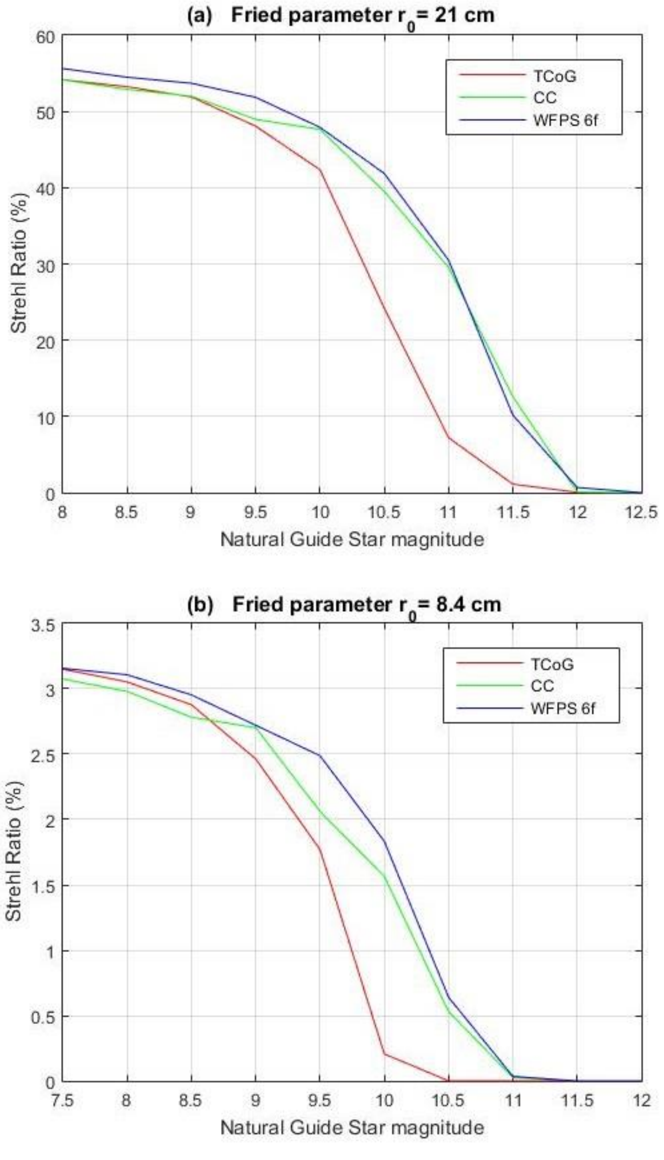

Figure 5-7. Strehl Ratio in percentage units obtained by Marechal's approximation as a function of star magnitude for two atmospheric conditions: (a) 21 cm r_0 and (b) 8.4 cm r_0; and three centroiding algorithms: TCoG (red traces), CC (green traces) and WFPS with 6 spatial frequencies (blue traces). System's aperture is 4.2 m wide, with a central obscuration of 8.4%. Optical throughput is the default unity. SHWFS has 20 x 20 square subapertures and a ~2.7" FoV in (a) or ~3.8" FoV in (b) with Nyquist sampling. Phase recovery is modal with optimal method and number of modes selected for each star magnitude.

When studying and comparing the sensitivity of the various selected centroiding algorithms in the previous chapter, for example in section 4.7 for square shaped subapertures, the conclusion was reached that WFPS and CC outperform TCoG for light levels around 20 to 200 photons, the former having for example the same performance at ∼60 incident photons as the latter at 100 incident photons. At that point, the performance was assessed and conclusions were reached only at a subpupil level, without considering the global fitting error at the pupil level. In the present section, results are shown in Figure 5-7 of achieved Strehl Ratios after turbulence compensation at the whole pupil as a function of the NGS magnitude.

The system configuration keeps on being the one studied in the previous sections: a 4.2 m aperture with 8.4% central obscuration and 20 x 20 square subapertures for wavefront sensing. NGS wavelength is 550 nm and optical throughput is unity. Light integration period is determined by the system working frequency of 500 Hz. The range of 200 to 20 incident photons per subpupil corresponds to NGS magnitudes of ∼9 to ∼11.5. For the results corresponding to a 21 cm Fried parameter r_0, shown in panel (a), the SHWFS's FoV is ∼2.7" or 10x10 pixels at Nyquist sampling, whereas for the 8.4 cm r_0 in panel (b), the FoV is ∼3.8" or 14x14 pixels at Nyquist sampling. The three centroiding algorithms under study are TCoG (red traces), CC (green traces) and WFPS involving six spatial frequencies (blue traces), all tuned to estimate Z-Tilt at the subpupil. Phase recovery at the whole pupil is modal and uses matrix pseudo-inversion. The two-step method (slopes to phases and phases to modes) is used for light levels over 50 photons per subpupil (over NGS magnitude 10.5) for the TCoG algorithm and for light levels over 30 photons per subpupil (over NGS magnitude 11) for the CC and WFPS algorithms. For lower light levels, the one step method (modes directly from slopes) is used. The number of recovered modes is allowed to vary and an optimal value is taken, ranging from 110 to 140, predominating the value of ∼130 optimal number of Zernike modes. The SHWFS's detector parameters are, as usual, a 97% QE, an EMCCD gain of 1000, a 0.05 e^-/pixel/frame CIC noise and a 50 rms e^- RON. Finally, Strehl Ratios[14] are computed through Marechal approximation, without the need of obtaining a PSF.

Results in Figure 5-7 are in very good coincidence with the conclusions obtained in chapter 4 where comparisons were made at a subpupil level. First of all, CC and WFPS algorithms show a similar sensitivity behaviour, outperforming the TCoG algorithm by allowing to work with higher NGS magnitudes for a particular performance level evaluated as a Strehl Ratio. Second, the range of NGS magnitudes for which CC and WFPS show this improvement in phase estimation goes from ∼9 to ∼12 for 21 cm r_0, which corresponds to ∼200 to ∼12 photons per subpupil, and from ∼8.5 to ∼11 for 8.4 cm r_0, corresponding to ∼300 to ∼30 photons per subpupil. This is again in good coincidence with the results at subpupil level. And third, when measurement noise at subpupil level dominates, i.e., when SR decays for higher NGS magnitudes, the difference in NGS magnitude between the TCoG and the WFPS algorithms for a particular performance is ∼0.6 to ∼0.7 for most of the light level range, corresponding to a linear factor of ∼1.7 to ∼1.9 in light level, which is again in accordance with the results seen at the subpupil level.

---

[14] Note that this is a Strehl Ratio for a simulation workflow as shown in Figure 5-3. Thus, only measurement error at the subpupil level and sensor's fitting error at the pupil level are being considered. Other sources of noise such as anisoplanatism, corrective mirror fitting error, optical alignement errors or errors due to correction temporal delays are not being considered here. Hence, the obtained Strehl Ratios in this simulation should be regarded as higher than the expected in a real AO system.

5.4. Encircled Energy as a function of NGS magnitude

(a) Fried parameter r_0 = 21 cm

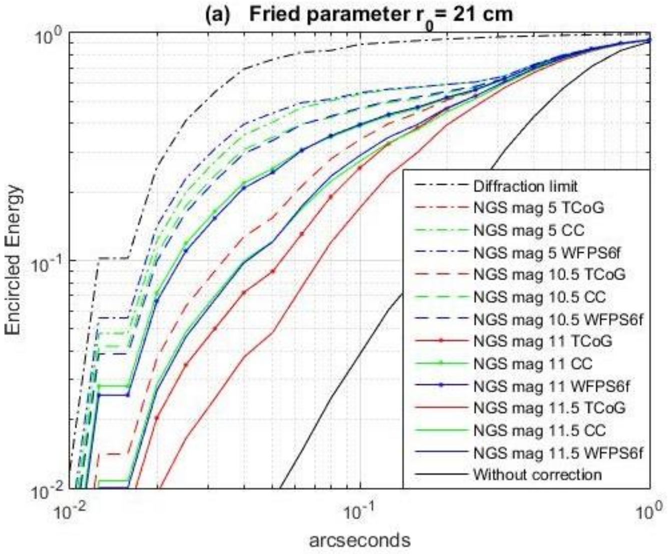

(b) Fried parameter r_0 = 8.4 cm

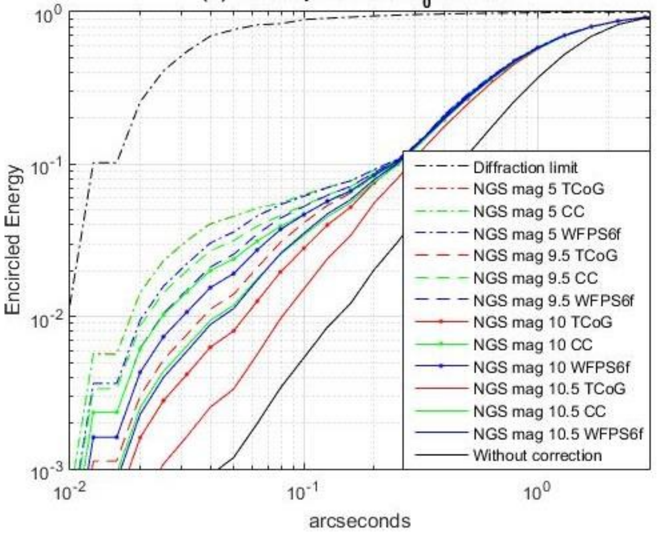

Figure 5-8. Encircled Energy graphs as a function of star magnitude for two atmospheric conditions: (a) 21 cm r_0 and (b) 8.4 cm r_0; and three centroiding algorithms: TCoG (red traces), CC (green traces) and WFPS with 6 spatial frequencies (blue traces), all tuned to estimate G-Tilt. Diffraction limited and no correction cases are shown in black traces. System's aperture is 4.2 m wide, with a central obscuration of 8.4%. Optical throughput is the default unity. SHWFS has 20 x 20 square subapertures and a ~2.7" FoV in (a) or ~3.8" FoV in (b) with Nyquist sampling. Phase recovery is modal through pseudo-inverson with optimal method selected for each star magnitude and a fixed number of 130 Zernike modes.

In this section, for the same system configuration as in section 5.3, i.e., a 4.2 m aperture with 8.4% central obscuration and 20 x 20 square subapertures for wavefront sensing, a comparison is made between the TCoG, CC and WFPS algorithms (the last involving 6 spatial frequencies) for two Fried parameters, 21 cm and 8.4 cm, and several NGS magnitudes, this time assessing the performance by means of Encircled Energy graphs. In agreement with the conclusion which was arrived at section 5.2, the algorithms are tuned to estimate G-Tilt at the subpupil level. Another difference with respect to the methodology at section 5.3 is that the number of modes employed at the modal phase recovery has been fixed to 130. Finally, the EE graph is computed over the PSF obtained by integration during 4 seconds of the light from the whole pupil at the focal plane with an *imager* object (200 frames separated 20 miliseconds from each other). System frequency, SHWFS's fields of view and detector's gain and noise parameters, and modal phase recovery methods, are the same as in sections 5.2 and 5.3.

Results are shown in Figure 5-8 in a double logarithmic scale, with panel (a) corresponding to the 21 cm r_0 case and panel (b) corresponding to the 8.4 cm r_0 case. TCoG results for various NGS magnitudes are shown in red traces with different line styles; the same magnitudes and line styles for the CC algorithm are shown in green traces; and blue traces are used for the WFPS algorithm. For a comparison purpose, the diffraction limited case and the turbulence uncompensated case are shown in black traces as best and worst limits, respectively.

Results are in good agreement with the Strehl Ratios shown in Figure 5-7. The CC and WFPS algorithms show a similar performance, that outperforms the one shown by the TCoG algorithm. For the 21 cm r_0 case in panel (a), and for a bright NGS of magnitude 5, the performace is similar for the three algorithms, with the red trace of the TCoG being right below the green trace of the CC, and thus being not visible. For NGS magnitudes of 10.5, 11 and 11.5, the difference in performance becomes very noticeable, with TCoG reaching similar levels of EE as CC and WFPS for a dimmer NGS, with a magnitude somewhere between 0.5 and 1 higher. For the 8.4 cm r_0 case in panel (b), the EE is one order of magnitude lower than in the 21 cm r_0 case for FoV's smaller than 0.1", in agreement with the SR decrease. Here again CC and WFPS allow for a dimmer NGS than the required by TCoG, with a magnitude ~0.5 to ~1 higher. It may seem that CC slightly outperforms WFPS, but this is only apparent and due to the logarithmic abscissa scale. A more careful inspection of the figure reveals that WFPS actually reaches higher EE values than CC does for higher than 0.15" FoV's. It is the author's opinion that, as WFPS does not threshold the image and makes a better estimation of G-Tilt than CC, it achieves PSF's with more concentrated energies but less peak values, and this translates into smaller EE values for the initial FoV's around the PSF's main lobe width that give place to higher EE values when the FoV's increase. This effect is more noticeable in the 8.4 cm r_0 case than in the 21 cm r_0 case, such as the difference between G-Tilt and Z-Tilt is higher for the first case than for the second.

5.5. Conclusions of the present chapter

The comparison in performance between the TCoG, CC and WFPS algorithms has been translated from the SHWFS subpupil level to the whole pupil level, thus including fitting error due to the pupil spatial sampling. The OOMAO tool has been used for this purpose, with some extensions implemented by the author. Results are shown in the form of Strehl Ratios and Encircled Energies as a function of NGS magnitudes.

There is a very good coincidence between the performances seen at subpupil and at pupil level. In high light level scenarios, that is, when fitting error dominates, all the algorithms perform similarly. When measurement noise at subpupil level dominates, that is, at low light level scenarios, CC and WFPS allow to use dimmer NGS's, of about ~0.6 to ~0.7 higher magnitudes, than the required by the TCoG algorithm, for a certain performance as measured by a SR or an EE.

This study has been reported for a 4.2 m aperture with 8.4% central obscuration, which are the William Herschel Telescope's dimensions. A 20 x 20 matrix of square shaped subapertures has been considered for wavefront measurement at the SHWFS. And two turbulence strength conditions have been simulated: a 21 cm r_0, equal to the subaperture side size, and an 8.4 cm r_0, 2.5 smaller than the subaperture side size. Open loop wavefront sensing has been assumed. Other spatial sampling configurations were tested and also showed coherent results, but are not shown here.

The WFPS's capacity to tune itself for Z-Tilt or G-Tilt estimation has been taken advantage of to assess the effect of such a choice over the wavefront estimation at the pupil level. It seems that Z-Tilt estimation at the subpupil level leads to a modest increase in SR, and G-Tilt estimation leads to an also modest increase in EE. Though this should be confirmed with more extensive simulation, it has been used as a criterion for tuning all the algorithms when obtaining the results of SR and EE.

Chapter 6. Laboratory tests

The present chapter presents the description and results of a modest laboratory test conducted mainly in order to show the necessary basic steps to apply the WFPS algorithm in a real case. It has been achieved by taking advantage of the laboratory setup of the EDiFiSE (Equalized and Diffraction limited Field Spectrograph Experiment) project at the Technology Division of the IAC (Instituto de Astrofísica de Canarias). This setup is not, in principle, thought for centroiding methods characterization. However, tests have been conducted as far as the system would allow and a very good coincidence with the numerical simulations is seen in the sensitivity test results, thereby confirming that the real system's geometry is correctly characterized and paving the way for moving the WFPS algorithm from simulation into reality.

6.1. The EDiFiSE project

EDiFiSE is a prototype instrument in development at the IAC's Technology Division, in which the author has participated during the execution of the present work. It is a high resolution integral field spectrograph intended for the observation of high-contrast objects as an alternative to coronographs. For this purpose, it combines an Adaptive Optics (AO) system and an Equalized Integral Field Unit (EIFU). It is designed to be tested at the GHRIL (Ground-based High Resolution Imaging Laboratory) platform of the 4.2m William Herschel Telescope (WHT) at the Roque de los Muchachos Observatory in the island of La Palma. A detailed description of the instrument and its scientific goals can be found at García-Lorenzo et al, 2008.

The technologies under test are basically two. One is the Field Programmable Gate Array (FPGA) as an electronic component to fully implement the wavefront sensing and control computation of the AO system (Chulani et al, 2016). The other one is a fiber optics based EIFU where the central fibers are intensity regulated with variable attenuators, thereby allowing to decrease the contrast of bright objects with respect to its surroundings and to detect nearby faint objects or structures.

At present, the AO system has successfully been integrated at the IAC laboratory facilities, and tested using the IAC's Atmosphere and Telescope (IACAT) simulator (see Moreno-Raso et al, 2010, for a description of this simulation facility).

6.2. The laboratory test

6.2.1. The laboratory setup

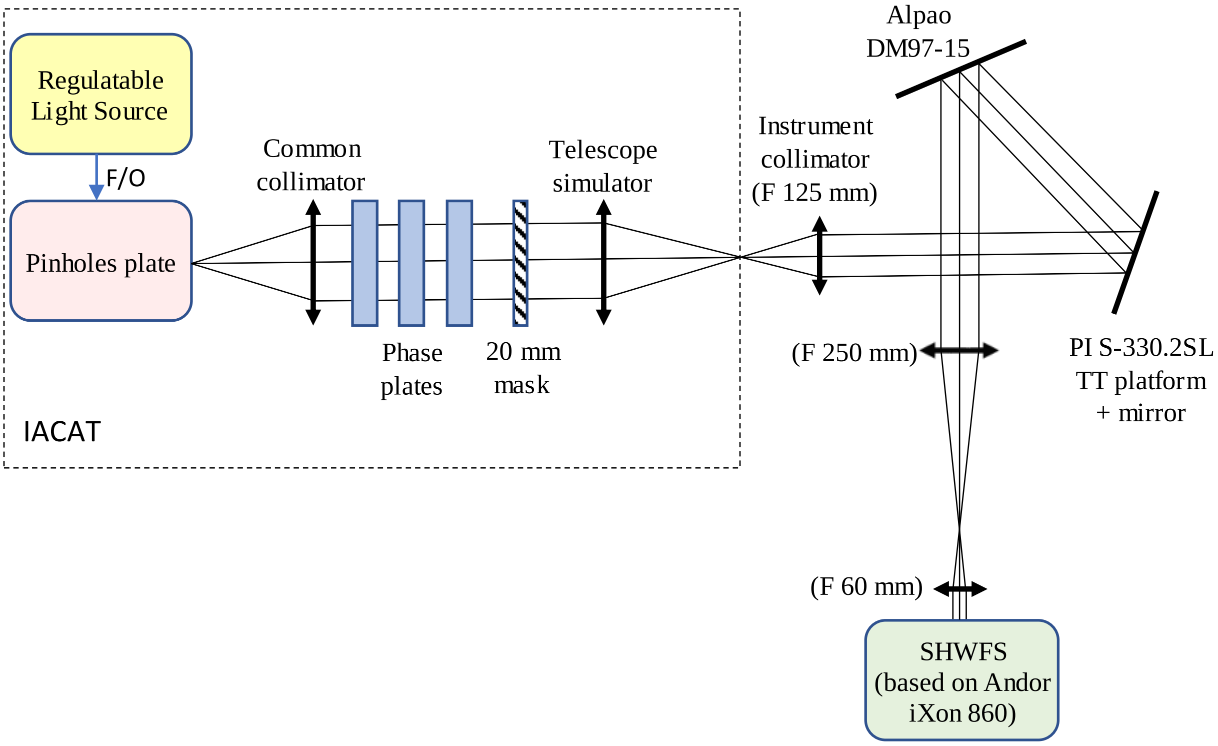

Figure 6-1. Diagram of the portion of the optical laboratory setup of the EDiFiSE project which has been employed for the laboratory test in the present work.

Figure 6-1 is a diagram of the portion of EDiFiSE's laboratory optical setup which has been employed in the present work. The IACAT simulator is provided with a regulatable light source that feeds with white light a pinholes plate through optical fibers, thus being able to simulate a single Natural Guide Star (NGS) or an asterism. Five phase plates that emulate Kolomogorov turbulence are available, each with a different Fried parameter. Upto three of them can be simultaneously motorized and mounted on the optical bench. Light is collimated and passed through these phase plates and a 2 cm circular mask emulating the system's aperture and secondary's central obscuration, till the telescope simulator. The characteristics of the WHT have been selected, with a focal ratio $f/10.94$.

EDiFiSE's AO system comprises two full-FPGA parallel control closed-loops, one for tip/tilt (TT) correction and the other for higher order modes correction. The former has the S-330.2SL TT platform and mirror from Physik Instrumente (PI) as the corrective element, whereas the latter employs the DM97-15 deformable mirror (DM) from the Alpao manufacturer. Closed loop correction means that these corrective elements come before the sensing elements in the optical path. Hence, Figure 6-1 shows the Shack-Hartmann wavefront sensor (SHWFS) at the end of the optical path. This WFS comprises an array of square microlenses and an EMCCD (Electronic Multiplication Charge Coupled Device) Andor iXon 860 detector. An instrument collimator lens with 125 mm focal length at the instrument's interface with the IACAT creates a ∼11.43 mm wide collimated beam that incides on the corrective elements, and which is further reduced by the pair of lenses with 250 and 60 mm focal lengths, in order to fit into the SHWFS detector size, which is ∼3.07 mm in size per side (the detector comprises 128 x 128 pixels and pixel size is 24 x 24 microns). The square microlens size is ∼310 microns per side, and so we have a 10 x 10 subpupils SHWFS configuration for a 4.2 m aperture telescope.

Figure 6-1 is a simplified diagram of the laboratory setup, with the necessary components to explain the test performed in the context of this work. Just to give the reader an idea of the real appearance of the setup, Figure 6-2 is a shot of the same from a nice viewpoint, courtesy by Dr. Félix Gracia Témich, from the EDiFiSE project team. In the foreground, the SHWFS components, i.e., the Andor iXon 860 detector and the microlens array mechanical mount are shown. In the middle ground, the two corrective elements can be seen, that is, the Alpao's DM and the TT platform from PI. The Kolmogorov phase plates are situated in the background of the photograph.

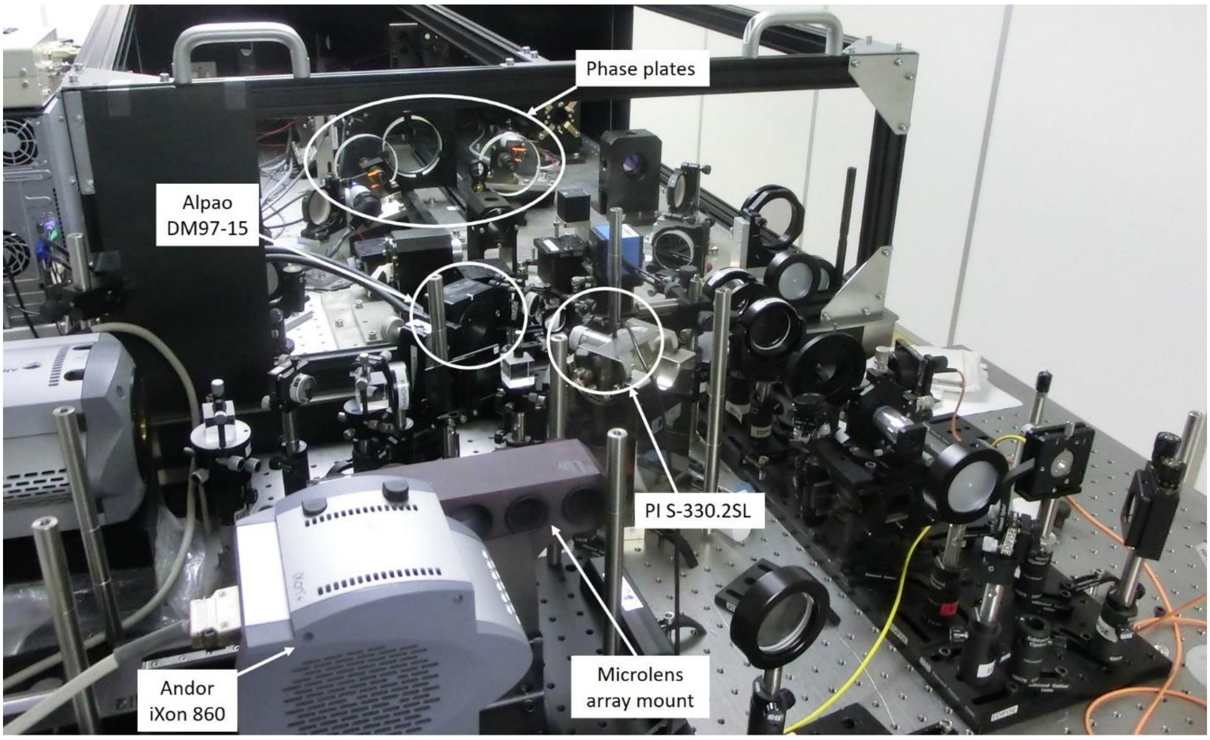

Figure 6-2. View of the optical setup of the EDiFiSE project at the laboratory facilities of the IAC, courtesy by Dr. Félix Gracia Temich, from the EDiFiSE team.

6.2.2. Description of the test

As it was said in the introduction of this chapter, the described setup in the previous point is not meant for centroiding methods performance assessment. First of all, the optical path spans a portion of the phase plates, and there is not any means of knowing the true applied phase therefrom, such as a second SHWFS with a very high spatial resolution. Second, the system was not designed to automatically acquire SHWFS image sequences with a varying atmospheric phase in a repetitive manner and with different light levels. The light source is manually regulatable through a knob, and the phase plates control software and SHWFS data acquisition software are not interconnected. An automated system would have facilitated to make statistics from acquired image sequences. However, it was out of the scope of the present work to develop such a system. And third, the optical setup is that of a closed-loop controlled system, and the SHWFS has been configured for such a control mode. The microlenses' focal length is ~25 mm, giving a spot FWHM size at diffraction limit of ~2.5 pixels. The assigned portion of the detector to each subpupil can be at most 12 x 12 pixels, which is good enough for closed loop control, but unsufficient for open loop sensing with such a big spot when the Fried parameter goes below the subaperture side size. This leaves no margin at all for FoV variation assessment tests.

Bearing in mind the mentioned limitations, a test has been designed to assess the sensitivity performance of the WFPS centroiding method against the TCoG and CC algorithms. The corrective elements have been employed as passive reflectors, only giving the DM the necessary shape to compensate for static aberrations in the optical path from the light source to the SHWFS (leaving the phase plates aside). Therefore, wavefront sensing has been as in an open loop mode. The phase plates have been kept still, thus emulating a static atmospheric aberration. For every static aberration emulated, SHWFS image sequences of 5000 frames have been taken, each with a different light source level. Also, accumulations of 10000 frames with the same light levels have been taken, in order to assess the incident light level per subpupil in the SHWFS. The acquired image sequences have been processed offline in order to assess the wavefront sensing degradation as the light level decreases. This has been done with all the centroiding methods under evaluation: the TCoG, the CC, and the WFPS with the six lowermost spatial frequencies involved and two 2D-FFT sizes, 12 x 12 and 14 x 14. A reasonable and fair estimation of the true applied phase has been considered to be at the halfway in the range between the minimum and maximum coordinate values for each centroid at each subpupil[15], dealing separately with horizontal and vertical coordinates, computed over the accumulated frame with the highest light level.

The tuning of all the centroiding methods has been aimed to estimate Z-Tilt, and has been done by simulating the real system's geometry at a subpupil level. In this regard, two are the main system parameters that need to be determined: the Fried parameter and the FWHM of the diffraction spot at the subpupil in pixel units.

Three have been the static turbulent aberrations emulated and, so, three have been the Fried parameter values to determine. In the first case, a single plate has been used which the manufacturer specifies as having a phase drawing with r_0 = 2.32 mm at λ = 632nm, which scales to a 48.7 cm r_0 at the WHT (the Fried parameter values of the phase plates and their combinations, scaled to the WHT, have been taken from Fuensalida, 2015). The Andor iXon 860 quantum efficiency curve shows a pass band centered at 600 nm, and for this wavelength

---

[15] As some philosophical currents would state, virtue is in the midpoint between all extremes.

the r_0 decreases to ~45.75 cm. Finally, the subaperture size to Fried parameter ratio has been approximated to unity: $D/r_0 \sim 1$. For the second case, a single plate has been used as well, with a drawing r_0 of 1.36 mm at λ = 632 nm. This scales to an r_0 = ~26.87 cm at λ = 600 nm at the WHT, and the approximation of $D/r_0 \sim 1.5$ has been made. As for the third turbulence case, the combination of the two previous plates has been used, which gives a Fried paramenter value r_0 = ~21.9 cm at λ = 600 nm at the WHT, and D/r_0 has been approximated to ~2. The last two cases correspond to Fried parameter values of ~21.6 cm and ~17.6 cm at a 500 nm wavelength, which would be good seeing situations at the Roque de los Muchachos Observatory in La Palma. Smaller r_0's would have required a larger FoV than the available one to deal with the spots' tilt.

As regards the FWHM size, the actual value sought is the λ/D ratio, with *D* being the square subaperture side size. For a 600 nm wavelength and a 42 cm subaperture side size, the λ/D ratio is ~0.295". The scale plate at the SHWFS is ~0.129"/pixel, and so the value in pixels of the the λ/D ratio is ~2.3. When illuminating the SHWFS with a flat wavefront, somewhat wider spots were seen, perhaps due to the effect of the higher wavelengths in the white light, and FWHM values ~2.7 - 2.9 pixels were obtained when fitting the spots to 2D Gaussian shapes. Finally, a 2.5 pixels value has been selected for the λ/D ratio in the simulation, which corresponds to a ~650 nm wavelength. This has been obtained at the simulation by assigning a 32 x 32 pixels resolution to the square subpupil, and employing an 80 x 80 2D-FFT to obtain the Fraunhofer image at the focal plane (see equation [Eq. 4-16]). Out of the full image obtained, a 12 x 12 pixels central portion is finally selected.

The other simulation parameters of importance are related to the detector sensitivity, gain and noise values. A sensitivity value of 16 e^-/ADU has been introduced in the simulation. The real EMCCD gain has been seen to be a ~20% lower than the programmed gain with the detector's cooling system set at -80ºC. Two gain values were programmed: 1000 for light levels below 1000 incident photons per subpupil, and 200 for higher levels. So, the values introduced in the simulation have been 800 and 160, respectively. As for the noises, a CIC value of 0.155 e^-/pixel/frame and a RON of 50 rms e^- have been employed. Appendix B details how these values have been determined.

6.2.3. Test results

Having estimated the true phase for each of the three static turbulences applied as that obtained over the accumulation of frames with the highest light level, i.e., in a negligible detector noise situation, and as a fair compromise between all the centroiding methods, it is possible to estimate the phase error for every acquired frame in every sequence at each light level. This phase error has been first estimated at a subpupil level, as a difference in centroid coordinates at each subpupil. The rms value of such estimated phase tilt error throughout the whole image sequence, averaged among all the centroids in the image, is represented for each light level in panels labelled (a) of Figures 6-3, 6-4 and 6-5, for the three turbulence phases applied and the four centroid algorithms under evaluation. The units have been converted from rms pixels to rms tilt radians applying equation [Eq. 4-25].

The commands to the DM are calculated through MVM (Matrix Vector Multiplication) in the control loops in normal operation of the AO system of EDiFiSE. The same control matrixes have been employed to estimate the phase errors at the complete pupil. True phases have been estimated in the same manner as for the subpupil tilts, i.e., as a midpoint in the range of phases corresponding to the different centroiding methods for every DM actuator, obtained from the accumulated frame at the highest light level for each static turbulence applied. The phase at the pupil is then obtained for each frame, as corrective commands to the DM, by applying the control matrix to the obtained centroids vector, and the phase error is obtained at every DM actuator as the distance between its phase and the estimated true phase. The rms values of such distances throughout the whole image sequence, averaged among all the DM actuators, is represented for each light level in panels labelled (b) of Figures 6-3, 6-4 and 6-5, for the three turbulence phases applied and the four centroiding algorithms. As the fitting error is not actually being taken into account, the graph shapes are very similar to those in panels (a). The units are in rms percentage of peak to valley (PV) stroke at the DM. According to the manufacturer, the 100% PV stroke cannot be specified in length units as it depends on the mirror shape. The author estimates it should be around ~10 – 20 microns[16].

Figure 6-3 shows the results for the $D/r_0 \sim 1$ case. This turbulence phase has produced the least clear results among the three studied cases. As it was seen in chapter 4, the better the turbulence condition, the less difference will be appreciated between the different centroiding methods. In spite of this, the tendency of the TCoG algorithm to worsen its tilt estimation more rapidly than the other algorithms as the light decreases below 200 incident photons per subpupil is clearly seen in the figure. For higher light levels, the variation of all the centroiding methods with light level is similar. Note that these values should not be interpreted as tilt or phase estimation errors and used to compare the tilt or phase estimation capacity of each centroiding method, since they are actually distances to a midpoint which has been taken as a true phase. Centroiding methods that obtain an estimation which is closer to this midpoint will show lower values in the graph, but this does not mean a better estimation of the real phase. So, the graphs should only be used to corroborate that there is not much dispersion between the different methods at high light level, which is the case (0.1 rms radians is $\sim\lambda/60$); and to evaluate the estimated tilt variation as light decreases for every algorithm in order to assess its sensitivity.

Figure 6-4, for a $D/r_0 \sim 1.5$ case, shows a much clearer result than the previous one, perhaps because this phase had a strong tilt component, and the errors at low light level reach values which are more than double of those shown in the previous figure. Here, the difference in sensitivity of the TCoG algorithm with respect to the other algorithms is very visible, and the gap in estimated tilt between 20 and 200 incident photons per subpupil reminds the results obtained by simulation at a subpupil level in chapter 4. Similar comments can be said of the results shown in Figure 6-5 for the $D/r_0 \sim 2$ case, which confirm the improvement in sensitivity of the WFPS and CC algorithms with respect to the TCoG.

---

[16] From DM stroke specifications at the Alpao's web page for different Zernike modes.

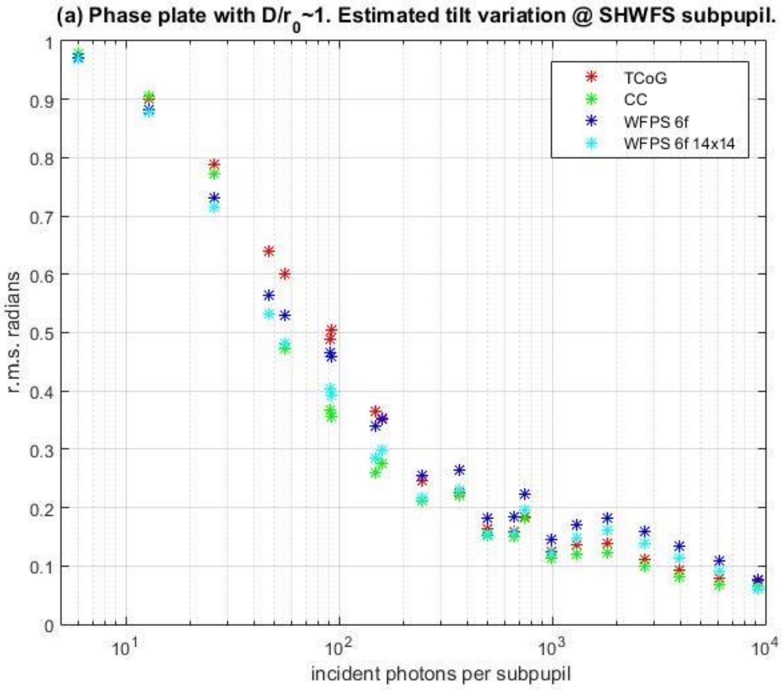

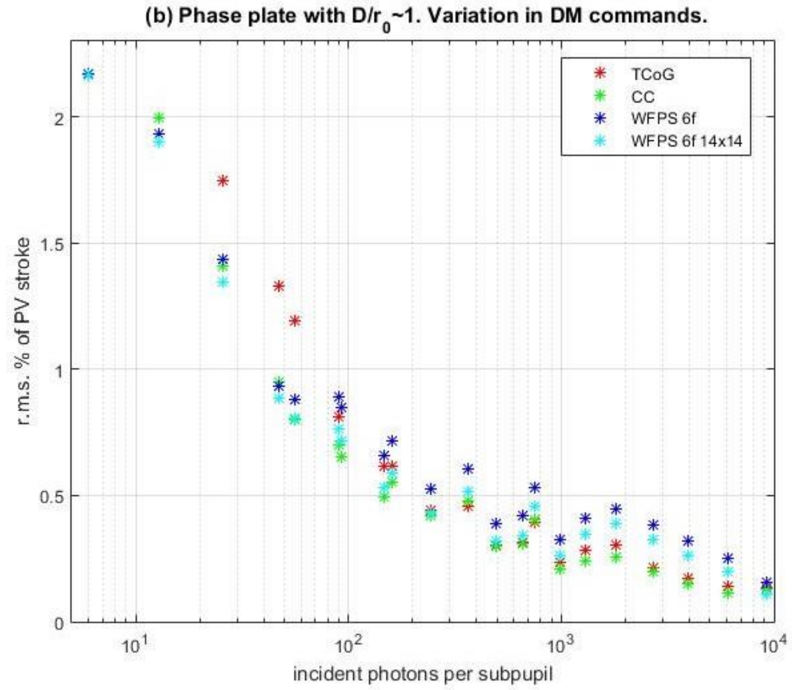

Figure 6-3. (a) rms value of differences between estimated tilt and estimated true tilt at the SHWFS subpupils as a function of incident light level for the applied static turbulence with D/r_0~1. Values are obtained as averages among all centroid coordinates in the SHWFS image. Stars in red are for the TCoG algorithm, in green for the CC algorithm, and in blue and cyan for the WFPS algorithm involving the six lowermost spatial frequencies with 12 x 12 and 14 x 14 sized 2D-FFT's, respectively. (b) rms value of differences between estimated phases and estimated true phases at the DM actuator's coordinates as a function of incident light level for the same applied static turbulence. Phases are obtained by applying the control matrix to the vector of centroid coordinates. Shown values are averages among all the DM actuators. Colour code is as for panel (a)

(a) Phase plate with D/r_0~1.5. Estimated tilt variation @ SHWFS subpupil.

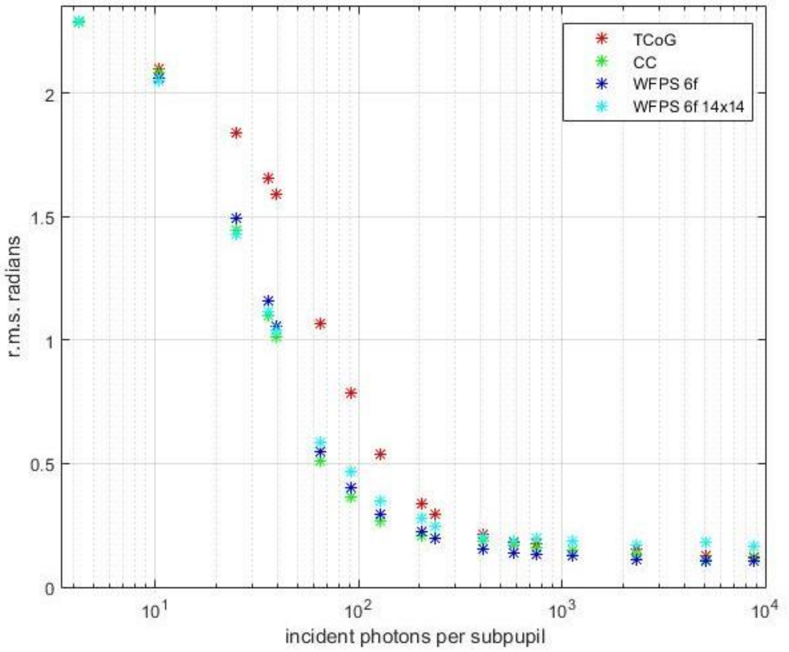

(b) Phase plate with D/r_0~1.5. Variation in DM commands.

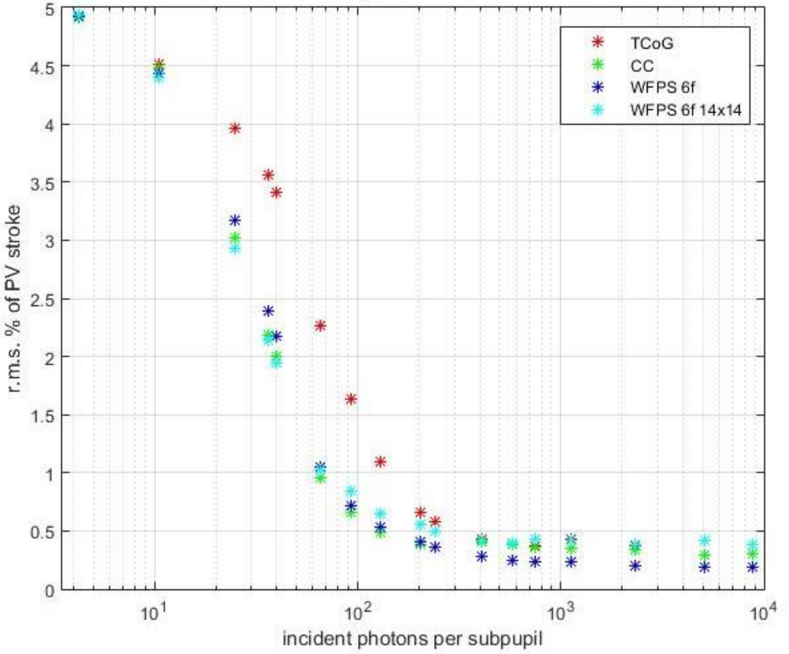

Figure 6-4. (a) rms value of differences between estimated tilt and estimated true tilt at the SHWFS subpupils as a function of incident light level for the applied static turbulence with D/r_0~1.5. Values are obtained as averages among all centroid coordinates in the SHWFS image. Stars in red are for the TCoG algorithm, in green for the CC algorithm, and in blue and cyan for the WFPS algorithm involving the six lowermost spatial frequencies with 12 x 12 and 14 x 14 sized 2D-FFT's, respectively. (b) rms value of differences between estimated phases and estimated true phases at the DM actuator's coordinates as a function of incident light level for the same applied static turbulence. Phases are obtained by applying the control matrix to the vector of centroid coordinates. Shown values are averages among all the DM actuators. Colour code is as for panel (a)

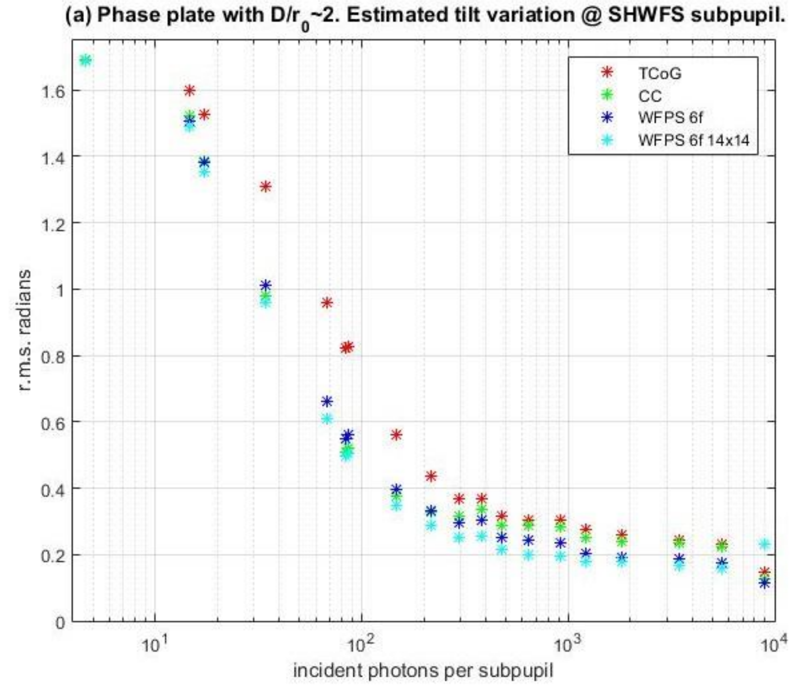

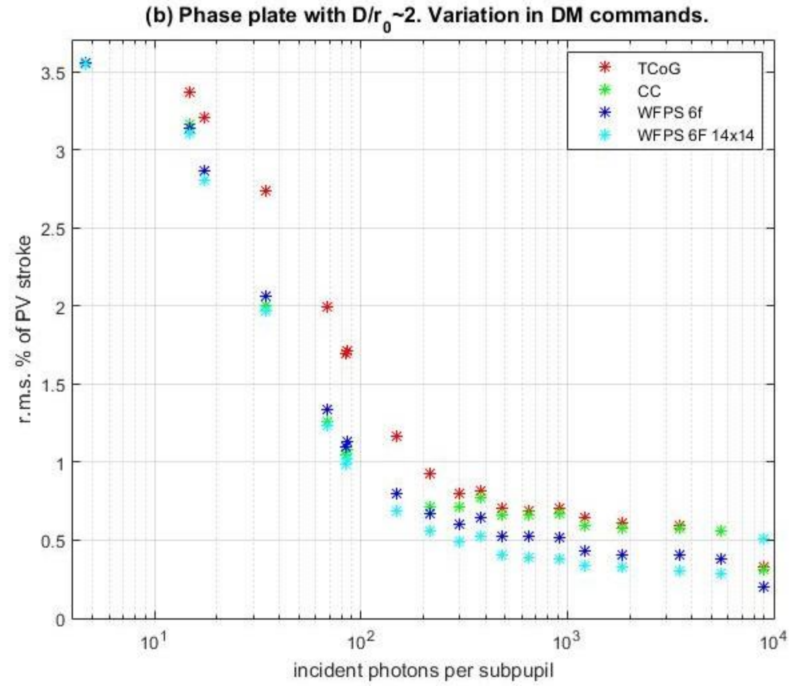

Figure 6-5. (a) rms value of differences between estimated tilt and estimated true tilt at the SHWFS subpupils as a function of incident light level for the applied static turbulence with D/r_0~2. Values are obtained as averages among all centroid coordinates in the SHWFS image. Stars in red are for the TCoG algorithm, in green for the CC algorithm, and in blue and cyan for the WFPS algorithm involving the six lowermost spatial frequencies with 12 x 12 and 14 x 14 sized 2D-FFT's, respectively. (b) rms value of differences between estimated phases and estimated true phases at the DM actuator's coordinates as a function of incident light level for the same applied static turbulence. Phases are obtained by applying the control matrix to the vector of centroid coordinates. Shown values are averages among all the DM actuators. Colour code is as for panel (a)

6.3. Conclusions of this chapter

A test has been conducted at the laboratory facilities of the IAC taking advantage of the AO subsystem setup of the EDiFiSE project.

The results show, in the first place, that the method of determining the WFPS Bayesian weights, i.e., of tuning the algorithm, by simulating the real system's geometry at a subpupil level, is correct. This has been deducted from the similarity in tilt estimation results of the WFPS algorithm and the control algorithms, the TCoG and the CC, at high light level.

And in the second place, a very good coincidence between the laboratory test and the simulation at subpupil level has been found as regards the sensitivity performance of the algorithms under evaluation, which confirms the improvement in performance of the WFPS algorithm over the TCoG algorithm for light levels of 20 to 200 incident photons per subpupil, in a very similar manner as the CC algorithm does.

This test has been conducted with three values of turbulence strength, leading to $D/r_0 \sim 1$, $D/r_0 \sim 1.5$ and $D/r_0 \sim 2$ ratio values, with *D* being the square subaperture size, and with a single sample of static turbulence phase for each r_0. Wavefronts have been sensed as in an open loop correction mode. The FWHM of the SHWFS subpupil's spot at diffraction limit has been estimated as 2.5 pixels, and the FoV size has been 12 x 12 pixels.

Chapter 7. General conclusions and future work

7.1. General conclusions

Shack-Hartmann wavefront sensors (SHWFS) are by far the most commonly used wavefront sensors in astronomy, and those with the most matured and known techonology. However, they face new challenges as adaptive optics (AO) systems evolve. Recent Multi Object Adaptive Optics (MOAO) systems work in open loop correction mode, and present their sensors the need to balance sensitivity in low light level conditions with a large dynamic range that copes with the uncorrected atmospheric turbulence. This requirement falls directly upon the centroiding method employed at the subpupil of the SHWFS, and invites new studies and proposals on this subject. This work presents a novel, optimized, Fourier domain based centroiding method which is real time implementable. The following are the main conclusions which can be extracted from this work.

1. A new centroiding method for SHWFS's has been formulated, as a Bayesian estimator of the tilt at the subpupil, from the image's Fourier phase slopes. Phase slopes are obtained without phase computation and unwrapping, and the computational cost is one order of magnitude lower than for the Cross-Correlation (CC) algorithm. Its applicability to wavefront sensing with point-like guiding souces has been shown. It has been named *Weighted Fourier Phase Slope* (*WFPS*).

2. Numerical simulations both at the subpupil and at the pupil level, as well as experimental results at the laboratory, show that the WFPS and CC algorithms have a similar sensitivity, which outperforms the Thresholded Centre of Gravity (TCoG) algorithm, for light levels in the range of 20 to 200 incident photons per subpupil and in the presence of detector noises and turbulence high order perturbations. Sky coverage is thus improved, as the NGS can be magnitude 0.6 – 0.7 higher

3. As a consequence of the improved sensitivity, the algorithm's optimal working FoV is higher than for the TCoG algorithm, and similar to the CC algorithm's, becoming an algorithm of choice when large FoV's are required, such as in open loop sensing and in strong turbulence conditions. This point, and the following, have been shown through numerical simulations at the subpupil level.

4. The WFPS algorithm keeps a relationship with low pass cepstrum filtering, and it can be tuned to estimate Z-Tilt or G-Tilt in the presence of noise, without thresholding the image at any step. As a consequence, it outperforms the CC and TCoG algorithms when estimating G-Tilt at high light level and large enough FoV, for it can take into account the low light level portion at the skirt of the spot.

5. As for Z-Tilt estimation at high light level, the three algorithms, TCoG, CC and WFPS, perform similarly as long as a large enough FoV is spanned so as to avoid spot's truncation. In the case of a smaller FoV, and since the WFPS algorithm does not threshold the image, it will need to employ a larger 2D-FFT than the image size in order to simmetrize the spot and compensate for its partial truncation.

7.2. Future work

The following natural step is the algorithm verification in a fully operational adaptive optics system at the lab, and then at a telescope. The necessary steps to achieve this goal would be:

1. The values of real world systems' defining parameters constantly vary in time. In long term observations, the turbulence Fried parameter, and even the received light from the guiding source, change. It would be necessary therefore to devise a means to adapt the algorithm (its Bayesian weights) to this changing working environment. Further simulations are necessary in this line to determine the algorithm's performance degradation when utilizing non-optimal weights, so as to establish the weights update period in long term real observations.

2. It has been seen that this algorithm shows an important advantage over the CC as regards computational cost. This is based upon the computation of partial 2D-FFT's, i.e., their computation at only a limited number of spatial frequencies. It becomes therefore necessary to efficiently programme this partial bi-dimensional discrete Fourier transform computation for its execution in the platforms of choice of the AO systems at the telescopes: CPU's, GPU's, FPGA's, etc.
   The variation in computational cost with respect to existing centroiding algorithms should then be measured. This variation will probably require a tuning of the stabilizing filters at the correction loops of the AO systems.

3. Appropriate working AO systems should be sought, such as MOAO systems that correct in open loop, in order to test the algorithm's performance against the traditional ones, first at the lab and then at telescopes.

Moving on to another issue, throughout this work only point-like guiding sources have been considered. However, the applicability of the algorithm in the field of AO for astronomy is broader:

1. Firstly, the WFPS algorithm, such as it has been formulated in this work, is applicable to wavefront sensing with LGS's, where spots are seen elongated at the SHWFS's subpupils. This should be confirmed by numerical simulations first, determining the 2D-FFT required sizes, number of spatial frequencies involved, optimal weights, etc. Elongated spots mean big required working FoV's and large number of pixels per subpupil involved, even in closed loop correction mode, and this is where the WFPS algorithm outperforms the traditional CoG based ones. Also, its simmetrizing capacity could be of advantage when the source is asymmetric right from the start.

2. Second, if the elongated spot's structure should be taken into account, then the WFPS algorithm could be reformulated as a weighted average of differences of Fourier phase slopes corresponding to the live images and a reference image. This is applicable also to the wavefront sensing with extended objects such as in solar AO. The effectiveness first, and then the performance of this reformulated WFPS algorithm should be shown through numerical simulations in principle. A possible advantage over the traditional CC algorithm could be a considerable decrease in computational cost, as it has been seen in this work.

Bibliography

Andersen D. et al, 2014. “Comparing the performance of open loop centroiding techniques in the Raven MOAO system”, Adaptive Optics Systems IV, Proc. SPIE 9148.

Arines J. and Ares J., 2002. “Minimum variance centroid thresholding”, Optics Letters, Vol 27, No 7, pp. 497-499.

Assémat F., Gendron E. and Hammer F., 2007. “The FALCON concept: multi-object adaptive optics and atmospheric tomography for integral field spectroscopy – principles and performance on an 8-m telescope”, Mon. Not. R. Astron. Soc. 376, pp. 287-312.

Carmon Y. and Ribak E. N., 2003. “Phase retrieval by demodulation of a Hartmann-Shack sensor”, Optics Communications, 215, pp. 285-288.

Chulani H. M. and Rodríguez-Ramos J. M., 2013. “Weighted Fourier Phase Slope as a centroiding method in a Shack-Hartmann wavefront sensor: A Z-tilt estimation method in the Fourier domain, optimizable to the system’s geometry”, IEEE 12th Workshop on Information Optics (WIO’2013).

Chulani H.M. et al, 2016. “EDIFISE full-FPGA adaptive optics. First laboratory results using the IACAT optical ground support equipment”, Adaptive Optics Systems V, Proc. SPIE 9909.

Chulani H. M. and Rodríguez-Ramos J. M., 2017. “Preliminary performance results of the Weighted Fourier Phase Slope centroiding method for Shack Hartmann wavefront sensors obtained with the OOMAO simulator”, accepted for presentation at the 5th Adaptive Optics for Extremely Large Telescopes (AO4ELT5) Conference.

Conan R. and Correia C., 2014. “Object-oriented Matlab adaptive optics toolbox”, Adaptive Optics Systems IV, Proc. SPIE 9148.

Fillard J.P., 1992. “Subpixel accuracy location estimation from digital signals”, Optical Engineering, Vol 31, No 11, pp. 2465-2471.

Fillard J.P. et al, 1993. “Computer simulation of super-resolution point source image detection”, Optical Engineering, Vol 32, No 11, pp. 2936-2944.

Fried, D.L., 1965. “Statistics of a Geometric Representation of Wavefront Distortion”, J. Opt. Soc. Am. 55(11), pp. 1427-1435.

Fried, D.L., 1977. “Least-square fitting a wave-front distortion estimate to an array of phase-difference measurements”, J. Opt. Soc. Am., Vol 67, No 3, pp. 370-375.

Fuensalida J. J., 2015. “Combinación de placas de fase de IACAT en configuración WHT para EDiFiSE”. IAC internal report. Ref. IP/TN-EDI/170.

Fusco T. et al, 2004. “Optimisation of a Shack-Hartmann-based wavefront sensor for XAO system”, Advancements in Adaptive Optics, Proc. SPIE 5490, pp. 1155-1166.

García-Lorenzo B. et al, 2008. “EDiFiSE: equalized and diffraction-limited field spectrograph experiment”, Proc. SPIE 7014.

Gavel D., 2006. “Multi-Object Adaptive Optics and Multi-Conjugate Adaptive Optics Architectures. System Design Trade Study.” Keck Next Generation Adaptive Optics. Draft.

Ghiglia D.C. and Pritt M.D., 1998. “Two-Dimensional Phase Unwrapping: Theory, Algorithms and Software”, New York: Wiley-Interscience.

Goldstein R.M., Zebken H.A. and Werner C.L., 1988. “Satellite radar interferometry: Two-dimensional phase unwrapping”, Radio Science, Vol 23, No 4, pp. 713–720.

Goodman, J.W., 1985. “Statistical Optics”, John Wiley and Sons, New York, N.Y.

Goodman, J.W., 2005. “Introduction to Fourier Optics”, 3rd ed., Roberts & Co Publishers.

Gradatour D. et al, 2010. “Comparing centroiding methods for Shack-Hartmann wavefront sensing with laser guide stars on an ELT”. Adaptive Optics Systems II, Proc. SPIE 7736.

Guzmán D. et al, 2010. “Deformable mirror model for open-loop adaptive optics using multivariate adaptive regression splines”, Optics Express, Vol 18, No 7, pp. 6492-6505.

Hardy, J.W., 1998. “Adaptive Optics for Astronomical Telescopes”, New York, Oxford University Press.

Hartmann J., 1900. “Bemerkungen über den Bau und die Justirung von Spectrographen”, Zeitschrift für Instrumentenkunde, Berlin, Julins Springer, 20: 17-27, 47-58.

Herrmann J., 1980. “Least squares wave front errors of minimum norm”, J. Opt. Soc. Am., Vol 70, No 1, pp. 28-35.

Hirsch M. et al, 2013. “A Stochastic Model for Electron Multiplication Charge-Coupled Devices – From Theory to Practice”, PLoS ONE, Vol 8, Issue 1: e53671.

Hudgin R.H., 1977. “Wavefront reconstruction for compensated imaging”, J. Opt. Soc. Am., Vol 67, No 3, pp. 375-378.

Kolmogorov, A., 1961. “The local structure of turbulence in incompressible viscous fluids for very large Reynolds’ numbers”, Turbulence, Classic Papers on Statistical Theory, S. K. Friedlander and L. Topper eds. Wiley-Interscience Publishers Inc., New York, NY.

Lardière O. et al, 2010. “Compared performance of different centroiding algorithms for high-pass filtered laser guide star Shack-Hartmann wavefront sensors”, Adaptive Optics Systems II, Proc. SPIE 7736.

Lardière O. et al, 2014. “Multi-Object Adaptive Optics On-sky Results with RAVEN”, Adaptive Optics Systems IV, Proc. SPIE 9148.

Leroux C. and Dainty C., 2010. "Estimation of centroid positions with a matched filter algorithm: relevance for aberrometry of the eye", Optics Express, Vol 18, No 2, pp. 1197-1206.

Li T., Huang L. and Gong M., 2014. "Wavefront sensing for a nonuniform intensity laser beam by Shack-Hartmann sensor with modified Fourier domain centroiding", Optical Engineering, Vol 53, No 4.

Lukin V.P. et al, 2010: "Wavefront sensors and algorithms for adaptive optical systems", Adaptive Optics System II, Proc. SPIE 7736.

Marlon V., 2014. "Investigación del problema inverso de reconstrucción tomográfica en óptica adaptativa para astronomía a través de técnicas de minería de datos e inteligencia artificial", PhD Dissertation, Oviedo University, Spain.

Moreno-Raso J. et al, 2010. "Atmosphere and telescope simulator for new adaptive optics methods development", Adaptive Optics Systems II, Proc. SPIE 7736.

Nicolle M. et al, 2004. "Improvement of Shack-Hartmann wave-front sensor measurement for extreme adaptive optics", Optics Letters, Vol 29, No 23, pp. 2743-2745.

Noll, R.J., 1976. "Zernike polynomials and atmospheric turbulence", J. Opt. Soc. Am., Vol 66, No 3, pp. 207-211.

Oppenheim A. V. and Schafer R. W., 1989. "Discrete Time Signal Processing", Prentice Hall International, Inc.

Pinna F., 2014. "Modelado y caracterización de cámaras EMCCD (Electron Multiplication Charge Coupled Devices) de uso en óptica adaptativa, a partir de un modelo estocástico conocido de las mismas. Validación con imágenes reales." IAC's internal report DE/PR-DE/033v.1.

Platt, B.C. and Shack, R.V., 2001. "History and Principles of Shack-Hartmann Wavefront Sensing", J. of Refractive Surgery, Vol 17, No 5, pp. S573-577.

Poyneer L.A. et al, 2005. "Experimental results for correlation-based wavefront sensing", Advanced Wavefront Control: Methods, Devices and Applications III, Proc. SPIE 5894.

Quirós F., 2007. "Reconstruction and Control Laws for Multi-conjugate Adaptive Optics in Astronomy", PhD Dissertation, Imperial College, London, UK.

Ragazzoni R., 1996. "Pupil plane wavefront sensing with an oscillating prism", Journal of Modern Optics, Vol 43, No 2, pp. 289-293.

Rigaut F.J., Ellerbroek B.L. and Flicker R., 2000. "Principles, limitations and performance of multiconjugate adaptive optics", Proc. SPIE Vol 4007, pp. 1022-1031.

Rigaut F., 2002. "Ground conjugate wide field adaptive optics for the ELTs". Beyond Conventional Adaptive Optics, ESO Conference and Workshop Proc., 58, pp.11-16.

Robbins M.S. and Hadwen B.J., 2003. "The noise performance of Electron Multiplying Charge-Coupled Devices". IEEE Transactions on Electron Devices, Vol 50, No 5.

Roddier F., 1981. "The effects of atmospheric turbulence in optical astronomy", Progress in Optics XIX, E. Wolf eds., North Holland.

Roddier F., Roddier C. and Roddier N., 1988. "Curvature Sensing: A New Wavefront Sensing Method", Proc. SPIE Vol 0976, Statistical Optics.

Roddier N., 1990. "Atmospheric wavefront simulation and Zernike polynomials", Proc. SPIE Vol 1237, Amplitude and Intensity Spatial Interferometry, pp. 668-679.

Rodríguez-Ramos J.M., 1998. "Detección de frente de onda. Aplicación a técnicas de alta resolución espacial y alineamiento de superficies ópticas segmentadas", PhD Dissertation, La Laguna University, Spain.

Rodriguez-Ramos J.M. et al, 2008: "2D-FFT implementation on FPGA for wavefront phase recovery from the CAFADIS camera", Adaptive Optics Systems, Proc. SPIE 7015.

Rousset G. et al, 2011. "First star images corrected by multi-object adaptive optics", SPIE Newsroom, DOI 10.1117/2.1201109.003736

Ruggiu J.M., Solomon C.J. and Loos G., 1998. "Gram-Charlier matched filter for Shack-Hartmann sensing at low light levels", Optics Letters, Vol 23, No 4, pp. 235-237.

Sallberg S.A., Welsh B.M. and Roggemann M.C., 1997. "Maximum a posteriori estimation of wave-front slopes using a Shack-Hartmann wave-front sensor", J. Opt. Soc. Am. A, Vol 14, No 6.

Sarver E.J., Schwiegerling J. and Applegate R.A., 2006. "Extracting Wavefront Error from Shack-Hartmann Images Using Spatial Demodulation". J. Refract. Surg., 22(9), pp. 949-953.

Shack, R.V., 1971. "Production and use of a lenticular Hartmann screen", J. Opt. Soc. Am. (Oral presentation). Ramada Inn, Tucson, Arizona. Smith, F. Dow, ed. Vol 61, No 5, p. 656.

Sidick E. et al, 2008. "Adaptive cross-correlation algorithm for extended scene Shack-Hartmann wavefront sensing", Optics Letters, Vol 33, No 3, pp. 213-215.

Srinath M.D. and Rajasekaran P.K., 1979. "An Introduction to Statistical Signal Processing with Applications", John Wiley & Sons.

Stephenson P., 2014. "Recurrence relations for the Cartesian derivatives of the Zernike polynomials", J. Opt. Soc. Am. A, Vol 31, No 4, pp. 708-715.

Talmi A. and Ribak E.N., 2004. "Direct demodulation of Hartmann-Shack patterns". J. Opt. Soc. Am. A., Vol 21, No 4.

Tatarski, V.I., 1961. "Wave Propagation in a Turbulent Medium", McGraw-Hill Book Company, New York, NY.

Thomas S. et al, 2006: “Comparison of centroid computation algorithms in a Shack-Hartmann sensor”, Mon. Not. R. Astron. Soc. 371, pp. 323-336.

Tyler G.A., 1994. “Bandwidth considerations for tracking through turbulence”, J. Opt. Soc. Am. A, Vol 11, No 1, pp. 358-367.

Tyson, R.K., 1991. “Principles of Adaptive Optics”, Academic Press, New York.

Van Dam M.A. and Lane R.G., 2000. “Wave-front slope estimation”, J. Opt. Soc. Am. A, Vol 17, No 7, pp. 1319-1324.

Vyas A., Roopashree M. B. and Prasad B. R., 2009(a). “Optimization of Existing Centroiding Algorithms for Shack Hartmann Sensor” Proc. National Conference on Innovative Computational Intelligence & Security Systems, Sona College of Technology, Salem, pp. 400-405.

Vyas A., Roopashree M. B. and Prasad B. R., 2009(b). “Denoising Shack Hartmann sensor Spot Pattern using Zernike Reconstructor”, International Journal of Power Control Signal and Computation (IJPCSC) Vol 2, No 2.

Vyas A., Roopashree M. B. and Prasad B. R., 2010. “Centroid Detection by Gaussian Pattern Matching in Adaptive Optics”, 2010 International Journal of Computer Applications. Vol 1, No 26, pp 30-35.

Yura H.T. and Tavis M.T., 1985. “Centroid anisoplanatism”, J. Opt. Soc. Am. A, Vol 2(5), pp. 765-773.

Appendix A. Cepstrum analysis and homomorphic deconvolution

The introduction and definitions of *complex cepstrum*, *homomorphic system* and *homomorphic deconvolution* in this appendix, and even the notation in the equations, have been taken from Oppenheim and Schafer, 1989. The examples are original of this work.

Though chapter 3 is self-contained and completely defines the algorithm evaluated in the present work, this appendix introduces some image processing techniques that are behind and have inspired the algorithm, providing the reader a deeper insight into the essence of the same.

The term *cepstrum* is a derivation of the term *spectrum* by inverting the order of the first letters, and it refers to a signal transform into a domain where customary operations in the time side are performed in the frequency side, and vice versa[17]. That is, the convolution operation, which is habitually applied in the time domain, is in cepstrum techniques applied in the frequency domain; and so, a low pass filter in the cepstrum domain, for example, actually smoothes the rapid variations of the signal's spectrum shape. This technique is very much applied in the treatment of echoed signals in disciplines such as processing speech signal, seismic signals, biomedical signals, old acoustic recordings and sonar signals.

Homomorphic systems are a non-linear type of systems in the classical sense, but which satisfy a generalized superposition principle; i.e., input signals and their corresponding responses are superimposed or combined by an operation having the same algebraic properties as addition. A particular but very extended case of homomorphic systems involve the convolution operation at their inputs and outputs. The concept of the cepstrum is a fundamental part of the theory of homomorphic systems for processing signals that have been combined by convolution.

---

[17] In the introduction of this appendix, time and frequency domains are mentioned, following the discussion in Oppenheim and Schafer, 1989, and also because cepstrum analysis was first applied to time domain signals. In the following sections of the appendix, the same concepts will be extended to a bi-dimensional case and image and spatial frequency will be talked about.

A.1. Definition of the complex cepstrum

Consider an image $I(x,y)$ whose Fourier transform is

$$\mathcal{F}\{I(x,y)\}|_{\omega_x,\omega_y} = \mathbb{I}(\omega_x,\omega_y) = |\mathbb{I}(\omega_x,\omega_y)|e^{j\sphericalangle\mathbb{I}(\omega_x,\omega_y)} \qquad \text{[Eq. A-1]}$$

where $|\mathbb{I}(\omega_x,\omega_y)|$ and $\sphericalangle\mathbb{I}(\omega_x,\omega_y)$ are the magnitude and angle, respectively, of the complex number $\mathbb{I}(\omega_x,\omega_y)$. The *complex cepstrum* corresponding to $I(x,y)$ is defined to be the image $\hat{I}(x,y)$ for which the Fourier transform is

$$\hat{\mathbb{I}}(\omega_x,\omega_y) = log[\mathbb{I}(\omega_x,\omega_y)] = log|\mathbb{I}(\omega_x,\omega_y)| + jarg\left(\mathbb{I}(\omega_x,\omega_y)\right) \qquad \text{[Eq. A-2]}$$

log in equation [Eq. A-2] is the natural logarithm and arg is the "unwrapped" phase defined such that it satisfies the requirement of continuity:

$$arg\left(\mathbb{I}(\omega_x,\omega_y)\right) = ARG\left(\mathbb{I}(\omega_x,\omega_y)\right) + 2\pi r(\omega_x,\omega_y) \qquad \text{[Eq. A-3]}$$

$ARG\left(\mathbb{I}(\omega_x,\omega_y)\right)$ is the principal value of the phase, and is not necessarily a continuous surface, but is limited to an interval of length 2π as would typically be obtained from an arctangent subroutine:

$$-\pi < ARG\left(\mathbb{I}(\omega_x,\omega_y)\right) \leq \pi \qquad \text{[Eq. A-4]}$$

$r(\omega_x,\omega_y)$ takes on the appropriate integer values to make $arg\left(\mathbb{I}(\omega_x,\omega_y)\right)$ a continuous surface. In summary, the cepstrum transform in the image domain implies a new Fourier transform whose real part is the log-magnitude of the original Fourier transform and whose imaginary part is the unwrapped phase of the original one.

A.2. Homomorphic deconvolution

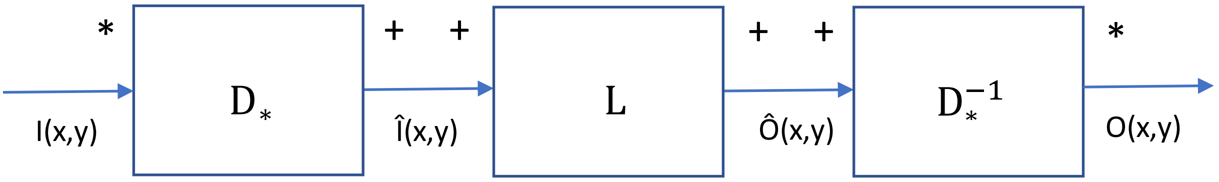

Figure A-1. Canonic form for homomorphic systems with convolution as the input and the output operations. See text for an explanation.

Figure A-1 shows the canonic representation of a homomorphic system that obeys a generalized principle of superposition for convolution, both at its input and at its output. Specifically, if the input is

$$I(x,y) = I_1(x,y) * I_2(x,y) \quad \text{[Eq. A-5]}$$

with $*$ being the convolution operation, then the corresponding output is

$$O(x,y) = O_1(x,y) * O_2(x,y) \quad \text{[Eq. A-6]}$$

with $O_1(x,y)$ and $O_2(x,y)$ being the outputs of the system to inputs $I_1(x,y)$ and $I_2(x,y)$, respectively. The use of such a system to remove or alter one of the components of a convolution is called *homomorphic deconvolution*.

$D_*[\cdot]$ represents the characteristic system for convolution, which means that, for an input expressed as in [Eq. A-5], then

$$\hat{I}(x,y) = \hat{I}_1(x,y) + \hat{I}_2(x,y) \quad \text{[Eq. A-7]}$$

In particular, $D_*[\cdot]$ can be chosen to be the complex cepstrum transform. Effectively, for an input which is the convolution of inputs, such as in [Eq. A-5], there is a multiplication relationship in the Fourier domain among inputs, such that

$$\mathbb{I}(\omega_x,\omega_y) = \mathbb{I}_1(\omega_x,\omega_y) \times \mathbb{I}_2(\omega_x,\omega_y) \quad \text{[Eq. A-8]}$$

and then, for the complex cepstrum's Fourier transform:

$$\begin{aligned}\hat{\mathbb{I}}(\omega_x,\omega_y) &= log[\mathbb{I}(\omega_x,\omega_y)] = log[\mathbb{I}_1(\omega_x,\omega_y)] + log[\mathbb{I}_2(\omega_x,\omega_y)] \\ &= \hat{\mathbb{I}}_1(\omega_x,\omega_y) + \hat{\mathbb{I}}_2(\omega_x,\omega_y)\end{aligned} \quad \text{[Eq. A-9]}$$

from which [Eq. A-7] follows by linearity of the inverse Fourier transform.

On the other hand, $D_*^{-1}[\cdot]$ is the inverse of the characteristic system for convolution and, equivalently, can be chosen to be the inverse of the complex cepstrum transform. For an image $\hat{O}(x,y)$ that is a sum of images and can be expressed as

$$\hat{O}(x,y) = \hat{O}_1(x,y) + \hat{O}_2(x,y) \quad \text{[Eq. A-10]}$$

or, in the Fourier domain, as

$$\hat{\mathbb{O}}(\omega_x,\omega_y) = \hat{\mathbb{O}}_1(\omega_x,\omega_y) + \hat{\mathbb{O}}_2(\omega_x,\omega_y) \quad \text{[Eq. A-11]}$$

then the inverse complex cepstrum transform implies an exponential operation in the Fourier domain, such that

$$\begin{aligned}\mathbb{O}(\omega_x,\omega_y) &= exp\left(\widehat{\mathbb{O}}(\omega_x,\omega_y)\right) = exp\left(\widehat{\mathbb{O}}_1(\omega_x,\omega_y) + \widehat{\mathbb{O}}_2(\omega_x,\omega_y)\right)\\ &= exp\left(\widehat{\mathbb{O}}_1(\omega_x,\omega_y)\right)\times exp\left(\widehat{\mathbb{O}}_2(\omega_x,\omega_y)\right)\\ &= \mathbb{O}_1(\omega_x,\omega_y)\times\mathbb{O}_2(\omega_x,\omega_y)\end{aligned} \qquad \text{[Eq. A-12]}$$

from where [Eq. A-6] follows in the image domain.

Finally, the middle box in Figure A-1, represented by L, is a linear filter in the usual sense; i.e., linear for the addition operation at its input and output. The class of linear *frequency-invariant* filters has proved to be most useful for deconvolution in this kind of systems. The point here is that, for an image $I(x,y)$ expressed as in [Eq. A-5], we might want to remove the effect of $I_2(x,y)$ and obtain $O(x,y) = I_1(x,y)$, which means that $\hat{O}(x,y) = \hat{I}_1(x,y)$. Now, the logarithm in equation [Eq. A-9] has a twofold effect over the input image $I(x,y)$. First, it converts the convolution in [Eq. A-5] into the sum in [Eq. A-7]. Second, logarithm in the Fourier domain widens the spectrum shapes (small magnitudes are amplified, whereas large magnitudes are not), and so shapes in the image domain should shrink. Hence, many a time, $\hat{I}_1(x,y)$ and $\hat{I}_2(x,y)$ will have nonoverlapping nonzero regions, either exactly or approximately, and can be separated by an operation of the type

$$\hat{O}(x,y) = L(x,y)\times\hat{I}(x,y) \qquad \text{[Eq. A-13]}$$

with $L(x,y)$ a linear frequency-invariant filter defined as

$$L(x,y) = \begin{cases}1, & (x,y) \in R\\ 0, & otherwise\end{cases} \qquad \text{[Eq. A-14]}$$

By appropriately choosing the nonzero region R, $\hat{I}_2(x,y)$ for example can be removed from $\hat{I}(x,y)$, leaving $\hat{O}(x,y) = \hat{I}_1(x,y)$.

The product in [Eq. A-13] means a convolution is performed in the Fourier domain, and so

$$\widehat{\mathbb{O}}(\omega_x,\omega_y) = \mathbb{L}(\omega_x,\omega_y) * \widehat{\mathbb{I}}(\omega_x,\omega_y) \qquad \text{[Eq. A-15]}$$

This is the interchange of roles between image and Fourier domains which was mentioned at the beginning of this appendix, and which justifies the term *cepstrum analysis* for this type of homomorphic deconvolution.

The following are examples of the use of this deconvolution technique. First, de-echoing examples of mono- and bi-dimensional signals will be shown. Then, simulated Shack-Harmann images of a single subaperture will be analysed to obtain their centroids with and without cepstrum technique.

A.3. De-echoing a unidimensional signal

Let us take as an example a triangular unidimensional sequence $t[n]$ with a rapid attack and a slower decay, that resembles the envelope of a typical acoustical signal. The signal is twenty-seven samples in length, but an echo is added with half of $t[n]$'s amplitude at sample twenty, and the total length becomes forty-six samples. So, in this deconvolution example, the input signal $i[n]$ is the convolution of a triangular signal $t[n]$ with a sum of two Dirac delta functions (Figure A-2-a, solid line):

$$i[n] = t[n] * (\delta[n] + 0.5\times\delta[n-20]) \qquad \text{[Eq. A-16]}$$

$t[n]$ and its echo are overlapping, with the echo being summed to the last portion of $t[n]$'s decay. By homomorphic deconvolution, an output $o[n]$ as close as possible to $t[n]$ is sought.

Let us call $i_2[n]$ the sum of the two Dirac delta functions, such that

$$i_2[n] = \delta[n] + 0.5\times\delta[n-20] \;\; \rightarrow \;\; i[n] = t[n] * i_2[n] \qquad \text{[Eq. A-17]}$$

and let us call $\hat{\imath}_2[n]$ to the complex cepstrum transform of $i_2[n]$. Now, the Fourier transform of a Dirac delta function $\delta[n]$ is unity, and the logarithm of the Fourier transform of $i_2[n]$ can be developed into a Taylor expansion of the logarithm function around unity. It is, then, straightforward to see that $\hat{\imath}_2[n]$ is a train of Dirac delta functions starting at sample 20 and continuing at samples multiple of 20, that is, 40, 60, etc., with zero value for $n < 20$. By defining a frequency-invariant linear filter $l[n]$ such that:

$$l[n] = \begin{cases} 1, & -19 \le n \le 19 \\ 0, & otherwise \end{cases} \qquad \text{[Eq. A-18]}$$

which is applied to the complex cepstrum of the input $\hat{\imath}[n]$ such that $\hat{o}[n] = l[n]\times\hat{\imath}[n]$, and finally, by inverting the cepstrum transform, an output $o[n]$ is obtained that is close to $t[n]$, as can be seen in Figure A-2-a (dashed line).

In the Fourier domain, the echo at the input of the deconvolution system translates into a ripple, both in the magnitude (Figure A-2-b, solid line) and in the phase (Figure A-2-c, solid line). A 1024-point FFT has been employed to shift to the Fourier domain, a large enough length to avoid aliasing effects in the cepstrum domain. Low pass frequency-invariant filtering means a convolution with $l[n]$'s Fourier transform in the Fourier domain, whose effect is seen at the output of the deconvolution system as the smoothing of the ripple present at the input (Figure A-2-b and Figure A-2-c, dashed lines).

In summary, a triangular unidimensional signal has been successfully separated from an overlapping echo by low pass frequency-invariant linear filtering in the cepstrum domain. This is equivalent to smoothing the ripple present in the magnitude and phase of the signal's Fourier transform.

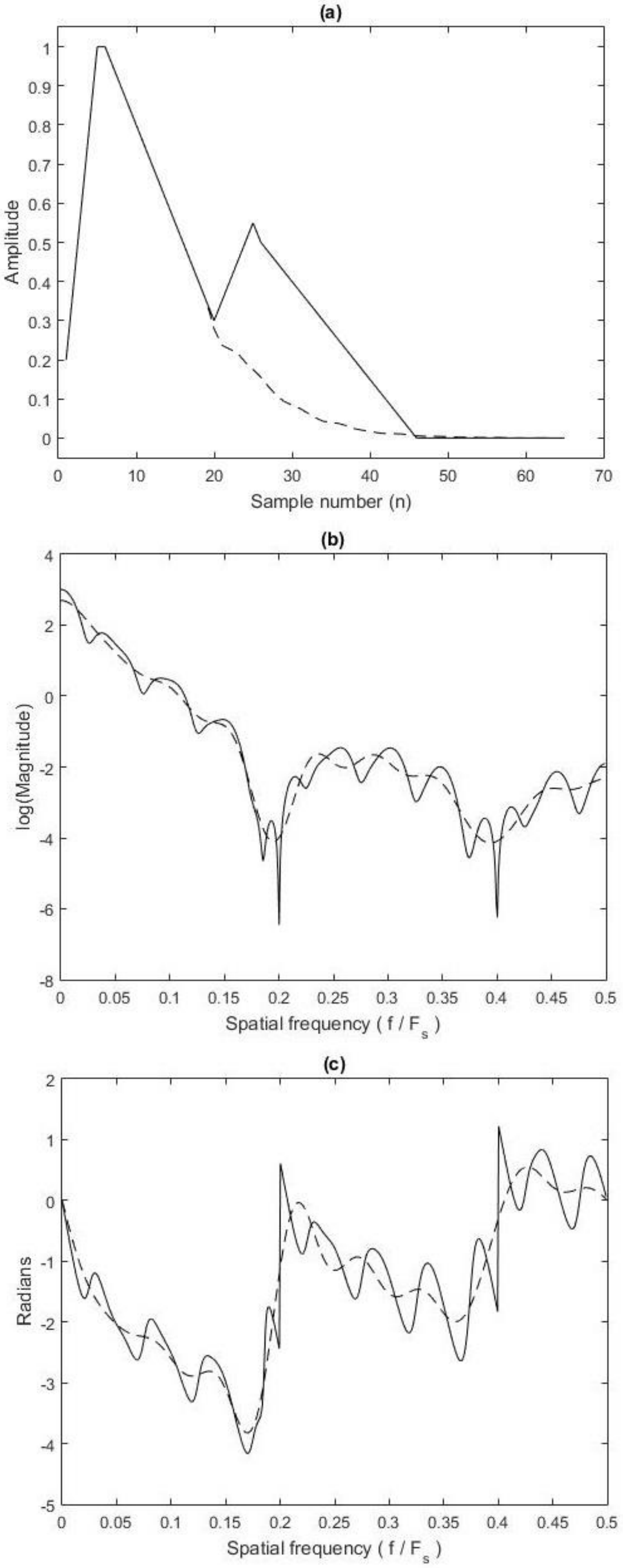

Figure A-2. Homomorphic deconvolution of a triangular sequence with an echo. (a) Input (solid line) and output (dashed line) sequences. (b) log-magnitude of the Fourier transform or, equivalently, real part of the complex cepstrum's Fourier transform of the input (solid line) and the output (dashed line). (c) Unwrapped phase of the Fourier transform or, equivalently, imaginary part of the complex cepstrum's Fourier transform of the input (solid line) and the output (dashed line).

A.4. De-echoing a bi-dimensional signal

Figure A-3-a illustrates a synthetic 2D Gaussian shape, symmetric with respect to its centre, with 10 samples of standard deviation both in the horizontal and the vertical axes, to which an overlapping echo at a distance of 20 samples in each axis and of half the amplitude of the main Gaussian has been added. Here, same as in the previous example, the objective of de-echoing the image by homomorphic deconvolution is pursued, and so, this is a bi-dimensional extension of the unidimensional case.

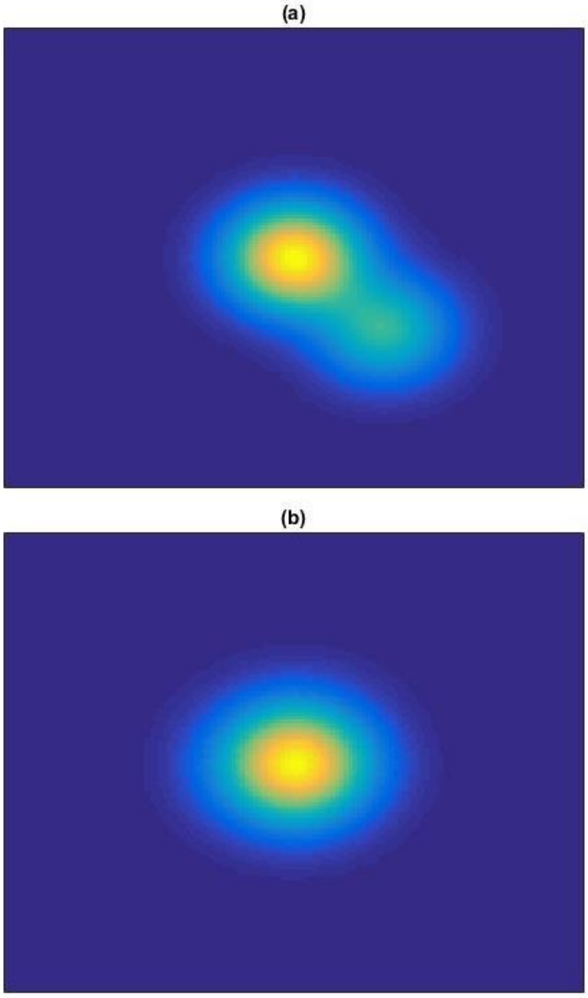

Figure A-3. 2D Gaussian shape with an echo before (a) and after (b) homomorphic deconvolution.

128-point by 128-point bi-dimensional FFT and inverse-FFT have been used to shift to the cepstrum domain, as this FFT's size is large enough to avoid aliasing effects. A 2D phase unwrapping function called *GoldsteinUnwrap2D_function.m* has been downloaded from the Mathworks' web page *File Exchange* section, in order to unwrap the 2D phase of the bi-dimensional Fourier transform of the image. This function implements the Goldstein's branch cut phase unwrapping method described in Goldstein, Zebken and Werner (1988) and in Ghiglia and Pritt (1998).

A bi-dimensional version of the frequency-invariant linear filter has been defined as:

$$L[x,y] = \begin{cases} 1, & -15 \leq x \leq 15 \\ & -15 \leq y \leq 15 \\ 0, & otherwise \end{cases} \qquad \text{[Eq. A-19]}$$

The result of homomorphic deconvolution and successful de-echoing is shown in Figure A-3-b.

A.5. De-noising Shack-Hartmann subaperture images

As explained in chapter 3, the algorithm object of study in the present work has two steps to estimate the centroid of a SHWFS subaperture image:

- Calculating the phase slope ([Eq. 3-14]) or, equivalently, the spot's displacement ([Eq. 3-15]) in the Fourier domain.
- Averaging the phase slopes with optimized weights $W_{k.l}^{x}$ and $W_{k.l}^{y}$ calculated with a MAP criterion according to equation [Eq. 3-23].

Though the weights for this second step are calculated in the first quadrant of the Fourier domain, since the image is real and, hence, its Fourier transform symmetric around zero spatial frequency, the weighting operation is actually applied over the four quadrants in a symmetric manner around zero spatial frequency. Besides, taking the phase slope at the origin of spatial frequencies or zero spatial frequency is equivalent to calculating the pure CoG in the image domain (equation [Eq. 3-12]). These facts lead us to the relationship between the proposed algorithm and deconvolution in the cepstrum domain: averaging the phase slope around the origin of spatial frequencies in the Fourier domain implies smoothing the Fourier's phase or, equivalently, low pass frequency-invariant linear filtering of the image in the cepstrum domain, and subsequently taking the CoG of the filtered image in the original domain.

The frequency-invariant linear filter $L[x,y]$ can be calculated from the weights $W_{k.l}^{x}$ and $W_{k.l}^{y}$ by replicating them in the four quadrants as necessary to get a pair of symmetric sets of weights around the spatial frequency origin; then normalizing each set to sum unity, and finally taking the bi-dimensional Fourier transform of both of them and multiplying:

$$L[x,y] = 2D\_FFT\{W_{4q}^{x}\} \times 2D\_FFT\{W_{4q}^{y}\} \qquad \text{[Eq. A-20]}$$

with W_{4q}^{x} and W_{4q}^{y} the extended symmetric and normalized sets of weights and $2D\_FFT$ the discrete version of the bi-dimensional Fourier transform as defined in equation [Eq. 3-13]. Symmetrisation of the weights guarantees that $L[x,y]$ is real, and their normalization guarantees that $L[x,y]$ equals unity at the origin. Multiplying both Fourier transforms in [Eq. A-20] means the phase in the Fourier domain is smoothed in both orthogonal axes.

Examples concerning three of the main reasons of measurement noise in the subaperture of a SHWFS as defined in point 1.2.2.2 will be presented here: the centroid anisoplanatism or phase high order aberrations in the spot, additive noise coming from the detector and spot's truncation due to limited FoV.

A.5.1. High order aberrations in the spot

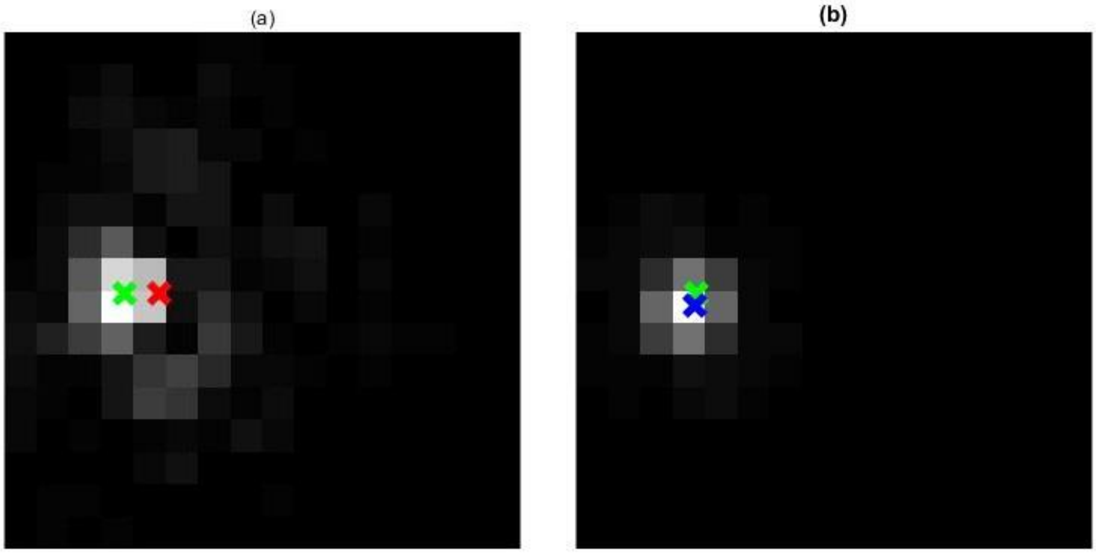

Figure A-4. (a) Simulated subaperture image for D_{sub}/r_0=2.5, FWHM(diff)=2 pixels, FoV=16x16 pixels, 5000 photons flux, CIC=0.05 e^-/pix/frame, G_{emccd}=80, RON=50 e^- rms. Green cross points to the perfect Z-tilt estimation; red cross is the image's CoG. Difference is mainly due to high order aberrations in the subpupil. (b) Same image after filtering in the cepstrum domain. Green cross points to the perfect Z-tilt estimation; blue cross is the image's CoG.

This example starts from a simulated SHWFS subaperture image sequence with a circular subaperture of a diameter size 2.5 times the Fried parameter, a FWHM of the spot at diffraction of 2 pixels in size, a FoV of 16 x 16 pixels in an open loop situation, a light flux regime of 5000 photons in the subaperture, a CIC noise of 0.05 e^-/pixel/frame, an EMCCD gain of 80 and a readout noise (RON) of 50 e^- rms. The employed simulation tool is described in chapter 4, section 4.1. Figure A-4-a shows one of the images so obtained, which presents a considerable amount of asymmetric high order phase aberration, which drags the CoG of the image (red cross) more than one pixel apart from the desired Z-tilt estimation (green cross).

Weights of the phase slope have been calculated at 4 x 4 spatial frequencies at the lowest frequencies border of the first quadrant of the Fourier domain, by employing the same simulation tool, and the linear frequency-invariant filter to be applied in the cepstrum domain has been calculated according to equation [Eq. A-20]. Result of the filtering is shown in Figure A-4-b at the original image domain. The distance between the CoG of the filtered image (blue cross) and the desired perfect Z-tilt estimation (green cross) has been much reduced in comparison to the unfiltered image. In a certain way, asymmetries in the subpupil phase which are not very pronounced will derive in a non-symmetrical diffused “tail” in the spot. This “tail” resembles a set of echoes or reverberation of the main spot and can be adequately dealt with by cepstrum deconvolution.

A.5.2. Low light flux level

This second example starts from a simulated SHWFS subaperture image sequence with a circular subaperture of a diameter size 2.5 times the Fried parameter, a FWHM of the spot at diffraction of 2 pixels in size, a FoV of 16 x 16 pixels in an open loop situation, a light flux regime of 50 photons in the subaperture, a CIC noise of 0.05 e^-/pixel/frame, an EMCCD gain of 1000 and a readout noise (RON) of 50 e^- rms. Figure A-5-a shows one of the images so obtained, which shows a spot near a corner of the FoV and spurious CIC noise randomly distributed across the FoV, with a considerable portion far apart from the spot. Thus, the CoG of the image is dragged towards its centre (red cross), at around 3 pixels of distance from the desired Z-tilt estimation (green cross).

A 3 x 3 set of weights has been calculated for each axis of the Fourier phase slope, and the frequency-invariant linear filter obtained through equation [Eq. A-20]. Result of the cepstrum filtering as reflected in the original image domain is shown in Figure A-5-b. The CoG of the filtered image (blue cross) is almost over the centre of the most luminous pixel, very much closer to the desired Z-tilt estimation (green cross) than before filtering. Spurious charge noise very much resembles echoes of the main spot, and can be tackled successfully by cepstrum low pass frequency-invariant filtering.

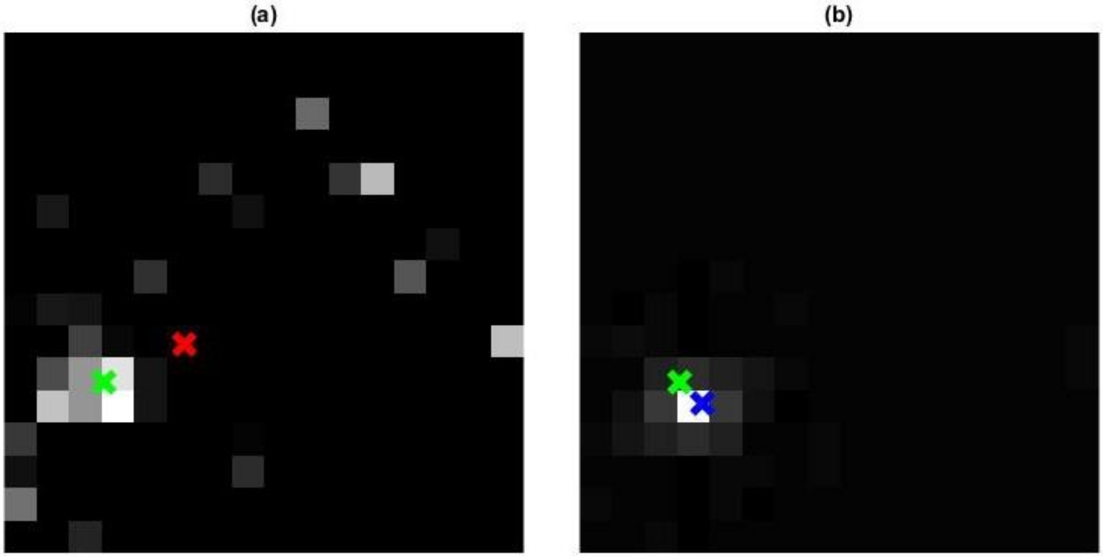

Figure A-5. (a) Simulated subaperture image for D_{sub}/r_0=2.5, FWHM(diff)=2 pixels, FoV=16x16 pixels, 50 photons flux, CIC=0.05 e^-/pix/frame, G_{emccd}=1000, RON=50 e^- rms. Green cross points to the perfect Z-tilt estimation; red cross is the image’s CoG. Difference is mainly due to spurious charge noise in a large FoV. (b) Same image after filtering in the cepstrum domain. Green cross points to the perfect Z-tilt estimation; blue cross is the image’s CoG.

A.5.3. Limited field of view

In this third example, the FoV has been reduced to 12 x 12 pixels in open loop observation and light flux regime is high, with 5000 photons over the subaperture. Rest of parameters are: a circular subaperture of a diameter size 2.5 times the Fried parameter, a FWHM of the spot at diffraction of 2 pixels in size, a CIC noise of 0.05 e^-/pixel/frame, an EMCCD gain of 80 and a readout noise (RON) of 50 e^- rms. Figure A-6-a shows one of the obtained images, selected such that the spot is at the border of the FoV, which easily happens due to the reduced FoV in comparison to the tilt of the spot at D_{sub}/r_0=2.5. Truncation of the spot leads to the CoG of the image to shift towards the centre of FoV (red cross) whereas the desired estimator of the Z-tilt is over the spot at the border of the FoV (green cross).

In this example, the image is zero padded to make up 16 x 16 pixels before shifting to the cepstrum domain with 16- x 16-point 2D_FFT's. Same size of 2D_FFT's are employed in the simulation tool to obtain a pair of sets of 4 x 4 weights for the Fourier phase slope, and the linear frequency-invariant filter is obtained through equation [Eq. A-20]. After filtering, the new CoG (blue cross in Figure A-6-b) is almost at the desired Z-tilt estimator position (green cross). This example is showing an increase in the sensed dynamic range of the SHWFS when the number of pixels in the detector imposes a limitation in the sensor's FoV. Truncation of the spot can be seen as the sum with a negative echo, and therefore is adequately dealt with by cepstrum deconvolution.

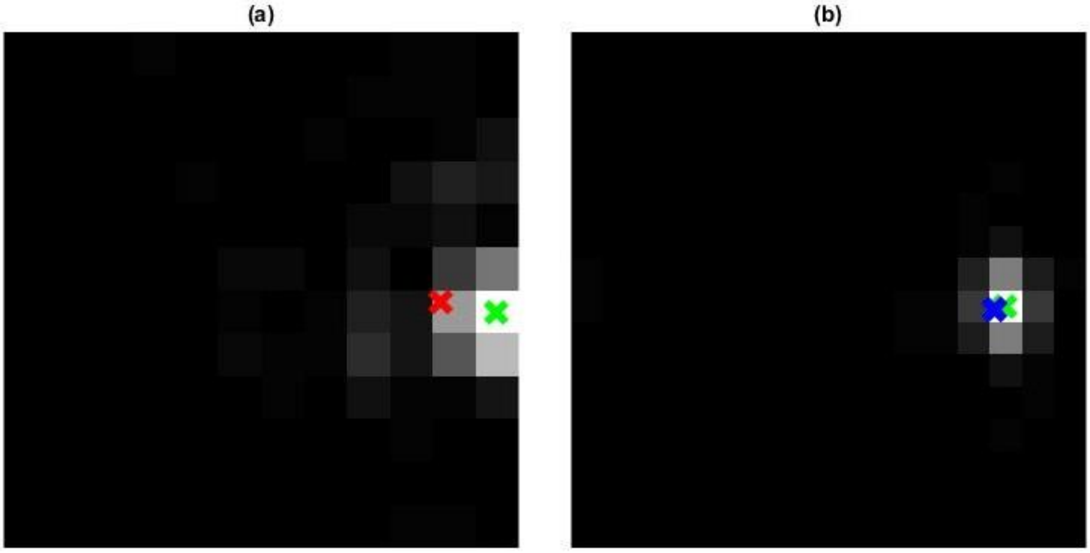

Figure A-6. (a) Simulated subaperture image for D_{sub}/r_0=2.5, FWHM(diff)=2 pixels, FoV=12x12 pixels, 5000 photons flux, CIC=0.05 e^-/pix/frame, G_{emccd}=80, RON=50 e^- rms. Green cross points to the perfect Z-tilt estimation; red cross is the image's CoG. Difference is mainly due to truncation of the spot in a limited FoV. (b) Same image after filtering in the cepstrum domain, employing 16x16-point 2D-FFT's. Green cross points to the perfect Z-tilt estimation; blue cross is the image's CoG.

Appendix B. Characterization of EDiFiSE's EMCCD camera

The gain and noise model of the EMCCD (Electronic Multiplying Charge Coupled Device) detector has been taken from Hirsch et al, 2013, and explained in point 4.1.3. This model has been utilized in the simulations at subpupil level shown in chapter 4, and in those at the entire pupil level shown in chapter 5. When tuning by simulations the WFPS algorithm to be used in a real AO system, as it was done in chapter 6, and this applies to any other algorithm too, it is important to properly model the real EMCCD detector that is going to create the SHWFS images. This means, a proper estimation of its quantum efficiency q, Clock Induced Charge (CIC) noise c, EMCCD gain g, Read Out Noise (RON) r, and sensitivity f. The purpose of the present appendix is to explain how these parameters have been estimated in the context of the present work. This characterization has been done over the EDiFiSE's Andor iXon 860 detector with serial number X-4131.

The quantum efficiency q value has been taken from the detector's manufacturer specifications, in the same way as it was done in the work reported at Hirsch et al, 2013. Concretely, the value 0.97 or 97% has been employed throughout this work, which is the value at the peak of the quantum efficiency curve and a good approximation for the wavelength range from ∼500 to ∼650 nm. This means that the assumption has been made in the simulations throughout this work that the sensing wavelength is somewhere in the mentioned range. It also means that, when incident photons have been estimated in chapter 6, again the simplifying assumption of the light being concentrated in this wavelength range was made.

For the sensitivity estimation, the mean-variance method is proposed at Hirsch's paper, which can be expressed as:

$$\hat{f} = \bar{n}_{ic} / \sigma_{n_{ic}}^2 \qquad \text{[Eq. B-1]}$$

with $\bar{n}_{ic}$ the mean of image counts level and $\sigma_{n_{ic}}^2$ its variance. Here, the assumptions are made that the EMCCD gain is turned off and that the image counts variance is dominated by Poisson distributed noise. This implies a high light level, well above RON, and a well stabilized light source. This last condition was not met in the present work's case, because the characterization was made in-situ, in the same setup described in point 6.2.1, and not in any specifically designed characterization setup. A workaround was therefore needed, and this is explained in the following paragraphs.

As for the EMCCD gain, a similar mean-variance method is proposed again at Hirsch's paper, according to the following expression:

$$\hat{g} = f\,\frac{\sigma^2_{n^g_{ic}}}{2\bar{n}^g_{ic}} \qquad \text{[Eq. B-2]}$$

where the superscript g has been added to $\bar{n}_{ic}$ just to indicate that the image counts are obtained with the EMCCD gain applied. Here again the assumption is made that Poisson noise dominates, which is easily achieved when applying a moderate gain. Also, by applying the gain, acquired image sequences will span a much shorter time period than for the sensitivity estimation for the same final light level, and hence stability of the light source for such shorter periods is easily achieved. The factor of 2 in the denominator of [Eq. B-2] is the so called Excess Noise Factor (ENF), which has been seen to be of this value for gains over 100 (Robbins and Hadwen, 2003), and is a consequence of the Electronic Multiplication stochastic process.

Another method to estimate the EMCCD gain could simply be to compute the ratio of light levels with and without applied gain:

$$\hat{g} = \frac{\bar{n}^g_{ic}}{\bar{n}_{ic}} \qquad \text{[Eq. B-3]}$$

In this case, any offset applied by the electronics of the detector should be subtracted from the measured signal. This second method of gain estimation has the advantage to be independent of sensitivity estimation. In the present work, the method in equation [Eq. B-3] has been utilized first, and then the method in equation [Eq. B-2] has been employed to estimate the sensitivity value, by equalling the estimated gains obtained by both methods. This has been done for five values of programmed EMCCD gains and with the detector cooled at -80ºC. The measured gains and sensitivity values obtained thereof are listed in Table B-1.

Programmed G_{emccd}	***Measured G_{emccd}***	***Sensitivity f in e^-/ADU***
10	8.6	16.35
100	80.63	15.72
300	226.10	15.47
500	385.99	16.08
1000	860.15	17.80

Table B-1. Measured EMCCD gains vs. programmed gains, and sensitivity values obtained thereof.

It is necessary for the estimation of the detector noises to have an estimated sensitivity value, as will be seen further on. A sensitivity value of 16 e^-/ADU has been selected. As for the EMCCD gain, the value obtained by equation [Eq. B-2] with the mentioned sensitivity of 16 will be taken as the estimated gain.

Till now, the sensitivity and gain parameters have been estimated from illuminated images. Noise parameters need to be estimated from dark images. In Hirsch et al, 2013, the employed estimation method for the noise parameters is the Maximum Likelihood (ML) method, or maximization of the log-likelihood function, given the observation of a series of dark images and assuming a concrete parametric model for dark images, with c, g, r and f as the parameters, and with a Poisson, a gamma and a normal components, as explained in point 4.1.3. The sensitivity f and the gain g are obtained by mean-variance methods over illuminated images (equations [Eq. B-1] and [Eq. B-2], respectively). Read out noise r and CIC noise c are determined jointly by maximization of the mentioned likelihood function.

In the present work, noises are estimated by minimization of the difference between the observed histogram of a dark image sequence and the histogram obtained from the parametric model proposed in Hirsch's work. The difference with the mentioned work is that only one parameter is estimated, which is the bias offset at the dark image, and the r and c noise components are obtained as a function of the observed values and the estimated offset. This is done on a pixel by pixel basis over a selection of random pixels throughout the whole image, and final values are obtained by averages among all evaluated pixels. This method was validated by characterizing other detectors from the same manufacturer, in a work by a student at the IAC and co-tutored by the author (Pinna F., 2014).

After offset subtraction in an observed dark image, negative image counts are due to negative normal RON exclusively. Therefore, r in rms electron units can be estimated from such negative image counts as:

$$\hat{r} = f\left[\overline{(n_{ic} - offset)^2}\right]^{1/2} \quad „ \qquad n_{ic} < offset \qquad \text{[Eq. B-4]}$$

Whereas CIC noise is the reason for a positive mean in the observed dark image[18], and can therefore be estimated in electron units as:

$$\hat{c} = (\bar{n}_{ic} - offset)\, f/g \qquad \text{[Eq. B-5]}$$

Finally, the electronic offset is estimated by the minimization of the distance between the probability density function (PDF) obtained from the observed dark image counts and the one obtained from the model at Hirsch's work:

$$\varepsilon_p = \int \left| p(n_{ic}; observed) - p(n_{ic}; q, c, g, r, f, offset) \right| dp \qquad \text{[Eq. B-6]}$$

$p(n_{ic}; observed)$ is the PDF which depends only on the observed values in the dark image, and $p(n_{ic}; q, c, g, r, f, offset)$ is the parametric model from Hirsch's paper with an *offset* added. q, g and f are determined as previously explained. c and r are estimated by equations [Eq. B-5] and [Eq. B-4], respectively. And so, the only left parameter to estimate is the *offset*,

---

[18] Dark images were taken with the detector's shutter off.

and this is accomplished by minimizing ε_p. By multiplying ε_p by 100, a histogram relative fitting error in percentage units is obtained.

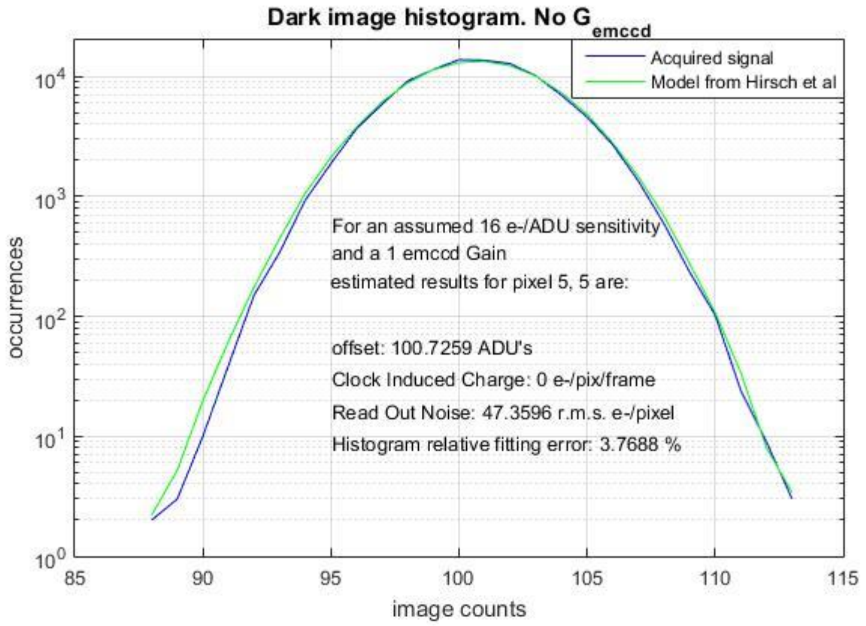

Figure B-1. Histograms of dark images for a situation without EMCCD gain. Blue trace is for a real acquired signal from a single pixel of EDiFiSE's SHWFS detector. Green trace is for a simulated signal following the EMCCD model described in Hirsch et al, 2013.

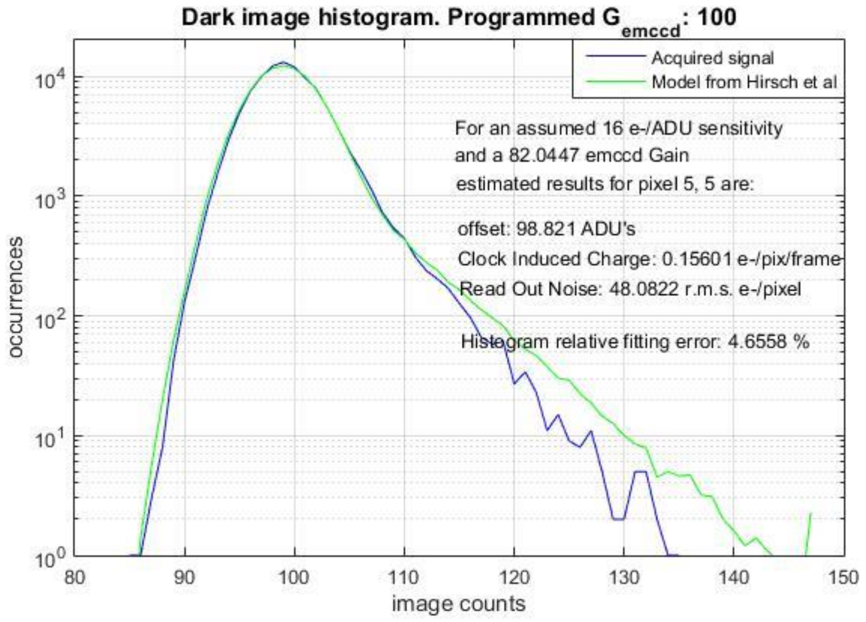

Figure B-2. Histograms of dark images for a situation with programmed EMCCD gain of 100. Blue trace is for a real acquired signal from a single pixel of EDiFiSE's SHWFS detector. Green trace is for a simulated signal following the EMCCD model described in Hirsch et al, 2013.

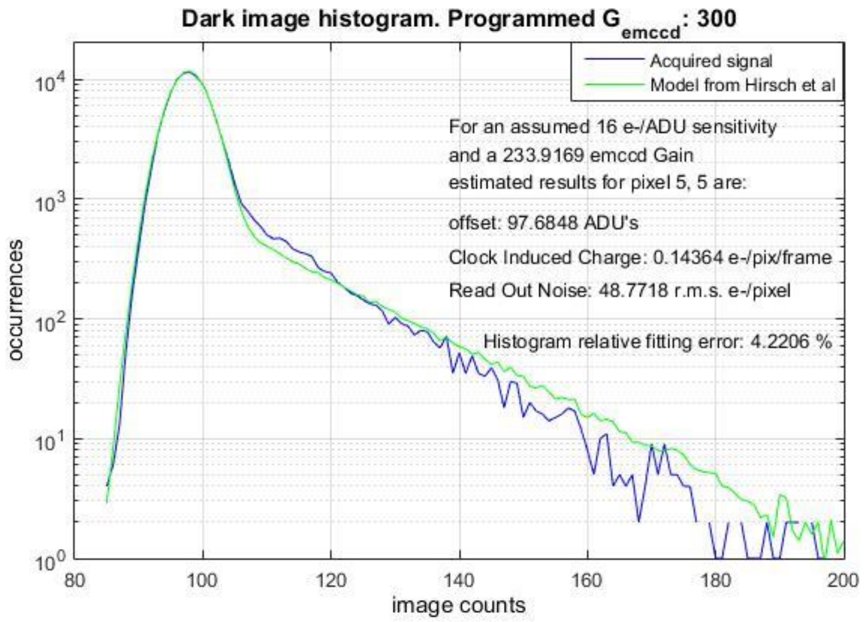

Figure B-3. Histograms of dark images for a situation with programmed EMCCD gain of 300. Blue trace is for a real acquired signal from a single pixel of EDiFiSE's SHWFS detector. Green trace is for a simulated signal following the EMCCD model described in Hirsch et al, 2013.

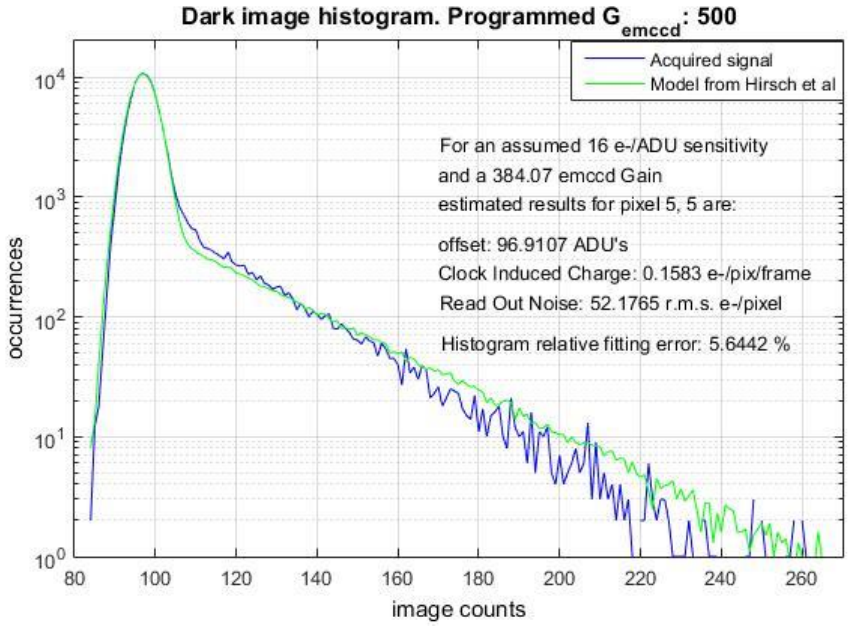

Figure B-4. Histograms of dark images for a situation with programmed EMCCD gain of 500. Blue trace is for a real acquired signal from a single pixel of EDiFiSE's SHWFS detector. Green trace is for a simulated signal following the EMCCD model described in Hirsch et al, 2013.

Figures B-1 to B-5 show the results of a dark image histogram fitting for a single pixel and programmed EMCCD gains of 1 (no gain), 100, 300, 500 and 1000. Blue traces are for the observed image counts, and green traces are from the parametric model. It is interesting to see how, for the tails due to CIC noise, the model always gives less occurrences for lower image counts and more occurrences for higher image counts. This is quite probably because the model assumes that CIC noise is only produced in the charge transfers before the EM register, whereas actually some CIC noise is produced in the EM register itself and is affected by lower EMCCD gains than the total gain.

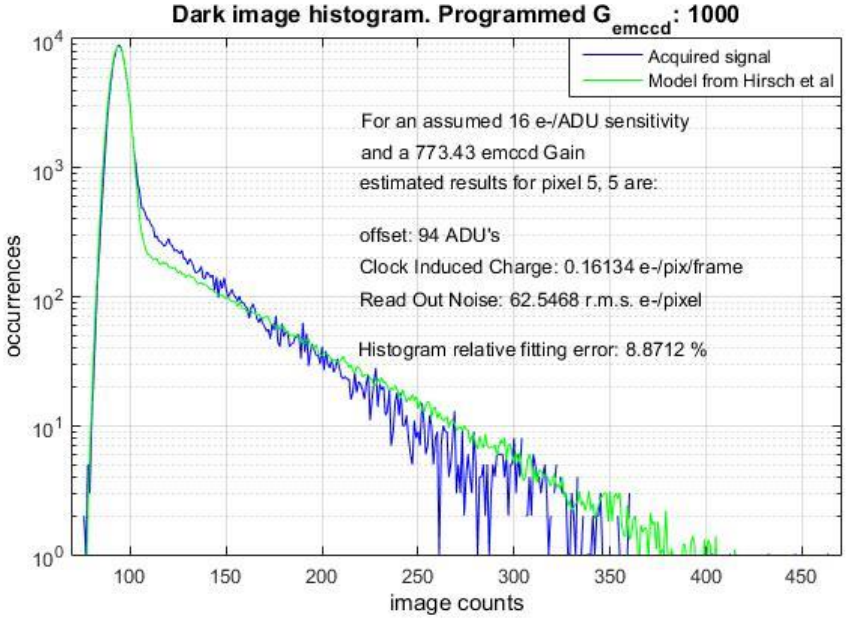

Figure B-5. Histograms of dark images for a situation with programmed EMCCD gain of 1000. Blue trace is for a real acquired signal from a single pixel of EDiFiSE's SHWFS detector. Green trace is for a simulated signal following the EMCCD model described in Hirsch et al, 2013.

Programmed ***G_{emccd}***	***Estimated*** ***G_{emccd}***	***CIC (e^-)***	***RON*** ***(rms e^-)***	***Estimated*** ***offset***	***ε_p*** ***(%)***
1	1	0	47.36	100.7	3.77
100	82.04	0.156	48.08	98.8	4.66
300	233.92	0.144	48.77	97.7	4.22
500	384.07	0.158	52.18	96.9	5.64
1000	773.43	0.161	62.55	94.0	8.87

Table B-2. Estimated offset and subsequent CIC and RON values obtained by dark images histogram fitting for the listed programmed EMCCD gains.

Table B-2 collects the results for offset, CIC and RON estimation from the previous figures. Also, the gains introduced in the parametric model are listed, as well as the final histogram fitting error.

Finally, a good approximation for the parameters introduced in the model of EDiFiSE's SHWFS detector have been: a sensitivity of 16 e^-/ADU; a gain which is 20% less than the programmed one, i.e., 160 for a programmed gain of 200, and 800 for a programmed 1000 gain; a CIC noise of 0.155 e^-/pixel/frame; a RON of 50 rms e^-; and a QE of 97%.